MICROTECHNOLOGY AND MEMS

MICROTECHNOLOGY AND MEMS

Series Editors: H. Fujita   D. Liepmann

The series Microtechnology and MEMS comprises text books, monographs, and state-of-the-art reports in the very active field of microsystems and microtechnology. Written by leading physicists and engineers, the books describe the basic science, device design, and applications. They will appeal to researchers, engineers, and advanced students.

R.G. Ballas

Piezoelectric Multilayer Beam Bending Actuators

Static and Dynamic Behavior
and Aspects of Sensor Integration

With 143 Figures and 17 Tables

Springer

Dr. Rüdiger G. Ballas
Darmstadt University of Technology
Institute for Electromechanical Design
Merckstraße 25
64283 Darmstadt
Germany
e-mail: r.ballas@emk.tu-darmstadt.de

Series Editors:

Prof. Dr. Hiroyuki Fujita
University of Tokyo, Institute of Industrial Science
4-6-1 Komaba, Meguro-ku, Tokyo 153-8505, Japan

Prof. Dr. Dorian Liepmann
University of California, Department of Bioengineering
6117 Echteverry Hall, Berkeley, CA 94720-1740, USA

Dedicated to my parents Helga and Egon Ballas

Preface

In recent years, solid state devices utilizing piezoelectric effects have drawn much attention both scientifically and technologically because piezoelectric actuators, sensors and transducers have been widely used in many electromechanical applications including active and passive vibration damping, ultrasonic motors, ultrasonic biomedical imaging, loudspeakers, accelerometers, resonators, micropositioner, acoustic sensor, etc. Many new devices and applications are explored intensively, and many new technological developments based on these devices are emerging. In the field of piezoelectric actuators, one of the major parts is represented by beam bending actuators, which are in the focus of the book.

The broad field of industrial applications for piezoelectric beam bending actuators as actuating and high precision positioning systems necessitates an adjustment of their performance for the particular task. Regarding piezoelectric beam benders in multilayer technology, a deeper inside look and understanding of their mechanical, elastic and electromechanical characteristics is required. This deeper understanding discloses the possibility of making statements about the beam bender's static and dynamic behavior and its influencing by appropriate measures within the scope of structural mechanics.

The book is divided into five parts. Part 1 gives an introduction to the topic and highlights the individual aspects presenting the focus of the book. Part 2 consists of chapters 2 to 7. In these chapters, theoretical approaches concerning the description of the static and dynamic behavior of piezoelectric multilayer beam bending actuators are discussed in detail. The achieved results are represented in closed form analysis. Part 3 of the book dwells on the experimental characterization of piezoelectric bending actuators represented in the chapters 8 and 9. Different static and dynamic characteristics of a realized bending actuator are determined experimentally and compared with analytical calculations based on the theoretical considerations made before. Part 4 of the book consists of chapters 10 to 12 addressing the sensor inte-

gration into a piezoelectric bending actuator. By means of both, a capacitive and inductive displacement sensor, the tip deflection of a bending actuator is measured. The aspect of sensor integration allows for new applications where high-accuracy positioning is required. Part 5 of the book contains a detailed appendix with important mathematical and physical aspects, that would go beyond the scope of the book's mainmatter. The book is suitable as a reference for graduate students, engineers and scientists working in industry and academia. An introductory course on meachanics of materials, elasticity, theoretical mechanics, electronics and network theory should prove to be helpful but not necessary because the basics are included in the relevant chapters.

Darmstadt, November 2006   *Rüdiger G. Ballas*

Contents

Part V Appendix

List of Symbols

Symbol	Quantity	Unit
A	surface	m^2
$\mathbf{A}$	two-port network	
A_i	surface of the ith layer	m^2
A_{tot}	total gain factor	1
A_ν	flux cross-section in section ν	m^2
A_0, A_1, A_2	gain factors	1
$\underline{A}_1, \underline{A}_2$	integration constants	A
a	coil radius	m
$\underline{a}$	acceleration	m s^{-2}
a_j	coefficient (ansatz function)	
a, c	crystal axes	
a_1, b_1	coefficients	
$\mathbf{B}$	vector of magnetic induction	T
B_0	transfer coefficient	V F^{-1}
B_ν	magnetic induction in section ν	T
B_{n1}, B_{n2}	normal components of the mag. induction	T
$\underline{B}_0$	total transfer function	1
$\underline{B}_1, \underline{B}_2, \underline{C}_1$	integration constants	A
$\underline{B}_3, \underline{B}_4, \underline{B}_g$	transfer functions	
b	width (dielectric)	m
C	flexural rigidity	N m^2
	capacitance	F
C_b	translatory fixed capacitance	F
C_{tot}	total capacitance	F
C_i	capacitance of layer i	F
C_{ref}	reference capacitance	F
C_x	capacitance to be measured	F
C'_F, C'_{Piezo}	capacitance per unit length	F m^{-1}
C_0, C_T, C_{x0}	nominal capacitance	F

Symbol	Quantity	Unit
c_{pq}^E	modulus of elasticity at const. elec. field	$\mathrm{N\,m^{-2}}$
c_{ijkl}, c_{pq}, E	modulus of elasticity	$\mathrm{N\,m^{-2}}$
D	Rayleigh's dissipation function	$\mathrm{J\,s^{-1}}$
	finger width (interdigital structur)	m
$\mathbf{D}$	vector of electric displacement	$\mathrm{C\,m^{-2}}$
$D_j, \underline{D}_j$	component of elec. displacement vector	$\mathrm{C\,m^{-2}}$
$D_{j,i}, \underline{D}_{j,i}$	component of elec. displacement (ith layer)	$\mathrm{C\,m^{-2}}$
d_a	planar coil distance	m
d_b	effective diameter (planar coils)	m
d_{Fe}	layer thickness (iron core)	m
d_{air}	air gap	m
d_{Ni}	layer thickness (thermal adjustment layer)	m
d_{jq}	piezoelectric coefficient	$\mathrm{m\,V^{-1}}$
$d_{jq,i}$	piezoelectric coefficient (ith layer)	$\mathrm{m\,V^{-1}}$
$d_F, d_{F,1}$	interdigital periode	m
$\mathbf{E}$	vector of electric field	$\mathrm{V\,m^{-1}}$
E_c	coercive field strength	$\mathrm{V\,m^{-1}}$
$E_j, \underline{E}_j$	components of electric field vector	$\mathrm{V\,m^{-1}}$
$E_{j,i}, \underline{E}_{j,i}$	comp. of elec. field vector (ith layer)	$\mathrm{V\,m^{-1}}$
e_{iq}	piezoelectric modulus	$\mathrm{C\,m^{-2}}$
$\mathbf{e}_r, \mathbf{e}_\varphi, \mathbf{e}_z$	unit vectors (cylindrical coordinates)	
$\mathbf{e}_x, \mathbf{e}_y, \mathbf{e}_z$	unit vectors (Cartesian coordinates)	
F	force, extensive quantity	N
$\mathbf{F}$	force vector	N
F_b	actuator force	N
F_G	total error	
F_j	components of force vector	N
F_N	axial force	N
F_Q	lateral force	N
F_{tot}	total force	N
F_{Hys}	hysteresis error	
$\mathbf{F}_i^{(ext)}$	vector of ext. force on mass point i	N
$\mathbf{F}_i^{(r)}$	vector of frictional force on mass point i	N
$\mathbf{F}_i^{(z)}$	vector of constraining force on mass point i	N
F_j	components of force vector	N
$\mathbf{F}_{ij}$	interaction force	N
$F_{j,i}$	axial force in the ith layer	N
F_{Lin}	linearity error	
$\underline{F}_r$	frictional force	N
$\underline{F}_s$	force generated by a bender's tip	N
F_{Piezo}	piezoelectric force	N
$\mathbf{F}_i, \mathbf{F}_i^{(a)}$	force applied on mass point i	N
$\underline{F}, \underline{F}_1, \underline{F}_2$	force (translatory flow quantity)	N
f_0	resonant frequency	Hz
f_A	force per unit area	$\mathrm{N\,m^{-2}}$
f_e	effective frequency	Hz

Symbol	Quantity	Unit
f_s	switching frequency	Hz
f_T	carrier frequency	Hz
f_u	lower frequency	Hz
$f_{\max}$	maximum frequency	Hz
f_{meas}	measured frequency	Hz
f_{mod}	modulation frequency	Hz
f_{Piezo}	piezoelectric force per voltage	$\mathrm{N\,V^{-1}}$
$f, \underline{f}$	load per unit length	$\mathrm{N\,m^{-1}}$
f_1, f_2	eigenfrequencies	Hz
f_{Mess1}, f_{Mess2}	measured frequencies	Hz
f_{osc1}, f_{osc2}	resonant frequencies	Hz
$f_{out}, \underline{f}_{out}, f_{schmitt}$	output frequencies (ASIC)	Hz
f_x, f_y, f_z	volume forces	$\mathrm{N\,m^{-3}}$
G_x	parallel conductance of capacitance	S
g	gravitational acceleration	$\mathrm{m\,s^{-2}}$
$\mathbf{H}$	vector of magnetic field	$\mathrm{A\,m^{-1}}$
$\mathbf{H}, \underline{\mathbf{H}}$	admittance matrix	
H_e	electrical enthalpy	$\mathrm{J\,m^{-3}}$
H_ν	magnetic field in section ν	$\mathrm{A\,m^{-1}}$
$H_{e,i}$	electrical enthalpy of the ith layer	$\mathrm{J\,m^{-3}}$
$\underline{H}_{coil}, \underline{H}'_{coil}$	magnetic field in the circular loop plane	$\mathrm{A\,m^{-1}}$
H_{t1}, H_{t2}	tangential components of magnetic field	$\mathrm{A\,m^{-1}}$
$\underline{H}(t), \underline{H}'(t)$	complex time function of magnetic field	$\mathrm{A\,m^{-1}}$
h	layer thickness (inductive sensor layer)	m
h_i	height of ith layer	m
h	layer thickness (piezoelectric sensor layer)	m
$h_{ij}, \underline{h}_{ij}$	matrix elements of the admittance matrix	
$h_{i,o}$	upper distance of ith layer from neutral axis	m
$h_{i,u}$	lower distance of ith layer from neutral axis	m
h_0, h_1	layer thickness (dielectrics)	m
$\underline{h}, \underline{h}_1, \underline{h}_2$	mechanical admittance	$\mathrm{s\,kg^{-1}}$
I_{coil}	coil current	A
I_{yy}	geometrical moment of inertia	$\mathrm{m^4}$
$\underline{I}(t)$	complex time function of current	A
$\underline{I}, \underline{L}_1, \underline{L}_s$	complex current amplitudes	A
$\underline{i}$	current (electric flow quantity)	A
i_s	eddy current	A
$\underline{i}_w$	transducer current	A
i_1, i_2	alternating current	A
i, j	summation indices	
$\mathbf{J}$	vector of current density	$\mathrm{A\,m^{-2}}$
J_0, J_1	Besselfunctions of first kind (order 0 and 1)	
K_{NI}	motor parameter	$\mathrm{N\,A^{-1}}$
k	wavenumber	$\mathrm{m^{-1}}$
	amount of ansatz functions	
	k-factor	1
k_m	wavenumber of the mth eigenmode	$\mathrm{m^{-1}}$

Symbol	Quantity	Unit
$k\left(x\right)$	coupling factor (transformer)	1
$k_{31,i}^2$	electromechanical coupling factor	1
L	Lagrangian function	J
	inductance of magnetic circuit	H
L_0	nominal inductance	H
	overlap (interdigital structure)	m
L_e	effective inductance	H
L_s	inductance (inductive sensor layer)	H
L_1, L_2	inductances	H
l	length of bending actuator	m
	length of coil	m
	length of dielectric	m
l_ν	average length of field line	m
M	bending moment, extensive quantity	N m
$M\left(x\right)$	mutual inductance	H
$\mathbf{M}$	coupling matrix	
M_{tot}	total moment	N m
$\underline{M}_w$	transducer moment	N m
m	vibrational mode	
	symbol for a symmetry plane	
m_A	moment per unit area	$\mathrm{N\,m^{-1}}$
m_i	point mass	kg
m_{ij}	matrix element of the coupling matrix	
M_{Piezo}	piezoelectric moment	N m
m_{Piezo}	piezoelectric moment per voltage	$\mathrm{N\,m\,V^{-1}}$
$\underline{M}, \underline{M}_1, \underline{M}_2$	moment (rotatory flow quantity)	N m
N_e	amount of carrier	1
N_F	amount of interdigital periods	1
n	amount of layers	1
n_0	translatory reference compliance	$\mathrm{m\,N^{-1}}$
n_R	torsional compliance	$\mathrm{N^{-1}\,m^{-1}}$
n_R'	torsional compliance per unit length	$\mathrm{N^{-1}\,m^{-2}}$
n_{Rk}	torsional short-circuit compliance	$\mathrm{N^{-1}\,m^{-1}}$
N, N_1, N_2	turns	1
$\mathbf{P}$	vector of electrical polarization	$\mathrm{C\,m^{-2}}$
$\mathbf{P}_r$	vector of remanent polarization	$\mathrm{C\,m^{-2}}$
$\mathbf{P}_s$	vector of spontaneous polarization	$\mathrm{C\,m^{-2}}$
p	pressure load, extensive quantity	bar
	amount of holonomic constraints	
$\mathbf{p}_i$	impuls of mass point i	N s
Q	charge	C
	thermal energy density	$\mathrm{J\,m^{-3}}$
	Q-factor	1
$\underline{Q}$	charge (complex)	C
Q_j	generalized force	
Q_m	Q-factor of the mth vibrational mode	1
Q_{tot}	total charge	C

Symbol	Quantity	Unit
$\tilde{Q}$	thermal energy	J
$Q_j^{(ext)}$	external generalized force	
$Q_j^{(k)}$	conservative generalized force	
$Q_j^{(r)}$	generalized frictional force	
$Q_i, \underline{Q}_i$	charge in the ith layer	C
q	amount of periods	1
	transformation ratio	m
q_j	generalized coordinate	
$\dot{q}_j$	generalized velocity	
R	resistance	Ω
R_e	effective resistance	Ω
R_m	magnetic resistance	$\mathrm{A\,Wb^{-1}}$
R_s	resistance (inductive sensor layer)	Ω
R_{int}	resistance (integrator)	Ω
r	radius	m
	coefficient of friction	$\mathrm{N\,s\,m^{-1}}$
$\mathbf{r}$	position vector	m
$\mathbf{r}_d$	difference vector	m
r_a	coefficient of friction per unit length	$\mathrm{N\,s\,m^{-2}}$
r, φ, z	cylindrical coordinates	
R_2, R_{ref}	resistance of potentiometer	Ω
R_{air}, R_{Ni}, R_{Fe}	magnetic resistances	$\mathrm{A\,Wb^{-1}}$
R_1, R_2, R_3, R_4	resistances (Wheatstone bridge)	Ω
S	mechanical strain	1
	degrees of freedom	
	integral of action	
$\overline{S}$	average mechanical strain	1
$\underline{S}$	mechanical strain (complex)	1
S_r	remanent strain	1
S_{ij}, S_p	strain tensor	1
$\tilde{S}, \tilde{C}, \tilde{s}, \tilde{c}$	Rayleigh functions	
s_n	standardized frequency	1
s_{pq}^E	elastic compliances at const. elec. field	$\mathrm{m^2\,N^{-1}}$
$s_{pq,i}$	elastic compliance of the ith layer	$\mathrm{m^2\,N^{-1}}$
$s_{pq,i}^E$	elast. compl. of ith layer at const. el. field	$\mathrm{m^2\,N^{-1}}$
s_{ijkl}, s_{pq}	elastic compliances	$\mathrm{m^2\,N^{-1}}$
T	kinetic energy	J
	oscillation period	s
	temperature	K
$\mathbf{T}$	vector of mechanical stress	$\mathrm{N\,m^{-2}}$
T_0	room temperature	K
T_C	Curie temperatur	K
T_{ij}, T_q	stress tensor	$\mathrm{N\,m^{-2}}$
$T_{q,i}, \underline{T}_{q,i}$	mechanical stress in the ith layer	$\mathrm{N\,m^{-2}}$
t	time	s
U	voltage, extensive quantity	V
	internal energy density	$\mathrm{J\,m^{-3}}$

Symbol	Quantity	Unit
U	bridge voltage	V
U_s	driving voltage	V
$\tilde{U}$	internal energy	J
$\underline{U}_0$	voltage (circuit representation of a transformer)	V
$\underline{U}_e$	driving voltage	V
$\hat{U}_e$	peak value	V
U_{DC}	DC offset	V
U_{agl}	rectified voltage	V
U_{force}	controller signal	V
U_{pos}	position proportional voltage	V
$U_{\max}$	maximum driving voltage	V
U_{Range}	voltage range	V
U_{set}	set value	V
U_{0x}	DC offset of sensor electronics component x	V
U_0, U_{offset}	offset voltage	V
$\underline{U}_a, \underline{U}_{a1}, \underline{U}_{a2}$	output voltages	V
$\mathbf{u}$	vector of total displacement	m
u	eigenvalues (continuous spectrum)	m^{-1}
u_0	displacement in x-direction	m
	voltage amplitude	V
u_n	eigenvalues (discret spectrum)	m^{-1}
$u_{f/U}$	output voltage (f/U converter)	V
$\underline{u}$	voltage (electrical difference quantity)	V
$\underline{u}_N$	nominal voltage	V
$\underline{u}_{mod}$	modulation voltage	V
$\underline{u}_{mod,ss}$	peak-to-peak voltage (modulation voltage)	V
$\underline{u}_{net}$	output voltage network analyzer	V
$\underline{u}_{Piezo}$	output voltage amplifier stage	V
$\underline{u}_{tri}$	output voltage laser triangulator	V
u_1, u_2	voltages (transformer)	V
u, v, w	displacement	m
V	volume	m^3
	volume displacement	m^3
	potential energy, potential function	J
V_0, V_1	volume (dielectrics)	m^3
$\mathbf{v}_i$	vector of velocity of mass point i	m s^{-1}
$\underline{v}_s$	translatory velocity	m s^{-1}
$\underline{v}, \underline{v}_i$	velocity	m s^{-1}
W_a	final value work	J
W_e	electrical energy	J
W_m	mechanical work	J
W_F	mechanical work (force)	J
W_M	mechanical work (moment)	J
W_p	mechanical work (pressure load)	J
W_r	frictional work	J
W_{tot}	total energy	J
$W_{tot,i}$	total energy in the ith layer	J

Symbol	Quantity	Unit
w_e	electrical energy density	$\mathrm{J\,m^{-3}}$
w_{tot}	total energy density	$\mathrm{J\,m^{-3}}$
w_i	width of ith layer	m
w_L	gap (interdigital structure)	m
w_m	energy density of elastic deformation	$\mathrm{J\,m^{-3}}$
$w_{tot,i}$	total energy density in the ith layer	$\mathrm{J\,m^{-3}}$
$X(x)$	eigenfunction, eigenmode	
$X_m(x)$	eigenfunction m, eigenmode m	
X_k, Z	coordinate axes, crystal axes	
$\underline{x}_a$	output quantity	
$\underline{x}_e$	input quantity	
x_0	point of affecting load	m
	starting position	m
$\mathbf{x}_p, \mathbf{x}_{p'}$	position vectors	m
$x, \underline{x}$	distance	m
x, y, z	Cartesian coordinates	m
x_i, y_i, z_i	components of ith mass point	m
$\mathbf{Y}$	gyrator constant	$\mathrm{C^{-1}}$
$\mathbf{Y}'$	integrated gyrator constant	$\mathrm{m\,C^{-1}}$
$\underline{Z}$	impedance	Ω
z	distance from the neutral axis	m
$\overline{z}$	neutral axis position	m
$\underline{z}_1$	mechanical impedance	$\mathrm{kg\,s^{-1}}$
z_{ij}	elements of the dynamic admittance matrix	
α	bending angle	rad
$\beta_m(\omega)$	admittance of the mth vibrational mode	$\mathrm{s\,kg^{-1}}$
ΔA_i	surface segment (layer i)	$\mathrm{m^2}$
ΔC_b	translatory fixed capacitance	F
$\Delta C, \Delta C_x$	capacitance change	F
Δf	frequency change	Hz
Δf_T	carrier frequency change	Hz
$\underline{\Delta F}$	resulting force (actuator segment)	N
$\underline{\Delta i}$	current (actuator segment)	A
$\underline{\Delta i}_w$	transducer current (actuator segment)	A
$\Delta L_1, \Delta L_{Range}$	inductance change	H
Δl	length change	m
Δm	mass (actuator segment)	kg
Δn_R	torsional compliance (actuator segment)	$\mathrm{N^{-1}\,m^{-1}}$
Δn_{Rk}	torsional short-circuit compliance	$\mathrm{N^{-1}\,m^{-1}}$
$\underline{\Delta Q}_i$	charge in the ith layer (actuator segment)	C
$\underline{\Delta R}$	resistance change	Ω
Δr	coefficient of friction (actuator segment)	$\mathrm{N\,s\,m^{-1}}$
Δt	time difference	s
ΔU	voltage step	V
$\underline{\Delta U}$	induced voltage	V
$\Delta U_{agl}, \Delta \hat{U}_e$	voltage changes	V
Δx	length (actuator segment)	m

Symbol	Quantity	Unit
$\Delta\Phi$	change of magnetic flux	Wb
$\Delta\varphi, \Delta\underline{\phi}$	angle difference	rad
$\Delta\omega$	frequency change	$\mathrm{s^{-1}}$
$\Delta\underline{\Omega}$	angular velocity (actuator segment)	$\mathrm{s^{-1}}$
δ	variational operator	
	equivalent conductive layer thickness	m
$\delta(x)$	Dirac delta function	$\mathrm{m^{-1}}$
$\delta\mathbf{x}, \delta\mathbf{x}_i$	virtual displacements	m
$\delta\boldsymbol{\phi}$	virtual torsion	rad
ε	permittivity	$\mathrm{F\,m^{-1}}$
ε^0	strain of the neutral axis	1
ε_r	relative permittivity	1
ε_{eff}	effective permittivity	$\mathrm{F\,m^{-1}}$
ε_{jk}	permittivity tensor	$\mathrm{F\,m^{-1}}$
ε_{jk}^S	permittivity at constant strain	$\mathrm{F\,m^{-1}}$
ε_{jk}^T	permittivity at constant stress	$\mathrm{F\,m^{-1}}$
$\varepsilon_{jk,i}^S$	permittivity of ith layer at constant strain	$\mathrm{F\,m^{-1}}$
$\varepsilon_{jk,i}^T$	permittivity of ith layer at constant stress	$\mathrm{F\,m^{-1}}$
ζ_m	attenuation constant of mth eigenmode	1
$\eta(x)$	test function	
η_m	fequency ratio	1
Θ	temperature	K, °C
κ	conductivity	$\mathrm{S\,m^{-1}}$
κ^0	bend of the neutral axis	$\mathrm{m^{-1}}$
Λ	logarithmic decrement	1
λ_m	eigenvalue of the mth eigenmode	$\mathrm{m^{-4}}$
λ_{Piezo}	capacitance per unit length	$\mathrm{F\,m^{-1}}$
μ	mass per unit length	$\mathrm{kg\,m^{-1}}$
	permeability	$\mathrm{N\,A^{-2}}$
μ_e	carrier mobility	$\mathrm{m^2\,Wb^{-1}}$
μ_N	physical nominal measured quantity	
μ_r	relative permeability	1
μ_ν	permeability in section ν	$\mathrm{N\,A^{-2}}$
$\xi, \underline{\xi}$	deflection	m
ξ_j	ansatz function	m
ξ_0	displacement in z-direction	m
$\xi_{\max}$	maximum deflection	m
ξ_{Range}	absolute deflection range	m
Π	total potential energy	J
ρ	charge density	$\mathrm{C\,m^{-3}}$
ρ_i	mass density of the ith layer	$\mathrm{kg\,m^{-3}}$
$\tilde{\Sigma}$	entropy	$\mathrm{J\,K^{-1}}$
σ_A	surface density	$\mathrm{C\,m^{-3}}$
τ_m^d	period (subcritically damped oscillation)	s
Φ_{coil}	magnetic flux (coil plane)	Wb
Φ, Φ_1, Φ_2	magnetic flux	Wb
ϕ	phase angle	rad

Symbol	Quantity	Unit
$\phi_m^h(t)$	homogeneous solution (free damped vibration)	m
$\phi_m^p(t)$	particular solution (forced vibration)	m
ϕ_0, ϕ_p	maximum amplitude	m
φ	electric potential	V
	angle	rad
φ_{out}	phase of the output signal	rad
Ψ	phase angle	rad
ω	frequency	s^{-1}
Ω	excitation frequency	s^{-1}
$\Omega, \underline{\Omega}_i$	angular velocity	s^{-1}
ω_0	frequency of the fundamental mode	s^{-1}
	cutoff frequency	s^{-1}
ω_m	frequency of the mth vibrational mode	s^{-1}
ω_m^d	frequency (free damped flexural vibration)	s^{-1}
$\underline{\Omega}_w$	angular velocity (rotatory difference quantity)	s^{-1}

Part I

Focus of the Book

1

Introduction

The piezoelectric effect, which was discovered for the first time by the brothers Pierre and Jacques Curie, combines electrical with mechanical quantities and vice versa. If piezoelectric materials (e.g. quartz, turmalin) are subjected to electrical signals along certain crystal orientations, deformations along well-defined crystal orientations appear. Contrary, a mechanical deformation results in a generation of polarization charges. However, the piezoelectric effect can not be assigned to monocrystalline materials only. Conditional on the development of polycrystalline materials with piezoelectric properties, the piezoelectrics achieved an enormous technical relevance as functional materials. Nowadays, polycrystalline ceramics like *barium titanate* (BaTiO$_3$) and *lead zirconate titanate* (PZT) belong to the most commonly used piezoelectric materials, in particular due to the low manufacturing costs and the almost arbitrary shaping possibilities compared to single crystalline piezoelectrics. Furthermore, they have outstanding piezoelectric and dielectric properties, which makes them particularly indispensable for the field of actuators [1].

1.1 Application Areas of Piezoelectric Actuators

The field of application of piezoelectric actuators extends over mass production applications like sound transmitters, ultrasonic power transducers and sensors, bending actuators for textile machines, ink print heads, beam benders in valves, in braille displays, in optical systems and newly as monolithic multilayer actuators for automotive injection systems. Reasons are their compact and space-saving constructions, high actuating precision, extremely short response times, absence of friction, vacuum and clean room capability and the possibility of operation at cryogenic temperatures [2–4].

The major part of piezoelectric actuators is represented by stack and beam bending actuators. Stack actuators, which are based on the longitudinal piezoelectric effect, consist of several ceramic layers with changing polarity. Inbe-

tween, contact electrodes for actuator driving are provided. With this type of actuator very high forces with however small elongations in the lower μm-range and very high driving voltages in the kV-range can be realized. Stack actuators are used for different applications, e.g. in the automotive industries as injecting valve drives and in the optics as high precision drives.

Beam bending actuators however are based on the transverse piezoelectric effect and are applied where large deflections are needed. The small transversal length variations of the active piezoelectric layers effected by the structure of actuator and the external clamping, result in an internal piezoelectric moment, which is the cause for the bending deformation. Thus, large deflections in the range of several hundred microns are realizable. Due to the larger compliances of beam bending actuators compared to those of stack actuators lower driving voltages are necessary, that lie in the range of approx. 24 - 200 V [5].

The *monomorph* (one active piezoelectric and one passive flexible layer), the *bimorph* (two active piezoelectric layers) and the *trimorph* (one passive flexible layer symmetrically surrounded by two active piezoelectric layers) belong to the most well known representatives of piezoelectric beam bending actuators. Newer developments have resulted in the realization of monomorph beam structures in *multilayer technology*, i.e. the actuator consists of several passive flexible and active piezoelectric layers. The multilayer technology implies the advantage to work with even lower driving voltages extending significantly the field of industrial applications, piezoelectric beam bending actuators can be used for.

1.2 Motivation and Aim of the Book

The consideration of piezoelectric beam bending actuators as a system consisting of a multiplicity of layers (multilayer beam benders) with different mechanical and electromechanical characteristics form the first main emphasis of the present book.

The broad field of industrial applications for piezoelectric beam bending actuators as actuating and high precision positioning systems necessitate an adjustment of their performance for the particular task. Regarding piezoelectric multilayer beam benders, a deeper look and understanding of their mechanical, elastic and electromechanical characteristics is required. This deeper understanding discloses the possibility of making statements about the beam bender's static and dynamic behavior and affecting this behavior by appropriate measures within the scope of structural mechanics.

An essential aim of this book consists in deriving the static and dynamic behavior for any kind of clamped-free piezoelectric beam bending actuator

consisting of n layers in closed form analysis for any point over the entire beam length. The origin of these considerations are the stress and deformation states of a bending bar. In particular, the main focus is turned to the influences on the resulting static and dynamic bending behavior caused by external affecting mechanical quantities, like forces, moments and pressures but also internal piezoelectric moments caused by an external driving voltage. The modeling is to consider any layer sequence consisting of passive elastic and active piezoelectric layers with respect to their geometrical, elastic and electromechanical characteristics. Within the scope of the dynamic characterization, the emphasis is particularly laid on the spatial and temporal resolution of the dynamic vibration behavior.

Piezoelectric bending actuators are really a prime example for an electromechanical system. Generally, electromechanical systems consist of interacting electrical, mechanical and acoustical subsystems, that can be described by circuit representations within the scope of the network theory. This kind of representation provides deep insights into the interconnecting structure between electrical and mechanical subsystems and extends the systematic understanding in the field of actuators as well as in the field of sensor technology. Starting from the attained knowledge concerning the dynamic behavior of piezoelectric multilayer beam bending actuators, the systematic development of their equivalent network representation is effected in a next step within the scope of the network theory.

In order to verify the developed structural dynamic formulations as well as the equivalent circuit representation within the context of the network theory, real measurement results of different kind at a monomorph beam bending actuator in multilayer technology will be carried out with the help of an especially realized measurement setup for piezoelectric bending actuators. In a next step, analytical computations based on the developed formalisms will be compared to the achieved measurement results.

The second main focus of the this book concentrates on the development and realization of a smart sensor-actuator-system. Due to the high electrical driving voltages inside of the piezoceramic layers, microphysical domain processes proceed, resulting in hysteresis, creep and drift effects on a macroscopic level. These effects turn out to be a significant disadvantage, thus piezoelectric bending actuators can only be employed for high accuracy positioning applications under certain circumstances.

For applications where precise switching and exact position control are needed, action has to be taken for the compensation of the inherent piezoelectric creep and hysteresis effects as as well as the external subjecting quantities, such as varying mechanical loads and vibrations. With the help of an integrated sensor and additional sensor electronics the disturbing effects can be detected. The

implementation of such a sensor-actuator-system into a closed loop control allows for compensation of disturbing effects, whereby high efficient piezoceramics with high elongation and force characteristics can be used for high-accuracy positioning.

A part of the content of the present book is embedded in the federal german research project EPIETEC (*Effektive piezokeramische Multilayer-Technologie für integrierte Niedervolt-Piezobieger*), which has been financially supported by the German Federal Ministry of Education and Research (BMBF) by contract No. 03N1076A. Within this project, a new pneumatic micro valve has been realized. The heart of this micro valve is a smart piezoelectric low-voltage multilayer beam bending actuator with an integrated sensor for tip deflection measurements.

1.3 State of the Scientific Research

In the scientific literature, a huge number of publications concerning the static and dynamic behavior of piezoelectric beam bending actuators and their electromechanical network representation can be found. Thereby monomorphs, bimorphs, trimorphs and multilayer beam bending structures are in the focus of attention. Mentioning all important works in this area in its completeness would go beyond the scope of the present book. Instead, the most important publications serving as a base for this book are presented briefly.

Statics of Piezoelectric Beam Bending Actuators

The electromechanical coupling mechanisms of monomorphs and bimorphs are discussed on the base of the deformation state describing equations by *Wang* and *Cross* [6]. In a further step, the investigation of the nonlinear behavior of piezoelectric bimorph structures under exposure to high electric fields takes place both, in analytic and experimental form [7]. *Cunningham*, *Jenkins* and *Bakush* pursue in their work the optimization of the layer thickness of a piezoelectric actuator in order to reach maximum deflection of a coupled flexible, non-piezoelectric layer [8]. *Küppers* presents the realization of a miniaturized piezoelectric bending actuator in a monomorph design. In order to optimize the actuator characteristics, analytical computations regarding the deflection of a two layer system are carried out [9]. The modeling of asymmetrical piezoelectric bimorph structures is discussed in the work by *Brissaud*, *Ledren* and *Gonnard*. Considering the neutral axis position, the static behavior regarding the expected bending moment is determined [10]. An analytical description of the free tip deflection of a piezoelectric bimorph by means of matrix calculus is presented by *Huang*, *Lin* and *Tan* [11].

Low and *Guo* as well as *Wang* and *Cross* extend the universal deformation state equations to trimorph bending structures [12, 13]. *Tadmor* and *Kósa*

present the bending behavior of a trimorph beam bending structure with respect to the influence of the electromechanical coupling coefficient on the deviation moment of each individual layer [14]. *Smits* and *Choi* describe the electromechanical characteristic of heterogeneous bimorph bending structures subjected to different external mechanical and electrical quantities. Assuming thermodynamic equilibrium, they derive the universal deformation state equations for the tip of a bimorph by means of energetical considerations [15].

In the paper of *DeVoe* and *Pisano* a new model for the determination of the free tip deflection of piezoelectric multilayer beam bending actuators under the influence of an electrical load is presented. Thereby, the analytical formulation is based on a matrix equation combining mechanical, geometrical and elastic quantities of the individual layers [16]. *Meng*, *Mehregany* and *Deng* also consider piezoelectric bending actuators as multilayer system. Here, the analytical formulation of the beam bender's tip is in the forground of discussion [17]. *Weinberg* extends the modeling of piezoelectric multilayer beam bending actuators taking the neutral axis position into account. The description of the deformation state with respect to external quantities such as force, moment and electrical voltage is restricted to the tip of the free bender [18].

All contributions mentioned above are characterized by extremely expanded analytical computations concerning the description of the static behavior of the interesting bending structure. The analytical calculations of deflection, bending angle, volume displacement and electrical charge effected by externally subjecting quantities are carried out partially and mostly for the bender's tip only. Based on this fact, the serious disadvantage arises, that the deformation state of the spatially expanded bending actuator can not be derived for arbitrary points over the entire length of the beam. Thus, important information is lost.

In order to disengage from special bending actuator types, the analytical formulation of a piezoelectric multilayer beam bending actuator consisting of n layers is pursued in the present book. Thereby, both passive elastic and active piezoelectric behavior is to be assigned each individual layer. The possibility of computing the deflection, bending angle, volume displacement and electrical charge effected by externally subjecting quantities such as force, bending moment, pressure load and electrical voltage for arbitrary points over the entire length of the beam shall be provided by an energetical description. The formulation of the equations describing the static behavior is to be kept in such a general form, allowing both users in industry and research organisations to derive the appropriate formulation for their given bender design.

Dynamics of Piezoelectric Beam Bending Actuators

Regarding the analytical description of the dynamic behavior of piezoelectric bending actuators such as a monomorph, bimorph, trimorph and also

a multilayer system, a large number of publications have been published in the scientific literature, too. In the following some representative works are summarized.

Smits and *Ballato* describe the dynamic behavior of a bimorph bending structure, which is excited to bending vibrations by external harmonic quantities such as forces, bending moments, pressure loads and electrical driving voltages [19]. The resulting harmonic quantities deflection, bending angle, volume displacement and generated charge are combined by a dynamic admittance matrix with the externally affecting loads. The dynamic behavior of a homogeneous bimorph structur caused by a harmonic driving voltage is described in a work by *Coughlin*, *Stamenovic* and *Smits* in order to determinate the modulus of elasticity of different materials [20]. Thereby, the shifting of the resonance frequency is a measure for the modulus of elasticity being determined.

In a publication of *Smits*, *Choi* and *Ballato* the development of the first fundamental mode and its transition to the first antiresonance is discussed amongst the description of the resonance behavior of a bimorph bending structure [21]. The starting point for these considerations is the dynamic admittance matrix of a piezoelectric bimorph formulated by *Smits* and *Ballato* [19]. *Yao* and *Uchino* extend a dynamically driven bimorph with a flexible plate attached at the free bender's tip [22]. The resonance behavior of the realized structure is described as an electromechanical system with lumped parameters. Computational results based on the theoretical formulation are compared to measurement results. In the work of *Sitti*, *Campolo*, *Yan* and *Fearing* the dynamic behavior of a unimorph beam bending structure is discussed [23]. Thereby, the derivation of design criteria for the specific influence of the resonance behavior of piezoelectric two-layer systems is in the foreground of discussion.

On the base of Hamilton's principle *Fernandes* and *Pouget* formulate the system of differential equations describing the dynamics of a bimorph [24]. Thereby, a special attention is turned to the layer-wise modeling of the electrical potential. The publication of *Brissaud*, *Ledren* and *Gonnard* elaborates on the analytical formulation of the dynamic behavior of piezoelectric two-layer systems in addition to the description of their static behavior [10]. Thereby, the determination of the position-dependent fundamental mode and the associated resonant frequency are in the focus. *Seitz* and *Heinzl* present a micro fluidic device based on piezoelectric bimorph structures [25]. The modeling of the dynamic behavior of the actuator structures takes place with the help of the simplified differential equation for flexural vibrations.

The description of the dynamics of a trimorph bending structure is the content of a publication of *Rogacheva*, *Chou* and *Chang* [26]. The computational results prognosticated from the developed theoretical formulations are compared to measurement data. *Kyu Ha* formulates the admittance matrix of bimorph bending structures derived by *Smits* and *Choi* [15] for a symmetrically layered trimorph [27, 28]. Based on Hamilton's variation principle, the

differential equation system describing the dynamics is derived. The derivation of the admittance matrix is based on matrix calculus.

Energetical principles within the context of Lagrange's formalism and application of Hamilton's variation principle are presented in several publications in order to determine the dynamics describing differential equation system of piezoelectric multilayer beam bending actuators [29–33]. All analytical formulations are based on the linear theory of piezoelectricity and contain the coupling of mechanical deformations with the charge equation of electrostatics.

All work inherent is the serious disadvantage, that the equivalent viscose damping caused by internal and external friction effects remains unconsidered in the dynamic formulations. This fact leads to inevitable singularities concerning flexural vibrations in the case of resonance, which does not correspond at all to the development of bending vibrations. Furthermore, it should be noted, that the differential equation for flexural vibrations is a function of the beam length coordinate and time. In most publications, the separation formalism concerning the location and time functions remains unconsidered. However, it is this formalism, that in connection with the characteristic equation for clamped-free beam bending actuators allows for the analytical description of the temporal and spatial development of the fundamental and higher order vibrational modes.

Therefore, in the present book, the describing differential equation system of a piezoelectric multilayer beam bending actuator consisting of n layers is derived for the first time, based on Hamilton's principle with respect to Rayleigh's dissipation function. In a next step, the analytical formulation of the spatial and temporal vibration response of piezoelectric multilayer actuators both, for the fundamental mode and for the modes of higher order follows. With the help of the general formulation, the engineer and scientist working in practice shall be given the possibility to prognosticate the dynamic behavior for any design of beam bending actuators. By variation of selected mechanical, geometrical and elastic parameters, the dynamic characteristic of any kind of piezoelectric bending actuators can be affected purposefully.

Equivalent Circuit Representation of Piezoelectric Beam Bending Actuators

The description of piezoelectric bending actuators as electromechanical systems within the context of the network theory has been also described in a large number of publications.

In a publication of *Ballato* the equivalent network representation of a piezoelectric two-layer system is worked out [34] based on the admittance matrix formulated by *Smits* and *Choi* [15]. Thereby, the description is concentrated

on the free tip of the bender. *Sherrit*, *Wiederick*, *Mukherjee* and *Sayer* develop an electromechanical circuit representation for a three-layered piezoelectric stack actuator concentrating on the low frequency range up to the first resonance [35]. A theoretical formulation of the dynamic behavior of a bimorph bending structure within the context of the network theory based on distributed parameters is the content of the publication by *Tilmans* [36]. However, the represented structure of the electromechanical network can only be applied for low frequencies. The electromechanical network representation of a trimorph bender in form of a five-port structure (ten-poles) is presented by *Cho*, *Pak*, *Han* and *Ha. Kyu Ha* describes an asymmetrical trimorph bending structure by means of an impedance matrix [28]. By means of this matrix, he derives a four-port network representation (eight-poles). Based on the dynamics describing differential equation system of a multilayer beam bending actuator [29], *Aoyagi* and *Tanaka* present the electrical network representation of piezoelectric multilayer bending actuators [37]. The admittances and resonant frequencies are calculated and compared with experimental results.

In all publications mentioned above the formulation of the electromechanical circuit representation is based on complex analytical equations. A clear representation of the mechanically interacting quantities such as masses, coefficients of friction and compliances and their interconnection is lost. Furthermore, the circuit representation is only formulated for the resonance of the fundamental mode. Modes of higher order remain unconsidered in their electromechanical representation. Therefore, in the present book the equivalent network representation of piezoelectric bending actuators consisting of n layers is developed step by step. Particularly, the description of the higher order modes within the context of the network theory is in the focus of discussion.

Bending Actuators with Integrated Sensors

Concerning the realization of piezoelectric actuators with integrated sensor technology, a large number of publications can be found [38–65]. The realized sensor concepts are based e.g. on the sensor characteristics of piezoceramic materials or the resistance change of thick film and metallic strain gage sensors. As a rule, the suggested solutions show one or more restrictions meaning that one of the demanded boundary conditions is not satisfied for the sensor completely integrated in the actuator. The solutions are characterized by the fact, that the sensor needs external components and is not able to detect the bender's tip deflection independently of external influences. A further restriction is the suitability for dynamic applications, however static and quasi-static applications are not possible [66].

The doctoral thesis of A. J. Schmid [67], written within the federal german research project EPIETEC mentioned above, describes the conceptual draw up, development and realization of an economical sensor for detecting forces and

deflections based on a capacitive strain gage. Hence, in this book a detailed and separate presentation is abandoned, instead a summarized overview will be given. On the one hand this book focuses on the realization of a sensor electronics for capacitive strain sensors and on the other on the development and realization of an inductive proximity sensor in combination with a high-accuracy electronic circuit for tip deflection measurements. Particularly, the inductive sensor principle offers the possibility of static, quasi-static and dynamic measurements.

1.4 Textual Focus of the Book

The present book is devided into the chapters described below.

Chapter 2 concentrates upon the phenomenological description of the direct and inverse piezoelectric effect. Thereby, the piezoelectric lead zirconate titanate system PZT is in the foreground of discussion. Its behavior in the low-level and high-level signal mode is described on the base of micro-physical domain and domain switching processes. Thus, the understanding of the macroscopic behavior of piezoelectric transducers is opened generally. With the transition to the standard forms of piezoelectric bending actuators the important terms of the bending structures used in practice are defined.

The description of the strain and stress state as well as the elastic behavior of a piezoelectric crystal structure follows in chapter 3. Their knowledge provides a basis for the derivation of the piezoelectric constitutive equations of state corresponding to the repective application. With the help of the constitutive equations, the electrical enthalpy by means of Legendre's transformation is deduced, being indispensable for the formulation of the dynamic behavior of piezoelectric bending actuators. The term of strain energy forms the fundamental of the structural dynamics consideration. The energy density of the elastic deformation and the energy density of the electric field are described in detail serving as starting point for all further considerations.

The formulation of the static behavior of n layered piezoelectric beam bending actuators in closed form analysis is the content of chapter 4. Thereby, Bernoulli's hypothesis of bending theory is the physical base. In combination with the basic laws of elastostatics, Bernoulli's hypothesis allows for the calculation of the neutral axis position. It is integrated into the general formulation of the flexural rigidity and the internal piezoelectric moment and represents one of the central quantities in all further considerations. With respect to the linear piezoelectric constitutive equations, energetical considerations lead to the total stored energy of a bending actuator in deformation state. With the principle of minimum total potential energy the combining equations between extensive affecting quantities such as force, bending moment, pressure load

and electrical driving voltage and the resulting intensive quantities like deflection, bending angle, volume displacement and electrical charge are derived for any point over the entire length of the actuator. The combining equations are presented in form of a coupling matrix.

Chapter 5 addresses the fundamentals concerning the description of the dynamics of piezoelectric bending actuators. At first, the important Lagrange formalism within the context of theoretical mechanics is developed considering dissipative forces, which extract energy from an oscillating system. Thereby, the internal and external frictional forces are integrated into Lagrange's formalism based on Rayleigh's dissipation function. In the next step, the transition to the modified Hamilton principle follows, which can be applied directly to the electrical enthalpy formulated in chapter 3. From Hamilton's principle the describing differential equations of a piezoelectric multilayer beam bending actuator are deduced in concentrated form.

In chapter 6 the differential equation system gained in chapter 5 is used for the description of the time-harmonic, dynamic behavior of piezoelectric multilayer actuators in closed form analysis. In analogy to the static description, the connection of the extensive dynamic quantities with the resulting intensive dynamic quantities is presented for arbitrary points over the entire length of the actuator by means of a dynamic admittance matrix.

The systematic development of a general circuit representation of piezoelectric multilayer beam bending actuators within the context of the network theory is the content of chapter 7. Particularly, the frictional forces arising with bending vibrations are considered in the sense of the equivalent viscous damping. Considering the differential bending behavior of an electrically driven multilayered actuator segment, the general representation of the electromechanical coupling of electrical and mechanical quantities will follow by means of a gyratoric two-port (four-pole) network. The combination of the two-port network with the translatory and rotatory quantities coupling four-port network leads to the general representation of a piezoelectric multilayer beam bending actuator as an electromechanical system with respect to the development of higher order modes.

A special measurement setup for piezoelectric beam benders as well as the experimental characterization of the static and dynamic behavior of a realized monomorph beam bending actuator in multilayer technology form the main focus of chapter 8 and 9. Amongst the the functionality of the measurement setup, the individual measurement tasks and their experimental realization are discussed in detail. The measurement setup allows for the experimental validation of the derived theoretical models. In order to verify the theoretical formulations, analytical calculations are compared to measurement data.

In chapter 10 the transition to the second main focus of the present book follows. Thereby, the development and realization of a smart sensor-actuator-system in the form of a pneumatic micro valve with integrated deflection sensor are in the focus of discussion. The requirements for the integrated deflection sensor are presented and serve as a selection base of favoured sensor concepts.

In order to detect the beam bender's tip deflection, the conceptual draw up, development and realization of a sensor electronics for capacitive strain sensors have been occurred within the research project EPIETEC. In chapter 11 the working principle of a capacitive strain sensor for tip deflection measurement is discussed. Furthermore, the sensor electronics and its structure are discussed in detail. The characterization of the realized sensor-actuator-system in combination with the developed sensor electronics follows.

Besides the realization of a sensor electronics for capacitive strain sensors, additionally, a second deflection sensor based on an inductive proximity principle has been developed. The inductive proximity sensor, which is based on eddy current effects, offers the possibility of sensor integration in smallest spaces in combination with a high-accuracy electronic circuit. In chapter 12 the essential structure and the operational mode of the inductive proximity sensor are discussed. In order to determine analytically the relative change of inductance as a function of the beam bender's tip deflection, an electro-dynamic approach is formulated verifying experimental measurement results in an outstanding way. By theoretical formulation, a deep physical understanding of the mechanism of the inductive proximity sensor based on eddy current effects is given simultaneously. In a next step, the characterization of the inductive proximity sensor concerning its static and dynamic transient behaviour is in the foreground of discussion.

Chapter 13 summarizes the results of the present book. An extension of the formulated structure dynamical aspects is presented. Furthermore, new application possibilities for smart piezoelectric multilayer beam bending actuators are outlined. An outlook on continuing scientific works and technical application fields conclude this book.

Theoretical Aspects and Closed Form Analysis

2

Piezoelectric Materials

In this chapter, it is dwelled on the discovery of piezoelectricity and the formation of the direct and the inverse piezoelectric effect is described qualitatively. The development of the technical application of piezoelectric materials shows, how various their application fields are. Especially, the attention is given to the technical importance of the piezoelectric lead zirconate titanate system PZT. For a better understanding of its behavior in the low-level and high-level signal mode, it is necessary to dwell on the domain and domain switching processes. The electromechanical behavior of the piezoelectric ceramic system PZT provides the realization of piezoelectric beam bending actuators, which are of highest importance in many application fields piezoelectric actuators and sensors are applied.

2.1 Discovery of Piezoelectricity

In the year 1880, the piezoelectricity was discovered by the brothers Pierre and Jacques Curie [68]. However, this did not happen randomly. A long time ago, in India and Ceylon the mysterious behavior of tourmalins was already well-known. If tourmalins were put into hot ash, at one side they attracted ash particles, at the opposite side they were rejected. After some time the effect of attraction and rejection inverted. At the beginning of the 18th century, traders brought the tourmalin crystals to Europe. 1747 Linné called the tourmalin crystals *lapis electricus*. In the following century, some researchers endeavored to find a connection between the mechanical pressure effect and the electricity. Becquerel was aware of the fact, that such an effect could be particularly expected with crystals. In the year 1877, Lord Kelvin established the correlation between pyroelectricity and piezoelectricity. It could be verified, that the most part of the pyroelectric charge of the tourmalin is ascribed to the formation of piezoelectric surface charge caused by the elastic crystal deformation under temperature changes. First, the brothers Pierre and Jacques

Curie discovered the direct piezoelectric effect at tourmalin crystals. They recognized, that a mechanical deformation in certain directions causes opposite electrical surface charges at opposite crystal faces being proportional to the mechanical deformation. This effect, which was also found subsequently with quartz and other crystals without symmetry center, has been called piezoelectric effect (greek: *piezein = press*). The inverse piezoelectric effect was predicted by Lippmann [69] based on thermodynamic considerations and afterwards confirmed experimentally by the brothers Curie.

2.2 Direct and Inverse Piezoelectric Effect

The piezoelectric effect is found with those crystal structures, which do not have a symmetry center regarding the positive and negative ions of the crystal lattice. Thus, the condition for the occurrence of the piezoelectric effect is the existence of polar axes within the crystal structure. Polar means, that there is an electrical dipole moment in axis directions caused by the distribution of the electrical charge in the chemical bond. For a better understanding, the structure cell of α-quartz is considered (see Fig. 2.1).
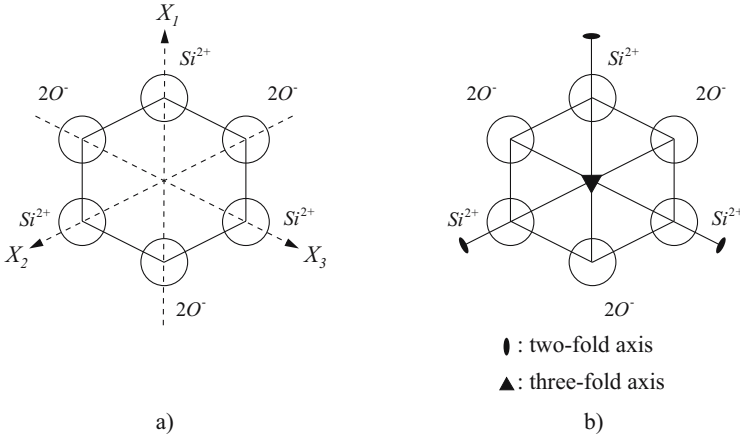
Fig. 2.1. Simplified structure cell of quartz. - **(a)** arrangement of Si- and O-ions with the main crystal axes; **(b)** two- and three-fold axes

It consists of negative charged O-ions and positive charged Si-ions and has three two-fold polar rotation axes X_1, X_2 and X_3 in the drawing plane and a three-fold rotation axis Z perpendicular to the drawing plane. Seen from an outer point of view, the crystal is electrically neutral. If there is a deformation

of the quartz structure along the polar X_1-axis, an additional electrical polarization $\mathbf{P}$ performs along this axis. The electrical polarization is caused by the displacement of the positive and negative ions of the crystal lattice against each other (see Fig. 2.2a) resulting in an electrical charge on the appropriate crystal surfaces perpendicular to the X_1-axis and thus in an outside electrical polarization voltage. This effect is called *direct longitudinal piezoelectric effect*. An exposure to compression and tensile stresses acting perpendicularly to the X_1-axis results in an additional electrical polarization with opposite sign in X_1-axis direction (see Fig. 2.2b). This behavior is called *direct transversal piezoelectric effect*.

a)   b)
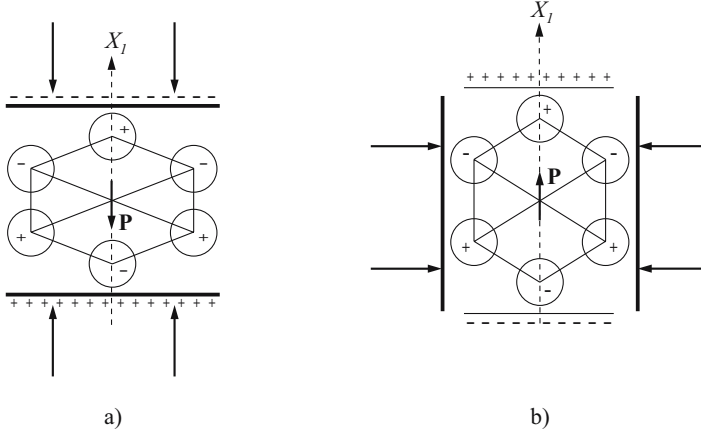
Fig. 2.2. Direct piezoelectric effect within a structure cell of quartz. - **(a)** longitudinal piezoelectric effect; **(b)** transversal piezoelectric effect

Both effects are reversible, i.e. a contraction or dilatation of the quartz structure performs under the influence of accordingly orientated electric fields. This effect is called *inverse piezoelectric effect*.

2.3 Piezoelectric Ceramics

With the discovery of polycrystalline ceramics with piezoelectric characteristics, piezoelectrics achieved an enormous technical importance after the Second World War. At first view, the term *piezoelectric ceramics* comprises a contradiction, because a polycrystalline compound shows an isotropic behavior and a macroscopic inversion center due to the statistical orientation of the individual grains [70]. For this reason, piezoceramics do not have a macroscopic piezoelectric behavior, although the individual single-crystal grain has piezoelectric characteristics. If the ceramic compound has a single polar axis,

that can be reorientated by an external electric field. With ceramics, the spontaneous polarization can be reoriented by an external electric field remaining the spontaneous polarization adjustment in absence of an external electric field, are called *ferroelectrics*.

Nowadays, polycrystalline ceramics like barium titanate ($BaTiO_3$) and lead zirconate titanate (PZT) belong to the most commonly used piezoelectric materials, in particular due to the low manufacturing costs and the almost arbitrary shaping possibilities compared to single crystalline piezoelectrics. Furthermore, they have outstanding piezoelectric and dielectric properties, which make them particularly indispensable for the field of actuators [71].

2.4 Perovskit Structure of PZT

Lead zirconate titanate (PZT) is found in the *Perovskit structure* of ferroelectric crystals of the kind ABO_3. Within the Perovskit structure, A represents a double positive charged ion (lead), B and O represent a four-fold positive charged ion (titanium, zircon) and a double negative charged oxygen ion, respectively. Above a certain temperature T_C, called *Curie temperature*, the elementary cell of PZT provides a cube texture (see Fig. 2.3a). Within this crystal structure no piezoelectricity arises caused by its existing symmetry center.

$\bullet: A^{2+}$
$\cdot: B^{4+}$
$\bigcirc: O^{2-}$

$T > T_C$

$T < T_C$

a)

b)
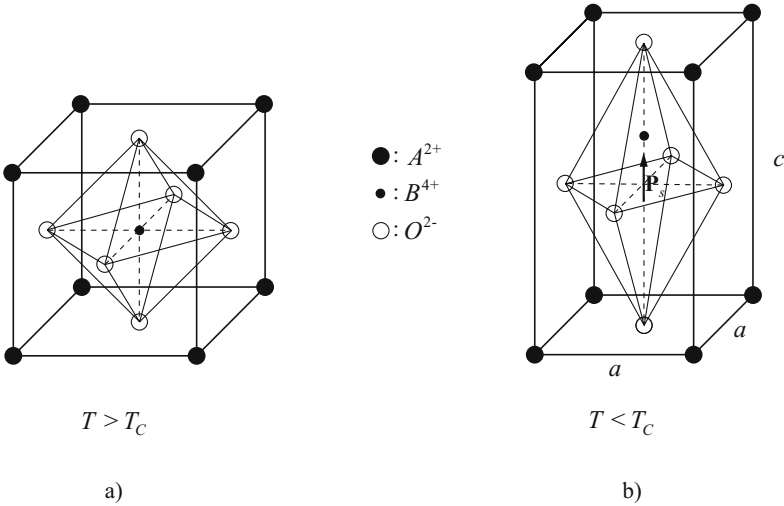
Fig. 2.3. Perovskit structur of ferroelectric crystals of the kind ABO_3. - **(a)** cube texture above the Curie temperature; **(b)** tetragonal texture below the Curie temperature

Falling below the Curie temperature, the cube texture of the crystal lattice turns to the tetragonal texture spontaneously due to energetic reasons [72]. Thereby, the oxygen ion lattice within the tetragonal case is shifted towards the crystallographic c-axis, at the same time a displacement of the positive ion lattice towards the opposite direction occurs. This results in an expansion of the elementary cell towards the c-axis, while a contraction towards the two a-axis occurs simultaneously (see Fig. 2.3b). The distortion caused by the transition of the paraelectric phase into the ferroelectric phase is called *spontaneous deformation*.

A dipole moment associated with the spontaneous deformation results from the center asymmetry of the tetragonal unit cell. The quantity of the dipole moment related to the volume of the unit cell is called *spontaneous polarization* $\mathbf{P}_s$, which is in parallel or antiparallel with the c-axis. Therefore, the transition of the cube texture to the tetragonal structure permits three directions for the spontaneous expansion and six directions for the spontaneous polarization, respectively [73]. Applying an external electric field, additional induced polarization and deformation effects are generated due to the force impact on the existing centers of charge within the distorted tetragonal elementary cell. The higher the degree of parallelism between the directions of the spontaneous polarization and spontaneous deformation on the one hand and the direction of the external electric field on the other hand is, the more polarizations and deformations are induced (inverse piezoelectric effect).

Subjecting the elementary cell by an external mechanical load resulting in an associated mechanical stress field, the centers of charge of the elementary cell are displaced. This effect causes an additional polarization and deformation (direct piezoelectric effect). For a better understanding of the electromechanical behavior of ferroelectric ceramics, e.g. PZT, it is necessary to dwell on the domain and domain switching processes of PZT.

2.5 Domain and Reversion Processes of PZT

In a piezoelectric singlecrystalline material, e.g. α-quartz, the spontaneous polarization directions of the unit cell are predetermined. The dipoles of the unit cells interact in such a manner, that regions of uniform dipole orientations are generated. These regions are called *Weiss domains*. The peripheral zone of individual domains is called *domain wall*. Ferroelectrics have a polycrystalline structure. Each individual crystallite of the ceramic compound can be considered as a ferroelectric single crystal separated again into individual domains below the Curie temperature [71]. Figure 2.4 represents the polycrystalline structure of ferroelectric ceramics.

Like mentioned above, below the Curie temperature ferroelectrics exhibit a tetragonal crystal structure. According to the possible polarization directions, within tetragonal crystal structures one differentiates between the so-called 180° and 90° domains. 180° domains are characterized by having opposite
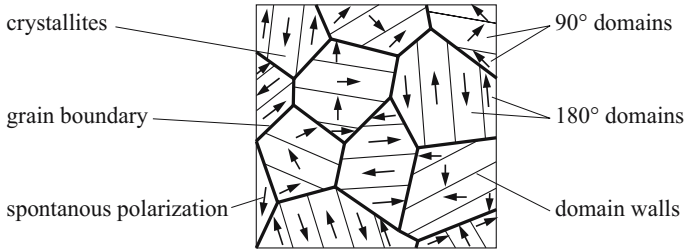
Fig. 2.4. Schematic representation of the polycrystalline structure of ferroelectric ceramics below the Curie temperature

polarization directions in neighboring regions, whereas 90° domains exhibit polarization directions aligned perpendicularly to each other. Falling below the Curie temperature, the crystallites of ferroelectrics decompose into a large number of statistically distributed domains, if there is no external electric field. Therefore, ferroelectrics are non-polarized concerning their macroscopic behavior (see Fig. 2.5a) [74].
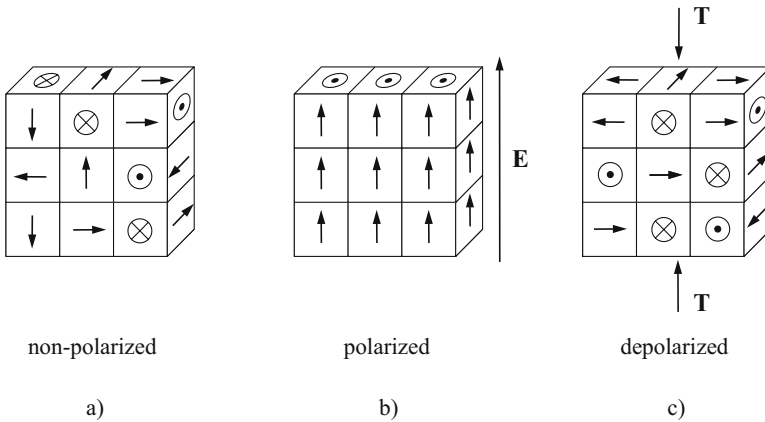
Fig. 2.5. Domain orientation within a ferroelectric single crystal. - **(a)** non-polarized crystal; **(b)** polarized crystal; **(c)** depolarized crystal

Applying a sufficient electric field **E** with defined direction to the ferroelectric crystallites, the domains can be aligned with the field direction. This behavior is illustrated in figure 2.5b. Thereby, the number of domains aligned parallely with the electric field grows at cost of antiparallelly or perpendicularly aligned domains. The reorientation behavior of the spontaneous polarization of ferroelectrics influenced by an external electric field can be effected by two different

domain processes, that can happen individually or at the same time [75]. This is a matter of the 180° and the 90° domain process, respectively. With the 180° domain process, the spontaneous polarization switches gradually around 180°, until the entire polarization is aligned parallely with the electric field. With the 90° domain process, at first the spontaneous polarization switches from an antiparallel direction into an energetically more favorable, metastable position perpendicular to the external electric field. By increasing the external field **E**, the alignment of the spontaneous polarization with the electrical field direction is generated by a second 90° domain process.

180° domain processes exhibit a more intense change of the spontaneous polarization. Compared to this fact, 90° domain processes cause a distortion of the crystallite associated directly with the different lenghts of the a- and c-axes within the unit cells (see Fig. 2.3b). Affecting the crystallite by external mechanical stresses, only 90° domain processes appear. This fact results in a depolarization of the crystal (see Fig. 2.5c). A reversion of polarity by external mechanical loads is not possible.

non-polarized   polarized   depolarized

a)   b)   c)
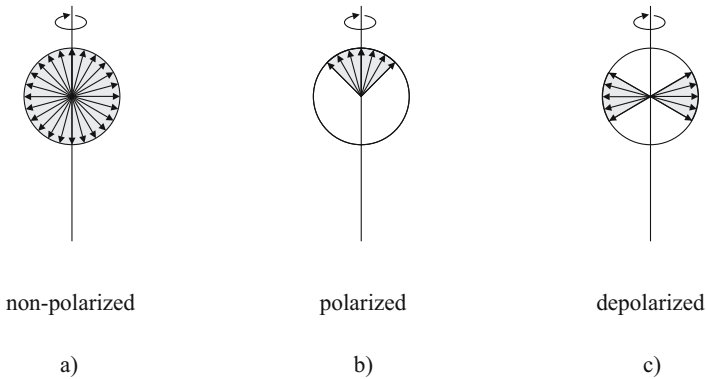
Fig. 2.6. Domain distribution within ferroelectric ceramics. - **(a)** non-polarized ceramics; **(b)** polarized ceramics; **(c)** depolarized ceramics

Compared to the single crystal, the orientation of the crystal axes of the individual crystallites in polycristalline PZT ceramics is statistically distributed. Since the polarization direction is coupled to the crystal axis system of each crystallite, the polarization is also statistically distributed in all directions. Thus, an exact alignment of the spontaneous polarization within all crystallites in parallel with the external electric field will not be possible. Instead, the domain alignment of PZT ceramics is effected only in a narrow region around the field direction. Figure 2.6 represents schematically the non-polarized, the polarized and the depolarized state of a PZT ceramics [74].

2.6 Electromechanical Behavior

The domain processes in ferroelectric ceramics caused by external electric fields are superposed by the dielectric and the invers piezoelectric behavior. Due to the domain processes, a *nonlinear* and *hysteresis affected* correlation exists between the polarization P and the applied electric field E. Depending on the previous history of the ceramics, strongly varying domain configurations can arise, thus for a certain instantaneous value of the electric field different polarization values exist. Therefore, a hysteresis affected correlation between polarization and field strength exists for sufficiently low-frequency electric fields (see Fig. 2.7).
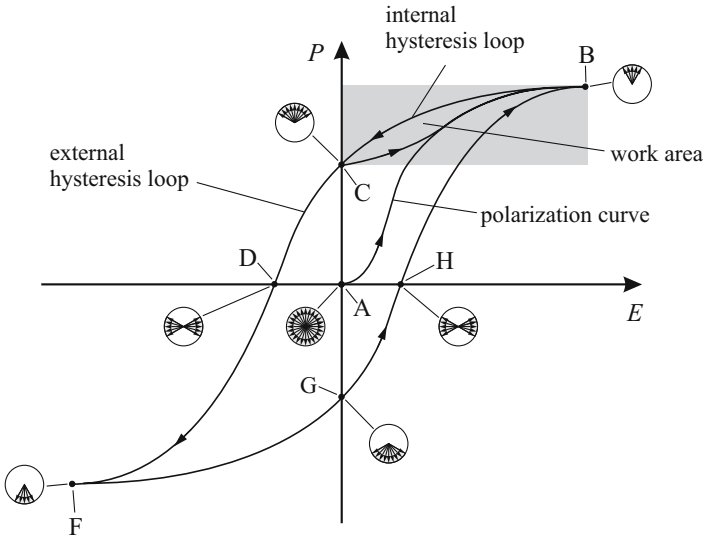
Fig. 2.7. Polarization P dependent on the electric field E

Starting from a non-polarized state (origin of the coordinate system of the E-P plane), the domains orientate themselves to the increasing electric field until they are all aligned with its direction. Thus, the polarization curve represented in figure 2.7 develops between the points A and B. If the electric field decreases in value to zero, a small part of the domains will fold back due to the mechanical stresses within the ceramics. The remaining polarization is called *remanent polarization* P_r. This correlation is represented by the curve between the points B and C in figure 2.7. If an electric field is applied in opposite direction, the domains will be gradually realigned in the appropriate direction until all domains are aligned with the field direction. For this case, the pair of variates (E, P) passes the curve along the points C-D-F. At point

D, the electric field reaches a level, the ceramic material is depolarized concerning the external behavior. The appropriate electric field is called *coercive field strength* E_c. If the electric field is reorientated again, the domains will be gradually realigned until all domains are aligned with the lines of electric flux. In this case, the pair of variates (E, P) passes the curve along the points F-G-H-B. The curves along the points B-C-D-F and F-G-H-B form *external hysteresis loops*. However, if the direction of the external electric field is reversed before all domains are aligned, the pair of variates (E, P) branches out to a hysteresis area surrounded by external hysteresis loops. Within this hysteresis area, the so-called *internal hysteresis loops* are formed.

In the following, the hysteresis affected correlation between the strain S of the ceramics and the electric field E is represented. Thereby, the previous load history of the ceramics should be the same as already shown in figure 2.7. Due to the characteristic curve progression in figure 2.8, this curve is also called *butterfly curve*.
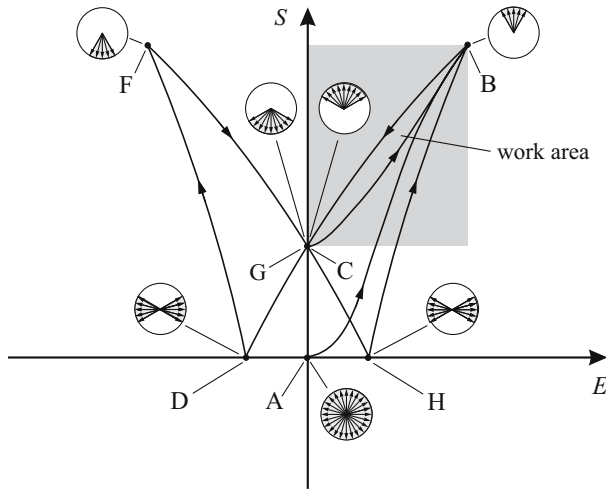
Fig. 2.8. Strain S dependent on the electric field E

A non-polarized ceramic body represents the starting point of the following considerations (point A). By applying an external electric field, the domains are aligned with the field direction associated with a strain S of the ceramics. Thereby, the pair of variates (E, S) passes the curve between the points A-B. If the electric field decreases in value to zero, a small part of domains will fold back, that's why a residual strain S_r of the ceramics is found (point C). If the electric field is applied in opposite direction, all domains will be statistically distributed, and the strain S of the ceramics decreases in value to zero at point

D. A further increasing of the field strength results in gradual realignment of the domains with their tetragonal lattice structure in field direction, thus the strain of the ceramic body increases again. The pair of variates (E, S) passes along the curve C-D-F. If the electric field is reorientated again, the domains will also be realigned. The pair of variates (E, S) passes along the curve F-G-H-B, thus the characteristic butterfly curve is formed.

Normally, the range of the electric fields, piezoelectric ceramics are driven with, extends from $0\,\mathrm{kV/mm}$ to $2\,\mathrm{kV/mm}$. In the figures 2.7 and 2.8, the work area is marked in grey color. On the one hand, driving piezoelectric ceramics within this range, the piezoelectric effect is optimal used caused by the uniform domain alignment. On the other hand, the hysteresis affected nonlinearity in the electrical transient characteristic effected by domain switching processes is reduced associated with a decrease of dissipation loss. In order to syntonize piezoelectric ceramics to this work area, at the end of the manufacturing process, the ceramic material is polarized in the desired direction by applying a strong electric field somewhat below the Curie temperature. In practise, piezoelectric ceramics are only driven with positive electric fields.

Investigations in the scientific literature concerning mechanically induced domain processes are restricted to compressive loads, since ferroelectric ceramics are destroyed by low tensile loads. In order to design actuators consisting of piezoelectric ceramics, the fact mentioned above has to be considered. Considering the strain behavior of ferroelectric PZT ceramics discussed before, the general functionality of piezoelectric beam bending actuators is described in the following section.

2.7 Piezoelectric Beam Bending Actuators

All kinds of piezoelectric actuators use the inverse piezoelectric effect. By applying an external electric field to the piezoelectric material, expansions and compressions appear, dependent on either the orientation relative to the crystal structure of monocrystalline materials or the remanent polarization of ferroelectric ceramics. The length variation of piezoelectric material can be used for the realization of linear actuators (*stack actuators*), utilizing the longitudinal piezoelectric effect. This kind of transducers are characterized by small deflections and high forces [76]. Linear piezoelectric actuators are employed in different application fields, e.g. as water ultrasonic transducers, in the automobile industry as injecting valve drives with hydraulic deflection-increasing systems and as high-accuracy control drives in optics. The very small deformations at high electrical voltages (1-10 kV) are disadvantageous for this kind of actuators.

However, the small length variations can also be transformed mechanically. As already discussed before, applying an electric field in the direction of the remanent polarization P_r of ferroelectric PZT ceramics results in a spatial alignment of the individual domains. With respect to the remanent strain

S_r of the polarized ceramic material (see the points C and G in Fig. 2.8), an increase or a decrease of the total strain along the electric field direction occurs, respectively. The longitudinal expansion or compression are combined with either a transverse compression or expansion perpendicular to the electric field direction (transverse piezoelectric effect). These facts are illustrated in figure 2.9.
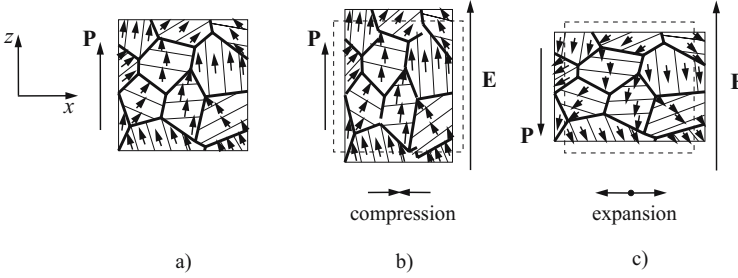
Fig. 2.9. Transverse strain behavior of PZT ceramics. - **(a)** polarized state; **(b)** electric field **E** aligned parallely, **(c)** electric field **E** aligned antiparallely to the remanent polarization

This characteristic of ferroelectric PZT ceramics can be used for the realization of a so-called *monomorph structure* as shown in figure 2.10.
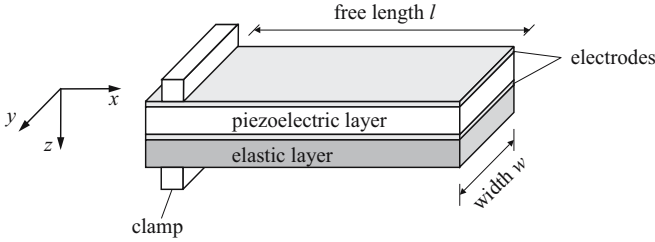
Fig. 2.10. Layer sequence of a monomorph

A monomorph consists of one active piezoceramic and one passive elastic layer. If the piezoceramic component consists of one single layer, then one alludes to *singlelayer* technology. If the piezoceramic component consists of several active piezoelectric layers with electrodes inbetween, one alludes to piezoceramics in *multilayer* technology [77].

The movement of the piezoceramic component resulting from its expansion or compression is restricted by the passive elastic component. As a consequence,

an internal piezoelectric moment arises deforming the monomorph as shown in figure 2.11. The total deflection in z-direction is much larger than the deformation of the piezoelectric component in x-direction. Due to the mechanical transformation of small length variations of the piezoceramic component into a bending deformation, it is possible to generate large deflections in z-direction, even the actuator is driven by low electric voltages (24-200 V).
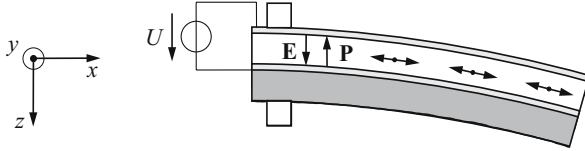
Fig. 2.11. Behavior of a monomorph subjected by an electrical voltage (**E** and **P** are aligned antiparallelly; see fig. 2.9c)

In order to increase the deflection of the beam bending actuator, the passive elastic component can be replaced by a second active piezoceramic component. This actuator structure is called *bimorph*.

In the following a bimorph in singlelayer technology is considered. If the polarization directions of both layers are identical and if they are driven in an electrical parallel connection, then the structure is called *parallel bimorph*. However, if the polarization directions of the two layers are aligned in oppositely and if they are driven in an electrical series connection, then the structure is called *serial bimorph* (see Fig. 2.12) [78].
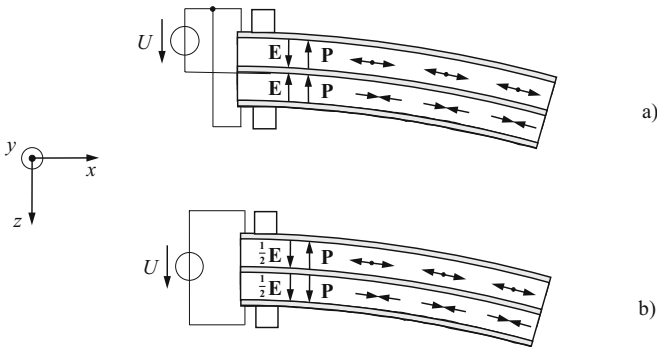
Fig. 2.12. Behavior of a bimorph subjected by an electrical voltage. - **(a)** parallel bimorph; **(b)** serial bimorph

The series connection has the advantage, that no contact has to be made with the internal electrode. However, within one single layer the value of the electric field is almost half as large as with the parallel bimorph.

In figure 2.13, a monomorph beam bending actuator consisting of a piezoceramic component in multilayer technology is shown, as it has been used for experimental investigations within the scope of this book.

multilayered ceramic

internal electrodes

slipping component

contact blades

carrier

contact pads

thermal adjustment layer
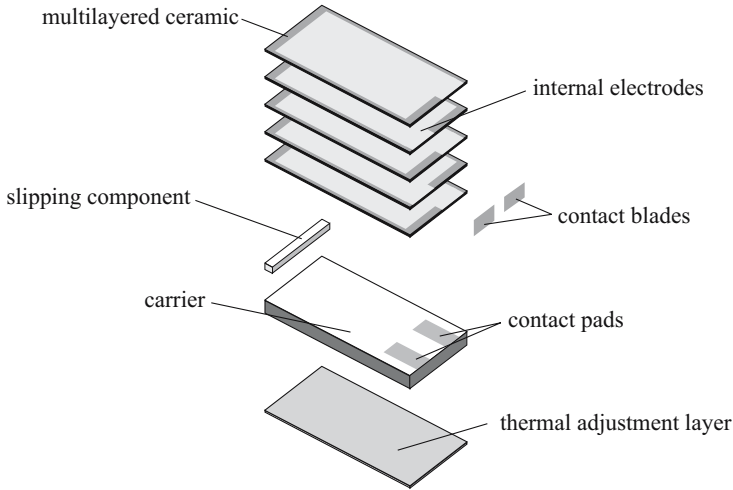
Fig. 2.13. Structure of a monomorph beam bending actuator in multilayer technology

The piezoceramic component consists of five active piezoelectric layers combined with a passive component consisting of one carrier layer and one thermal adjustment layer. Furthermore, the bending actuator consists of a slipping component. With its help, the deflections and forces caused by bending deformations can be passed on external mechanics. The thermal adjustment layer serves to compensate the different thermal expansion coefficients of the materials used for the bending actuator. The thermal adjustment layer consists of a nickel based alloy of the type NiCo 2918. Usually, the electrodes are mutually interconnected, so an alternating polarity of neighbouring layers is ensured (driving the piezoceramic layers in an electrical parallel connection). Compared to singlelayered ceramics, the lower driving voltage represents the advantage of multilayered ceramics [79]. Conventional bending actuators in singlelayer technology are driven with an operating voltage of 200 V or more. However, with the multilayer technology it is possible to reduce the operating voltage up to 24 V.

The present book does not elaborate the technological realization of beam bending actuators in multilayer technology. For more details concerning the manufacturing processes of piezoelectric beam benders, the doctoral thesis of A. J. Schmid is recommended [67], that is also embedded in the federal german research project EPIETEC (*Effektive piezokeramische Multilayer-Technologie für integrierte Niedervolt-Piezobieger*). In order to be able to use piezoelectric bending actuators usefully in technical applications, it is necessary to have a detailed knowledge concerning their static and dynamic behavior. The geometrical dimensions of the individual active and passive layers, their sequence within the multilayer compound as well as their elastic and electromechanical characteristics play a fundamental role. The analytical description of the static and dynamic behavior of piezoelectric multilayer beam bending actuators provides an emphasis in the present book. Because of the pronounced nonlinearity of the S-E characteristic in figure 2.8, the further views concentrate on the low-level signal range, i.e. in illustration 2.8, a linear approximation is effected around the point C or G, respectively. In order to achieve an analytical formulation, it necessitates a detailed consideration of the linear theory of piezoelectric materials. On the basis of the linear theory of piezoelectric materials, a general formulation in closed form analysis of piezoelectric multilayer beam bending actuators can be derived.

3

Linear Theory of Piezoelectric Materials

In order to describe the static and dynamic characteristics of piezoelectric beam bending actuators in closed form analysis, it is necessary to dwell on the phenomenological description of the strain and stress state as well as on the elastic behavior of a piezoelectric crystal. Their knowledge is decisive for the derivation of the thermodynamic potentials and the piezoelectric constitutive equations corresponding to the appropriate application. Furthermore, the thermodynamic potentials and the piezoelectric constitutive equations provide the basis for the theoretical modeling. The consideration of crystal symmetry of PZT ceramics leads to matrices of the material coefficients, which are directly enclosed in the theoretical modeling. Since all following analytical considerations are based on energetic approaches, it is important to dwell on the aspects of the deformation energy. Due to the piezoelectric characteristics of PZT ceramics and the associated electromechanical interconnection, first of all, the energy densities concerning the flexible deformation and the electric field respectively have to be specified. They form the starting point for all following considerations.

3.1 Energy Density of the Elastic Deformation

For a better understanding of the stress-strain relationship throughout a solid body, an infinitesimal volume element dV is considered. For convenience, this element is orientated in such a manner, that one coordinate axis is perpendicular to each of its faces. Now, a Cartesian coordinate system is introduced, thus the element has the form of a rectangular solid orientated in such a way, that its three intersecting edges coincide with the coordinate axes of the Cartesian coordinate system [80]. Since the mechanical stresses are continuously distributed throughout the solid, a continuous load is applied to each face of the element in the free-body diagram. The resulting stress components can be attached to the centers of the faces (see Fig. 3.1).

$$T_{xy} = T_{yx}$$
$$T_{xz} = T_{zx}$$
$$T_{yz} = T_{zy}$$
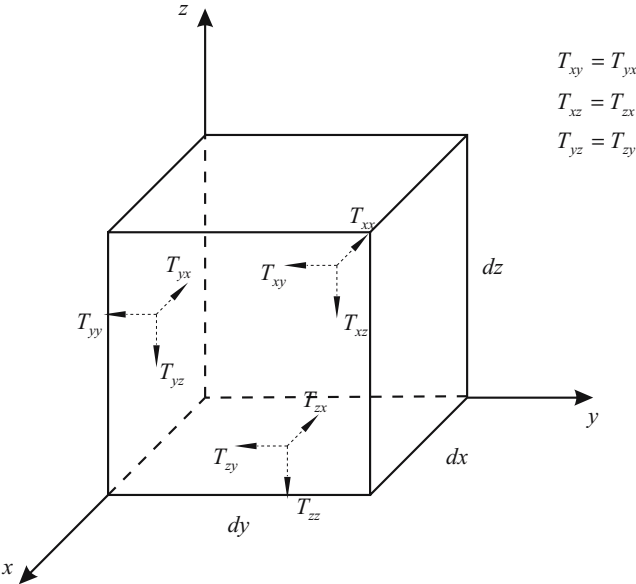
Fig. 3.1. Stress components in Cartesian coordinates
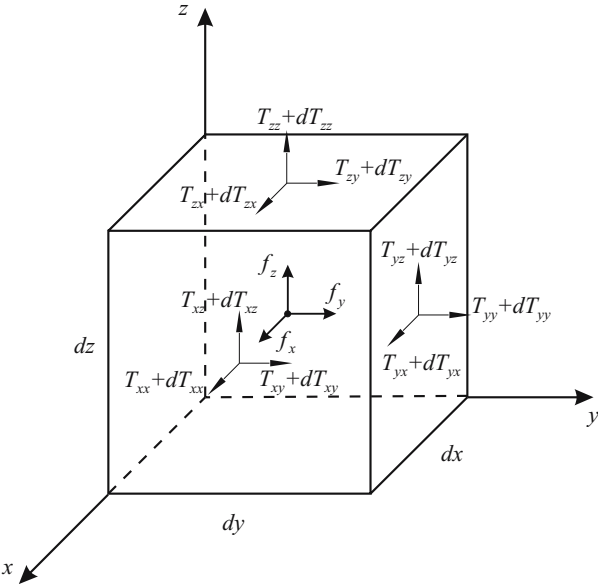
Fig. 3.2. Stress components with respect to the body forces

The stress matrix is symmetric. Furthermore, the individual body forces f_x, f_y and f_z are to be considered. They act at the geometrical center of the volume element resulting in stress components at the front surfaces of the volume element as they are illustrated in figure 3.2.

In order to simplify the calculation of the energy density of the deformed volume element, in the following only the work done by stresses acting in x-direction is considered. The work done by stresses acting in y- and z-direction is calculated similarly. Figure 3.3 represents the volume element (see Fig. 3.1 and 3.2) in its undeformed and deformed configuration in the x-y plane.

Fig. 3.3. Volume element in its undeformed and deformed configuration (x-y plane)

Due to the stress T_{xx} acting on the left of the volume element, the force is equal to $T_{xx}dydz$, where dz is the thickness of the element in z-direction. The displacement of the midpoint of side $A'D'$, the stress resultant is assumed to act on, is the displacement of point A' plus the additional displacement of the midpoint of side $A'D'$ relative to A'. The displacement of the midpoint of side $A'D'$ results from the notations shown in figure 3.3:

$$u_{A'D'} = u + \frac{1}{2}\frac{\partial u}{\partial y}dy \qquad (3.1)$$

With equation (3.1), the work done by the mechanical stress T_{xx} results in:

$$dW^{(1)}_{T_{xx}} = -T_{xx}d\left(u + \frac{1}{2}\frac{\partial u}{\partial y}dy\right)dydz \tag{3.2}$$

Taking the midpoint displacements of the sides $B'C'$, $A'B'$ and $D'C'$ into account caused by the accordingly resulting mechanical stresses (see Fig. 3.2) and including the body force f_x, results in the total work done dW_{x_1} in x-direction with $dxdydz = dV$ (derivation see appendix A):

$$dW_{x_1} = \left[T_{xx}dS_{xx} + T_{xy}d\left(\frac{\partial u}{\partial y}\right)\right]dV \tag{3.3}$$

In equation (3.3), the strain of the material according to

$$d\left(\frac{\partial u}{\partial x}\right) = dS_{xx} \tag{3.4}$$

is considered. The variable S_{xx} denotes the strain in x-direction with respect to the mechanical axial stress T_{xx} acting in the same direction. Similarly, the work done by mechanical stresses acting in y-direction results in:

$$dW_{x_2} = \left[T_{yy}dS_{yy} + T_{xy}d\left(\frac{\partial v}{\partial x}\right)\right]dV \tag{3.5}$$

The total work in the x-y plane done by the mechanical stresses results from the summation of (3.3) and (3.5):

$$dW_x = [T_{xx}dS_{xx} + T_{yy}dS_{yy} + 2T_{xy}S_{xy}]dV \tag{3.6}$$

In equation (3.6) the following correlation for the transverse strain S_{xy} is used [81]:

$$S_{xy} = \frac{1}{2}\left(\frac{\partial u}{\partial y} + \frac{\partial v}{\partial x}\right) \tag{3.7}$$

The total energy dW_m caused by the elastic deformation of the total volume element dV results in:

$$dW_m = (T_{xx}dS_{xx} + T_{yy}dS_{yy} + T_{zz}dS_{zz} + T_{xy}dS_{xy}$$
$$+ 2T_{xy}dS_{xy} + 2T_{yz}dS_{yz} + 2T_{xz}dS_{xz})\,dV \tag{3.8}$$

The explicit derivation of equation (3.8) is also effected in appendix A. Often, the individual coordinate directions x, y and z are replaced by the indices 1, 2 and 3. Then equation (3.8) can be written as follows:

$$dW_m = \left(\sum_{i=1}^{3}\sum_{j=1}^{3}T_{ij}dS_{ij}\right)dV \tag{3.9}$$

Finally, the energy density of the elastic deformation is achieved from equation (3.9) with respect to the *Einstein summation convention*:

$$dw_m = T_{ij}dS_{ij} \tag{3.10}$$

and

$$w_m = \frac{1}{2}T_{ij}S_{ij}, \tag{3.11}$$

respectively. Equation (3.11) plays an essential role in further considerations.

3.2 Energy Density of the Electrostatic Field

The electrical energy density w_e is a further important quantitiy concerning the modeling, described in more detail in the section below. Neglecting losses, the energy of the electrostatic field has to be equal to the work being necessary for the generation of the electric field [82]. Moving the charge $dQ > 0$ from a cathode to an anode, the work $dW_e = UdQ$ is necessary. Increasing the electrical voltage or charge from zero to its final value, the performed work W_e yields with respect to $Q = CU$ [83]:

$$W_e = \frac{1}{2}QU \tag{3.12}$$

The correlation between the charge density ϱ and the charge Q is given by

$$Q = \iiint\limits_{V} \varrho dV. \tag{3.13}$$

Introducing the electric potential φ, the performed work W_e can be calculated by insertion of (3.13) in (3.12) and using Maxwell's equation $\varrho = \operatorname{div}\mathbf{D}$:

$$W_e = \frac{1}{2}\iiint\limits_{V} \varphi\operatorname{div}\mathbf{D}dV \tag{3.14}$$

With the general vector algebraic relationship [84]

$$\operatorname{div}(\varphi\mathbf{D}) = \varphi\operatorname{div}\mathbf{D} + \mathbf{D}\cdot\operatorname{grad}\varphi,$$

from (3.14) follows

$$W_e = \frac{1}{2}\iiint\limits_{V} \operatorname{div}(\varphi\mathbf{D})\,dV - \frac{1}{2}\iiint\limits_{V} \mathbf{D}\cdot\operatorname{grad}\varphi dV. \tag{3.15}$$

The first term of equation (3.15) can be transformed into a surface integral over a closed surface A with the help of Gauss's theorem [85]:

$$\iiint\limits_{V} \operatorname{div}\left(\varphi \mathbf{D}\right) dV = \oint\limits_{A} \left(\varphi \mathbf{D}\right) \cdot d\mathbf{A} \tag{3.16}$$

Assuming that the charge distribution disappears in infinity ($\varrho\left(\infty\right) = 0$), the potential φ decreases at least with $1/r$ as well as the electric displacement $\mathbf{D}$ decreases at least with the second power of distance r.

$$\varphi \sim \frac{1}{r}, \quad |\mathbf{D}| \sim \frac{1}{r^2} \tag{3.17}$$

In the infinity, the surface integral disappears, since the surface increases with r^2, however, the integrand decreases with $1/r^3$. Thus, equation (3.15) results in:

$$W_e = -\frac{1}{2} \iiint\limits_{V} \mathbf{D} \cdot \operatorname{grad} \varphi \, dV \tag{3.18}$$

Due to $\operatorname{curl} \mathbf{E} = \mathbf{0}$, the electric field $\mathbf{E}$ can be mathematically represented as gradient of a scalar potential φ.

$$\mathbf{E} = -\operatorname{grad} \varphi \tag{3.19}$$

With respect to equation (3.19), equation (3.18) results in:

$$W_e = \frac{1}{2} \iiint\limits_{V} \mathbf{E} \cdot \mathbf{D} \, dV \tag{3.20}$$

Thus, the electrical energy density w_e can be calculated according to equation (3.20):

$$w_e = \frac{1}{2} \mathbf{E} \cdot \mathbf{D} \tag{3.21}$$

(3.21) can be represented in index notation:

$$w_e = \frac{1}{2} E_i D_i \tag{3.22}$$

Like equation (3.11), also equation (3.22) plays an essential role in further considerations.

3.3 Thermodynamics of Deformation

An aim is the calculation of the work being necessary for the deformation of a piezoelectric body. The body is considered to be a thermodynamically closed system, i.e. the mass remains constant.

On principle a system exchanges energy with its environment. Particularly, the force impact of the environment on the investigated system results in surface and body forces. With respect to the motion of the system, surface

and body forces perform work resulting in a change of its energy. In addition to the mechanical interaction of the system with its environment, electrical and thermal interactions can effect its change of energy, too. At the moment, only mechanical and thermal interactions with the environment are taken into account. In the next section, the considerations are extended to electrical interactions.

The general experience shows, that processes run automatically within any closed system until an *equilibrium state* appears. The equilibrium state can be clearly determined by a certain amount of macroscopically measurable parameters, that are called *independent state variables*. A special kind of energy belongs to each of these state variables. With respect to the *first law of thermodynamics*, in a closed system the total energy remains constant. The total thermal energy of a system caused by the kinetic energy of the molecules and atoms is called internal energy $\tilde{U}$ of the system. This definition was suggested by Lord Kelvin. According to the first law of thermodynamics, the internal energy can only be changed, if energy is exchanged with the environment beyond the system borders.

The change of the internal energy $d\tilde{U}$ is equal to the sum of the supplied heat $\delta\tilde{Q}$ and the supplied mechanical work δW_m [86]. Thus, it can be written:

$$d\tilde{U} = \delta\tilde{Q} + \delta W_m \qquad (3.23)$$

The terms $\delta\tilde{Q}$ and δW_m show, that the amounts of supplied heat and work are infinitesimally small, however, they do not represent differentials. δ is not a linear operator and the rules of differential calculus may not be applied to the right side of equation (3.23). Since the internal energy of a system is proportional to its mass, it can be related to the volume unit dV, thus the internal energy density U is obtained.

$$dU = \delta Q + \delta w_m \qquad (3.24)$$

It should be noted, that Q and w_m represent extensive quantities (affecting from outside). Due to the fact, that $\oint dU = 0$ representing a reversible process, dU is a state variable. According to the *second law of thermodynamics*, the heat δQ reversibly supplied to the system at temperature Θ can be expressed by following equation:

$$\delta\tilde{Q} = \Theta d\tilde{\Sigma} \qquad (3.25)$$

The extensive state variable $\tilde{\Sigma}$ is called *entropy*. Entropy related to volume is called *entropy density* and is represented by the variable Σ. Thus, from equation (3.24) follows:

$$dU = \Theta d\Sigma + \delta w_m \qquad (3.26)$$

It should be noticed, that δw_m is still written in equation (3.26).

In the following, a geometric linearization is justified due to the very small deformations of the body. The change of the deformation energy related to the unit volume has already been defined in equation (3.10):

$$\delta w_m = T_{ij}\delta S_{ij} \tag{3.27}$$

Considering reversible processes and infinitesimally homogeneous deformations, insertion of (3.27) in (3.26) yields:

$$dU = \Theta d\Sigma + T_{ij}\delta S_{ij} \tag{3.28}$$

An *adiabatic process* with $d\Sigma = 0$ (no heat exchange with the environment) results in:

$$dU = T_{ij}dS_{ij} \tag{3.29}$$

In addition, for an *isothermal process* ($\Theta = const.$), the equation (3.28) yields:

$$d\left(U - \Theta\Sigma\right) = T_{ij}dS_{ij} \tag{3.30}$$

Thus, the internal energy with respect to adiabatic and isothermal changes of state can be formulated as follows:

$$dU = \Theta d\Sigma + T_{ij}dS_{ij} \tag{3.31}$$

For the further understanding of the piezoelectric constitutive equations, the following essential and important remark is to be made. The physical pairs of variates arising together within a form of energy can be separated into *extensive* and *intensive quantities*. Concerning the formulation of different categories of energy, extensive quantities (state variables) are written behind the differential character, whereas the intensive quantities represent the factors in front of the differential characters.

3.3.1 Internal Energy of Elastic Piezoelectric Materials

In the following, the previous macroscopic considerations of the mechanical and thermodynamic behavior of a solid are extended to elastic dielectrics with piezoelectric characteristics. They provide a basis for the physical description of the static and dynamic behavior of piezoelectric n-layered beam bending actuators.

The power density of the electrostatic field yields:

$$dw_e = \mathbf{E}\cdot d\mathbf{D} \tag{3.32}$$

Taking the Einstein summation convention into account, equation (3.32) can be written as follows:

$$dw_e = E_i dD_i \tag{3.33}$$

In combination with (3.31), the internal energy density results in:

$$dU = \Theta d\Sigma + T_{ij}dS_{ij} + E_i dD_i \qquad (3.34)$$

Equation (3.34) represents the basis for the thermodynamics of flexible dielectrics with piezoelectric characteristics. By means of (3.34), a thermodynamic potential is described with respect to the extensive quantities Σ, D_i and S_{ij}. For the following considerations it is assumed, that either the temperature Θ or the entropy density Σ are kept constant. Therefore, the material constants being found in the constitutive equations are valid for adiabatic and isothermal processes.

3.3.2 Linear Constitutive Equations and Electrical Enthalpy

Equation (3.34) implies, that the total differential of dU can be described by the right side terms. Thus, it can be written:

$$dU = \left(\frac{\partial U}{\partial D_i}\right)_S dD_i + \left(\frac{\partial U}{\partial S_{ij}}\right)_D dS_{ij} \qquad (3.35)$$

The indices attached to the partial derivations refer to the state variables, that are kept constant. The conjugated and dependent state variables E_i and T_{ij} are functions of the independent state variables D_i and S_{ij}. Applying the total differential yields:

$$dE_i = \left(\frac{\partial E_i}{\partial D_k}\right)_S dD_k + \left(\frac{\partial E_i}{\partial S_{kl}}\right)_D dS_{kl} \qquad (3.36)$$

$$dT_{ij} = \left(\frac{\partial T_{ij}}{\partial D_k}\right)_S dD_k + \left(\frac{\partial T_{ij}}{\partial S_{kl}}\right)_D dS_{kl} \qquad (3.37)$$

The equations (3.36) and (3.37) are called *linear constitutive equations*. In the further considerations the field quantities $(\mathbf{T}, \mathbf{E})$ and $(\mathbf{S}, \mathbf{E})$ are considered to be independent variables. With respect to their choice the appropriate thermodynamic potentials have to be defined.

The *Legendre transformation* provides the transition of the internal energy density to a new thermodynamic potential, that is to be understood as energy density further on. The Legendre transformation is often used in thermodynamics, in order to transform state quantities to other state variables [87–89].

Constitutive Equations - Extensive Quantities (T, E)

The following total differentials are formed:

$$d\left(T_{ij}S_{ij}\right) = \frac{\partial\left(T_{ij}S_{ij}\right)}{\partial T_{ij}}dT_{ij} + \frac{\partial\left(T_{ij}S_{ij}\right)}{\partial S_{ij}}dS_{ij}$$
$$\Leftrightarrow d\left(T_{ij}S_{ij}\right) = S_{ij}dT_{ij} + T_{ij}dS_{ij} \tag{3.38}$$

$$d\left(E_i D_i\right) = \frac{\partial\left(E_i D_i\right)}{\partial E_i}dE_i + \frac{\partial\left(E_i D_i\right)}{\partial D_i}dD_i$$
$$\Leftrightarrow d\left(E_i D_i\right) = D_i dE_i + E_i dD_i \tag{3.39}$$

The subtraction of the two left side terms of the equations (3.38) and (3.39) from the left side term of equation (3.34) yields:

$$d\left(U - T_{ij}S_{ij} - E_i D_i\right) = -D_i dE_i - S_{ij}dT_{ij} \tag{3.40}$$

With the definition of the enthalpy H

$$H = U - T_{ij}S_{ij} - E_i D_i, \tag{3.41}$$

it follows

$$dH = -D_i dE_i - S_{ij}dT_{ij}. \tag{3.42}$$

According to equation (3.35), dH results in:

$$dH = \left(\frac{\partial H}{\partial E_i}\right)_T dE_i + \left(\frac{\partial H}{\partial T_{ij}}\right)_E dT_{ij}$$

The conjugated and dependent state variables D_i and S_{ij} are functions of the independent state variables E_i and T_{ij}. Applying the total differential yields:

$$dD_i = \left(\frac{\partial D_i}{\partial E_k}\right)_T dE_k + \left(\frac{\partial D_i}{\partial T_{kl}}\right)_E dT_{kl} \tag{3.43}$$

$$dS_{ij} = \left(\frac{\partial S_{ij}}{\partial E_k}\right)_T dE_k + \left(\frac{\partial S_{ij}}{\partial T_{kl}}\right)_E dT_{kl} \tag{3.44}$$

The equations (3.43) and (3.44) represent a system of constitutive equations for the extensive pair of variates $(\mathbf{T}, \mathbf{E})$, the individual material constants and the constant extensive quantities can be derived from. Furthermore, the material constants specified in Table 3.1 are defined [90].

Table 3.1. Definition of the material constants - extensive pair of variates (**T,E**)

material constant	notation	SI unit
$\partial D_i/\partial E_k = \varepsilon_{ik}$	permittivity	$[\varepsilon_{ik}] = 1\,\mathrm{F/m}$
$\partial D_i/\partial T_{kl} = \partial S_{ij}/\partial E_k = d_{ikl}$	piezoelectric coefficient	$[d_{ikl}] = 1\,\mathrm{m/V}$
$\partial S_{ij}/\partial T_{kl} = s_{ijkl}$	eleastic coefficient	$[s_{ijkl}] = 1\,\mathrm{m^2/N}$

The constitutive equations for the extensive pair of variates (**T, E**) can be summarized with respect to the material constants defined in Table 3.1:

$$D_i = \varepsilon_{ik}^T E_k + d_{ikl} T_{kl} \qquad (3.45)$$

$$S_{ij} = d_{ijk} E_k + s_{ijkl}^E T_{kl} \qquad (3.46)$$

Later on, the constitutive equations (3.45) and (3.46) are used for the derivation of the static behavior of a piezoelectric n-layered beam bending actuator. The fundamental base for the derivation of the *dynamic behavior* of a beam bending actuator is the *electrical enthalpy* H_e, that will be generally derived in the section below. The additional linear constitutive equations will be formulated, too.

Electrical Enthalpy and Constitutive Equations - Extensive Quantities $(\mathbf{S, E})$

Since S and E are considered to be independent variables, a new thermodynamic potential results from the Legendre transformation called *electrical enthalpy* H_e. Using equation (3.39) and applying the difference with respect to dU, (3.34) results in:

$$d\left(U - E_i D_i\right) = T_{ij} dS_{ij} - D_i dE_i \qquad (3.47)$$

With the definition of the electrical enthalpy H_e

$$H_e = U - E_i D_i, \qquad (3.48)$$

it follows

$$dH_e = T_{ij} dS_{ij} - D_i dE_i. \qquad (3.49)$$

According to equation (3.35), dH_e yields:

$$dH_e = \left(\frac{\partial H_e}{\partial S_{ij}}\right)_E dS_{ij} - \left(\frac{\partial H}{\partial E_i}\right)_S dE_i \qquad (3.50)$$

The conjugated and dependent state variables T_{ij} and D_i are functions of the independent state variables E_i and S_{ij}. Applying the total differential results in:

$$dT_{ij} = \left(\frac{\partial T_{ij}}{\partial S_{kl}}\right)_E dS_{kl} + \left(\frac{\partial T_{ij}}{\partial E_k}\right)_S dE_k \tag{3.51}$$

$$dD_i = \left(\frac{\partial D_i}{\partial S_{kl}}\right)_E dS_{kl} + \left(\frac{\partial D_i}{\partial E_k}\right)_S dE_k \tag{3.52}$$

The equations (3.51) and (3.52) represent a system of constitutive equations for the extensive pair of variates $(\mathbf{S}, \mathbf{E})$, the individual material constants and the constant extensive quantities can be derived from. Furthermore, the material constants specified in Table 3.2 are defined [90].

Table 3.2. Definition of the material constants - extensive pair of variates $(\mathbf{S},\mathbf{E})$

material constants	notation	SI-unit
$\partial T_{ij}/\partial S_{kl} = c_{ijkl}$	modulus of elasticity	$[c_{ijkl}] = 1\,\mathrm{N/m^2}$
$\partial T_{ij}/\partial E_k = -\partial D_i/\partial S_{kl} = -e_{ijk}$	piezoelectric modulus	$[e_{ijk}] = 1\,\mathrm{C/m^2}$

For the extensive pair of variates $(\mathbf{S}, \mathbf{E})$, the constitutive equations can be summarized in the following form:

$$T_{ij} = c_{ijkl}^E S_{kl} - e_{ijk} E_k \tag{3.53}$$

$$D_i = e_{ikl} S_{kl} + \varepsilon_{ik}^S E_k \tag{3.54}$$

Now, in combination with the constitutive equations (3.53) and (3.54) the electrical enthalpy H_e can be generally formulated, that provides a basis for the derivation of the dynamic behavior of a piezoelectric n-layered beam bending actuator.

The integration of equation (3.34) being valid for isothermal or adiabatic processes and following insertion in equation (3.48) yields the electrical enthalpy H_e:

$$H_e = \frac{1}{2}T_{ij}S_{ij} - \frac{1}{2}E_i D_i \tag{3.55}$$

With respect to the equations (3.53) and (3.54), equation (3.55) results in:

$$H_e = \frac{1}{2}\left(c_{ijkl}^E S_{kl} - e_{kij} E_k\right) S_{ij} - \frac{1}{2}\left(e_{ikl} S_{kl} + \varepsilon_{ik}^S E_k\right) E_i$$

$$\Leftrightarrow H_e = \frac{1}{2}c_{ijkl}^E S_{kl} S_{ij} - e_{iij} E_i S_{ij} - \frac{1}{2}\varepsilon_{ik}^S E_k E_i \tag{3.56}$$

So far, all previous equations have been formulated in tensor notation. In combination with the symmetry characteristics of piezoelectric PZT ceramics, it is more useful to exchange to the matrix notation, that will be introduced in the section below.

3.3.3 Condensed Notation of Elastic and Piezoelectric Tensors

In the literature concerning the theory of piezoelectricity, the use of the shorter matrix indices has been generally accepted instead of the consistent tensor notation by tensor indices. The reason for this is the symmetry of the strain and stress tensor. In order to attain to a compressed notation, the tensor double indices (ij) and (kl) are replaced by the matrix indices p and q. The appropriate correlations are specified in Table 3.3 [90].

Table 3.3. Correlation between the matrix indices and the tensor double indices

ij or kl	11	22	33	23 or 32	31 or 13	12 or 21
p or q	1	2	3	4	5	6

Introducing the matrix indices, the linear constitutive equations and the electrical enthalpy formulated in the both previous sections can be expressed in compressed notation.

The linear constitutive equations (3.45) and (3.46) considering the extensive pair of variates $(\mathbf{T}, \mathbf{E})$ can be formulated as follows:

$$D_i = \varepsilon_{ik}^T E_k + d_{iq} T_q \tag{3.57}$$

$$S_p = d_{pk} E_k + s_{pq}^E T_q \tag{3.58}$$

The linear constitutive equations (3.53) and (3.54) considering the extensive pair of variates $(\mathbf{S}, \mathbf{E})$ result in:

$$T_p = c_{pq}^E S_q - e_{pk} E_k \tag{3.59}$$

$$D_i = e_{iq} S_q + \varepsilon_{ik}^S E_k \tag{3.60}$$

Furthermore, the electrical enthalpy H_e can be formulated according to equation (3.56):

$$H_e = \frac{1}{2} c_{pq}^E S_q S_p - e_{ip} E_i S_p - \frac{1}{2} \varepsilon_{ik}^S E_k E_i \tag{3.61}$$

The equations (3.57) - (3.61) provide the basis for all further theoretical considerations. Due to the possibility of describing the elastic, piezoelectric and

dielectric constants by means of the two indices p and q, the matrices of the individual material constants can be listed. The matrices for any anisotropic material (triclinic) without symmetry center are [91]:

elastic compliance matrix

$$s^E_{pq} = \begin{pmatrix} s_{11} & s_{12} & s_{13} & s_{14} & s_{15} & s_{16} \\ s_{12} & s_{22} & s_{23} & s_{24} & s_{25} & s_{26} \\ s_{13} & s_{23} & s_{33} & s_{34} & s_{35} & s_{36} \\ s_{14} & s_{24} & s_{34} & s_{44} & s_{45} & s_{46} \\ s_{15} & s_{25} & s_{35} & s_{45} & s_{55} & s_{56} \\ s_{16} & s_{26} & s_{36} & s_{46} & s_{56} & s_{66} \end{pmatrix} \tag{3.62}$$

elastic stiffness matrix

$$c^E_{pq} = \begin{pmatrix} c_{11} & c_{12} & c_{13} & c_{14} & c_{15} & c_{16} \\ c_{12} & c_{22} & c_{23} & c_{24} & c_{25} & c_{26} \\ c_{13} & c_{23} & c_{33} & c_{34} & c_{35} & c_{36} \\ c_{14} & c_{24} & c_{34} & c_{44} & c_{45} & c_{46} \\ c_{15} & c_{25} & c_{35} & c_{45} & c_{55} & c_{56} \\ c_{16} & c_{26} & c_{36} & c_{46} & c_{56} & c_{66} \end{pmatrix} \tag{3.63}$$

piezoelectric coefficient matrix

$$d_{iq} = \begin{pmatrix} d_{11} & d_{12} & d_{13} & d_{14} & d_{15} & d_{16} \\ d_{12} & d_{22} & d_{23} & d_{24} & d_{25} & d_{26} \\ d_{13} & d_{23} & d_{33} & d_{34} & d_{35} & d_{36} \end{pmatrix} \tag{3.64}$$

piezoelectric constant matrix

$$e_{ip} = \begin{pmatrix} e_{11} & e_{12} & e_{13} & e_{14} & e_{15} & e_{16} \\ e_{12} & e_{22} & e_{23} & e_{24} & e_{25} & e_{26} \\ e_{13} & e_{23} & e_{33} & e_{34} & e_{35} & e_{36} \end{pmatrix} \tag{3.65}$$

permittivity matrix

$$\varepsilon^E_{ik} = \begin{pmatrix} \varepsilon_{11} & \varepsilon_{12} & \varepsilon_{13} \\ \varepsilon_{12} & \varepsilon_{22} & \varepsilon_{23} \\ \varepsilon_{13} & \varepsilon_{23} & \varepsilon_{33} \end{pmatrix} \tag{3.66}$$

Polarized ferroelectric ceramics such as PZT exhibit a hexagonal crystal symmetry belonging to the crystal class $C_{6v} = 6mm$ [90].

elastic compliance matrix of PZT

$$
s_{pq}^{E} = \begin{pmatrix}
s_{11} & s_{12} & s_{13} & 0 & 0 & 0 \\
s_{12} & s_{11} & s_{13} & 0 & 0 & 0 \\
s_{13} & s_{13} & s_{33} & 0 & 0 & 0 \\
0 & 0 & 0 & s_{44} & 0 & 0 \\
0 & 0 & 0 & 0 & s_{44} & 0 \\
0 & 0 & 0 & 0 & 0 & 2\left(s_{11}-s_{12}\right)
\end{pmatrix}
\tag{3.67}
$$

elastic stiffness matrix of PZT

$$
c_{pq}^{E} = \begin{pmatrix}
c_{11} & c_{12} & c_{13} & 0 & 0 & 0 \\
c_{12} & c_{11} & c_{13} & 0 & 0 & 0 \\
c_{13} & c_{13} & c_{33} & 0 & 0 & 0 \\
0 & 0 & 0 & c_{44} & 0 & 0 \\
0 & 0 & 0 & 0 & c_{44} & 0 \\
0 & 0 & 0 & 0 & 0 & 2\left(c_{11}-c_{12}\right)
\end{pmatrix}
\tag{3.68}
$$

piezoelectric coefficient matrix of PZT

$$
d_{iq} = \begin{pmatrix}
0 & 0 & 0 & 0 & d_{15} & 0 \\
0 & 0 & 0 & d_{15} & 0 & 0 \\
d_{31} & d_{31} & d_{33} & 0 & 0 & 0
\end{pmatrix}
\tag{3.69}
$$

piezoelectric constant matrix of PZT

$$
e_{ip} = \begin{pmatrix}
0 & 0 & 0 & 0 & e_{15} & 0 \\
0 & 0 & 0 & e_{15} & 0 & 0 \\
e_{31} & e_{31} & e_{33} & 0 & 0 & 0
\end{pmatrix}
\tag{3.70}
$$

permittivity matrix of PZT

$$
\varepsilon_{ik}^{E} = \begin{pmatrix}
\varepsilon_{11} & 0 & 0 \\
0 & \varepsilon_{22} & 0 \\
0 & 0 & \varepsilon_{33}
\end{pmatrix}
\tag{3.71}
$$

4

Theory of the Static Behavior of Piezoelectric Beam Bending Actuators

In the previous chapter, the energy density of the elastic deformation and the electrical energy density of a solid body have been described and derived. They provide a basis for the description of the deformation and stress state of piezoelectric materials within the scope of thermodynamics. This approach directly results in the piezoelectric constitutive equations being essential for the description of the static behavior of piezoelectric multilayer beam bending actuators. With respect to the constitutive equations, the consideration of the crystal symmetry of PZT provides a basis for the description of the static behavior of n-layered beam benders. The extensive state variables $(\mathbf{T}, \mathbf{E})$ are the starting point for the static behavior modeling. In combination with the linear piezoelectric constitutive equations, the total stored energy of the bending actuator can be formulated.

The *theorem of minimum total potential energy* provides the combination of the extensive parameters such as mechanical moment M, force F, pressure load p and driving voltage U with the intensive parameters angular deflection α, deflection ξ, volume displacement V and the electric charge Q as functions of any point x over the entire length of the bending actuator.

4.1 Sectional Quantities of a Bending Beam

A beam can be described by its main inertia axis (also called neutral axis or beam axis, respectively) and the cross sections assigned to each point of the main inertia axis [92]. Thereby, the beam axis connects the centroids of the beam's cross sections aligned perpendicularly to the beam axis. Furthermore, a flexural resistant beam is assumed, i.e. it opposes a resistance concerning a bending movement.

If external loads affect a beam, internal mechanical loads will arise. In order to determine the arising internal loads, a beam is intersected in two seperated bodies just at this position, internal forces and moments are of interest. Each separated body must be in equilibrium concerning its remaining outside loads

and affecting sectional loads, thus the equilibrium of the total system is assured. In order to define the *positive* sectional loads a right-handed Cartesian coordinate system is carried along the beam's cross-sectional area (see Fig. 4.1).
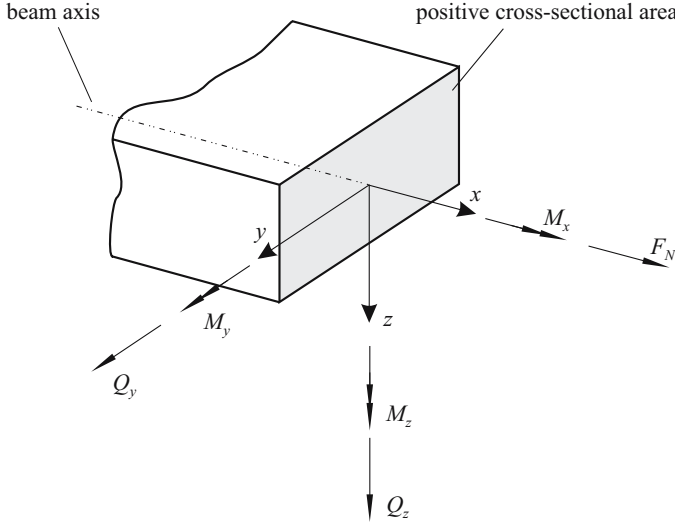
Fig. 4.1. Sectional loads within a beam

At the intersection position, the *positive* and *negative* cross-sectional areas are distinguished. A cross-sectional area is called positive, if the x-axis points out of the sectional plane. If the x-axis points into the sectional plane, a cross-sectional area is called negative. For the further considerations, planar loads of planar beam cantilevers are assumed, i.e. the principal axis of the planar loads is located in the x-z plane. Thus, in figure 4.1 only the sectional quantities like axial force F_N in x-direction, transverse force F_Q in z-direction and bending moment M_b around the y-axis remain (see Fig. 4.2).

Sectional loads resulting from distributed forces in the cross section (mechanical stresses) are referred to the centroid, thus they affect the beam axis.
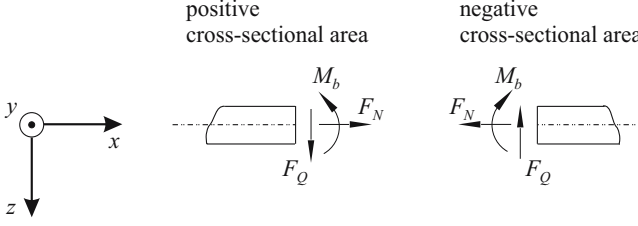
Fig. 4.2. Sectional loads and associated cross-sectional areas

4.2 Bernoulli Hypothesis of Beam Bending Theory

In the following, the kinematics of the deformation of the planar beam bender is analyzed in more detail. The *Bernoulli hypothesis of beam bending theory* provides a basis for the kinematics of deformation [93]:

All points of a planar plane perpendicular to the main inertia axis are still located in a planar plane after a pure bending deformation. Even so, the planar plane is aligned perpendicularly to the deformed main inertia axis.

In order to describe the kinematics of the planar beam, figure 4.3 is considered:
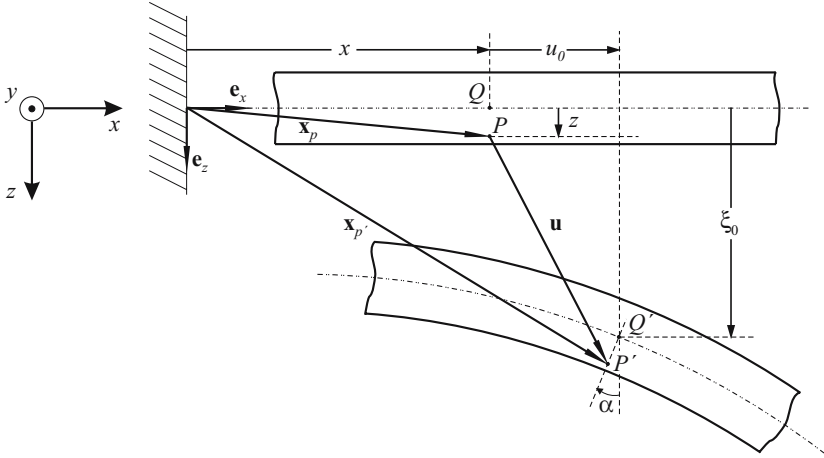
Fig. 4.3. Kinematics concerning the deformation of a beam bender

Figure 4.3 shows the location of the point P in the non-deformed state and the location of the same point P' in the deformed state. The coordinate system

is chosen in such a way, that the unit vector $\mathbf{e}_x$ coincides with the main inertia axis. The Cartesian coordinate system is defined in accordance with the definition of the sectional quantities affecting the positive cross-sectional area of a beam bender. u_0 and ξ are the displacements in x- and z-direction, respectively. $\mathbf{x}_P$ and $\mathbf{x}_{P'}$ are the position vectors of the points P and P'.

The total displacement $\mathbf{u}$ from P to P' results in

$$\mathbf{u} = \mathbf{x}_{P'} - \mathbf{x}_P, \tag{4.1}$$

with

$$\mathbf{x}_P = x\mathbf{e}_x + z\mathbf{e}_z \tag{4.2}$$

$$\mathbf{x}_{P'} = (x + u_0 - z\sin\alpha)\,\mathbf{e}_x + (\xi_0 + z\cos\alpha)\,\mathbf{e}_z \tag{4.3}$$

For small angles α, following simplifications can be made applying Taylor's theorem:

$$\sin\alpha \approx \alpha \quad \text{und} \quad \cos\alpha \approx 1 \tag{4.4}$$

Thus, in combination with (4.2) - (4.4), the displacement $\mathbf{u}$ in equation (4.1) yields:

$$\mathbf{u} = \underbrace{(u_0 - z\alpha)}_{u}\mathbf{e}_x + \underbrace{\xi}_{w}\,\mathbf{e}_z \tag{4.5}$$

The components of the displacement vector in the x-z plane (see Fig. 4.3) and the displacement w in z-direction result directly from (4.5):

$$u = u_0 - z\alpha \tag{4.6}$$

$$v = 0 \tag{4.7}$$

$$w = \xi \tag{4.8}$$

Considering the definitions for the mechanical strains (3.4) and (3.7), the individual strain components in the x-z plane can be calculated according to the equations (4.6) - (4.8):

$$S_{xx} = \frac{\partial u_0}{\partial x} - z\frac{\partial\alpha}{\partial x} \tag{4.9}$$

$$S_{yy} = \frac{\partial v}{\partial z} = 0 \tag{4.10}$$

$$2S_{xz} = \frac{\partial w}{\partial x} + \frac{\partial u}{\partial z} = \frac{\partial\xi}{\partial x} - \alpha \tag{4.11}$$

However, within the scope of Bernoulli's hypothesis of beam bending theory no transverse strains can develop. Thus, it can be written:

$$S_{xz} = 0$$

Finally, from equation (4.11) it follows:

$$\alpha = \frac{\partial \xi}{\partial x} \tag{4.12}$$

The strain S_{xx} of a planar beam results from insertion of equation (4.12) in (4.9) [94]:

$$S_{xx}(x, z) = \frac{\partial u_0}{\partial x} - z \frac{\partial^2 \xi}{\partial x^2} \tag{4.13}$$

For further considerations, the following quantities are defined:

$$\varepsilon^0 = \frac{\partial u_0}{\partial x} \quad \text{(strain of the neutral axis)}$$

$$\kappa^0 = \frac{\partial^2 \xi}{\partial x^2} \quad \text{(bend of the neutral axis)}$$

Finally, the strain S_{xx} of a planar beam can be formulated in compressed tensor notation (see Table 3.3):

$$S_1(x, z) = \varepsilon^0 - z\kappa^0 \tag{4.14}$$

It should be noted, that a strain of the neutral axis only develops, if an axial force F_N affects the positive cross-sectional area. In further considerations, no external affecting axial forces are assumed, thus the neutral axis is not expanded and it can generally be written $\varepsilon^0 = 0$. Equation (4.14) denotes a linear behavior of the strain S_1 over the entire cross section of the beam bender, whereas z defines the distance from the neutral axis [94].
The strain can only be determined if the neutral axis position is known. For a *homogeneous* and *planar* beam, this position directly results from its symmetry characteristics. By contrast, the neutral axis position of a multilayered structure has to be calculated explicitly.

4.3 Neutral Axis Position of a Multilayered Beam Bender

A piezoelectric bending actuator consisting of n layers can also be described as a beam. However, the difference consists in the different geometrical dimensions of the individual layers and their material properties generally resulting in a change of the neutral axis position $\overline{z}$. Moreover, it is suitable to define
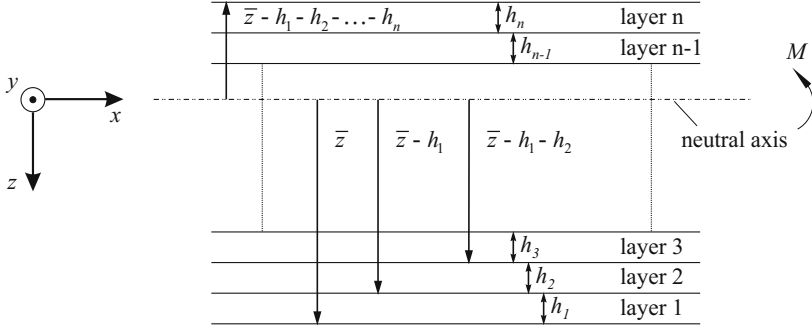
Fig. 4.4. Derivation of the neutral axis position - schematics of a multilayered beam segment

the neutral axis position as the distance to the lower edge of the multilayered beam bender (see Fig. 4.4) [95].

Following three conditions are necessary for the derivation of the neutral axis position:

1. In the case of an affecting external bending moment M, the sum of all forces in x-direction is zero [93].

$$\sum_{i=1}^{n} F_{1,i} = 0 \tag{4.15}$$

2. Assuming equation (4.14) and taking the neutral axis position into account, the strain results in:

$$S_1(x, z) = -z\kappa^0 \tag{4.16}$$

3. For elastic materials, Hooke's law is valid, thus the mechanical stresses $T_{1,i}$ arising in x-direction can be calculated according to equation (4.16):

$$T_{1,i}(x, z) = -\frac{z\kappa^0}{s_{11,i}} \tag{4.17}$$

Compared to the mechanical strain, equation (4.17) indicates a linear behavior of the mechanical stress only in sections.

The mechanical stress of the ith layer results in:

$$T_{1,i} = \frac{dF_{1,i}}{dA_i} \tag{4.18}$$

In equation (4.18), dA_i denotes a surface segment of the cross-sectional area of the ith layer in the y-z plane.

Rearranging (4.18) with respect to $dF_{1,i}$ and following integration with respect to the width w_i and the layer thickness of the ith layer yields in combination with (4.17) the axial force in the ith layer:

$$F_{1,i} = -\int_{h_{i,u}}^{h_{i,o}} \frac{w_i \kappa^0}{s_{11,i}} z \, dz \qquad (4.19)$$

Considering equation (4.15) yields in combination with (4.19):

$$\sum_{i=1}^{n} \frac{w_i}{s_{11,i}} \int_{h_{i,u}}^{h_{i,o}} z \, dz = 0 \qquad (4.20)$$

The variables $h_{i,u}$ and $h_{i,o}$ represent the lower and upper integration limits of the ith layer. They can be defined according to figure 4.4.

1. Lower integration limit $h_{i,u}$:

$$h_{i,u} = \bar{z} - \sum_{j=1}^{i} h_j \qquad (4.21)$$

2. Upper integration limit $h_{i,o}$:

$$h_{i,o} = \bar{z} - \sum_{j=1}^{i-1} h_j \qquad (4.22)$$

The evaluation of the integral sum (4.20) results with the definitions of the integration limits (4.21) and (4.22) in

$$\sum_{i=1}^{n} \frac{w_i}{s_{11,i}} \left[h_{i,o}^2 - h_{i,u}^2 \right] = 0$$

$$\Leftrightarrow \sum_{i=1}^{n} \frac{w_i}{s_{11,i}} \left[\left(\bar{z} - \sum_{j=1}^{i-1} h_j \right)^2 - \left(\bar{z} - \sum_{j=1}^{i} h_j \right)^2 \right] = 0$$

$$\Leftrightarrow \sum_{i=1}^{n} \frac{w_i}{s_{11,i}} \left[2\bar{z} \left(\sum_{j=1}^{i} h_j - \sum_{j=1}^{i-1} h_j \right) + \left(\sum_{j=1}^{i} h_j - h_i \right)^2 - \left(\sum_{j=1}^{i} h_j \right)^2 \right] = 0$$

$$\Leftrightarrow \sum_{i=1}^{n} \frac{w_i}{s_{11,i}} \left[2\bar{z} h_i - 2 h_i \sum_{j=1}^{i} h_j + h_i^2 \right] = 0,$$

and the neutral axis position can be calculated according to:

$$\overline{z} = -\frac{\sum\limits_{i=1}^{n} \frac{w_i}{s_{11,i}} h_i^2 - 2 \sum\limits_{i=1}^{n} \frac{w_i}{s_{11,i}} h_i \sum\limits_{j=1}^{i} h_j}{2 \sum\limits_{i=1}^{n} \frac{w_i}{s_{11,i}} h_i} \tag{4.23}$$

In the further considerations, equation (4.23) will play an important role. In order to ensure the transition to an energetic consideration of piezoelectric multilayer beam bending actuators, it necessitates the representation of the neutral axis bend κ^0 dependent on external and internal moments. Thus, it is possible to define the mechanical stresses in each individual layer by externally and internally affecting moments and to turn to the energetic description of a piezoelectric multilayered system.

4.4 Forces and Moments within a Multilayer System

In the following considerations, each individual layer of the bending actuator is assumed to consist either of a flexible or a piezoelectric material. Thus, in the further formalism it is necessary to consider the electromechanical interconnections by means of the piezoelectric constitutive equations.

At first, the following conditions are defined:

1. The vector of the electric field $\mathbf{E}$ develops only in z-direction.

$$E_1 = E_2 = 0 \tag{4.24}$$

2. Only one mechanical stress component develops along the x-direction (transverse piezoelectric effect; only the bending along the neutral axis is of interest).

$$T_2 = \ldots = T_6 = 0 \tag{4.25}$$

3. According to the pair of variates $(\mathbf{T}, \mathbf{E})$, the constitutive equations (3.57) and (3.58) are used.

$$D_3 = \varepsilon_{33}^T E_3 + d_{31} T_1 \tag{4.26}$$

$$S_1 = d_{31} E_3 + s_{11}^E T_1 \tag{4.27}$$

The mechanical stress within the ith layer can be calculated with respect to (4.14) and (4.27). Taking $\varepsilon^0 = 0$ into account, it can be written:

$$T_{1,i} = \frac{1}{s_{11,i}^E} \left[-z\kappa^0 - d_{31,i} E_{3,i} \right] \tag{4.28}$$

The resulting bending moment M is calculated according to [93]:

$$M = \sum_{i=1}^{n} w_i \int_{h_{i,u}}^{h_{i,o}} T_{1,i} z \, dz \qquad (4.29)$$

Insertion of (4.28) into (4.29) yields:

$$M = -\kappa^0 \frac{1}{3} \underbrace{\sum_{i=1}^{n} \frac{w_i}{s_{11,i}^E} \left[h_{i,o}^3 - h_{i,u}^3 \right]}_{\equiv C} - \underbrace{\frac{1}{2} \sum_{i=1}^{n} \frac{w_i}{s_{11,i}^E} d_{31,i} E_{3,i} \left[h_{i,o}^2 - h_{i,u}^2 \right]}_{\equiv M_{Piezo}} \qquad (4.30)$$

With the definition of the kinematic quantities C and M_{Piezo}, equation (4.30) results in:

$$M = -C\kappa^0 - M_{Piezo} \qquad (4.31)$$

After some algebraic calculations and taking the definition of the integration limits (4.21) and (4.22) into account, the kinematic quantities can be formulated as follows :

$$C = \frac{1}{3} \sum_{i=1}^{n} \frac{w_i}{s_{11,i}^E} \left[3h_i \left(\overline{z} - \sum_{j=1}^{i} h_j \right) \left(\overline{z} - \sum_{j=1}^{i-1} h_j \right) + h_i^3 \right] \qquad (4.32)$$

$$M_{Piezo} = \frac{1}{2} \sum_{i=1}^{n} \frac{w_i}{s_{11,i}^E} d_{31,i} E_{3,i} \left[2\overline{z} h_i - 2h_i \sum_{j=1}^{i} h_j + h_i^2 \right] \qquad (4.33)$$

The quantities C and M_{Piezo} represent the *total flexural rigidity* and the *piezoelectric bending moment* of the multilayered system, respectively. The bend κ^0 results with respect to equation (4.31) in:

$$\kappa^0 = -\frac{M + M_{Piezo}}{C} \qquad (4.34)$$

Equation (4.34) shows, that the kinematics of the beam bender is described by the external moment M, the piezoelectric bending moment M_{Piezo} and the total flexural rigidity C (4.32).

4.5 Total Stored Energy within a Multilayer System

Since the mechanical stress of each individual layer can now be described with respect to externally and internally affecting moments, it is possible to turn to the energetic consideration of a multilayered system.

The total energy density w_{tot} can be determined by means of the sum of the energy density of the elastic deformation w_m (3.11) and the energy density of the electrostatic field w_e (3.22):

$$w_{tot} = \frac{1}{2}E_i D_i + \frac{1}{2}T_{ij}S_{ij} \tag{4.35}$$

Considering the conditions (4.24) and (4.25), equation (4.35) results in

$$w_{tot} = \frac{1}{2}E_3 D_3 + \frac{1}{2}T_1 S_1. \tag{4.36}$$

Insertion of the piezoelectric constitutive equations (4.26) and (4.27) into (4.36) yields

$$w_{tot} = \frac{1}{2}\varepsilon_{33}^T E_3^2 + d_{31}E_3 T_1 + \frac{1}{2}s_{11}^E T_1^2. \tag{4.37}$$

4.5.1 Total Energy in a Single Layer

The energy density of the ith layer of the multilayer beam bending actuator results with respect to equation (4.37) in:

$$w_{tot,i} = \frac{1}{2}\varepsilon_{33,i}^T E_{3,i}^2 + d_{31,i}E_{3,i}T_{1,i} + \frac{1}{2}s_{11,i}^E T_{1,i}^2 \tag{4.38}$$

The volume integration of a single layer yields the total stored energy $W_{tot,i}$:

$$W_{tot,i} = \int_{h_{i,u}}^{h_{i,o}} \int_0^{w_i} \int_0^l w_{tot,i}\,dxdydz \tag{4.39}$$

Applying equation (4.38) provides $W_{tot,i}$:

$$W_{tot,i} = \int_{h_{i,u}}^{h_{i,o}} \int_0^{w_i} \int_0^l \left[\frac{1}{2}\varepsilon_{33,i}^T E_{3,i}^2 + d_{31,i}E_{3,i}T_{1,i} + \frac{1}{2}s_{11,i}^E T_{1,i}^2\right] dxdydz \tag{4.40}$$

After some algebraic transformations of equation (4.40), it can be written in combination with (4.28):

$$W_{tot,i} = \frac{1}{2}\int_0^l \left[\varepsilon_{33,i}^T E_{3,i}^2 w_i\left(h_{i,o} - h_{i,u}\right)\right] dx$$

$$+ \frac{1}{6}\int_0^l \left[\frac{w_i}{s_{11,i}^E}\left(h_{i,o}^3 - h_{i,u}^3\right)\left(\kappa^0\right)^2\right] dx$$

$$- \frac{1}{2}\int_0^l \left[\frac{w_i}{s_{11,i}^E}d_{31,i}^2 E_{3,i}^2\left(h_{i,o} - h_{i,u}\right)\right] dx \tag{4.41}$$

Integration with respect to the beam bender's length l is not effected yet. Thus, the *theorem of minimum total potential energy* will be applied subsequently. In the following, the total stored energy of the multilayered system can be determined with respect to equation (4.41).

4.5.2 Energy in an n-layered System

The energy within the multilayered system results from summation of the individual energy amounts (4.41) of each individual layer.

$$W_{tot} = \sum_{i=1}^{n} W_{tot,i} \tag{4.42}$$

Insertion of (4.41) into (4.42) yields:

$$W_{tot} = \frac{1}{2} \sum_{i=1}^{n} \int_{0}^{l} \left[\varepsilon_{33,i}^{T} E_{3,i}^{2} w_i \left(h_{i,o} - h_{i,u} \right) \right] dx$$

$$+ \frac{1}{6} \sum_{i=1}^{n} \int_{0}^{l} \left[\frac{w_i}{s_{11,i}^{E}} \left(h_{i,o}^{3} - h_{i,u}^{3} \right) \left(\kappa^0 \right)^{2} \right] dx$$

$$- \frac{1}{2} \sum_{i=1}^{n} \int_{0}^{l} \left[\frac{w_i}{s_{11,i}^{E}} d_{31,i}^{2} E_{3,i}^{2} \left(h_{i,o} - h_{i,u} \right) \right] dx \tag{4.43}$$

Using the definition for the total flexural rigidity C in (4.30), (4.43) can be formulated as follows:

$$W_{tot} = \frac{1}{2} \sum_{i=1}^{n} \int_{0}^{l} \left[\varepsilon_{33,i}^{T} E_{3,i}^{2} w_i h_i \right] dx - \frac{1}{2} \sum_{i=1}^{n} \int_{0}^{l} \left[\frac{w_i}{s_{11,i}^{E}} d_{31,i}^{2} E_{3,i}^{2} \left(h_{i,o} - h_{i,u} \right) \right] dx$$

$$+ \frac{1}{2} \int_{0}^{l} \underbrace{\left[C \left(\kappa^0 \right)^{2} \right]}_{(*)} dx \tag{4.44}$$

The term $(*)$ in the last integral of equation (4.44) is determined by applying the definition (4.34) for the bend of the neutral axis. After some algebraic calculations, the total energy W_{tot} can be formulated in its final form:

$$W_{tot} = \frac{1}{2} \sum_{i=1}^{n} \int_{0}^{l} \left[\varepsilon_{33,i}^{T} E_{3,i}^{2} w_i h_i \right] dx - \frac{1}{2} \sum_{i=1}^{n} \int_{0}^{l} \left[\frac{w_i h_i}{s_{11,i}^{E}} d_{31,i}^{2} E_{3,i}^{2} \right] dx$$

$$+ \int_{0}^{l} \left[\frac{M^2}{2C} + \frac{M M_{Piezo}}{C} + \frac{M_{Piezo}^2}{2C} \right]^{2} dx \tag{4.45}$$

Equation (4.45) provides a basis for the calculation of the coupling matrix connecting the intensive and extensive quantities. In the next section, these quantities are considered in more detail.

4.6 Canonical Conjugates and Coupling Matrix

The term of the *canonical conjugates* is originally used within the context of Hamilton's mechanics [96, 97]. Concerning the description of the static behavior of a piezoelectric bending actuator based on energetic considerations, canonical conjugates are directly connected with the concept of the total stored deformation energy W_{tot} [15].

In the further considerations the extensive quantities like bending moment M, force F, pressure load p and driving voltage U are assumed to affect a clamped-free piezoelectric beam bending actuator (see Fig. 4.5) with respect to the following boundary conditions:

1. The multilayer beam bender is subjected to an external static moment M at the tip.
2. The beam bending actuator is subjected to an external static force F perpendicularly to the tip.
3. The beam bender is subjected to a uniform pressure load p applied over the entire length l and width w of the bender.
4. The active piezoelectric layers are subjected to the same driving voltage U over their entire length l and width w (electrical parallel connection).
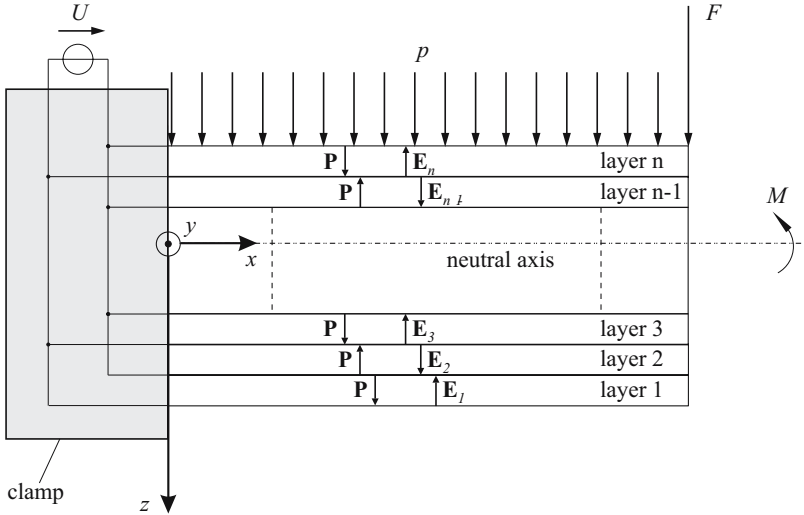
Fig. 4.5. Extensive parameters M, F, p and U

Subjecting the beam bending actuator to the external loads mentioned above results in a change of its total stored deformation energy W_{tot}. The following partial derivation of W_{tot} with respect to the individual extensive quantitiy yields the appropriate canonical conjugate. In Table 4.1,

the extensive parameters and their corresponding intensive parameters (canonical conjugates) are represented.

Table 4.1. Extensive parameters and their corresponding intensive parameters

extensive parameters		intensive parameters
bending moment	$M \longleftrightarrow \alpha$	bending angle
force	$F \longleftrightarrow \xi$	deflection
pressure load	$p \longleftrightarrow V$	volume displacement
electrical voltage	$U \longleftrightarrow Q$	charge

In each case, the multiplication of two corresponding pairs of variates results in a physical quantity with the dimensions of an energy. In further considerations, the canonical conjugates designate the *intensive quantities* [15]. In figure 4.6 the corresponding intensive quantities like bending angle α, deflection ξ, volume displacement V and generated charge Q are illustrated.
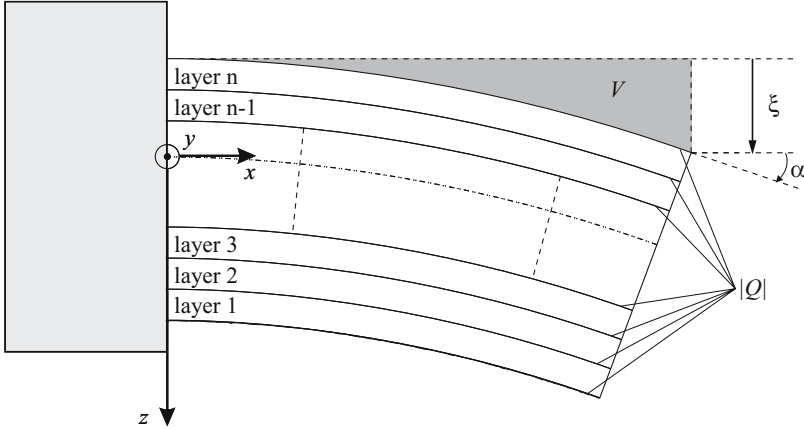
Fig. 4.6. Resulting intensive quantities α, ξ, V und Q

By means of partial derivation of the total stored deformation energy W_{tot} with respect to an extensive size, the appropriate intensive size can only be determined at the *affecting point* x_0. These facts are also summarized in CASTIGLIANO's theorem, which is only suitable for the determination of deformations of an elastic system with respect to especially chosen points [18, 98]. Thus, no information can be obtained concerning the behavior of the bending

angle α, the deflection ξ, the volume displacement V and the generated charge Q at arbitrary points $x \neq x_0$.

By means of the *theorem of minimum total potential energy* in combination with the *Ritz method*, the behavior of the intensive quantities can be described for arbitrary points x over the entire length of the beam bender. Furthermore, the dependence of the individual intensive sizes on the non-corresponding extensive sizes is of interest. In order to allow for a general consideration, this dependence can be represented by means of a *coupling matrix* $\mathbf{M}$ connecting the intensive and extensive quantities:

$$
\underbrace{\begin{pmatrix} \alpha\left(x\right) \\ \xi\left(x\right) \\ V\left(x\right) \\ Q\left(x\right) \end{pmatrix}}_{\text{intensive sizes}} = \underbrace{\begin{pmatrix} m_{11}\left(x\right) & m_{12}\left(x\right) & m_{13}\left(x\right) & m_{14}\left(x\right) \\ m_{21}\left(x\right) & m_{22}\left(x\right) & m_{23}\left(x\right) & m_{24}\left(x\right) \\ m_{31}\left(x\right) & m_{32}\left(x\right) & m_{33}\left(x\right) & m_{34}\left(x\right) \\ m_{41}\left(x\right) & m_{42}\left(x\right) & m_{43}\left(x\right) & m_{44}\left(x\right) \end{pmatrix}}_{\text{coupling matrix } \mathbf{M}} \underbrace{\begin{pmatrix} M \\ F \\ p \\ U \end{pmatrix}}_{\text{extensive sizes}}
\tag{4.46}
$$

In the two following sections, the relevant principles of mechanics are discussed in more detail, which allow for the determination of the matrix elements m_{ij} of the coupling matrix $\mathbf{M}$ formulated in equation (4.46).

4.7 Principle of Virtual Work

In order to achieve a generalized representation between the canonically conjugated pair of variates M and α, F and ξ, p and V as well as U and Q, some preliminary considerations have to be made.

Generally, the physical work W is defined as scalar product of a displacement $d\mathbf{x}$ and the corresponding force $\mathbf{F}$. In order to apply the term of physical work also to static considerations, where no displacements develop, virtual displacements $\delta\mathbf{x}$ are defined with following characteristics [99]:

1. Virtual displacements (conceivable ones, not necessarily actually developing ones) and virtual twists, respectively are infinitesimally small and can be considered like differentials!
2. Virtual displacements must be compatible with the geometrical system boundaries!

$$\Longrightarrow \text{virtual work done by a force:} \quad \delta W = \mathbf{F} \cdot \delta\mathbf{x}$$

$$\Longrightarrow \text{virtual work done by a moment:} \quad \delta W = \mathbf{M} \cdot \delta\boldsymbol{\varphi}$$

The principle of virtual work means:

A mechanical system will be in equilibrium, if the virtual work done by external forces and moments corresponding with virtual displacements and twists regarding equilibrium position disappears:

$$\delta W = \sum_j \mathbf{F}_{j,ex} \cdot \delta \mathbf{x}_j + \sum_j \mathbf{M}_{j,ex} \cdot \delta \boldsymbol{\varphi}_j = 0 \tag{4.47}$$

In the following, the principle of the virtual work will be used for the formulation of the theorem of total potential energy.

4.8 Theorem of Minimum Total Potential Energy

Conservative forces (e.g. weight, spring force) distinguish themselves from the path independence of the performed work concerning the movement from a point 1 to a point 2. The performed work only depends on the position of the points. For example, if a particle mass m performs a virtual displacement δz from point 1 to point 2 in the gravitational field (representing a conservative field), thus the performed work of the weight results in $\delta W = -mg\mathbf{e}_z \cdot \delta z \mathbf{e}_z = -mg\delta z$ (see Fig. 4.7).
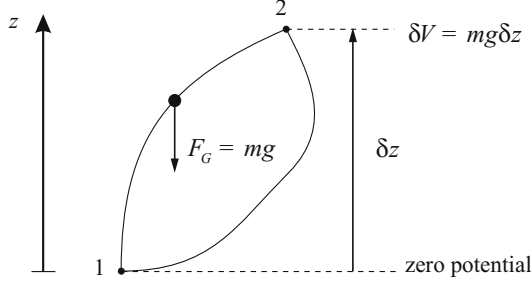
Fig. 4.7. Virtual work in a conservative field

However, the work performed by the weight is associated to an increase of the potential energy according to $\delta V = mg\delta z$. Thus, it can be written:

$$\delta W = -\delta V \tag{4.48}$$

If a system is solely loaded by potential forces, then the principle of virtual work (4.47) can also be formulated by means of the potential energy according to equation (4.48):

$$\delta V = 0 \tag{4.49}$$

In case of a clamped-free beam bending actuator, it can not be assumed any longer, that externally affecting forces are exclusively potential forces. Nevertheless, in order to apply the principle of virtual work, in the following the stored deformation energy W_{tot} (4.45) within the multilayered system is to be expressed by the potential energy, whereas the work performed by external forces is taken into consideration separately using the quantity W_a.

If only a part of the load can be described by the potential energy, thus equation (4.49) can be modified in the following way:

$$\delta\left(V - W\right) = 0 \tag{4.50}$$

With the separate representation of W_{tot} and W_a, it has to be written:

$$\delta\left(W_{tot} - W_a\right) = 0 \tag{4.51}$$

The difference $W_{tot} - W_a$ is called *total potential energy* Π. With the knowledge, that the potential energy possesses a relative minimum in a stable steady state, following theorem can be formulated [100]:

Theorem of total potential energy
A system is in a steady state, if the variation of the total potential energy vanishes.

$$\delta\left(W_{tot} - W_a\right) = \delta\Pi = 0 \tag{4.52}$$

or

$$\Pi = W_{tot} - W_a \Longrightarrow \text{minimum} \tag{4.53}$$

It should be noted, that W_a is to be formulated in such a way, as if the force has obtained its maximum value along the entire deformation path. In this case, the quantity W_a is also called *final value work*. In the following, the matrix elements m_{ij} of the coupling matrix $\mathbf{M}$ (4.46) are derived by means of the theorem of minimum total potential energy.

4.9 Derivation of the Coupling Matrix

Using equation (4.53) in combination with the total stored deformation energy W_{tot} (4.45) within the piezoelectric beam bender, the total potential energy Π results in

$$\Pi = \frac{1}{2}\sum_{i=1}^{n}\int_{0}^{l}\left[\varepsilon_{33,i}^{T}E_{3,i}^{2}w_{i}h_{i}\right]dx - \frac{1}{2}\sum_{i=1}^{n}\int_{0}^{l}\left[\frac{w_{i}h_{i}}{s_{11,i}^{E}}d_{31,i}^{2}E_{3,i}^{2}\right]dx$$

$$+ \int_{0}^{l}\left[\frac{M^2}{2C} + \frac{MM_{Piezo}}{C} + \frac{M_{Piezo}^2}{2C}\right]dx - W_a. \tag{4.54}$$

Now, it is a goal to find a function minimizing the sum of the integral expressions in equation (4.54). This basic idea is described by the *Ritz method*, designated by Walter Ritz (1878 - 1909). It means, that for the unknown displacement function $\xi(x)$ an approach with k comparison functions $\xi_j(x)$ and unknown coefficients a_j in the form

$$\xi(x) = \sum_{j=1}^{k} a_j \xi_j(x) \tag{4.55}$$

has to be chosen, whereas each function $\xi_j(x)$ has to satisfy the geometrical boundary conditions of the mechanical system. The coefficients a_j are determined in such a way, that the total potential energy Π possesses a minimum value for the formulation (4.55). The necessary conditions

$$\frac{\partial \Pi}{\partial a_i} = 0 \quad \text{with} \ \ j \le i \le k \tag{4.56}$$

form a linear set of equations with k equations for the k coefficients a_j. If there are unsuitable comparison functions among the selected ansatz functions, then they will be automatically eliminated by the method [101].

4.9.1 Multilayer Beam Bender Subjected to an External Static Moment

According to (4.54), the final value work W_a performed by the external moment M must be formulated. Taking the canonically cojugated pair of variates (see Table 4.1) and the affecting point of the moment at the bender's tip $(x = l)$ into account, the final value work results in:

$$W_a = M\alpha(l) = M\frac{\partial \xi}{\partial x}\bigg|_{x=l} \tag{4.57}$$

Furthermore, the ordinary differential equation of the bending line is used [102]:

$$M = -C\frac{\partial^2 \xi}{\partial x^2} \tag{4.58}$$

The quantity C denotes the defined total flexural rigidity (4.32) of the multilayer system. Thus, with respect to (4.57) and (4.58), the total potential energy Π (4.54) is equal to:

$$\Pi = \frac{1}{2}\sum_{i=1}^{n}\int_0^l \left[\varepsilon_{33,i}^T E_{3,i}^2 w_i h_i\right] dx - \frac{1}{2}\sum_{i=1}^{n}\int_0^l \left[\frac{w_i h_i}{s_{11,i}^E} d_{31,i}^2 E_{3,i}^2\right] dx$$

$$+ \int_0^l \left[\frac{C}{2}\left(\frac{\partial^2 \xi}{\partial x^2}\right)^2 - \left(\frac{\partial^2 \xi}{\partial x^2}\right) M_{Piezo} + \frac{M_{Piezo}^2}{2C}\right] dx - M\frac{\partial \xi}{\partial x}\bigg|_{x=l} \tag{4.59}$$

According to the Ritz method, the following ansatz function

$$\xi\left(x\right) = \sum_{j=2}^{k} a_j x^j \tag{4.60}$$

with respect to equation (4.55) is chosen, where $\xi_j\left(x\right) = x^j$. Insertion of (4.60) in (4.59) and following partial derivation with respect to the coefficients a_i for $j \leq i \leq k$ yields in combination with (4.56) the integral minimum of the total potential energy Π:

$$\frac{\partial \Pi}{\partial a_i} = \int_0^l \frac{\partial}{\partial a_i}\left(\frac{\partial^2 \xi}{\partial x^2}\right)\left[C\left(\frac{\partial^2 \xi}{\partial x^2}\right) - M_{Piezo}\right] dx - M\frac{\partial}{\partial a_i}\left(\frac{\partial \xi}{\partial x}\right)\Bigg|_{x=l} = 0 \tag{4.61}$$

Furthermore, the ansatz function (4.60) yields:

$$\frac{\partial \xi}{\partial x} = \sum_{j=2}^{k} j a_j x^{j-1} \tag{4.62}$$

$$\frac{\partial^2 \xi}{\partial x^2} = \sum_{j=2}^{k} j\left(j-1\right) a_j x^{j-2} \tag{4.63}$$

Using (4.62) and (4.63), the partial derivatives with respect to the coefficient a_i result in:

$$\frac{\partial}{\partial a_i}\left(\frac{\partial \xi}{\partial x}\right)\Bigg|_{x=l} = i l^{i-1} \tag{4.64}$$

$$\frac{\partial}{\partial a_i}\left(\frac{\partial^2 \xi}{\partial x^2}\right) = i\left(i-1\right) x^{i-2} \tag{4.65}$$

Insertion of (4.63), (4.64) and (4.65) into equation (4.61) and evaluation of the integral yields after some algebraic rearranging:

$$\left(i-1\right)\sum_{j=2}^{k}\frac{j\left(j-1\right)}{j+i-3} a_j l^{j-2} = \frac{M}{C} + \frac{M_{Piezo}}{C} \tag{4.66}$$

Equation (4.66) represents a linear system of equations, the coefficients a_j of the ansatz function $\xi\left(x\right)$ can be derived from. In order to set up the linear system of equations, $k = 4$ is chosen. Detailed calculations are presented in appendix B.1.

Evaluation of the linear system of equations (4.66) yields the nontrivial solution for the coefficient a_2:

$$a_2 = \frac{1}{2}\left[\frac{M}{C} + \frac{M_{Piezo}}{C}\right] \tag{4.67}$$

Since all active layers are driven with the same voltage U, M_{Piezo} from equation (4.33) can be formulated as follows:

$$M_{Piezo} = U m_{Piezo} \qquad (4.68)$$

The quantity m_{Piezo} represents the piezoelectric moment referred to the driving voltage U. Considering equation (4.33), m_{Piezo} can be written in the following form:

$$m_{Piezo} = \frac{1}{2} \sum_{i=1}^{n} \frac{w_i d_{31,i}}{s_{11,i}^E h_i} \left[2\bar{z} h_i - 2h_i \sum_{j=1}^{i} h_j + h_i^2 \right] \qquad (4.69)$$

Insertion of the coefficient a_2 into (4.60) with respect to (4.68) yields the ansatz function standardized on the bending actuator length l:

$$\xi(x) = M \underbrace{\frac{l^2}{2C} \left(\frac{x}{l}\right)^2}_{=m_{21}(x)} + U \underbrace{\frac{m_{Piezo} l^2}{2C} \left(\frac{x}{l}\right)^2}_{=m_{24}(x)}. \qquad (4.70)$$

The derivative of the ansatz function $\xi(x)$ with respect to the length coordinate x yields the bending angle for small deflections $\tan \alpha(x) \approx \alpha(x) = d\xi(x)/dx$.

$$\alpha(x) = M \underbrace{\frac{l}{C} \left(\frac{x}{l}\right)}_{=m_{11}(x)} + U \underbrace{\frac{m_{Piezo} l}{C} \left(\frac{x}{l}\right)}_{=m_{14}(x)} \qquad (4.71)$$

The volume displacement $V(x)$ is calculated by means of integration of equation (4.70) according to

$$V(x) = \int_0^x \int_0^w \xi(x') \, dx' dy \qquad \text{, with } w = \max\{w_i \, \forall i \, | 1 \le i \le n\}. \quad (4.72)$$

Thus, the volume displacement results in

$$V(x) = M \underbrace{\frac{w l^3}{6C} \left(\frac{x}{l}\right)^3}_{=m_{31}(x)} + U \underbrace{\frac{m_{Piezo} w l^3}{6C} \left(\frac{x}{l}\right)^3}_{=m_{34}(x)}. \qquad (4.73)$$

At this point, the matrix elements m_{11}, m_{14}, m_{21}, m_{24}, m_{31} and m_{34} of the coupling matrix $\mathbf{M}$ are known for arbitrary points x over the entire length of the multilayer beam bending actuator.

4.9.2 Multilayer Beam Bender Subjected to an External Static Force

According to (4.54), the final value work W_a performed by the external force F has to be formulated. Taking the canonically cojugated pair of variates (see

Table 4.1) and the position the force affects the bender's tip into account, the final value work results in:

$$W_a = F\xi|_{x=l} \tag{4.74}$$

The integral minimum of the total potential energy Π yields with respect to equation (4.61):

$$\int_0^l \frac{\partial}{\partial a_i}\left(\frac{\partial^2 \xi}{\partial x^2}\right)\left[C\left(\frac{\partial^2 \xi}{\partial x^2}\right) - M_{Piezo}\right]dx - F\frac{\partial \xi}{\partial a_i}\bigg|_{x=l} = 0 \tag{4.75}$$

In order to formulate the ansatz function, equation (4.60) is used again. Taking (4.62) and (4.63) into account, it can be written:

$$\frac{\partial}{\partial a_i}\left(\frac{\partial^2 \xi}{\partial x^2}\right) = i\,(i-1)\,x^{i-2} \tag{4.76}$$

$$\frac{\partial \xi}{\partial a_i}\bigg|_{x=l} = l^i \tag{4.77}$$

Insertion of (4.63), (4.76) and (4.77) into equation (4.61) yields after some algebraic rearranging:

$$i\,(i-1)\sum_{j=2}^k \frac{j\,(j-1)}{j+i-3}a_j l^{j-2} = \frac{Fl}{C} + i\frac{M_{Piezo}}{C} \tag{4.78}$$

In order to set up the linear system of equations, $k = 4$ is chosen. Furthermore, $j \le i \le k$ is considered. Detailed calculations of the matrix elements associated with the force F are presented in appendix B.2.

The evaluation of the linear system of equations (4.78) yields the nontrivial solutions

$$a_2 = \frac{1}{2}\left(\frac{Fl}{C} + \frac{M_{Piezo}}{C}\right) \tag{4.79}$$

and

$$a_3 = -\frac{1}{6}\frac{F}{C}. \tag{4.80}$$

Insertion of the coefficients a_2 and a_3 into (4.60) with respect to (4.68) results in the ansatz function standardized on the bending actuator length l:

$$\xi(x) = F\underbrace{\frac{l^3}{6C}\left[3\left(\frac{x}{l}\right)^2 - \left(\frac{x}{l}\right)^3\right]}_{=m_{22}(x)} + Um_{24}(x) \tag{4.81}$$

The derivative of the ansatz function $\xi(x)$ with respect to the length coordinate x yields the bending angle for small deflections $\tan\alpha(x) \approx \alpha(x) = d\xi(x)/dx$.

$$\alpha(x) = F\underbrace{\frac{l^2}{2C}\left[2\left(\frac{x}{l}\right) - \left(\frac{x}{l}\right)^2\right]}_{=m_{12}(x)} + Um_{14}(x) \tag{4.82}$$

The volume displacement $V(x)$ is calculated by means of integration of equation (4.81) according to (4.72).

$$V(x) = F\underbrace{\frac{l^4}{24C}\left[4\left(\frac{x}{l}\right)^3 - \left(\frac{x}{l}\right)^4\right]}_{=m_{32}(x)} + Um_{34}(x) \tag{4.83}$$

Thus, the matrix elements m_{12}, m_{22}, and m_{32} of the coupling matrix $\mathbf{M}$ are known as a function of arbitrary points x over the entire length of the multilayer beam bending actuator.

4.9.3 Multilayer Beam Bender Subjected to a Uniform Pressure Load

According to (4.54), the final value work W_a performed by the external pressure load p has to be formulated. Taking the canonically cojugated pair of variates (see Table 4.1) and the boundary condition of a *uniform* pressure load affecting the beam bender over its entire length l and width w into account, the final value work results in:

$$W_a = pw\int_0^l \xi dx \tag{4.84}$$

According to equation (4.61), it can be written:

$$\int_0^l \frac{\partial}{\partial a_i}\left(\frac{\partial^2\xi}{\partial x^2}\right)\left[C\left(\frac{\partial^2\xi}{\partial x^2}\right) - M_{Piezo}\right]dx - pw\int_0^l \frac{\partial\xi}{\partial a_i}dx = 0 \tag{4.85}$$

In order to formulate the ansatz function, equation (4.60) is used. Taking (4.62) and (4.63) into account, it can be written:

$$\frac{\partial}{\partial a_i}\left(\frac{\partial^2\xi}{\partial x^2}\right) = i(i-1)x^{i-2} \tag{4.86}$$

$$\frac{\partial\xi}{\partial a_i} = x^i \tag{4.87}$$

Insertion of (4.63), (4.86) and (4.87) into equation (4.85) yields after some algebraic rearranging:

$$i\left(i^2-1\right)\sum_{j=2}^{k}\frac{j\left(j-1\right)}{j+i-3}a_j l^{j-2}=\frac{pwl^2}{C}+i\left(i+1\right)\frac{M_{Piezo}}{C} \tag{4.88}$$

In order to set up the linear system of equations, $k = 4$ is chosen. Furthermore, $j \leq i \leq k$ is considered. Detailed calculations of the matrix elements associated with the pressure load p are presented in appendix B.3. The evaluation of the linear system of equations (4.88) yields the nontrivial solutions

$$a_2 = \frac{1}{4}\left(\frac{pwl^2}{C}+\frac{2M_{Piezo}}{C}\right), \quad a_3 = -\frac{1}{6}\frac{pwl}{C} \tag{4.89}$$

and

$$a_4 = \frac{1}{24}\frac{pw}{C}. \tag{4.90}$$

With respect to (4.68), the insertion of the coefficients a_2, a_3 and a_4 into (4.60) results in the ansatz function standardized on the bending actuator length l:

$$\xi\left(x\right) = p\underbrace{\frac{wl^4}{24C}\left[6\left(\frac{x}{l}\right)^2-4\left(\frac{x}{l}\right)^3+\left(\frac{x}{l}\right)^4\right]}_{=m_{23}(x)}+Um_{24}\left(x\right) \tag{4.91}$$

The derivative of the ansatz function $\xi\left(x\right)$ with respect to the length coordinate x yields the bending angle for small deflections $\alpha\left(x\right)=d\xi\left(x\right)/dx$.

$$\alpha\left(x\right)=p\underbrace{\frac{wl^3}{6C}\left[3\left(\frac{x}{l}\right)-3\left(\frac{x}{l}\right)^2+\left(\frac{x}{l}\right)^3\right]}_{=m_{13}(x)}+Um_{14}\left(x\right) \tag{4.92}$$

The volume displacement $V\left(x\right)$ is calculated by means of integration of equation (4.91) according to (4.72).

$$V\left(x\right)=p\underbrace{\frac{w^2l^5}{120C}\left[10\left(\frac{x}{l}\right)^3-5\left(\frac{x}{l}\right)^4+\left(\frac{x}{l}\right)^5\right]}_{=m_{33}(x)}+Um_{34}\left(x\right) \tag{4.93}$$

Thus, the matrix elements m_{13}, m_{23}, and m_{33} of the coupling matrix $\mathbf{M}$ are known as a function of arbitrary points x over the entire length of the multilayer beam bending actuator.

4.9.4 Electrical Charge Generated by the Extensive Parameters

In order to calculate the generated charge Q dependent on the extensive quantities like moment M, force F, pressure load p and driving voltage U, the total potential energy Π (4.54) has to be formulated as a function of the charge Q. The detailed calculation is presented in appendix B.4.

Taking the boundary condition into account, that all active layers are driven with the same voltage $U_{3,i} = U$, equation (4.45) can be formulated as follows:

$$
W_{tot} = \frac{1}{2}\sum_{i=1}^{n}\int_{0}^{l}\left[\frac{\varepsilon_{33,i}^{T}w_i}{h_i}U^2\right]dx - \frac{1}{2}\sum_{i=1}^{n}\int_{0}^{l}\left[\frac{d_{31,i}^2 w_i}{s_{11,i}^E h_i}U^2\right]dx
$$

$$
+\int_{0}^{l}\frac{M_{Piezo}^2}{2C}dx + \int_{0}^{l}\left[\frac{M^2}{2C} + \frac{MM_{Piezo}}{C}\right]dx \tag{4.94}
$$

According to the definition of the quantity M_{Piezo} in (4.33), it can be written:

$$
\frac{M_{Piezo}^2}{2C} = U^2\frac{m_{Piezo}^2}{2C} \tag{4.95}
$$

The quantity $m_{Piezo}^2/2C$ physically corresponds to a capacity per unit length (unit: $1\,\mathrm{F/m}$). Now, equation (4.94) can be formulated in the following form using the definition (4.95):

$$
W_{tot}\left(x\right) = \frac{1}{2}\sum_{i=1}^{n}\int_{0}^{x}\left[\frac{\varepsilon_{33,i}^{T}w_i}{h_i}U^2\right]dx' - \frac{1}{2}\sum_{i=1}^{n}\int_{0}^{x}\left[\frac{d_{31,i}^2 w_i}{s_{11,i}^E h_i}U^2\right]dx'
$$

$$
+U^2\int_{0}^{x}\frac{m_{Piezo}^2}{2C}dx' + \int_{0}^{x}\left[\frac{M^2}{2C} + \frac{MM_{Piezo}}{C}\right]dx' \tag{4.96}
$$

In order to formulate the total potential energy Π, the driving voltage U combining the charge Q_i and the capacitance C_i of the ith layer of the piezoelectric multilayer beam bending actuator is considered. For the ith layer it can be written:

$$
U = \frac{Q_i}{C_i} \tag{4.97}
$$

(4.97) results in [103]:

$$
U = \frac{\sum\limits_{i=1}^{n}Q_i}{\sum\limits_{i=1}^{n}C_i} = \frac{Q_{tot}}{C_{tot}} \tag{4.98}
$$

Furthermore, the general correlations

$$C_{tot} = \frac{\partial Q_{tot}}{\partial U} \quad \text{and} \quad Q_{tot} = \frac{\partial W_{tot}}{\partial U}$$

yield:

$$C_{tot} = \frac{\partial^2 W_{tot}}{\partial U^2} \tag{4.99}$$

Double partial derivation of (4.96) with respect to U yields:

$$\frac{\partial^2 W_{tot}(x)}{\partial U^2} = x \underbrace{\left[\sum_{i=1}^{n} \frac{\varepsilon_{33,i}^T w_i}{h_i} - \sum_{i=1}^{n} \frac{d_{31,i}^2 w_i}{s_{11,i}^E h_i} + \frac{m_{Piezo}^2}{C} \right]}_{C'_{Piezo}} \tag{4.100}$$

In combination with the definition of the total capacity per unit length

$$C'_{Piezo} = \sum_{i=1}^{n} \frac{\varepsilon_{33,i}^T w_i}{h_i} - \sum_{i=1}^{n} \frac{d_{31,i}^2 w_i}{s_{11,i}^E h_i} + \frac{m_{Piezo}^2}{C}, \tag{4.101}$$

With respect to (4.100) and (4.99), it can be written:

$$\frac{\partial^2 W_{tot}(x)}{\partial U^2} = C'_{Piezo} x = C_{tot} \tag{4.102}$$

The calculation of the derivative

$$U = \frac{\partial Q}{\partial C_{tot}}$$

yields in combination with equation (4.102):

$$U = \frac{1}{C'_{Piezo}} \frac{\partial Q}{\partial x} \tag{4.103}$$

Thus, the total stored energy (4.94) can be defined in its final form including (4.68), (4.101) and (4.103):

$$W_{tot} = \int_0^l \frac{1}{2C'_{Piezo}} \left(\frac{\partial Q}{\partial x} \right)^2 dx + \int_0^l \frac{M^2}{2C} dx + \int_0^l \frac{M}{C} \frac{m_{Piezo}}{C'_{Piezo}} \left(\frac{\partial Q}{\partial x} \right) dx \tag{4.104}$$

In order to formulate the total potential energy, the final value work W_a performed by the extensive quantity U has to be determined. It can generally be written:

$$W_a = \int_0^{Q_{tot}} U dQ$$

Applying the total differential to $dQ = dQ(x)$ yields the final value work:

$$W_a = U \int_0^l \left(\frac{\partial Q}{\partial x}\right) dx \qquad (4.105)$$

Finally, the total potential energy Π can be formulated by means of (4.104) and (4.105):

$$\Pi = \frac{1}{2C'_{Piezo}} \int_0^l \left(\frac{\partial Q}{\partial x}\right)^2 dx + \frac{M}{C} \frac{m_{Piezo}}{C'_{Piezo}} \int_0^l \left(\frac{\partial Q}{\partial x}\right) dx + \int_0^l \frac{M^2}{2C} dx$$

$$-U \int_0^l \left(\frac{\partial Q}{\partial x}\right) dx \qquad (4.106)$$

According to the Ritz method, the following ansatz function

$$Q(x) = \sum_{j=1}^k a_j x^j \qquad (4.107)$$

is chosen. Insertion of (4.107) in (4.106) and following partial derivation with respect to the general coefficient a_i for $j \leq i \leq k$ yields the integral minimum of the total potential energy Π. With respect to the necessary condition (4.56) for the existence of a minimum, it follows:

$$\frac{1}{C'_{Piezo}} \int_0^l \frac{\partial}{\partial a_i} \left(\frac{\partial Q}{\partial x}\right) \left[\left(\frac{\partial Q}{\partial x}\right) + \frac{M}{C} m_{Piezo}\right] dx - U \int_0^l \frac{\partial}{\partial a_i} \left(\frac{\partial Q}{\partial x}\right) dx = 0$$

$$(4.108)$$

Furthermore, from the ansatz function (4.107) follows:

$$\frac{\partial Q}{\partial x} = \sum_{j=1}^k j a_j x^{j-1} \qquad (4.109)$$

The partial derivative with respect to the general coefficient a_i yields in combination with (4.109):

$$\frac{\partial}{\partial a_i} \left(\frac{\partial Q}{\partial x}\right) = i x^{i-1} \qquad (4.110)$$

External Static Moment

Insertion of (4.109) and (4.110) into equation (4.108) yields:

$$i \sum_{j=1}^k \frac{j}{j+i-1} a_j l^{j-1} = U C'_{Piezo} - \frac{M m_{Piezo}}{C} \qquad (4.111)$$

In order to set up the linear system of equations, $k = 3$ is chosen. Furthermore, $j \leq i \leq k$ is considered. The evaluation of the linear system of equations (4.111) yields the nontrivial solution

$$a_1 = UC'_{Piezo} - \frac{Mm_{Piezo}}{C}.$$

(4.112)

Insertion of the coefficient a_1 in (4.107) results in the ansatz function standardized on the bending actuator length l:

$$Q(x) = -M\underbrace{\frac{m_{Piezo}l}{C}\left(\frac{x}{l}\right)}_{=m_{41}(x)} + U\underbrace{\left[\sum_{i=1}^{n}\frac{w_i l}{h_i}\left(\varepsilon_{33,i}^T - \frac{d_{31,i}^2}{s_{11,i}^E}\right) + \frac{m_{Piezo}^2}{C}l\right]\left(\frac{x}{l}\right)}_{=m_{44}(x)}$$

(4.113)

It should be noted, that the bracket term after the integral sign can be summarized according to [104]:

$$\varepsilon_{33,i}^S = \varepsilon_{33,i}^T - \frac{d_{31,i}^2}{s_{11,i}^E}$$

(4.114)

Later on, this correlation will be used for the derivation of the dynamic behavior of piezoelectric multilayer beam bending actuators.

External Static Force

Subjecting the beam bending actuator to an external static force F perpendicularly to the tip (see Fig. 4.5) results in an internal bending moment M. In order to calculate the internal bending moment, the definition of the sectional quantities is considered. Figure 4.8 illustrates the correlation between the external force F and the internal bending moment M.
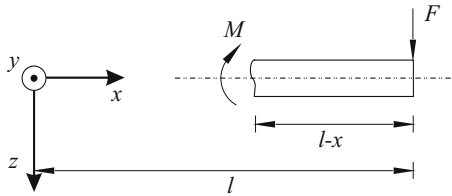
Fig. 4.8. Correlation between the external force F and the internal bending moment M

Considering equilibrium condition $\sum_i M_i = 0$, the internal bending moment M results in:

$$M = -F(l - x) \tag{4.115}$$

Thus, the integral minimum of the total potential energy yields according to (4.108) and by applying (4.115):

$$\frac{1}{C'_{Piezo}} \int_0^l \frac{\partial}{\partial a_i} \left(\frac{\partial Q}{\partial x} \right) \left[\left(\frac{\partial Q}{\partial x} \right) - \frac{F(l - x)}{C} m_{Piezo} \right] dx = U \int_0^l \frac{\partial}{\partial a_i} \left(\frac{\partial Q}{\partial x} \right) dx \tag{4.116}$$

Insertion of (4.109) and (4.110) into equation (4.116) yields:

$$i \sum_{j=1}^k \frac{j}{j + i - 1} a_j l^{j-1} = UC'_{Piezo} + \frac{1}{(i+1)} \frac{Fm_{Piezo}l}{C} \tag{4.117}$$

In order to set up the linear system of equations, $k = 3$ is chosen. The evaluation of the linear system of equations yields the nontrivial solutions

$$a_1 = UC'_{Piezo} + \frac{Fm_{Piezo}l}{C} \quad \text{and} \quad a_2 = -\frac{1}{2} \frac{Fm_{Piezo}}{C}. \tag{4.118}$$

Insertion of the coefficients a_1 and a_2 in (4.107) results in the ansatz function standardized on the bending actuator length l:

$$Q(x) = \underbrace{F \frac{m_{Piezo}l^2}{2C} \left[2 \left(\frac{x}{l} \right) - \left(\frac{x}{l} \right)^2 \right]}_{=m_{42}(x)} + Um_{44}(x) \tag{4.119}$$

External Uniform Pressure Load

Subjecting the beam bending actuator to an external uniform pressure load p perpendicularly to the x-y plane (see Fig. 4.5) also results in an internal bending moment M. Figure 4.9 shows the correlation between the external pressure load p and the internal bending moment M.
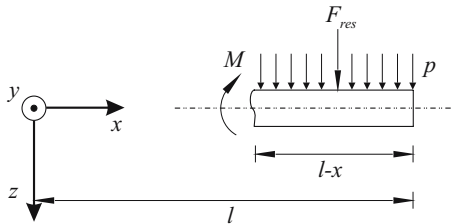
Fig. 4.9. Correlation between the external pressure load p and the internal bending moment M

Considering the width w of the bending actuator, the resulting force F_{res} caused by the uniform pressure load p is equal to:

$$F_{res} = pw\,(l - x) \tag{4.120}$$

Taking equilibrium condition $\sum_i M_i = 0$ into account, the internal bending moment M results in:

$$M = -pw\frac{(l - x)^2}{2} \tag{4.121}$$

Thus, the integral minimum of the total potential energy yields according to (4.108) and by applying (4.121):

$$\frac{1}{C'_{Piezo}} \int_0^l \frac{\partial}{\partial a_i}\left(\frac{\partial Q}{\partial x}\right)\left[\left(\frac{\partial Q}{\partial x}\right) - \frac{pwm_{Piezo}}{2C}(l - x)^2\right]dx = U\int_0^l \frac{\partial}{\partial a_i}\left(\frac{\partial Q}{\partial x}\right)dx \tag{4.122}$$

Insertion of (4.109) and (4.110) into equation (4.122) yields:

$$i\sum_{j=1}^k \frac{j}{j + i - 1}a_j l^{j-1} = \underbrace{UC'_{Piezo}}_{\equiv \nu} + \underbrace{\frac{1}{(i+1)(i+2)}\frac{pwm_{Piezo}l^2}{C}}_{\equiv \tau} \tag{4.123}$$

In order to set up the linear system of equations, $k = 3$ is chosen. The evaluation of the linear system of equations yields the nontrivial solutions

$$a_1 = UC'_{Piezo} + \frac{pwm_{Piezo}l^2}{C}, \qquad a_2 = -\frac{pwm_{Piezo}l}{2C} \tag{4.124}$$

and

$$a_3 = \frac{pwm_{Piezo}}{6C} \tag{4.125}$$

Insertion of the coefficients a_1, a_2 and a_3 into (4.107) results in the ansatz function standardized on the bending actuator length l:

$$Q(x) = p\underbrace{\frac{wm_{Piezo}l^3}{6C}\left[3\left(\frac{x}{l}\right) - 3\left(\frac{x}{l}\right)^2 + \left(\frac{x}{l}\right)^3\right]}_{=m_{43}(x)} + Um_{44}(x) \tag{4.126}$$

At this point all matrix elements m_{ij} of the coupling matrix $\mathbf{M}$ are known as functions of the length coordinate x. Thus, it is possible to describe the static behavior of any design of piezoelectric n-layered bending actuator in closed form analysis. The representation of the matrix elements in sum notation implies the advantage of easy calculation with usual mathematics software packages, particularly used in the physical and engineering sciences.

4.10 The Constituent Equations

In the following, the derived matrix elements $m_{ij}(x)$ are represented with respect to the columns of the coupling matrix $\mathbf{M}$.

1. First column of the coupling matrix $\mathbf{M}$

$$
\begin{pmatrix} m_{11}(x) \\ m_{21}(x) \\ m_{31}(x) \\ m_{41}(x) \end{pmatrix} = \begin{pmatrix} \frac{l}{C}\left(\frac{x}{l}\right) \\ \frac{l^2}{2C}\left(\frac{x}{l}\right)^2 \\ \frac{wl^3}{6C}\left(\frac{x}{l}\right)^3 \\ \frac{m_{Piezo}l}{C}\left(\frac{x}{l}\right) \end{pmatrix}
\tag{4.127}
$$

2. Second column of the coupling matrix $\mathbf{M}$

$$
\begin{pmatrix} m_{12}(x) \\ m_{22}(x) \\ m_{32}(x) \\ m_{42}(x) \end{pmatrix} = \begin{pmatrix} \frac{l^2}{2C}\left[2\left(\frac{x}{l}\right) - \left(\frac{x}{l}\right)^2\right] \\ \frac{l^3}{6C}\left[3\left(\frac{x}{l}\right)^2 - \left(\frac{x}{l}\right)^3\right] \\ \frac{l^4}{24C}\left[4\left(\frac{x}{l}\right)^3 - \left(\frac{x}{l}\right)^4\right] \\ \frac{m_{Piezo}l^2}{2C}\left[2\left(\frac{x}{l}\right) - \left(\frac{x}{l}\right)^2\right] \end{pmatrix}
\tag{4.128}
$$

3. Third column of the coupling matrix $\mathbf{M}$

$$
\begin{pmatrix} m_{13}(x) \\ m_{23}(x) \\ m_{33}(x) \\ m_{43}(x) \end{pmatrix} = \begin{pmatrix} \frac{wl^3}{6C}\left[3\left(\frac{x}{l}\right) - 3\left(\frac{x}{l}\right)^2 + \left(\frac{x}{l}\right)^3\right] \\ \frac{wl^4}{24C}\left[6\left(\frac{x}{l}\right)^2 - 4\left(\frac{x}{l}\right)^3 + \left(\frac{x}{l}\right)^4\right] \\ \frac{w^2l^5}{120C}\left[10\left(\frac{x}{l}\right)^3 - 5\left(\frac{x}{l}\right)^4 + \left(\frac{x}{l}\right)^5\right] \\ \frac{wm_{Piezo}l^3}{6C}\left[3\left(\frac{x}{l}\right) - 3\left(\frac{x}{l}\right)^2 + \left(\frac{x}{l}\right)^3\right] \end{pmatrix}
\tag{4.129}
$$

4. Fourth column of the coupling matrix $\mathbf{M}$

$$
\begin{pmatrix} m_{14}\left(x\right) \\ \\ m_{24}\left(x\right) \\ \\ m_{34}\left(x\right) \\ \\ m_{44}\left(x\right) \end{pmatrix} = \begin{pmatrix} \frac{m_{Piezo}l}{C}\left(\frac{x}{l}\right) \\ \\ \frac{m_{Piezo}l^2}{2C}\left(\frac{x}{l}\right)^2 \\ \\ \frac{m_{Piezo}wl^3}{6C}\left(\frac{x}{l}\right)^3 \\ \\ \left[\sum\limits_{i=1}^{n}\frac{w_i l}{h_i}\left(\varepsilon_{33,i}^T - \frac{d_{31,i}^2}{s_{11,i}^E}\right) + \frac{m_{Piezo}^2}{C}l\right]\left(\frac{x}{l}\right) \end{pmatrix}
\tag{4.130}
$$

In section 9.2, analytical calculations concerning the static behavior of piezo-electric multilayer beam bending actuators based on the derived coupling matrix are compared to measurement results achieved with a realized multilayer beam bender.

5

Piezoelectric Beam Bending Actuators and Hamilton's Principle

In addition to the static behavior of a piezoelectric multilayer beam bending actuator, the determination of the correlation between the *intensive harmonic* quantities and the *extensive harmonic* quantities M, F, p and U is of interest. This consideration provides the temporal and spatial vibration behavior of a piezoelectric beam bender as well as the fundamentals for the determination of the electromechanical circuit representation of an n-layered bending actuator. Similarly to the static behavior, the analytical formulation of the dynamic behavior of a piezoelectric multilayer beam bender consisting of n layers will be discussed in detail in the following sections. Thus, a general description is ensured and the corresponding equations for special bending transducer types can be derived.

The fundamental differential equations are achieved on the basis of both, thermodynamic considerations made before and *Hamilton's principle*. In order to be able to understand the approach at large, it is necessary to dwell on the relevant basic principles. First of all *Lagrange's formalism* is deduced, which is of significance within in the field of theoretical mechanics. In a next step, the Hamilton principle is derived providing a basis for further considerations. Hamilton's principle will be applied to the electrical enthalpy, that can be derived from the constitutive equations for piezoelectric materials determined already before. In particular, dissipative forces extracting energy of an oscillating system are considered within the scope of the analytical description. Thereby, internal and external frictional forces based on Rayleigh's dissipiation function are implemented into Lagrange's formalism and the Hamilton principle is modified accordingly.

5.1 Constraints and Generalized Coordinates

Newton's mechanics focus on systems of mass points (particles). Each of these mass points is characterized by an equation of motion in the following form:

$$m_i\ddot{\mathbf{x}}_i = \sum_{\substack{j=1 \\ j\neq i}}^{n} \mathbf{F}_i^{(ext)} + \mathbf{F}_{ij} = \frac{d\mathbf{p}_i}{dt} \tag{5.1}$$

The quantitiy x_i denotes the position vector of the ith mass point. $\mathbf{F}_i^{(ext)}$ and $\mathbf{F}_{ij}$ represent the *external force* affecting the particle i and the *internal force* the particle j affects the particle i, respectively. Thus, n particles result in a coupled system of $3n$ differential equations of second order. It is evident, that their solutions require the knowledge of a sufficient amount of initial conditions. Generally, particle motions of a macroscopic mechanical system are not completely free, because they are restricted by certain *constraining forces*. The consideration of the constraining forces by the interaction forces $\mathbf{F}_{ij}$ represents an almost unsolvable problem [105]. Thus, it is an aim to reformulate the mechanics in such a way, that constraining forces are eliminated. This procedure results in the *Lagrange formalism* of the classical mechanics. If p holonomic constraints are existent, the $3n$ coordinates (x_i, y_i, z_i) of the n mass points are no longer independent resulting in a reduction of the degrees of freedom f.

It can be written:

$$f = 3n - p \tag{5.2}$$

Holonomic constraints are defined by interconnections of particle coordinates and time in the following form:

$$f_\nu(\mathbf{x}_1, \mathbf{x}_2, \ldots, \mathbf{x}_n, t) = 0, \qquad \nu = 1, 2, \ldots, p \tag{5.3}$$

The mass point system can be completely described by $f = 3n - p$ suitable selected, independent position coordinates $q_1, q_2, \ldots q_f$. These coordinates are called *generalized coordinates*. The generalized coordinates define the position vectors $\mathbf{x}_1, \mathbf{x}_2, \ldots \mathbf{x}_n$ of the n mass points:

$$\begin{aligned} \mathbf{x}_1 &= \mathbf{x}_1(q_1, q_2, \ldots, q_f, t) \\ \mathbf{x}_2 &= \mathbf{x}_2(q_1, q_2, \ldots, q_f, t) \\ &\vdots \\ \mathbf{x}_n &= \mathbf{x}_n(q_1, q_2, \ldots, q_f, t) \end{aligned} \tag{5.4}$$

Thus, a system of equations with $3n$ transformation equations is achieved presenting the correlation between the dependent coordinates (x_i, y_i, z_i) and the independent generalized coordinates. Their time derivatives $\dot{q}_1, \dot{q}_2, \ldots \dot{q}_f$ are called *generalized velocities*. In order to derive the Lagrange equations, *D'Alembert's principle* has to be considered in more detail.

5.2 D'Alembert's Principle

The introduction of generalized coordinates avoids the difficulty, that the $3n$ coordinates (x_i, y_i, z_i) of a mass point system with holonomic constraints are

not independent of each other. However, there is the problem, that the constraints come along with constraining forces affecting the mass points. With respect to the equations of motion, these forces have to be taken into account, but they are a priori unknown. In order to find a formulation for the motion of mass point systems constraining forces are eliminated yet, the concept of virtual displacement is to be defined, that has already been used within the scope of the analytical description of the static behavior of piezoelectric bending actuators.

A virtual displacement of a mass point system can be understood as a set $\{\delta\mathbf{x}_i\}_{i=1...n}$ of instantanous infinitesimal changes of the positions $\mathbf{x}_i$ of the n mass points being compatible with the prevailing forces and constraints.

Instantanous means, that the displacement develops at a fixed time t and not during a time interval between t and $t + dt$. For following considerations, the principle of linear momentum (5.1) is consulted. For the entire mass point system, it can be written:

$$\sum_{i=1}^{n} m_i \ddot{\mathbf{x}}_i = \sum_{i=1}^{n}\sum_{\substack{j=1\\j\neq i}}^{n}\left(\mathbf{F}_i^{(ext)} + \mathbf{F}_{ij}\right) = \sum_{i=1}^{n}\mathbf{F}_i^{(ext)} + \sum_{i=1}^{n}\sum_{\substack{j=1\\j\neq i}}^{n}\mathbf{F}_{ij} \tag{5.5}$$

Due to Newton's third law (*actio = reactio*), the double sum over the interaction forces vanishes, thus it can be written

$$\sum_{i=1}^{n} m_i \ddot{\mathbf{x}}_i = \sum_{i=1}^{n}\mathbf{F}_i^{(ext)} = \sum_{i=1}^{n}\dot{\mathbf{p}}_i \tag{5.6}$$

resulting in

$$\mathbf{F}_i^{(ext)} = \dot{\mathbf{p}}_i. \tag{5.7}$$

The multiplication of equation (5.7) with the virtual displacement $\delta\mathbf{x}_i$ yields

$$\left(\mathbf{F}_i^{(ext)} - \dot{\mathbf{p}}_i\right) \cdot \delta\mathbf{x}_i = 0. \tag{5.8}$$

Following summation results in

$$\sum_{i=1}^{n}\left(\mathbf{F}_i^{(ext)} - \dot{\mathbf{p}}_i\right) \cdot \delta\mathbf{x}_i = 0. \tag{5.9}$$

Generally, $\mathbf{F}_i^{(ext)}$ denotes the sum of the *applied force* $\mathbf{F}_i^{(a)}$ and the *constraining force* $\mathbf{F}_i^{(z)}$. Thus, equation (5.9) can be expressed in following form:

$$\sum_{i=1}^{n}\left(\mathbf{F}_i^{(a)} - \dot{\mathbf{p}}_i\right) \cdot \delta\mathbf{x}_i + \sum_{i=1}^{n}\mathbf{F}_i^{(z)} \cdot \delta\mathbf{x}_i = 0 \tag{5.10}$$

At this point, it is important that the *virtual work of constraining forces* vanishes. However, this fact is only valid because of the instantaneous concept.

Therefore, from equation (5.10) follows:

$$\sum_{i=1}^{n} \left(\mathbf{F}_i^{(a)} - \dot{\mathbf{p}}_i \right) \cdot \delta \mathbf{x}_i = 0 \tag{5.11}$$

The constraining forces $\mathbf{F}_i^{(z)}$ are eliminated. (5.11) represents D'Alembert's principle providing a basis for the derivation of the Lagrange equations.

5.3 Lagrange's Equations

To simplify matters, in (5.11) the upper index (a) for applied forces is omitted, since the constraining forces do not occur any longer in further considerations. In combination with the transformation equations (5.4), the virtual displacements are rewritten as appropriate virtual displacements δq_j of the generalized coordinates.

This results in

$$\mathbf{x}_i = \mathbf{x}_i \left(q_j, t \right) \qquad \text{with} \qquad 1 \leq i \leq n \quad \wedge \quad 1 \leq j \leq f. \tag{5.12}$$

From (5.12) follows:

$$\delta \mathbf{x}_i = \sum_{j=1}^{f} \frac{\partial \mathbf{x}_i}{\partial q_j} \delta q_j + \frac{\partial \mathbf{x}_i}{\partial t} \delta t \tag{5.13}$$

Since the virtual displacements develop instantaneously, in equation (5.13) the partial derivative with respect to time vanishes resulting in:

$$\delta \mathbf{x}_i = \sum_{j=1}^{f} \frac{\partial \mathbf{x}_i}{\partial q_j} \delta q_j \tag{5.14}$$

By insertion of (5.14) into (5.11), D'Alembert's principle can be formulated with respect to $\mathbf{p}_i = m_i \dot{\mathbf{x}}_i$:

$$\sum_i \sum_j \mathbf{F}_i \cdot \frac{\partial \mathbf{x}_i}{\partial q_j} \delta q_j - \sum_i \sum_j m_i \ddot{\mathbf{x}}_i \cdot \frac{\partial \mathbf{x}_i}{\partial q_j} \delta q_j = 0 \tag{5.15}$$

With the definition of the *generalized forces*

$$Q_j = \sum_i \mathbf{F}_i \cdot \frac{\partial \mathbf{x}_i}{\partial q_j}, \tag{5.16}$$

the first term of equation (5.15) can be rewritten:

$$\sum_i \sum_j \mathbf{F}_i \cdot \frac{\partial \mathbf{x}_i}{\partial q_j} \delta q_j = \sum_j Q_j \delta q_j \tag{5.17}$$

Furthermore, the velocity $\dot{\mathbf{x}}_i$ is defined in following way:

$$\dot{\mathbf{x}}_i = \frac{d}{dt} (\mathbf{x}_i (q_j, t)) = \mathbf{v}_i \tag{5.18}$$

Applying the chain rule on (5.18) yields

$$\dot{\mathbf{x}}_i = \mathbf{v}_i = \sum_{j=1}^{f} \frac{\partial \mathbf{x}_i}{\partial q_j} \dot{q}_j + \frac{\partial \mathbf{x}_i}{\partial t}. \tag{5.19}$$

The derivative of equation (5.19) with respect to $\dot{q}_j$ results in:

$$\frac{\partial \mathbf{v}_i}{\partial \dot{q}_j} = \frac{\partial \mathbf{x}_i}{\partial q_j} \tag{5.20}$$

Insertion of (5.20) into (5.19) results in:

$$\frac{d}{dt} \frac{\partial \mathbf{x}_i}{\partial q_j} = \frac{\partial}{\partial q_j} \left(\sum_{k=1}^{f} \frac{\partial \mathbf{x}_i}{\partial q_k} \dot{q}_k + \frac{\partial \mathbf{x}_i}{\partial t} \right)$$

$$\Leftrightarrow \frac{d}{dt} \frac{\partial \mathbf{x}_i}{\partial q_j} = \frac{\partial \mathbf{v}_i}{\partial q_j} \tag{5.21}$$

The evaluation of the scalar product in the second term of equation (5.15) yields in combination with (5.20) and (5.21)

$$\ddot{\mathbf{x}}_i \cdot \frac{\partial \mathbf{x}_i}{\partial q_j} = \frac{d}{dt} \left(\dot{\mathbf{x}}_i \cdot \frac{\partial \mathbf{x}_i}{\partial q_j} \right) - \dot{\mathbf{x}}_i \cdot \frac{d}{dt} \frac{\partial \mathbf{x}_i}{\partial q_j}$$

$$= \frac{d}{dt} \left(\mathbf{v}_i \cdot \frac{\partial \mathbf{v}_i}{\partial \dot{q}_j} \right) - \mathbf{v}_i \cdot \frac{\partial \mathbf{v}_i}{\partial q_j}$$

$$= \frac{d}{dt} \left(\frac{\partial}{\partial \dot{q}_j} \frac{\mathbf{v}_i^2}{2} \right) - \frac{\partial}{\partial q_j} \frac{\mathbf{v}_i^2}{2} \tag{5.22}$$

For the second term of (5.15), it follows:

$$\sum_{i,j} m_i \ddot{\mathbf{x}}_i \cdot \frac{\partial \mathbf{x}_i}{\partial q_j} \delta q_j = \sum_{i,j} \left[\frac{d}{dt} \left(\frac{\partial}{\partial \dot{q}_j} \frac{m_i \mathbf{v}_i^2}{2} \right) - \frac{\partial}{\partial q_j} \frac{m_i \mathbf{v}_i^2}{2} \right] \delta q_j$$

$$= \sum_{j=1}^{f} \left[\frac{d}{dt} \left(\frac{\partial}{\partial \dot{q}_j} \frac{1}{2} \sum_{i=1}^{n} m_i \mathbf{v}_i^2 \right) - \frac{\partial}{\partial q_j} \frac{1}{2} \sum_{i=1}^{n} m_i \mathbf{v}_i^2 \right] \delta q_j \tag{5.23}$$

The total kinetic energy T of a mass point system is equal to:

$$T = \frac{1}{2} \sum_{i=1}^{n} m_i \mathbf{v}_i^2 \tag{5.24}$$

In combination with (5.24), equation (5.23) yields:

$$\sum_{i,j} m_i \ddot{\mathbf{x}}_i \cdot \frac{\partial \mathbf{x}_i}{\partial q_j} \delta q_j = \sum_{j=1}^{f} \left[\frac{d}{dt} \left(\frac{\partial T}{\partial \dot{q}_j} \right) - \frac{\partial T}{\partial q_j} \right] \delta q_j \tag{5.25}$$

(5.17) and (5.25) define both terms of D'Alembert's principle (5.15).

Thus, D'Alembert's principle can be formulated in the notation of generalized coordinates, velocities and forces:

$$\sum_{j=1}^{f} Q_j \delta q_j - \sum_{j=1}^{f} \left[\frac{d}{dt} \left(\frac{\partial T}{\partial \dot{q}_j} \right) - \frac{\partial T}{\partial q_j} \right] \delta q_j = 0$$

$$\Leftrightarrow \sum_{j=1}^{f} \left[\frac{d}{dt} \left(\frac{\partial T}{\partial \dot{q}_j} \right) - \frac{\partial T}{\partial q_j} - Q_j \right] \delta q_j = 0 \tag{5.26}$$

Since the generalized coordinates q_j are independent from each other, a virtual displacement δq_k for $k \neq l$ is independent of δq_l. Thus, equation (5.26) can only be satisfied, if the term in angular brackets is equal to zero.

For $j = 1 \ldots f$, this results in the *Lagrange equation of first type*:

$$\frac{d}{dt} \left(\frac{\partial T}{\partial \dot{q}_j} \right) - \frac{\partial T}{\partial q_j} = Q_j \tag{5.27}$$

The Lagrange equation of first type will be used later for the derivation of the differential equations of a piezoelectric multilayer beam bending actuator. Also the *Lagrange equation of second type* plays an important rule concerning the description of the dynamic behavior of piezoelectric bending actuators. As far as the external forces represent *conservative forces*, it can directly be derived from equation (5.27). A force is called conservative, if a scalar potential V exists and can be expressed by following correlation:

$$\mathbf{F}_i = - \operatorname{grad}_i V \tag{5.28}$$

In combination with (5.28), the generalized forces (5.16) are calculated according to:

$$Q_j = - \sum_{i=1}^{n} \operatorname{grad}_i V \cdot \frac{\partial \mathbf{x}_i}{\partial q_j} = -\frac{\partial V}{\partial q_j} \tag{5.29}$$

Thus, equation (5.27) results in:

$$\frac{d}{dt}\left(\frac{\partial T}{\partial \dot{q}_j}\right) - \frac{\partial T}{\partial q_j} = -\frac{\partial V}{\partial q_j}$$

$$\Leftrightarrow \frac{d}{dt}\left(\frac{\partial (T-V)}{\partial \dot{q}_j}\right) - \frac{\partial (T-V)}{\partial q_j} = 0 \tag{5.30}$$

The expression

$$T - V = L \tag{5.31}$$

is called *Lagrange function L*. For $j = 1 \ldots f$, the *Lagrange equation of second type* is achieved:

$$\frac{d}{dt}\left(\frac{\partial L}{\partial \dot{q}_j}\right) - \frac{\partial L}{\partial q_j} = 0 \tag{5.32}$$

Both types of Lagrange's equations will play an important role for the solution of the dynamic behavior of n-layered piezoelectric bending actuators. In order to determine the differential equations for any kind of piezoelectric beam bending actuator, Hamilton's principle will be taken into consideration. This principle includes both types of Lagrange's equations. However, in order to be able to use the Hamilton principle, some aspects of *calculus of variations* have to be discussed in more detail. The considerations result in the *Euler-Lagrange differential equation of calculus of variations* yielding the Hamilton principle in combination with Lagrange's equations.

5.4 Euler-Lagrange Differential Equation

A point x of a function $f(x)$ is referred to as stationary, if and only if this point is either a maximum, a minimum or an inflection point of the function $f(x)$. Thus, it applies:

$$f(x) \; stationary \; in \; x \iff f'(x) = 0 \tag{5.33}$$

Stationary points are characterized by the constant behavior of the function in its direct neighborhood (ϵ-neighborhood). Compared to a function depending on one or more variables, a *functional* is dependent on a whole function [106].

For a given function $f(x, y, z)$, the functional

$$I\{y(x)\} = \int_{x_1}^{x_2} f(x, y(x), y'(x)) \, dx \tag{5.34}$$

dependent on the function $y(x)$ is considered. It should be noted, that both the lower and upper integral limits x_1, x_2 are fixed [107]. If the facts mentioned

above are considered more generalized, then $I\{y(x)\}$ is called stationary for a special function $y(x)$ if $I\{y(x)\}$ does not change with infinitesimal *variations* of $y(x)$. The limits x_1, x_2 are fixed and the function $y(x)$ is not varied at x_1 and x_2, i.e.

$$y_1 = y(x_1) \quad \wedge \quad y_2 = y(x_2)$$

are fixed.

Such variations can be represented by

$$y(x, \epsilon) = y(x) + \epsilon \eta(x), \tag{5.35}$$

whereas the test function $\eta(x)$ and ϵ represent an arbitrary function with $\eta(x_1) = \eta(x_2) = 0$ and a small number, respectively (see Fig. 5.1).
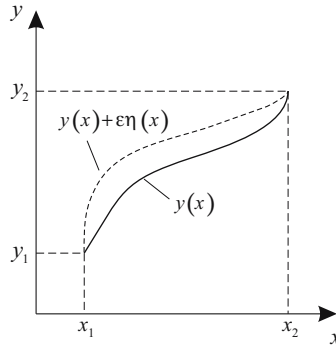
Fig. 5.1. Variation of the function $y(x)$ with the test function $\eta(x)$

According to (5.34) it can be written

$$I\{y(x, \epsilon)\} = \int_{x_1}^{x_2} f(x, y(x, \epsilon), y'(x, \epsilon)) \, dx. \tag{5.36}$$

The stationarity condition yields in accordance with (5.33)

$$\left.\frac{\partial I\{y(x, \epsilon)\}}{\partial \epsilon}\right|_{\epsilon=0} = 0. \tag{5.37}$$

If the *variation operator* δ is defined as

$$\delta = d\epsilon \frac{\partial}{\partial \epsilon}\bigg|_{\epsilon=0},$$

the variation from I results in

$$\delta I \left\{ y \left(x, \epsilon \right) \right\} = \left. \frac{\partial I \left\{ y \left(x, \epsilon \right) \right\}}{\partial \epsilon} \right|_{\epsilon = 0} d\epsilon = 0. \tag{5.38}$$

Equation (5.38) describes the necessary and sufficient condition for stationarity. Similarly,

$$\delta y \left(x \right) = \left. \frac{\partial y}{\partial \epsilon} \right|_{\epsilon = 0} d\epsilon = \eta \left(x \right) d\epsilon \tag{5.39}$$

is the variation of $y(x)$, which indeed disappears at the integral limits:

$$\delta y \left(x_1 \right) = \delta y \left(x_2 \right) = 0 \tag{5.40}$$

Thus, the condition for stationarity can be expressed in the following form:

$$I \left\{ y \left(x \right) \right\} \ stationary \iff \delta I \left\{ y \left(x \right) \right\} = 0 \tag{5.41}$$

In accordance to equation (5.38), the variation δI will be determined in the following. Derivation with respect to ϵ and integration over x can be interchanged. This yields:

$$\frac{\partial I \left\{ y \left(x, \epsilon \right) \right\}}{\partial \epsilon} = \int_{x_1}^{x_2} \frac{\partial}{\partial \epsilon} f \left(x, y \left(x, \epsilon \right), y' \left(x, \epsilon \right) \right) dx$$

$$= \int_{x_1}^{x_2} \frac{\partial f}{\partial y} \frac{\partial y}{\partial \epsilon} dx + \underbrace{\int_{x_1}^{x_2} \frac{\partial f}{\partial y'} \frac{\partial^2 y}{\partial \epsilon \partial x} dx}_{(*)} \tag{5.42}$$

The expression $(*)$ in equation (5.42) can be determined by means of partial integration [108].

$(*)$ results in:

$$\int_{x_1}^{x_2} \frac{\partial f}{\partial y'} \frac{d}{dx} \left(\frac{\partial y}{\partial \epsilon} \right) dx = \left. \frac{\partial f}{\partial y'} \frac{\partial y}{\partial \epsilon} \right|_{x_1}^{x_2} - \int_{x_1}^{x_2} \frac{d}{dx} \left(\frac{\partial f}{\partial y'} \right) \frac{\partial y}{\partial \epsilon} dx \tag{5.43}$$

Thus, insertion of (5.43) into (5.42) yields:

$$\frac{\partial I \left\{ y \left(x, \epsilon \right) \right\}}{\partial \epsilon} = \int_{x_1}^{x_2} \frac{\partial f}{\partial y} \frac{\partial y}{\partial \epsilon} dx + \underbrace{\left. \frac{\partial f}{\partial y'} \frac{\partial y}{\partial \epsilon} \right|_{x_1}^{x_2}}_{(**)} - \int_{x_1}^{x_2} \frac{d}{dx} \left(\frac{\partial f}{\partial y'} \right) \frac{\partial y}{\partial \epsilon} dx \tag{5.44}$$

Taking (5.35) into consideration, $(**)$ in (5.44) can be calculated according to

$$\frac{\partial f}{\partial y'} \frac{\partial y}{\partial \epsilon} \bigg|_{x_1}^{x_2} = \frac{\partial f}{\partial y'} \eta(x) \bigg|_{x_1}^{x_2} = 0 \quad \text{with} \quad \eta(x_1) = \eta(x_2) = 0. \tag{5.45}$$

Thus, (5.44) is equal to:

$$\frac{\partial I\{y(x, \epsilon)\}}{\partial \epsilon} = \int_{x_1}^{x_2} \frac{\partial f}{\partial y} \frac{\partial y}{\partial \epsilon} dx - \int_{x_1}^{x_2} \frac{d}{dx}\left(\frac{\partial f}{\partial y'}\right) \frac{\partial y}{\partial \epsilon} dx$$

$$= \int_{x_1}^{x_2} \left[\frac{\partial f}{\partial y} - \frac{d}{dx}\left(\frac{\partial f}{\partial y'}\right)\right] \frac{\partial y}{\partial \epsilon} dx \tag{5.46}$$

Multiplication of (5.46) with $d\epsilon$ finally results in the variation $\delta I\{y(x)\}$:

$$\frac{\partial I\{y(x, \epsilon)\}}{\partial \epsilon} \bigg|_{\epsilon=0} d\epsilon = \int_{x_1}^{x_2} \left[\frac{\partial f}{\partial y} - \frac{d}{dx}\left(\frac{\partial f}{\partial y'}\right)\right] \frac{\partial y}{\partial \epsilon} \bigg|_{\epsilon=0} d\epsilon dx = 0$$

$$\Leftrightarrow \delta I\{y(x)\} = \int_{x_1}^{x_2} \left[\frac{\partial f}{\partial y} - \frac{d}{dx}\left(\frac{\partial f}{\partial y'}\right)\right] \delta y(x) dx = 0 \tag{5.47}$$

Since $\delta y(x)$ can be chosen arbitrarily, the stationarity condition is fulfilled if and only if following equation is valid:

$$\frac{\partial f}{\partial y} - \frac{d}{dx}\left(\frac{\partial f}{\partial y'}\right) = 0 \tag{5.48}$$

Equation (5.48) represents the *Euler differential equation of calculus of variations* [107]. It is often applied in physics (e.g. the brachistochrone problem) [109].

In the following, the question of stationarity of the functional

$$I\{y_1(x), y_2(x), \ldots y_n(x)\} = \int_{x_1}^{x_2} f(x, y_1(x), \ldots, y_n(x), y_1'(x), \ldots, y_n'(x)) dx,$$

$$\tag{5.49}$$

which depends on n functions will be analyzed. The endpoints x_1, x_2 as well as the appropriate functional characteristics $y_1(x_1), y_2(x_1), \ldots, y_n(x_1)$ and $y_1(x_2), y_2(x_2), \ldots, y_n(x_2)$ are fixed.

Again, test functions $\eta_1(x) \ldots \eta_n(x)$ are defined with

$$\left.\begin{array}{l} y_1(x, \epsilon) = y_1(x) + \epsilon\eta_1(x) \\ \vdots \\ y_n(x, \epsilon) = y_n(x) + \epsilon\eta_n(x) \end{array}\right\} n - times$$

and
$$\eta_i\left(x_1\right)=\eta_i\left(x_2\right)=0 \quad \forall i \in \mathbb{N}.$$

Thus, the stationarity condition follows:

$$I\left\{y_1\left(x\right),y_2\left(x\right),\ldots y_n\left(x\right)\right\} \; stationary \; \Longleftrightarrow \; \delta I\left\{y_1\left(x\right),y_2\left(x\right),\ldots y_n\left(x\right)\right\}=0$$

Similarly to equation (5.47), it can be written:

$$\delta I\left\{y_1\left(x\right),y_2\left(x\right),\ldots y_n\left(x\right)\right\}=\int_{x_1}^{x_2}\sum_{i=1}^{n}\left[\frac{\partial f}{\partial y_i}-\frac{d}{dx}\left(\frac{\partial f}{\partial y_i'}\right)\right]\delta y_i\left(x\right)dx=0$$

$$(5.50)$$

Since the variations δy_i are independent from each other, the stationarity condition is fullfilled, if and only if the term in brackets in equation (5.50) vanishes. Thus, for $i=1\ldots n$ the *Euler-Lagrange differential equation of calculus of variations* can be achieved:

$$\frac{\partial f}{\partial y_i}-\frac{d}{dx}\left(\frac{\partial f}{\partial y_i'}\right)=0 \tag{5.51}$$

The Euler-Lagrange differential equation represents a generalization of the Euler differential equation. Its solutions are those curves $y_i(x)$, the functional $I\left\{y_1\left(x\right),y_2\left(x\right),\ldots y_n\left(x\right)\right\}$ is stationary and the appropriate variation δI vanishes, respectively.

5.5 Hamilton's Principle

For a conservative holonomic system with the Lagrange function $L\left(q_j,\dot{q}_j,t\right)$ the *integral of action S of a motion* on the space curve $q_1\left(t\right),\ldots,q_f\left(t\right)$ in the configuration space between the times t_1 and t_2 is defined as [110]:

$$S=\int_{t_1}^{t_2}L\left(q_j,\dot{q}_j,t\right)dt \tag{5.52}$$

A comparison with equation (5.49) yields the fact, that S is stationary and the variation of S is zero for $j=1\ldots f$, respectively, if and only if the following equation is valid:

$$\frac{\partial L}{\partial q_j}-\frac{d}{dt}\left(\frac{\partial L}{\partial \dot{q}_j}\right)=0 \tag{5.53}$$

Equation (5.53) is similar to equation (5.51) and represents exactly,except for the factor -1, the Lagrange equation, from which it is already known, that it is valid for the really passed trajectory of the system.

From this, *Hamilton's principle* follows:

The motion of a system (conservative, holonomic) between the times t_1 and t_2 proceeds in such a manner, that the integral of action

$$S = \int_{t_1}^{t_2} L\left(q_j, \dot{q}_j, t\right) dt$$

is stationary for the passed trajectory and the variation of the integral of action vanishes, respectively:

$$\delta S = \delta \int_{t_1}^{t_2} L\left(q_j, \dot{q}_j, t\right) dt = \delta \int_{t_1}^{t_2} L dt = 0 \tag{5.54}$$

At this point it should be noted, that equation (5.54) is valid for a conservative and holonomic system. However, external forces, which can not always be derived from a potential and so do not represent potential forces, can affect a system. Due to the possibility, that quantities such as pressure loads, forces and moments can affect a beam bender, equation (5.54) can not be considered on its own for the solution of the dynamic behavior of a piezoelectric beam bender. In fact, equation (5.54) has to be modified in such a manner, that external non-conservative forces as well as generalized frictional forces are taken into account. This will be discussed in the section below in more detail.

5.6 Consideration of Non-Conservative Forces

In previous considerations, a *conservative system* with *holonomic constraints* has been presupposed. In the following, these conditions will be diminished and the Hamilton principle will be modified, in order to consider non-conservative systems. So it is allowed, that external *affecting* forces $\mathbf{F}_i^{(ext)}$ are not derivable by a scalar potential as shown in (5.28). Furthermore, frictional forces $F_i^{(r)}$ are considered performing a negative work on the system resulting in an energy loss. Thus, such forces are *dissipative*. Similarly, frictional forces can not be derived from a generalized, velocity-independent potential V. They do not represent constraining forces in the actual sense and do not satisfy the D'Alembert principle, too [111]. In order to consider non-conservative forces, the Lagrange equation of first type is consulted:

$$\frac{d}{dt}\left(\frac{\partial T}{\partial \dot{q}_j}\right) - \frac{\partial T}{\partial q_j} = Q_j \tag{5.55}$$

By splitting up the generalized force Q_j into a conservative part $Q_j^{(k)}$, an external part $Q_j^{(ext)}$ and a generalized frictional force $Q_j^{(r)}$, equation (5.55) results in

$$\frac{d}{dt}\left(\frac{\partial T}{\partial \dot{q}_j}\right) - \frac{\partial T}{\partial q_j} = Q_j^{(k)} + Q_j^{(ext)} + Q_j^{(r)}. \tag{5.56}$$

Since $Q_j^{(k)}$ is derivable by a potential in accordance with (5.28), the Lagrange function $L = T - V$ can be introduced and (5.56) can be formulated as follows:

$$\frac{d}{dt}\left(\frac{\partial L}{\partial \dot{q}_j}\right) - \frac{\partial L}{\partial q_j} = Q_j^{(ext)} + Q_j^{(r)} \tag{5.57}$$

In (5.16), generalized forces have been defined before:

$$Q_j = \sum_{i=1}^{n} \mathbf{F}_i \cdot \frac{\partial \mathbf{x}_i}{\partial q_j}. \tag{5.58}$$

Using (5.58), equation (5.57) can be written as

$$\frac{d}{dt}\left(\frac{\partial L}{\partial \dot{q}_j}\right) - \frac{\partial L}{\partial q_j} = \sum_{i=1}^{n} \mathbf{F}_i^{(ext)} \cdot \frac{\partial \mathbf{x}_i}{\partial q_j} + \sum_{i=1}^{n} \mathbf{F}_i^{(r)} \cdot \frac{\partial \mathbf{x}_i}{\partial q_j}. \tag{5.59}$$

Assuming that frictional forces are velocity-dependent and that the force on each mass particle is opposed to its velocity, following approach can be made:

$$\mathbf{F}_i^{(r)} = -K_i\left(\mathbf{v}_i\right)\mathbf{v}_i \tag{5.60}$$

The quantity K_i denotes a coefficient of friction depending on the velocity $\mathbf{v}_i$. Using (5.60), the generalized frictional force $Q_j^{(r)}$ results in

$$Q_j^{(r)} = -\sum_{i=1}^{n} K_i\left(\mathbf{v}_i\right)\mathbf{v}_i \cdot \frac{\partial \mathbf{x}_i}{\partial q_j}. \tag{5.61}$$

Applying (5.20) yields

$$Q_j^{(r)} = -\sum_{i=1}^{n} K_i\left(\mathbf{v}_i\right)\mathbf{v}_i \cdot \frac{\partial \mathbf{v}_i}{\partial \dot{q}_j}. \tag{5.62}$$

Furthermore, it can be written

$$\mathbf{v}_i \cdot \frac{\partial \mathbf{v}_i}{\partial \dot{q}_j} = \frac{1}{2}\frac{\partial}{\partial \dot{q}_j}\left(\mathbf{v}_i \cdot \mathbf{v}_i\right) = \frac{1}{2}\frac{\partial v_i^2}{\partial \dot{q}_j} = v_i\frac{\partial v_i}{\partial \dot{q}_j}. \tag{5.63}$$

Assuming that the coefficients of friction are *independent of direction*, insertion of (5.63) into (5.62) yields

$$Q_j^{(r)} = -\sum_{i=1}^{n} K_i\left(v_i\right)v_i\frac{\partial v_i}{\partial \dot{q}_j}. \tag{5.64}$$

Equation (5.64) can be transformed with following mathematical equation of identity:

F may be an antiderivative of f, then it applies

$$\frac{d}{dx} \int_0^{a(x)} f(\tilde{x}) \, \tilde{x} \, d\tilde{x} = f(a(x)) \, a(x) \, \frac{da(x)}{dx}. \tag{5.65}$$

Applying (5.65) to (5.64) yields the generalized frictional forces

$$Q_j^{(r)} = -\frac{\partial}{\partial \dot{q}_j} \sum_{i=1}^n \int_0^{v_i} K_i(\tilde{v}_i) \, \tilde{v}_i \, d\tilde{v}_i = -\frac{\partial D}{\partial \dot{q}_j} \tag{5.66}$$

with the *dissipation function*

$$D = \sum_{i=1}^n \int_0^{v_i} K_i(\tilde{v}_i) \, \tilde{v}_i \, d\tilde{v}_i. \tag{5.67}$$

Insertion of (5.66) into (5.59) finally results in the modified Lagrange equation of second type

$$\frac{d}{dt}\left(\frac{\partial L}{\partial \dot{q}_j}\right) - \frac{\partial L}{\partial q_j} - \sum_{i=1}^n \mathbf{F}_i^{(ext)} \cdot \frac{\partial \mathbf{x}_i}{\partial q_j} + \frac{\partial D}{\partial \dot{q}_j} = 0. \tag{5.68}$$

Here, it is a question, whether the integral of action S is stationary for the sum of the Lagrange function L and the work W performed by non-conservative forces.

Following approach is considered:

$$\delta \int_{t_1}^{t_2} (L + W) \, dt \overset{!}{=} 0 \tag{5.69}$$

Since the time is not varied, from (5.69) it follows:

$$\int_{t_1}^{t_2} (\delta L + \delta W) \, dt = 0$$

$$\Leftrightarrow \int_{t_1}^{t_2} \delta L \, dt + \int_{t_1}^{t_2} \delta W = 0 \tag{5.70}$$

In combination with (5.53) and (5.66), it follows from equation (5.70):

$$\int_{t_1}^{t_2} \sum_{j=1}^{S} \left[\frac{\partial L}{\partial q_j} - \frac{d}{dt}\left(\frac{\partial L}{\partial \dot{q}_j}\right) \right] \delta q_j \, dt +$$

$$\int_{t_1}^{t_2} \sum_{j=1}^{S} \sum_{i=1}^{n} \mathbf{F}_i^{(ext)} \cdot \frac{\partial \mathbf{x}_i}{\partial q_i} \delta q_i \, dt + \int_{t_1}^{t_2} \sum_{j=1}^{S} \sum_{i=1}^{n} \mathbf{F}_i^{(r)} \cdot \frac{\partial \mathbf{x}_i}{\partial q_i} \delta q_i \, dt = 0$$

$$\Leftrightarrow \int_{t_1}^{t_2} \sum_{j=1}^{S} \left[\frac{\partial L}{\partial q_j} - \frac{d}{dt}\left(\frac{\partial L}{\partial \dot{q}_j}\right) + \sum_{i=1}^{n} \mathbf{F}_i^{(ext)} \cdot \frac{\partial \mathbf{x}_i}{\partial q_i} - \frac{\partial D}{\partial \dot{q}_j} \right] \delta q_j \, dt = 0$$

$$(5.71)$$

Since the variations δq_j are independent from each other, the stationarity condition is fullfilled if and only if the term in brackets in equation (5.71) vanishes. Thus, equation (5.68) and (5.71) are identical resulting in the conclusion, that the integral of action S is stationary for the sum of the Lagrange function L and the work W performed by external forces [29].

Thus, the expression

$$\int_{t_1}^{t_2} \delta L \, dt + \int_{t_1}^{t_2} \delta W \, dt = 0 \qquad (5.72)$$

denotes the *modified Hamilton principle*, which provides a basis for the determination of the differential equations and the boundary conditions in order to solve the equations of motion of a piezoelectric multilayered beam bending actuator. At first, the Lagrange function L of the system and the work W performed by extensive quantities have to be formulated.

5.7 Lagrange Function of Piezoelectric Beam Bending Actuators

According to (5.31), the Lagrange function L is equal to:

$$L = T - V \qquad (5.73)$$

The further calculations are based on the electrical enthalpy H_e (see eq. 3.61, section 3.3.3). It represents a thermodynamic potential corresponding physically to an energy density. Thus, in following considerations the kinetic energy T and the work W performed by external forces are referred to infinitesimal volume elements dV. The detailed calculations of the potential V and the kinetic energy T are presented in appendix C.

Volume integration of the electrical enthalpy $H_{e,i}$ of the ith layer and following summation over the number of layers yields the total potential V:

$$V = \sum_{i=1}^{n} \iiint_{V_i} H_{e,i} dV_i \tag{5.74}$$

The total kinetic energy of an n-layered system results in

$$T = \sum_{i=1}^{n} \iiint_{V_i} \frac{1}{2} \rho_i \left(\frac{\partial \xi(x,t)}{\partial t} \right)^2 dV_i. \tag{5.75}$$

The quantities $\xi(x,t)$ and ρ_i denote the deflection in z-direction (see Fig. 4.6, section 4.6) and the specific mass of the ith layer, respectively.

By means of (5.74) and (5.75), the Lagrange function L of a piezoelectric multilayer actuator in accordance with (5.73) is obtained in its simplest form:

$$L = \sum_{i=1}^{n} \iiint_{V_i} \left[\frac{1}{2} \rho_i \left(\frac{\partial \xi(x,t)}{\partial t} \right)^2 - H_{e,i} \right] dV_i \tag{5.76}$$

In order to evaluate the Lagrange function (5.76) the electrical enthalpy H_e has to be formulated. In accordance to equation (3.61), it can generally be written:

$$H_e = \frac{1}{2} c_{pq}^E S_q S_p - e_{ip} E_i S_p - \frac{1}{2} \varepsilon_{ik}^S E_k E_i \tag{5.77}$$

Furthermore, following boundary conditions are specified allowing for the calculation of (5.77):

1. The vector of the electric field $\mathbf{E}$ develops only in z-direction.

$$E_1 = E_2 = 0 \tag{5.78}$$

2. No strain in y- and z-direction and no beam bender torsion develop (see section 4.4).

$$S_2 = \ldots = S_6 = 0 \tag{5.79}$$

3. No mechanical normal stresses into y- and z-direction and no shear stresses develop (see section 4.4).

$$T_2 = \ldots = T_6 = 0 \tag{5.80}$$

4. The constitutive equations (3.57 - 3.60) according to the pairs of variates $(\mathbf{T}, \mathbf{E})$ and $(\mathbf{S}, \mathbf{E})$ are used.

$$D_3 = \varepsilon_{33}^T E_3 + d_{31} T_1 \tag{5.81}$$
$$S_1 = d_{31} E_3 + s_{11}^E T_1 \tag{5.82}$$

and

$$T_1 = c_{11}^E S_1 - e_{31} E_3 \tag{5.83}$$
$$D_3 = e_{31} S_1 + \varepsilon_{33}^S E_3 \tag{5.84}$$

5. The active piezoelectric layers consist of ferroelectric piezoelectric ceramics PZT, thus the represented matrices of material coefficients in (3.67) - (3.71) are of interest.

Taking the boundary conditions specified above into account, equation (5.77) can be simplified with respect to the Einstein sum convention [29]:

$$H_e = \frac{1}{2} c_{11}^E S_1^2 - e_{31} E_3 S_1 - \frac{1}{2} \varepsilon_{33}^S E_3^2 \tag{5.85}$$

In appendix D the calculation of the electrical enthalpy is presented in more detail.

Following relationships exist between the material parameters:

$$c_{11}^E = \frac{1}{s_{11}^E} \tag{5.86}$$

$$e_{31} = \frac{d_{31}}{s_{11}^E} \tag{5.87}$$

and

$$\varepsilon_{33}^S = \varepsilon_{33}^T - \frac{d_{31}^2}{s_{11}^E} \tag{5.88}$$

By means of coefficient comparison, the relationships can directly be achieved from the equations of state (5.81) - (5.84) (see appendix E).

Insertion of (5.85) into (5.76) and taking (5.86) and (5.87) into consideration, the Lagrange function L of a piezoelectric beam bending actuator can be formulated:

$$L = \sum_{i=1}^{n} \iiint_{V_i} \left[\frac{1}{2} \rho_i \left(\frac{\partial \xi(x,t)}{\partial t} \right)^2 - \frac{1}{2 s_{11,i}^E} S_{1,i}^2 + \frac{d_{31,i}}{s_{11,i}^E} E_{3,i} S_{1,i} + \frac{1}{2} \varepsilon_{33,i}^S E_{3,i}^2 \right] dV_i \tag{5.89}$$

The consideration of the static behavior of piezoelectric bending actuators on the basis of Bernoulli's hypothesis has already shown, that the strain $S_1(x,z)$ shows a linear behavior over the entire cross-sectional area of the bar. Due to the resulting continuity condition at the boundary layers of a multilayered actuator, the index number of the mechanical strain in equation (5.89) can be ignored. Applying the differential equation for the strain arising over the cross section of a beam bender (see eq. 4.13, section 4.2) and neglecting the strain

of the neutral axis $\left(\varepsilon^0 = 0\right)$, equation (5.89) can be formulated in following form, taking the necessary integration limits into consideration:

$$
L = \sum_{i=1}^{n} \int_{h_{i,u}}^{h_{i,o}} \int_{0}^{w_i} \int_{0}^{l} \left[\frac{1}{2}\rho_i \left(\frac{\partial \xi}{\partial t} \right)^2 - \frac{1}{2s_{11,i}^E} z^2 \left(\frac{\partial^2 \xi}{\partial x^2} \right)^2 \right.
$$

$$
\left. - \frac{d_{31,i}}{s_{11,i}^E} E_{3,i} z \left(\frac{\partial^2 \xi}{\partial x^2} \right) + \frac{1}{2} \varepsilon_{33,i}^S E_{3,i}^2 \right] dV_i \tag{5.90}
$$

The evaluation of the two external integrals yields with $dV_i = dxdydz$:

$$
L = \frac{1}{2} \underbrace{\sum_{i=1}^{n} \rho_i h_i w_i}_{(*)} \int_{0}^{l} \left(\frac{\partial \xi}{\partial t} \right)^2 dx - \frac{1}{2} \underbrace{\sum_{i=1}^{n} \frac{1}{3} \frac{w_i}{s_{11,i}^E} \left[h_{i,o}^3 - h_{i,u}^3 \right]}_{(**)} \int_{0}^{l} \left(\frac{\partial^2 \xi}{\partial x^2} \right)^2 dx
$$

$$
- \frac{1}{2} \sum_{i=1}^{n} \frac{d_{31,i}}{s_{11,i}^E} w_i \left[h_{i,o}^2 - h_{i,u}^2 \right] \int_{0}^{l} E_{3,i} \left(\frac{\partial^2 \xi}{\partial x^2} \right) dx + \sum_{i=1}^{n} \frac{1}{2} \varepsilon_{33,i}^S h_i w_i \int_{0}^{l} E_{3,i}^2 dx \tag{5.91}
$$

The expression $(*)$ in (5.91) is equivalent to the total mass m related to the actuator's length l and is defined as follows:

$$
\sum_{i=1}^{n} \rho_i h_i w_i = \frac{m}{l} \equiv \mu \tag{5.92}
$$

In accordance with equation (4.32), $(**)$ represents the flexural rigidity C. Thus, the Lagrange function L of a piezoelectric beam bending actuator results in the desired form

$$
L = \frac{1}{2} \mu \int_{0}^{l} \left(\frac{\partial \xi}{\partial t} \right)^2 dx - \frac{1}{2} C \int_{0}^{l} \left(\frac{\partial^2 \xi}{\partial x^2} \right)^2 dx
$$

$$
- \frac{1}{2} \sum_{i=1}^{n} \frac{d_{31,i}}{s_{11,i}^E} w_i \left[h_{i,o}^2 - h_{i,u}^2 \right] \int_{0}^{l} E_{3,i} \left(\frac{\partial^2 \xi}{\partial x^2} \right) dx
$$

$$
+ \sum_{i=1}^{n} \frac{1}{2} \varepsilon_{33,i}^S h_i w_i \int_{0}^{l} E_{3,i}^2 dx. \tag{5.93}
$$

Equation (5.93) indicates following general correlation:

$$
L = L \left(\frac{\partial \xi}{\partial t}, \frac{\partial^2 \xi}{\partial x^2}, E_{3,i} \right) \tag{5.94}
$$

5.8 Mechanical Work Done by Extensive Quantities and Frictional Force

In the next step, the external quantities affecting the beam bender and performing a mechanical work W are considered. The external affecting quantities, that have already been used for the consideration of the static behavior, are a bending moment M, a force F, a pressure load p and an electrical voltage U, respectively (see Fig. 4.5, section 4.6). Furthermore, the work done by dissipative frictional forces is considered.

Following boundary conditions are defined:

1. The beam bender is subjected to an external static moment M at the tip.
2. The beam bending actuator is subjected to an external static force F perpendicularly to the tip.
3. The lower surface of the beam bender (related to the defined z-direction) is subjected to a uniform pressure load p applied over the entire length l and width w of the bender.
4. The active piezoelectric layers are subjected to the same driving voltage U over their entire length l and width w (electrical parallel connection).
5. In order to describe the frictional forces, *Rayleigh's dissipation function*

$$D = \frac{1}{2}rv^2 \tag{5.95}$$

   is considered resulting from the integration of (5.67) with respect to a velocity-independent coefficient of friction $K(v) = r$ [112].

The aim is the representation of the total mechanical work W as volume integral, similarly to the Lagrange function L of a beam bending actuator. In the following, the results are briefly summarized. The detailed calculations with respect to each individual mechanical work done by the extensive quantities are presented in appendix F.

1. Beam bender affected by an external force
   The affecting force F causes a shear stress f_A in the y-z plane (see Fig. 5.2).
   The shear stress f_A results in:

$$f_A = \frac{dF_i}{dA_i} \tag{5.96}$$

   Taking (5.96) into account, the work done by the force F can be defined as a volume integral:

$$W_F = \sum_{i=1}^{n} \int_{h_{i,u}}^{h_{i,o}} \int_{0}^{w_i} \int_{0}^{l} f_A \left(\frac{\partial \xi}{\partial x}\right) dx\,dy\,dz \tag{5.97}$$
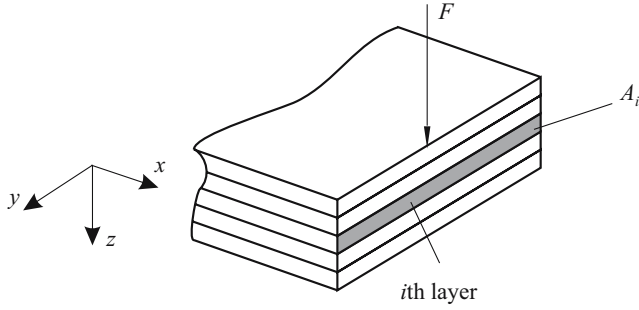
Fig. 5.2. Beam bender affected by an external force

2. Beam bender affected by an external moment
   The affecting moment M related to the y-z plane can be defined in the following form:

$$m_A = \frac{dM_i}{dA_i} \qquad (5.98)$$

Consideration of (5.98) allows for the representation of the work done by the external moment M by means of following integral equation:

$$W_M = -\sum_{i=1}^{n} \int_{h_{i,u}}^{h_{i,o}} \int_{0}^{w_i} \int_{0}^{l} m_A \left(\frac{\partial^2 \xi}{\partial x^2} \right) dxdydz \qquad (5.99)$$

3. Beam bender affected by a uniform pressure load
   The affecting uniform pressure load results in a bending deformation of the actuator and a certain over passed space volume. Here the work W_p done by the uniform pressure load p can be directly taken out of equation (4.84).
   It can be written:

$$W_p = pw \int_{0}^{l} \xi dx \qquad (5.100)$$

4. Beam bender affected by an electrical voltage
   A driving voltage U causes a change of charge dQ. The electrical work $W_{U,i}$ done in the ith layer yields

$$dW_{U,i} = dQ_i U, \qquad (5.101)$$

where dQ_i can be formulated by means of the surface charge density σ_A in accordance with

$$dQ_i = \sigma_A dA_i. \qquad (5.102)$$

The quantity dA_i denotes a two dimensional element in the x-y plane. The work done by the applied voltage U results in

$$W_U = -\sum_{i=1}^{n} \int_{h_{i,u}}^{h_{i,o}} \int_{0}^{w_i} \int_{0}^{l} \sigma_A \left(\frac{\partial U}{\partial z}\right) dx\,dy\,dz. \qquad (5.103)$$

The minus sign in (5.103) results from the fact, that in the Lagrange formalism the electrical enthalpy H_e (3.55) is found instead of the potential V. However, the effective part of the electrical energy of H_e has always another sign compared to the internal energy density [113].

5. Energy loss caused by frictional force
The frictional force will be described by means of Rayleigh's dissipation function (5.95). Its derivative with respect to the generalized coordinate $\dot{q} = v$ yields the generalized frictional force Q affecting a mass point. The generalized frictional force corresponds to the frictional force $F(r) = -rv$. In order to calculate the work W_r done by frictional forces and thus the corresponding energy loss, a differential beam segment as illustrated in figure 5.3 is considered.
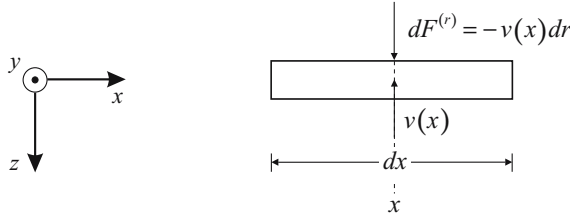
Fig. 5.3. Differential beam segment and affecting velocity-proportional frictional force $F^{(r)}$

Due to the velocity $v(x) = \partial\xi/\partial t$ of the differential beam element in z-direction and due to the *external* and *internal* friction dr, a velocity-proportional frictional force $dF^{(r)}$ (equivalent viscous damping) develops, opposite the movement direction. The affecting total frictional force results in

$$F^{(r)} = -\int_r \left(\frac{\partial\xi}{\partial t}\right) dr. \qquad (5.104)$$

With the definition of the coefficient of friction related to the actuator's length

$$r_a = \frac{dr}{dx}, \qquad (5.105)$$

(5.104) can be written in the following form:

$$F^{(r)} = -\int_0^l r_a \left(\frac{\partial \xi}{\partial t}\right) dx \qquad (5.106)$$

Thus, the work W_r done by the frictional force results in

$$W_r = -\int_0^l r_a \left(\frac{\partial \xi}{\partial t}\right) \xi dx. \qquad (5.107)$$

The work done by external quantities and the energy loss caused by frictional forces result from the sum of the particular parts of work (5.97), (5.99), (5.100), (5.103) and (5.107):

$$W = \sum_{i=1}^n \int_{h_{i,u}}^{h_{i,o}} \int_0^{w_i} \int_0^l f_A \left(\frac{\partial \xi}{\partial x}\right) dxdydz - \sum_{i=1}^n \int_{h_{i,u}}^{h_{i,o}} \int_0^{w_i} \int_0^l m_A \left(\frac{\partial^2 \xi}{\partial x^2}\right) dxdydz$$

$$+pw \int_0^l \xi dx - \sum_{i=1}^n \int_{h_{i,u}}^{h_{i,o}} \int_0^{w_i} \int_0^l \sigma_A \left(\frac{\partial U}{\partial z}\right) dxdydz - \int_0^l r_a \left(\frac{\partial \xi}{\partial t}\right) \xi dx$$

$$(5.108)$$

Here, both the Lagrange function L of a piezoelectric beam bending actuator and the work W done by external affecting quantities and affecting frictional forces are known. Thus, the functional δ can be applied to the equations (5.93) and (5.108).

5.9 Variation of the Lagrange Function

In accordance with the definition of the total differential, using the functional δ, equation (5.94) results in:

$$\delta L = \frac{\partial L}{\partial \left(\frac{\partial \xi}{\partial t}\right)} \delta \left(\frac{\partial \xi}{\partial t}\right) + \frac{\partial L}{\partial \left(\frac{\partial^2 \xi}{\partial x^2}\right)} \delta \left(\frac{\partial^2 \xi}{\partial x^2}\right) + \frac{\partial L}{\partial E_{3,i}} \delta E_{3,i} \qquad (5.109)$$

Applying equation (5.109) to (5.93) yields:

$$\delta L = \mu \int_0^l \left(\frac{\partial \xi}{\partial t}\right) \delta \left(\frac{\partial \xi}{\partial t}\right) dx - C \int_0^l \left(\frac{\partial^2 \xi}{\partial x^2}\right) \delta \left(\frac{\partial^2 \xi}{\partial x^2}\right) dx$$

$$-\frac{1}{2}\sum_{i=1}^{n}\frac{d_{31,i}}{s_{11,i}^{E}}w_{i}\left[h_{i,o}^{2}-h_{i,u}^{2}\right]\int_{0}^{l}E_{3,i}\delta\left(\frac{\partial^{2}\xi}{\partial x^{2}}\right)dx$$

$$-\frac{1}{2}\sum_{i=1}^{n}\frac{d_{31,i}}{s_{11,i}^{E}}w_{i}\left[h_{i,o}^{2}-h_{i,u}^{2}\right]\int_{0}^{l}\left(\frac{\partial^{2}\xi}{\partial x^{2}}\right)\delta E_{3,i}dx$$

$$+\sum_{i=1}^{n}\varepsilon_{33,i}^{S}h_{i}w_{i}\int_{0}^{l}E_{3,i}\delta E_{3,i}dx \tag{5.110}$$

Furthermore, the terms in (5.110) have to be summarized according to the appropriate δ-expressions. In order to determine the first term of Hamilton's principle (5.72), the functional δL has to be integrated with respect to time t inbetween the integral limits t_1 and t_2. As a result the integral of action of the Lagrange function is achieved. Due to the long calculations, only the final result is presented. The detailed variational calculations of the Lagrange function and the determination of the integral of action of the Lagrange function are elaborated in appendix G.

The integral of action of the Lagrange function L is equal to:

$$\int_{t_1}^{t_2}\delta L dt=\int_{t_1}^{t_2}\left[-\mu\int_{0}^{l}\left(\frac{\partial^{2}\xi}{\partial t^{2}}\right)\delta\xi dx-C\int_{0}^{l}\left(\frac{\partial^{4}\xi}{\partial x^{4}}\right)\delta\xi dx\right.$$

$$-C\left(\frac{\partial^{2}\xi}{\partial x^{2}}\right)\delta\left(\frac{\partial\xi}{\partial x}\right)\Big|_{0}^{l}+C\left(\frac{\partial^{3}\xi}{\partial x^{3}}\right)\delta\xi\Big|_{0}^{l}-M_{Piezo}\delta\left(\frac{\partial\xi}{\partial x}\right)\Big|_{0}^{l}$$

$$\left.+\sum_{i=1}^{n}\int_{h_{i,u}}^{h_{i,o}}\int_{0}^{l}w_{i}\frac{dD_{3,i}}{dz}\delta U dxdz-\sum_{i=1}^{n}w_{i}\int_{0}^{l}D_{3,i}\delta U\big|_{h_{i,u}}^{h_{i,o}}dx\right]dt \tag{5.111}$$

5.10 Variation of the Mechanical Work

From equation (5.108) it is evident, that

$$W=W\left(\frac{\partial\xi}{\partial x},\frac{\partial^{2}\xi}{\partial x^{2}},\xi,\frac{\partial U}{\partial z},\frac{\partial\xi}{\partial t}\right). \tag{5.112}$$

Applying the total differential to (5.112) yields the variation of the external work δW:

$$\delta W = \frac{\partial W}{\partial \left(\frac{\partial \xi}{\partial x}\right)} \delta \left(\frac{\partial \xi}{\partial x}\right) + \frac{\partial W}{\partial \left(\frac{\partial^2 \xi}{\partial x^2}\right)} \delta \left(\frac{\partial^2 \xi}{\partial x^2}\right) + \frac{\partial W}{\partial \xi} \delta \xi$$

$$+ \frac{\partial W}{\partial \left(\frac{\partial U}{\partial z}\right)} \delta \left(\frac{\partial U}{\partial z}\right) + \frac{\partial W}{\partial \left(\frac{\partial \xi}{\partial t}\right)} \delta \left(\frac{\partial \xi}{\partial t}\right) \tag{5.113}$$

Applying equation (5.113) to (5.108) and following integration with respect to time results in the integral of action of the external work:

$$\int_{t_1}^{t_2} \delta W = \int_{t_1}^{t_2} \left[\underbrace{\sum_{i=1}^{n} F_i \int_0^l \delta \left(\frac{\partial \xi}{\partial x}\right) dx}_{(1)} - \underbrace{\sum_{i=1}^{n} M_i \int_0^l \delta \left(\frac{\partial^2 \xi}{\partial x^2}\right) dx}_{(2)} + pw \int_0^l \delta \xi dx \right.$$

$$- \int_0^l r_a \left(\frac{\partial \xi}{\partial t}\right) \delta \xi dx - \underbrace{\sum_{i=1}^{n} w_i \int_0^l \int_{h_{i,u}}^{h_{i,o}} \sigma_A \delta \left(\frac{\partial U}{\partial z}\right) dz\, dx}_{(3)}$$

$$\left. - \int_0^l \underbrace{r_a \xi \delta \left(\frac{\partial \xi}{\partial t}\right) dx}_{(4)} \right] dt \tag{5.114}$$

In appendix H the calculation of the terms (1), (2), (3) and (4) in equation (5.114) is presented in detail. Thus, the integral of action of the external work W results in the following form:

$$\int_{t_1}^{t_2} \delta W\, dt = \int_{t_1}^{t_2} \left[F \delta \xi|_0^l - M \delta \left(\frac{\partial \xi}{\partial x}\right) \Big|_0^l + pw \int_0^l \delta \xi dx \right.$$

$$\left. - \int_0^l r_a \left(\frac{\partial \xi}{\partial t}\right) \delta \xi dx - \sum_{i=1}^{n} w_i \int_0^l \sigma_A \delta U|_{h_{i,u}}^{h_{i,o}}\, dx \right] dt \tag{5.115}$$

5.11 Differential Equations of a Piezoelectric Multilayer Beam Bender

Summarizing the equations (5.111) and (5.115) in accordance with (5.72) and following rearranging of the terms according to the individual δ-expression yields:

$$\int_{t_1}^{t_2} \delta L\, dt + \int_{t_1}^{t_2} \delta W\, dt = \int_{t_1}^{t_2} \left[-\int_{0}^{l} \left[\mu \left(\frac{\partial^2 \xi}{\partial t^2} \right) + C \left(\frac{\partial^4 \xi}{\partial x^4} \right) \right. \right.$$

$$\left. + r_a \left(\frac{\partial \xi}{\partial t} \right) - pw \right] \delta\xi\, dx$$

$$+ \left[\left[C \left(\frac{\partial^3 \xi}{\partial x^3} \right) + F \right] \delta\xi \Big|_{0}^{l} \right]$$

$$- \left[\left[C \left(\frac{\partial^2 \xi}{\partial x^2} \right) + M_{Piezo} + M \right] \delta\left(\frac{\partial \xi}{\partial x} \right) \Big|_{0}^{l} \right]$$

$$+ \sum_{i=1}^{n} w_i \int_{h_{i,u}}^{h_{i,o}} \int_{0}^{l} \left[\frac{dD_{3,i}}{dz} \right] \delta U\, dx\, dz$$

$$\left. - \sum_{i=1}^{n} w_i \int_{0}^{l} \left[D_{3,i} + \sigma_A \right] \delta U \Big|_{h_{i,u}}^{h_{i,o}}\, dx \right] dt$$

$$= 0 \qquad\qquad (5.116)$$

Since the variations are independent from each other, the stationarity condition is fulfilled if and only if the individual terms in brackets in front of the variational expressions in equation (5.116) vanish. Due to this fact, the differential equation for transversal bending motions of an n-layered piezoelectric bending actuator, the differential equation of the lateral force, the differential equation of the bending line, the charge equation of electrostatics and the equation for the transition of the electrical displacement at interfaces result, respectively. They are listed below:

1. Differential equation for transversal beam bending motions of an n-layered piezoelectric bending actuator [114, 115]:

$$C\frac{\partial^4 \xi\,(x,t)}{\partial x^4} + \mu\frac{\partial^2 \xi\,(x,t)}{\partial t^2} + r_a\frac{\partial \xi}{\partial t} = f\,(x,t) \qquad (5.117)$$

2. Differential equation of the lateral force:

$$C\frac{\partial^3 \xi\,(x,t)}{\partial x^3} = -F\,(t) \qquad (5.118)$$

3. Differential equation of the bending line:

$$C\frac{\partial^2 \xi\,(x,t)}{\partial x^2} = -\left(M_{Piezo}\,(t) + M\,(t) \right) \qquad (5.119)$$

4. Charge equation of electrostatics [116]:

$$\frac{dD_{3,i}}{dz} = 0 \qquad (5.120)$$

5. Transition of the electrical displacement at interfaces:

$$D_{3,i} + \sigma_A = 0 \qquad (5.121)$$

6

Theory of the Dynamic Behavior of Piezoelectric Beam Bending Actuators

In the previous chapter, the differential equations describing the dynamics of a piezoelectric multilayered bending actuator have been derived by means of the modified Hamilton principle. In the following, they provide the basis for the description of the dynamic behavior of piezoelectric multilayered actuators in closed form analysis. By analogy of the static behavior, an aim is the representation of the correlation between the *extensive dynamic quantities* and the *intensive dynamic quantities* in dependence of the bender's length variable x. The correlation is presented by means of a system matrix $\mathbf{H}$, which is called *dynamic admittance matrix*. The matrix equation is presented in (6.1) [19]:

$$
\underbrace{\begin{pmatrix} \alpha\left(x,t\right) \\ \xi\left(x,t\right) \\ V\left(x,t\right) \\ Q\left(x,t\right) \end{pmatrix}}_{\text{intensive quantities}} = \underbrace{\begin{pmatrix} h_{11}\left(x\right) & h_{12}\left(x\right) & h_{13}\left(x\right) & h_{14}\left(x\right) \\ h_{21}\left(x\right) & h_{22}\left(x\right) & h_{23}\left(x\right) & h_{24}\left(x\right) \\ h_{31}\left(x\right) & h_{32}\left(x\right) & h_{33}\left(x\right) & h_{34}\left(x\right) \\ h_{41}\left(x\right) & h_{42}\left(x\right) & h_{43}\left(x\right) & h_{44}\left(x\right) \end{pmatrix}}_{\text{Admittance matrix } \mathbf{H}(x)} \underbrace{\begin{pmatrix} M\cos\left(\Omega t\right) \\ F\cos\left(\Omega t\right) \\ p\cos\left(\Omega t\right) \\ U\cos\left(\Omega t\right) \end{pmatrix}}_{\text{extensive quantities}} \quad (6.1)
$$

6.1 Eigenmodes of a Clamped-Free Beam Bender

Equation (5.117) is the starting point of following considerations. In order to determine a general solution $\xi(x,t)$, the homogeneous differential equation

$$
C\frac{\partial^4 \xi_h\left(x,t\right)}{\partial x^4} + \mu\frac{\partial^2 \xi_h\left(x,t\right)}{\partial t^2} + r_a\frac{\partial \xi_h\left(x,t\right)}{\partial t} = 0 \quad (6.2)
$$

is considered. It is supposed, that the flexural rigidity C remains constant over the beam bender's length. In order to determine a solution of the boundary and initial value problem respectively, the following separation ansatz is

chosen [115, 117, 118]:

$$\xi_h(x,t) = X(x)\,\phi(t) = X(x)\,\phi_0 e^{j\omega t} \tag{6.3}$$

Equation (6.2) can be reformulated in combination with the separation ansatz according to [119]:

$$\frac{\partial^4 X(x)}{\partial x^4} - \left[\frac{\omega^2}{C}\mu - j\frac{\omega r_a}{C}\right] X(x) = 0 \tag{6.4}$$

At first, the damping r_a is neglected, since the eigenfunctions and eigenmodes of the undamped bending vibration are of interest [120, 121]. Equation (6.4) can be written in the following form

$$\frac{\partial^4 X(x)}{\partial x^4} - k^4 X(x) = 0, \tag{6.5}$$

whereas the quantity k denotes the wavenumber defined as follows [122]:

$$k^4 = \frac{\omega^2}{C}\mu \tag{6.6}$$

The determination of the general solution of the homogeneous differential equation (6.5) results from the Laplace transform (transformation of x on spatial frequencies s) taking the derivative rule into consideration [123].

$$\mathcal{L}\left\{\frac{\partial^4 X(x)}{\partial x^4}\right\} - \mathcal{L}\left\{k^4 X(x)\right\} = 0 \tag{6.7}$$

results in

$$X(s) = \frac{1}{s^4 - k^4}\left[s^3 X(0) + s^2\frac{dX}{dx}(0) + s\frac{d^2 X}{dx^2}(0) + \frac{d^3 X}{dx^3}(0)\right]. \tag{6.8}$$

Following inverse transform yields

$$X(x) = \tilde{C}(kx) X(0) + \frac{1}{k}\tilde{S}(kx)\frac{dX}{dx}(0) + \frac{1}{k^2}\tilde{c}(kx)\frac{d^2 X}{dx^2}(0) + \frac{1}{k^3}\tilde{s}(kx)\frac{d^3 X}{dx^3}(0), \tag{6.9}$$

whereas following equations are formulated as follows:

$$\tilde{S}(kx) = \frac{1}{2}\left[\sinh(kx) + \sin(kx)\right] \tag{6.10}$$

$$\tilde{C}(kx) = \frac{1}{2}\left[\cosh(kx) + \cos(kx)\right] \tag{6.11}$$

$$\tilde{s}(kx) = \frac{1}{2}\left[\sinh(kx) - \sin(kx)\right] \tag{6.12}$$

$$\tilde{c}(kx) = \frac{1}{2}\left[\cosh(kx) - \cos(kx)\right] \tag{6.13}$$

The equations (6.10) - (6.13) represent the so-called linearly independent *Rayleigh functions* generating a complete solution system for equation (6.5) [124]. Taking the wavenumber k into consideration, the functions $\tilde{S}(x)$, $\tilde{C}(x)$, $\tilde{s}(x)$ and $\tilde{c}(x)$ merge by means of differentiation in the order mentioned above.

In order to determine the general solution $X(x)$, the following derivatives are formulated using equation (6.9):

$$\frac{dX}{dx} = k\tilde{s}\left(kx\right)X\left(0\right) + \tilde{C}\left(kx\right)\frac{dX}{dx}\left(0\right) + \frac{1}{k}\tilde{S}\left(kx\right)\frac{d^2X}{dx^2}\left(0\right) + \frac{1}{k^2}\tilde{c}\left(kx\right)\frac{d^3X}{dx^3}\left(0\right)$$

(6.14)

$$\frac{d^2X}{dx^2} = k^2\tilde{c}\left(kx\right)X\left(0\right) + k\tilde{s}\left(kx\right)\frac{dX}{dx}\left(0\right) + \tilde{C}\left(kx\right)\frac{d^2X}{dx^2}\left(0\right) + \frac{1}{k}\tilde{S}\left(kx\right)\frac{d^3X}{dx^3}\left(0\right)$$

(6.15)

$$\frac{d^3X}{dx^3} = k^3\tilde{S}\left(kx\right)X\left(0\right) + k^2\tilde{c}\left(kx\right)\frac{dX}{dx}\left(0\right) + k\tilde{s}\left(kx\right)\frac{d^2X}{dx^2}\left(0\right) + \tilde{C}\left(kx\right)\frac{d^3X}{dx^3}\left(0\right)$$

(6.16)

The solution of equation (6.9) results from the boundary conditions of the clamped-free beam bending actuator.

1. Boundary conditions at the clamped side $(x = 0)$:

$$\xi\left(0,t\right) = 0 \quad \Rightarrow \quad X\left(0\right) = 0 \tag{6.17}$$

$$\frac{d\xi}{dx}\left(0,t\right) = 0 \quad \Rightarrow \quad \frac{dX}{dx}\left(0\right) = 0 \tag{6.18}$$

2. No moment and force (see eq. 5.118 and 5.119) at the free bender's tip $(x = l)$:

$$M\left(l,t\right) = 0 \quad \Rightarrow \quad \frac{d^2X}{dx^2}\left(l\right) = 0 \tag{6.19}$$

$$F\left(l,t\right) = 0 \quad \Rightarrow \quad \frac{d^3X}{dx^3}\left(l\right) = 0 \tag{6.20}$$

In combination with the boundary conditions (6.17) - (6.20), the equations (6.9) and (6.14) - (6.16) result in the following system of equations represented in matrix notation:

$$\begin{bmatrix} \tilde{C}\left(kl\right) & \frac{1}{k}\tilde{S}\left(kl\right) \\ k\tilde{s}\left(kl\right) & \tilde{C}\left(kl\right) \end{bmatrix} \begin{bmatrix} \frac{d^2X}{dx^2}\left(0\right) \\ \frac{d^3X}{dx^3}\left(0\right) \end{bmatrix} = \begin{bmatrix} 0 \\ 0 \end{bmatrix}$$

(6.21)

Since during a free vibration the moment and the transverse force are different from zero at the clamp $x = 0$, equation (6.21) can only be satisfied, if

$$\det \begin{bmatrix} \tilde{C}\left(kl\right) & \frac{1}{k}\tilde{S}\left(kl\right) \\ k\tilde{s}\left(kl\right) & \tilde{C}\left(kl\right) \end{bmatrix} = 0. \tag{6.22}$$

Thus, the following relationship

$$\tilde{C}^2\left(kl\right) - \tilde{s}\left(kl\right)\tilde{S}\left(kl\right) = 0 \tag{6.23}$$

results from (6.22), which can be rewritten to

$$1 + \cos\left(kl\right)\cosh\left(kl\right) = 0 \tag{6.24}$$

by means of the definitions (6.10) - (6.12).

Equation (6.24) represents the so-called *characteristic equation of a clamped-free bending bar*. It is not solvable in analytically closed form. A numerical computation of (6.24) results in m characteristic zeros $k_m l$, whereas $m = 1, 2, \ldots, \infty$ is valid and m physically corresponds to the appropriate natural propagationable mode. The first five solutions of the characteristic equation of a clamped-free beam bending actuator are listed in Table 6.1 [122, 125].

Table 6.1. Solutions of the characteristic equation

m	1	2	3	4	5	$\cdots$
$k_m l$	1.8751	4.6941	7.8548	10.9955	14.137	$\cdots$

Taking the beam length l into account, by means of the characteristic zeros $k_m l$ the natural frequencies of a clamped-free beam bending actuator can be determined from equation (6.6):

$$\omega_m = \frac{\left(k_m l\right)^2}{l^2}\sqrt{\frac{C}{\mu}} \tag{6.25}$$

Thus, the eigenmode $X_m(x)$ can be determined with respect to (6.9). It can be written:

$$X_m\left(x\right) = \frac{1}{k_m^2}\frac{d^2 X_m}{dx^2}\left(0\right)\left[\tilde{c}\left(k_m x\right) + \frac{1}{k_m}\tilde{s}\left(k_m x\right)\frac{\frac{d^3 X_m}{dx^3}\left(0\right)}{\frac{d^2 X_m}{dx^2}\left(0\right)}\right] \tag{6.26}$$

The first line of (6.21) yields:

$$\frac{\frac{d^3 X_m}{dx^3}\left(0\right)}{\frac{d^2 X_m}{dx^2}\left(0\right)} = -\frac{k_m \tilde{C}\left(k_m l\right)}{\tilde{S}\left(k_m l\right)} \tag{6.27}$$

Insertion of (6.27) into (6.26) results in:

$$X_m\left(x\right) = \frac{1}{k_m^2}\frac{d^2 X_m}{dx^2}\left(0\right)\left[\tilde{c}\left(k_m x\right) - \tilde{s}\left(k_m x\right)\frac{\tilde{C}\left(k_m l\right)}{\tilde{S}\left(k_m l\right)}\right] \qquad (6.28)$$

The *form* of the propagationable modes is characterized by the term in brackets in (6.28). The term in front of the brackets can have arbitrary values, thus the eigenmodes can be described by [126]

$$X_m\left(x\right) = \tilde{c}\left(k_m x\right) - \tilde{s}\left(k_m x\right)\frac{\tilde{C}\left(k_m l\right)}{\tilde{S}\left(k_m l\right)}. \qquad (6.29)$$

On the basis of the superposition principle, the function $\xi(x,t)$ yields as superposition of the propagationable modes in accordance with (6.3)

$$\xi\left(x,t\right) = \sum_{m=1}^{\infty} X_m\left(x\right)\phi_m\left(t\right). \qquad (6.30)$$

The representation of the function $\xi(x,t)$ by an infinite series absolutely converges for $m \to \infty$ [127].

In order to include the extensive quantities force, moment, pressure load and electrical voltage into the calculations, it is necessary to dwell on the *orthogonality properties* of the eigenfunctions X_m of a clamped-free beam bender.

6.2 Orthogonality of Eigenfunctions

Equation (6.5) can be written in the following form:

$$\frac{\partial^4 X_m}{\partial x^4} = \lambda_m X_m \qquad (6.31)$$

with

$$\lambda_m = k_m^4 = \frac{\omega_m^2}{C}\mu. \qquad (6.32)$$

(6.31) represents an eigenvalue problem, which is characterized by the fact, that the fourth derivative of the eigenfunction X_m corresponds to the product of the eigenfunction itself and its eigenvalue λ_m.

In order to analyze the orthogonality properties (linear independence) of the eigenfunctions, different modes m and p are to be assumed [128]:

$$\frac{\partial^4 X_m}{\partial x^4} = \lambda_m X_m \qquad (6.33)$$

$$\frac{\partial^4 X_p}{\partial x^4} = \lambda_p X_p \qquad (6.34)$$

Multiplication of (6.33) with X_p, multiplication of (6.34) with X_m and following integration with respect to the beam length l yields:

$$\int_0^l \frac{\partial^4 X_m}{\partial x^4} X_p dx = \lambda_m \int_0^l X_m X_p dx \tag{6.35}$$

$$\int_0^l \frac{\partial^4 X_p}{\partial x^4} X_m dx = \lambda_p \int_0^l X_m X_p dx \tag{6.36}$$

The integration of the left side of (6.35) and (6.36) yields by means of double integration by parts:

$$\frac{d^3 X_m}{dx^3} X_p \bigg|_0^l - \frac{d^2 X_m}{dx^2} \frac{dX_p}{dx} \bigg|_0^l - \int_0^l \frac{d^2 X_m}{dx^2} \frac{d^2 X_p}{dx^2} dx = \lambda_m \int_0^l X_m X_p dx \tag{6.37}$$

$$\frac{d^3 X_p}{dx^3} X_m \bigg|_0^l - \frac{d^2 X_p}{dx^2} \frac{dX_m}{dx} \bigg|_0^l - \int_0^l \frac{d^2 X_m}{dx^2} \frac{d^2 X_p}{dx^2} dx = \lambda_p \int_0^l X_m X_p dx \tag{6.38}$$

Taking the boundary conditions (6.17) - (6.20) into consideration results in combination with (6.37) and (6.38) in:

$$-\int_0^l \frac{d^2 X_m}{dx^2} \frac{d^2 X_p}{dx^2} dx = \lambda_m \int_0^l X_m X_p dx \tag{6.39}$$

$$-\int_0^l \frac{d^2 X_m}{dx^2} \frac{d^2 X_p}{dx^2} dx = \lambda_p \int_0^l X_m X_p dx \tag{6.40}$$

Following difference formation of (6.39) and (6.40) yields

$$(\lambda_m - \lambda_p) \int_0^l X_m X_p dx = 0. \tag{6.41}$$

Due to $\lambda_m \neq \lambda_p$ for $m \neq p$, equation (6.41) is only satisfied in general, if the following equation is valid:

$$\int_0^l X_m X_p dx = 0 \tag{6.42}$$

Furthermore, the insertion of (6.42) into (6.35) and (6.39) results in:

$$\int_0^l \frac{\partial^4 X_m}{\partial x^4} X_p dx = 0 \tag{6.43}$$

$$\int_0^l \frac{d^2 X_m}{dx^2} \frac{d^2 X_p}{dx^2} dx = 0 \tag{6.44}$$

The equations (6.42) - (6.44) demonstrate the orthogonality properties for bending waves arising on a bending beam. If $m = p$ is valid, from equation (6.42) follows

$$\int_0^l X_m^2 dx \neq 0. \tag{6.45}$$

Thus, from (6.35) and (6.39) follows:

$$\int_0^l \frac{\partial^4 X_m}{\partial x^4} X_m dx = -\int_0^l \left(\frac{d^2 X_m}{dx^2} \right)^2 dx = \lambda_m \int_0^l X_m^2 dx = \frac{\omega_m^2}{C} \mu \int_0^l X_m^2 dx \tag{6.46}$$

With this knowledge, the time-dependent behavior of the eigenmodes can be determined at arbitrary points x of the beam bender affected by an external line load $f(x,t)$.

6.3 Description of Flexural Vibrations with Respect to Time

The starting point of the further considerations is the inhomogenous differential equation (5.117).

$$C\frac{\partial^4 \xi(x,t)}{\partial x^4} + \mu \frac{\partial^2 \xi(x,t)}{\partial t^2} + r_a \frac{\partial \xi(x,t)}{\partial t} = f(x,t) \tag{6.47}$$

In combination with the general solution (6.30) for the clamped-free beam bender, equation (6.47) can be rewritten in the following form:

$$C \sum_{m=1}^{\infty} \frac{d^4 X_m}{dx^4} \phi_m + \mu \sum_{m=1}^{\infty} X_m \frac{d_m^2 \phi_m}{dt^2} + r_a \sum_{m=1}^{\infty} X_m \frac{d\phi_m}{dt} = f(x,t) \tag{6.48}$$

Multiplication on both sides of equation (6.48) with X_m and following integration with respect to the beam length l yields in combination with (6.42) and (6.43)

$$\sum_{m=1}^{\infty} \int_0^l f(x,t)\, X_m dx = C \sum_{m=1}^{\infty} \int_0^l \frac{d^4 X_m}{dx^4} X_m \phi_m dx$$

$$+ \mu \sum_{m=1}^{\infty} \int_0^l X_m^2 \frac{d^2 \phi_m}{dt^2} dx$$

$$+ r_a \sum_{m=1}^{\infty} \int_0^l X_m^2 \frac{d\phi_m}{dt} dx. \tag{6.49}$$

Taking the orthogonality properties (6.45) and (6.46) into account results in

$$\int_0^l f(x,t)\, X_m dx = C\lambda_m \phi_m \int_0^l X_m^2 dx + \mu \ddot{\phi}_m \int_0^l X_m^2 dx + r_a \dot{\phi}_m \int_0^l X_m^2 dx, \tag{6.50}$$

being valid for the mth mode. Division by $\int_0^l X_m^2 dx$ and μ on both sides of (6.50) and applying the relationship (6.32) results in combination with

$$\frac{r_a}{\mu} = \frac{r}{m} = 2\zeta_m \omega_m \tag{6.51}$$

in

$$\ddot{\phi}_m + 2\zeta_m \omega_m \dot{\phi}_m + \omega_m^2 \phi_m = \frac{\int_0^l f(x,t)\, X_m dx}{\mu \int_0^l X_m^2 dx}. \tag{6.52}$$

The quantity ξ_m denotes a dimensionless attenuation constant, ω_m corresponds to the natural frequency of the mth vibrational mode of an undamped, clamped-free beam bender. Equation (6.52) represents the basis for the determination of the temporal characteristics of the eigenmodes X_m taking the damping into consideration. In the following section, the temporal characteristics of the vibrational modes of a free damped flexural vibration are considered at first. Subsequently, the considerations are extended to an excitation by an alternating force and an alternating moment at the bender's tip as well as an alternating pressure load affecting the entire length l of the bender and an alternating electrical voltage, respectively.

6.4 The Free Damped Flexural Vibration

In case of a free damped flexural vibration ($f(x,t) = 0$), equation (6.52) can be formulated according to

$$\ddot{\phi}_m + 2\zeta_m \omega_m \dot{\phi}_m + \omega_m^2 \phi_m = 0. \tag{6.53}$$

In order to determine the homogeneous solution, the approach $\phi_m^h(t) = e^{\lambda t}$ is chosen resulting in the characteristic equation

$$\lambda^2 + 2\zeta_m \omega_m \lambda + \omega_m^2 = 0. \tag{6.54}$$

Its solution is equal to

$$\lambda_{1,2} = \omega_m \left(-\zeta_m \pm \sqrt{\zeta_m^2 - 1} \right). \tag{6.55}$$

In the following, the considerations of the dynamic behavior of clamped-free piezoelectric beam bending actuators refer to the case of the subcritical damping. In this case, the dimensionless attenuation constant is defined as follows:

$$\zeta_m < 1 \tag{6.56}$$

Thus, the solutions of the characteristic equation are complex:

$$\lambda_{1,2} = \omega_m \left(-\zeta_m \pm j\sqrt{1 - \zeta_m^2} \right) \tag{6.57}$$

The general homogeneous solution results in

$$\phi_m^h(t) = e^{-\omega_m \zeta_m t} \left(C_1 e^{j\omega_m^d t} + C_2 e^{-j\omega_m^d t} \right) \tag{6.58}$$

with

$$\omega_m^d = \omega_m \sqrt{1 - \zeta_m^2}. \tag{6.59}$$

From a physical point of view, only the real part of (6.58) is relevant resulting in the following homogeneous solution [129]:

$$\phi_m^h(t) = e^{-\omega_m \zeta_m t} \left[A_m \cos\left(\omega_m^d t\right) + B_m \sin\left(\omega_m^d t\right) \right] \tag{6.60}$$

With the initial conditions $\phi_m^h(0) = \phi_0$ and $\dot{\phi}_m^h(0) = 0$, the homogeneous solution is equal to

$$\phi_m^h(t) = \phi_0 e^{-\omega_m \zeta_m t} \left[\cos\left(\omega_m^d t\right) + \frac{\zeta_m}{\sqrt{1 - \zeta_m^2}} \sin\left(\omega_m^d t\right) \right]. \tag{6.61}$$

In combination with (6.30), the homogeneous solution (6.61) yields the time- and position-dependent representation of the deflection of a clamped-free subcritically damped beam bender:

$$\xi(x,t) = \phi_0 \sum_{m=1}^{\infty} X_m(x) e^{-\omega_m \zeta_m t} \left[\cos\left(\omega_m^d t\right) + \frac{\zeta_m}{\sqrt{1 - \zeta_m^2}} \sin\left(\omega_m^d t\right) \right] \tag{6.62}$$

In later measurements, the dimensionless attenuation constant ζ_m and the coefficient of friction r of a realized beam bending actuator will be determined in combination with equation (6.62) (see section 9.3.1). The coefficient of friction r is evident for an electromechanical circuit representation within the scope of the network theory.

6.5 Excitation by a Harmonic Force

In order to provide, that the force affecting the beam bender's tip $(x = l)$ corresponds to a linear distributed load $f(x, t)$ according to (6.52), the load per unit length is defined as follows [130]:

$$f(x, t) = F \cos(\Omega t) \delta(x - l) \tag{6.63}$$

$\delta(x)$ denotes the *Dirac delta function* with

$$\delta(x) = \begin{cases} 0 & \text{if } x \neq 0 \\ \infty & \text{if } x = 0 \end{cases}, \tag{6.64}$$

where

$$\int_{-\infty}^{\infty} \delta(x)\, dx = 1. \tag{6.65}$$

Thus, (6.52) can be written in combination with (6.63) in the following form:

$$\ddot{\phi}_m + 2\zeta_m \omega_m \dot{\phi}_m + \omega_m^2 \phi_m = \frac{F \cos(\Omega t) X_m(l)}{\mu \int_0^l X_m^2 dx} \tag{6.66}$$

The expression

$$\frac{X_m(l)}{\int_0^l X_m^2 dx}$$

in (6.66) can only be solved with great mathematical effort, thus the software package Mathematica® is used for the computation.

In combination with the eigenmodes (6.29) of the clamped-free beam bender and the Rayleigh functions (6.10) - (6.13), it can be written

$$\frac{X_m(l)}{\int_0^l X_m^2} = \frac{4}{l} \underbrace{\left[\frac{\cosh(k_m l) \sin(k_m l) - \cos(k_m l) \sinh(k_m l)}{\sin(k_m l) + \sinh(k_m l)} \right]}_{\equiv \alpha_F(k_m l)} = \frac{4}{l} \alpha_F(k_m l). \tag{6.67}$$

Thus, equation (6.66) can be reformulated as follows:

$$\ddot{\phi}_m + 2\zeta_m \omega_m \dot{\phi}_m + \omega_m^2 \phi_m = \frac{4F\alpha_F(k_m l)}{l\mu} \cos(\Omega t) \tag{6.68}$$

Here, $|\alpha_F(k_m l)| = 1$ is valid for all values $k_m l$ listed in Table 6.1 (proof see appendix I). It is an aim to find a particular solution of the inhomogenous differential equation (6.68). Following approach is made:

$$\phi_m^p (t) = A_m \cos (\Omega t) + B_m \sin (\Omega t) \tag{6.69}$$

In appendix J, the calculation of the particular solution $\phi_m^p (t)$ is discussed in more detail. The particular solution results in

$$\phi_m^p (t) = \frac{4F}{l\mu} \frac{\alpha_F (k_m l)}{\omega_m^2 \sqrt{(1 - \eta_m^2)^2 + (2\zeta_m \eta_m)^2}} \cos (\Omega t - \Psi_m), \tag{6.70}$$

where the quantity η_m corresponds to the dimensionless ratio of the excitation frequency and the frequency of the free, undamped oscillation with

$$\eta_m = \frac{\Omega}{\omega_m}. \tag{6.71}$$

The quantity Ψ_m denotes the phase angle in accordance with

$$\tan \Psi_m = \frac{2\zeta_m \eta_m}{1 - \eta_m^2}. \tag{6.72}$$

The general solution $\phi_m (t)$ results from the summation of the homogeneous (6.61) and particular solution (6.70). Since the damping ζ_m is different from zero, the homogeneous solution decays in time. Thus, after expiration of the transient time, the oscillation $\phi_m (t)$ yields the particular solution [131]

$$\phi_m (t) = \frac{F}{\frac{l\mu}{4}} \frac{\alpha_F (k_m l)}{\omega_m^2 \sqrt{(1 - \eta_m^2)^2 + (2\zeta_m \eta_m)^2}} \cos (\Omega t - \Psi_m). \tag{6.73}$$

With the exception of the factor $1/4$, equation (6.73) formally corresponds to the oscillation characteristics of a system consisting of a spring, a mass and a damper in case of excitation by a harmonic force [132]. The additional factor $1/4$ shows, that 25% of the total mass μl can be assumed to be concentrated at the bender's tip. This fact will play an important role for the electromechanical circuit representation of piezoelectric beam bending actuators.

Taking equation (6.30) into account, the spatial and temporal deflection of a bending actuator yields with respect to excitation by a harmonic force affecting the bender's tip

$$\xi (x, t) = \frac{4}{l\mu} \underbrace{\sum_{m=1}^{\infty} X_m (x) \frac{\alpha_F (k_m l)}{\omega_m^2 \sqrt{(1 - \eta_m^2)^2 + (2\zeta_m \eta_m)^2}}}_{= h_{22}(x)} F \cos (\Omega t - \Psi_m).$$

$$\tag{6.74}$$

By means of differentiation of the deflection $\xi (x, t)$ with respect to the length coordinate x, the bending angle $\alpha (x, t)$ results in

$$\alpha\left(x,t\right)=\frac{4}{l\mu}\sum_{m=1}^{\infty}\underbrace{\frac{dX_{m}}{dx}\left(x\right)\frac{\alpha_{F}\left(k_{m}l\right)}{\omega_{m}^{2}\sqrt{\left(1-\eta_{m}^{2}\right)^{2}+\left(2\zeta_{m}\eta_{m}\right)^{2}}}}_{=h_{12}(x)}F\cos\left(\Omega t-\Psi_{m}\right),$$

(6.75)

where

$$\frac{dX_{m}}{dx}\left(x\right)=k_{m}\left[\tilde{S}\left(k_{m}x\right)-\tilde{c}\left(k_{m}x\right)\frac{\tilde{C}\left(k_{m}l\right)}{\tilde{S}\left(k_{m}l\right)}\right].$$

(6.76)

Considering (4.72), the volume displacement $V\left(x,t\right)$ yields

$$V\left(x,t\right)=\frac{4w}{l\mu}\sum_{m=1}^{\infty}\underbrace{\int_{0}^{x}X_{m}\left(x'\right)dx'\frac{\alpha_{F}\left(k_{m}l\right)}{\omega_{m}^{2}\sqrt{\left(1-\eta_{m}^{2}\right)^{2}+\left(2\zeta_{m}\eta_{m}\right)^{2}}}}_{=h_{32}(x)}F\cos\left(\Omega t-\Psi_{m}\right)$$

(6.77)

where

$$\int_{0}^{x}X_{m}\left(x'\right)dx'=\frac{1}{k_{m}}\left[\tilde{s}\left(k_{m}x\right)-\frac{\tilde{C}\left(k_{m}l\right)}{\tilde{S}\left(k_{m}l\right)}\left(1-\tilde{C}\left(k_{m}x\right)\right)\right].$$

(6.78)

Thus, the matrix elements $h_{12}(x)$, $h_{22}(x)$ and $h_{32}(x)$ of the dynamic admittance matrix $\mathbf{H}$ of the piezoelectric beam bending actuator are known as functions of the length variable x.

6.6 Excitation by a Harmonic Moment

If the beam bender's tip is affected by an external dynamic moment around the y-axis according to figure 4.5, the bender performs a harmonic motion. The affecting bending moment can be formulated as a load per unit length using the Dirac delta function:

$$f\left(x,t\right)=M\cos\left(\Omega t\right)\frac{d\delta}{dx}\left(x-l\right)$$

(6.79)

Thus, (6.52) can be reformulated as follows:

$$\ddot{\phi}_{m}+\frac{r_{a}}{\mu}\dot{\phi}_{m}+\omega_{m}^{2}\phi_{m}=\frac{M\cos\left(\Omega t\right)\int_{0}^{l}\frac{d\delta}{dx}\left(x-l\right)X_{m}dx}{\mu\int_{0}^{l}X_{m}^{2}dx}$$

(6.80)

Using the relationship [127]

$$\int\limits_{a}^{c} \delta^{(n)}\left(\xi - b\right) f\left(\xi\right) d\xi = \left(-1\right)^{n} f^{(n)}\left(b\right) \quad \text{for } a \le b \le c \tag{6.81}$$

results in

$$\ddot{\phi}_m + \frac{r_a}{\mu}\dot{\phi}_m + \omega_m^2 \phi_m = -\frac{M \cos\left(\Omega t\right) \frac{dX_m}{dx}\left(l\right)}{\mu \int\limits_{0}^{l} X_m^2 dx}, \tag{6.82}$$

where

$$\frac{\frac{dX_m}{dx}\left(l\right)}{\mu \int\limits_{0}^{l} X_m^2} = \frac{4k_m l}{l^2} \underbrace{\frac{\sin\left(k_m l\right)\sinh\left(k_m l\right)}{\sinh\left(k_m l\right) + \sin\left(k_m l\right)}}_{\equiv \alpha_M\left(k_m l\right)} = \frac{4k_m l}{l^2} \alpha_M\left(k_m l\right). \tag{6.83}$$

In combination with (6.83), the particular approach results in:

$$\ddot{\phi}_m + \frac{r_a}{\mu}\dot{\phi}_m + \omega_m^2 \phi_m = -\frac{4M k_m l\, \alpha_M\left(k_m l\right)}{\mu l^2} \cos\left(\Omega t\right) \tag{6.84}$$

After expiration of the transient time, the vibration follows the particular solution (6.82). By analogy with the excitation by a force, the spatial and temporal deflection of the bending actuator yields with respect to an excitation by a harmonic moment M affecting the bender's tip:

$$\xi\left(x, t\right) = -\frac{4}{l^2 \mu} \sum_{m=1}^{\infty} X_m\left(x\right) \underbrace{\frac{k_m l\, \alpha_M\left(k_m l\right)}{\omega_m^2 \sqrt{\left(1 - \eta_m^2\right)^2 + \left(2\zeta_m \eta_m\right)^2}}}_{=h_{21}(x)} M \cos\left(\Omega t - \Psi_m\right)$$

$$\tag{6.85}$$

By means of differentiation of the deflection $\xi(x, t)$ with respect to the length coordinate x, the bending angle $\alpha(x, t)$ results in

$$\alpha\left(x, t\right) = -\frac{4}{l^2 \mu} \sum_{m=1}^{\infty} \frac{dX_m}{dx}\left(x\right) \underbrace{\frac{k_m l\, \alpha_M\left(k_m l\right)}{\omega_m^2 \sqrt{\left(1 - \eta_m^2\right)^2 + \left(2\zeta_m \eta_m\right)^2}}}_{=h_{11}(x)} M \cos\left(\Omega t - \Psi_m\right). \tag{6.86}$$

By means of double integration of (6.85) with respect to the length variable x and the width variable y, the volume displacement $V(x, t)$ can be calculated according to

$$V\left(x, t\right) = -\frac{4w}{l^2 \mu} \sum_{m=1}^{\infty} \underbrace{\int\limits_{0}^{x} X_m\left(x'\right) dx' \frac{k_m l\, \alpha_M\left(k_m l\right)}{\omega_m^2 \sqrt{\left(1 - \eta_m^2\right)^2 + \left(2\zeta_m \eta_m\right)^2}}}_{=h_{31}(x)}$$

$$\cdot M \cos\left(\Omega t - \Psi_m\right). \tag{6.87}$$

Thus, the matrix elements $h_{11}(x)$, $h_{21}(x)$ and $h_{31}(x)$ of the dynamic admittance matrix $\mathbf{H}$ of a piezoelectric beam bending actuator are known as functions of the length variable x.

6.7 Excitation by a Harmonic Uniform Pressure Load

In the following, the external dynamic pressure load is assumed to affect the entire lower surface of the bending actuator (see Fig. 4.5). Furthermore, no pressure load gradient arises over the beam bender's length variable x ($p(x) = p = const.$) and the pressure load varies sinusoidally with respect to time.

The load per unit length $f(x,t)$ results in

$$f(x,t) = pw\cos(\Omega t). \tag{6.88}$$

Thus, (6.52) can be reformulated according to

$$\ddot{\phi}_m + \frac{r_a}{\mu}\dot{\phi}_m + \omega_m^2\phi_m = \frac{pw\cos(\Omega t)\int_0^l X_m dx}{\mu\int_0^l X_m^2 dx}. \tag{6.89}$$

The quotient

$$\frac{\int_0^l X_m dx}{\int_0^l X_m^2 dx} = \frac{2}{k_m l}\alpha_p(k_m l) \tag{6.90}$$

can be calculated in combination with

$$\alpha_p(k_m l) = \frac{\cos(2k_m l) - 2\cos(k_m l) - 2\cosh(k_m l)}{\sinh(k_m l) + \sin(k_m l)}$$

$$+ \frac{2\cos(k_m l)\cosh(k_m l) + \cosh(2k_m l)}{\sinh(k_m l) + \sin(k_m l)}. \tag{6.91}$$

After expiration of the transient time, the vibration follows the particular solution (6.89). In combination with (6.90), the particular approach results in:

$$\ddot{\phi}_m + \frac{r_a}{\mu}\dot{\phi}_m + \omega_m^2\phi_m = \frac{2pw\alpha_p(k_m l)}{\mu k_m l}\cos(\Omega t) \tag{6.92}$$

With respect to an excitation by a harmonic pressure load p affecting the entire beam bender length l, the spatial and temporal deflection of the bending actuator yields:

$$\xi(x,t) = \underbrace{\frac{2w}{\mu} \sum_{m=1}^{\infty} X_m(x) \frac{\alpha_p(k_m l)}{\omega_m^2 k_m l \sqrt{(1-\eta_m^2)^2 + (2\zeta_m \eta_m)^2}}}_{=h_{23}(x)} p\cos(\Omega t - \Psi_m)$$

(6.93)

By analogy with the harmonic excitation by a force and a moment, the bending angle $\alpha(x,t)$ and the volume displacement $V(x,t)$ can be determined by means of differentiation and integration, respectively. It can be written:

$$\alpha(x,t) = \underbrace{\frac{2w}{\mu} \sum_{m=1}^{\infty} \frac{dX_m}{dx}(x) \frac{\alpha_p(k_m l)}{\omega_m^2 k_m l \sqrt{(1-\eta_m^2)^2 + (2\zeta_m \eta_m)^2}}}_{=h_{13}(x)}$$
$$\cdot p\cos(\Omega t - \Psi_m)$$

(6.94)

$$V(x,t) = \underbrace{\frac{2w}{\mu} \sum_{m=1}^{\infty} \int_0^x X_m(x')\,dx' \frac{\alpha_p(k_m l)}{\omega_m^2 k_m l \sqrt{(1-\eta_m^2)^2 + (2\zeta_m \eta_m)^2}}}_{=h_{33}(x)}$$
$$\cdot p\cos(\Omega t - \Psi_m)$$

(6.95)

Thus, the matrix elements $h_{13}(x)$, $h_{23}(x)$ and $h_{33}(x)$ of the dynamic admittance matrix $\mathbf{H}$ of a piezoelectric beam bending actuator are known as functions of the length variable x.

6.8 Excitation by a Harmonic Driving Voltage

In the following, the piezoelectric multilayer actuator is affected by a periodic alternating voltage. It should be noted, that further considerations refer to a multilayered beam bending actuator in parallel connection according to figure 4.5. Applying a voltage to the individual active piezoelectric layers along their length l causes periodically changing strains and compressive strains within the individual layers, respectively, depending on the mutual orientation of the electric field and polarization. Thus, mechanical stresses are caused within the individual layers resulting in an internal bending moment within the multilayered structure. It originates from the piezoelectric material characteristics and is referred to as piezoelectric moment M_{Piezo} in accordance with (4.33). According to (4.33), the piezoelectric moment is equal to

$$M_{Piezo} = U(t) \underbrace{\frac{1}{2} \sum_{i=1}^n \frac{d_{31,i} w_i}{s_{11,i}^E h_i} \left[2\bar{z} h_i - 2h_i \sum_{j=1}^i h_j + h_i^2 \right]}_{m_{Piezo}}.$$

(6.96)

The driving voltage is applied over the entire length l of the bending actuator, thus the resulting load per unit length $f(x,t)$ can be formulated by means of the Dirac delta function in following way:

$$f(x,t) = U m_{Piezo} \cos{(\Omega t)} \left[\frac{d\delta}{dx}(x-l) - \frac{d\delta}{dx}(x) \right] \qquad (6.97)$$

Applying the differentiation theorem to the Dirac delta function (6.81), it can be written

$$\ddot{\phi}_m + \frac{r_a}{\mu}\dot{\phi}_m + \omega_m^2 \phi_m = -\frac{U m_{Piezo} \cos{(\Omega t)} \frac{dX_m}{dx}(l)}{\mu \int\limits_0^l X_m^2 dx}. \qquad (6.98)$$

Equation (6.98) is equivalent to equation (6.82) representing the excitation by an external mechanical bending moment M. Thus, the bending angle $\alpha(x,t)$, the deflection $\xi(x,t)$ and the volume displacement $V(x,t)$ can be directly formulated as functions of the driving voltage U. The elements $h_{14}(x)$, $h_{24}(x)$ and $h_{34}(x)$ of the dynamic admittance matrix $\mathbf{H}$ are equal to:

$$h_{14}(x) = m_{Piezo} h_{11}(x) \qquad (6.99)$$

$$h_{24}(x) = m_{Piezo} h_{21}(x) \qquad (6.100)$$

$$h_{34}(x) = m_{Piezo} h_{31}(x) \qquad (6.101)$$

At this point, the matrix elements $h_{41}(x)$, $h_{42}(x)$, $h_{43}(x)$ and $h_{44}(x)$ of the dynamic admittance matrix $\mathbf{H}$ characterizing the generated charge dependent on the extensive dynamic quantities M, F, p and U are still not defined. In the next section, they are calculated on the basis of the piezoelectric constituent equations.

6.9 Electrical Charge Generated by Harmonic Extensive Parameters

The piezoelectric constituent equations (5.81) and (5.82), that have to be satisfied in each point of the bending actuator and correspond to the extensive quantities $(\mathbf{T}, \mathbf{E})$ provide a basis for the calculation of the matrix elements $h_{41}(x)$, $h_{42}(x)$, $h_{43}(x)$ and $h_{44}(x)$ of the admittance matrix $\mathbf{H}$.

The equations are transformed appropriately in such a manner that the strain S_1 and the electrical displacement D_3 denote the independent quantities. The electrical displacement of the ith layer yields according to (5.81)

$$D_{3,i} = \varepsilon_{33,i}^T E_{3,i} + d_{31,i} T_{1,i}. \qquad (6.102)$$

Rearranging with respect to $E_{3,i}$ results in

$$E_{3,i} = \frac{1}{\varepsilon_{33,i}^T} D_{3,i} - \frac{d_{31,i}}{\varepsilon_{33,i}^T} T_{1,i}. \tag{6.103}$$

Furthermore, the constitutive equation (5.82) is rearranged with respect to $T_{1,i}$ and inserted into (6.103), thus the electric field within the ith layer is equal to

$$E_{3,i} = -\frac{k_{31,i}^2}{d_{31,i}\left(1 - k_{31,i}^2\right)} S_1 + \frac{1}{\varepsilon_{33,i}^T\left(1 - k_{31,i}^2\right)} D_{3,i}. \tag{6.104}$$

Thereby, the mechanical strain S_1 is a function of the coordinate z, whereas the electrical displacement does not depend on z due to $\mathrm{div}\,\mathbf{D} = 0$ (see eq. 5.120). The quantity k_{31}^2 is referred to as electromechanical coefficient of coupling and is equal to

$$k_{31}^2 = \frac{d_{31}^2}{s_{11}^E \varepsilon_{33}^T}. \tag{6.105}$$

By means of integration of (6.104) with respect to z according to

$$U = \int_{h_{i,u}}^{h_{i,o}} E_{3,i}\,dz, \tag{6.106}$$

the transition to the driving voltage U can be done. Taking the mechanical stress (4.16) of a planar beam bender into account and insertion of (6.104) into (6.106), the driving voltage results in

$$U = \frac{k_{31,i}^2\left(h_{i,o}^2 - h_{i,u}^2\right)}{2d_{31,i}\left(1 - k_{31,i}^2\right)} \frac{\partial^2 \xi}{\partial x^2} + \frac{h_i}{\varepsilon_{33,i}^T\left(1 - k_{31,i}^2\right)} D_{3,i}. \tag{6.107}$$

The charge Q_i generated within the ith layer can be determined by rearranging (6.107) with respect to the electrical displacement and by applying *Gauss'* *theorem*

$$Q = \oint_A \mathbf{D} \cdot d\mathbf{A}. \tag{6.108}$$

In combination with the definition for m_{Piezo} in equation (6.96), the total charge Q yields:

$$Q = \sum_{i=1}^{n} Q_i = -m_{Piezo}\frac{\partial \xi}{\partial x} + U\sum_{i=1}^{n}\varepsilon_{33,i}^T\left(1 - k_{31,i}^2\right)\frac{w_i x}{h_i} \tag{6.109}$$

Taking (6.109) into account, the charge Q is a function of the length coordinate x, the driving voltage U and the bending angle $\partial \xi / \partial x$. Considering, that the extensive quantities are dynamic ones, the total charge Q of the multilayered actuator can be formulated as follows:

$$Q\left(x, t\right) = \left[-m_{Piezo} \frac{\partial \xi}{\partial x} + U \sum_{i=1}^{n} \frac{x w_i}{h_i} \left(\varepsilon_{33,i}^{T} - \frac{d_{31,i}^{2}}{s_{11,i}^{E}}\right)\right] \cos\left(\Omega t - \Psi_m\right)$$

(6.110)

From equation (6.110), the matrix elements $h_{41}(x)$, $h_{42}(x)$, $h_{43}(x)$ and $h_{44}(x)$ of the admittance matrix $\mathbf{H}$ can be calculated.

Since the elements $h_{41}(x)$, $h_{42}(x)$ and $h_{43}(x)$ are calculated with respect to mechanical quantities (M, F, p), the second term on the right side of (6.110) vanishes.

1. Charge $Q(x, t)$ dependent on a harmonic moment M:
   With respect to equation (6.86), for small bending angles $\alpha(x, t)$ it can be written :

   $$\frac{\partial \xi\left(x, t\right)}{\partial x} = h_{11}\left(x\right) M \cos\left(\Omega t - \Psi_m\right)$$

   (6.111)

   Thus, by insertion of (6.111) into (6.110), the total load $Q(x, t)$ can be formulated by following equation:

   $$Q\left(x, t\right) = \underbrace{-m_{Piezo} h_{11}\left(x\right)}_{h_{41}(x)} M \cos\left(\Omega t - \Psi_m\right)$$

   (6.112)

2. Charge $Q(x, t)$ dependent on a harmonic force F:
   With respect to equation (6.75), for small bending angles $\alpha(x, t)$ it can be written :

   $$\frac{\partial \xi\left(x, t\right)}{\partial x} = h_{12}\left(x\right) F \cos\left(\Omega t - \Psi_m\right)$$

   (6.113)

   Thus, by insertion of (6.113) into (6.110), the total load $Q(x, t)$ can be formulated by following equation:

   $$Q\left(x, t\right) = \underbrace{-m_{Piezo} h_{12}\left(x\right)}_{h_{42}(x)} F \cos\left(\Omega t - \Psi_m\right)$$

   (6.114)

3. Charge $Q(x, t)$ dependent on a harmonic uniform pressure load p:
   With respect to equation (6.94), for small bending angles $\alpha(x, t)$ it can be written :

   $$\frac{\partial \xi\left(x, t\right)}{\partial x} = h_{13}\left(x\right) p \cos\left(\Omega t - \Psi_m\right)$$

   (6.115)

   Thus, by insertion of (6.115) into (6.110), the total load $Q(x, t)$ can be formulated by following equation:

   $$Q\left(x, t\right) = \underbrace{-m_{Piezo} h_{13}\left(x\right)}_{h_{43}(x)} p \cos\left(\Omega t - \Psi_m\right)$$

   (6.116)

4. Charge $Q(x,t)$ dependent on an alternating voltage U:
   At this point, the second term of equation (6.110) has to be taken into account. With respect to equation (6.99), for small bending angles $\alpha(x,t)$ it can be written :

$$\frac{\partial \xi(x,t)}{\partial x} = m_{Piezo} h_{11}(x)\, U \cos(\Omega t - \Psi_m) \qquad (6.117)$$

Thus, by insertion of (6.117) into (6.110), the total load $Q(x,t)$ can be formulated by following equation:

$$Q(x,t) = \underbrace{\left[m_{Piezo} h_{11}(x) + \sum_{i=1}^{n} \frac{x w_i}{h_i}\left(\varepsilon_{33,i}^T - \frac{d_{31,i}^2}{s_{11,i}^E}\right)\right]}_{h_{44}(x)} U \cos(\Omega t - \Psi_m)$$

$$(6.118)$$

6.10 Dynamic Admittance Matrix

At this point all matrix elements $h_{ij}(x)$ are determined in closed form analysis. In the following, all matrix elements $h_{ij}(x)$ of the dynamic admittance matrix **H** are summarized column by column.

1. First column of the admittance matrix **H**

$$\begin{pmatrix} h_{11}(x) \\ h_{21}(x) \\ h_{31}(x) \\ h_{41}(x) \end{pmatrix} = \begin{pmatrix} -\frac{4}{l^2 \mu} \sum\limits_{m=1}^{\infty} \frac{dX_m}{dx}(x)\, \frac{k_m l\, \alpha_M(k_m l)}{\omega_m^2 \sqrt{(1-\eta_m^2)^2+(2\zeta_m \eta_m)^2}} \\[2ex] -\frac{4}{l^2 \mu} \sum\limits_{m=1}^{\infty} X_m(x)\, \frac{k_m l\, \alpha_M(k_m l)}{\omega_m^2 \sqrt{(1-\eta_m^2)^2+(2\zeta_m \eta_m)^2}} \\[2ex] -\frac{4w}{l^2 \mu} \sum\limits_{m=1}^{\infty} \int\limits_0^x X_m(x')\, dx'\, \frac{k_m l\, \alpha_M(k_m l)}{\omega_m^2 \sqrt{(1-\eta_m^2)^2+(2\zeta_m \eta_m)^2}} \\[2ex] -m_{Piezo} h_{11}(x) \end{pmatrix} \qquad (6.119)$$

2. Second column of the admittance matrix **H**

$$\begin{pmatrix} h_{12}(x) \\ h_{22}(x) \\ h_{32}(x) \\ h_{42}(x) \end{pmatrix} = \begin{pmatrix} \frac{4}{l\mu} \sum\limits_{m=1}^{\infty} \frac{dX_m}{dx}(x)\, \frac{\alpha_F(k_m l)}{\omega_m^2 \sqrt{(1-\eta_m^2)^2+(2\zeta_m \eta_m)^2}} \\[2ex] \frac{4}{l\mu} \sum\limits_{m=1}^{\infty} X_m(x)\, \frac{\alpha_F(k_m l)}{\omega_m^2 \sqrt{(1-\eta_m^2)^2+(2\zeta_m \eta_m)^2}} \\[2ex] \frac{4w}{l\mu} \sum\limits_{m=1}^{\infty} \int\limits_0^x X_m(x')\, dx'\, \frac{\alpha_F(k_m l)}{\omega_m^2 \sqrt{(1-\eta_m^2)^2+(2\zeta_m \eta_m)^2}} \\[2ex] -m_{Piezo} h_{12}(x) \end{pmatrix} \qquad (6.120)$$

3. Third column of the admittance matrix $\mathbf{H}$

$$
\begin{pmatrix} h_{13}\left(x\right) \\[2mm] h_{23}\left(x\right) \\[2mm] h_{33}\left(x\right) \\[2mm] h_{43}\left(x\right) \end{pmatrix} = \begin{pmatrix} \frac{2w}{\mu}\sum\limits_{m=1}^{\infty}\frac{dX_m}{dx}\left(x\right)\frac{\alpha_p(k_m l)}{\omega_m^2 k_m l\sqrt{(1-\eta_m^2)^2+(2\zeta_m\eta_m)^2}} \\[4mm] \frac{2w}{\mu}\sum\limits_{m=1}^{\infty}X_m\left(x\right)\frac{\alpha_p(k_m l)}{\omega_m^2 k_m l\sqrt{(1-\eta_m^2)^2+(2\zeta_m\eta_m)^2}} \\[4mm] \frac{2w}{\mu}\sum\limits_{m=1}^{\infty}\int\limits_0^x X_m\left(x'\right)dx'\frac{\alpha_p(k_m l)}{\omega_m^2 k_m l\sqrt{(1-\eta_m^2)^2+(2\zeta_m\eta_m)^2}} \\[4mm] -m_{Piezo}h_{13}\left(x\right) \end{pmatrix}
$$

$$(6.121)$$

4. Fourth column of the admittance matrix $\mathbf{H}$

$$
\begin{pmatrix} h_{14}\left(x\right) \\[2mm] h_{24}\left(x\right) \\[2mm] h_{34}\left(x\right) \\[2mm] h_{44}\left(x\right) \end{pmatrix} = \begin{pmatrix} m_{Piezo}h_{11}\left(x\right) \\[2mm] m_{Piezo}h_{21}\left(x\right) \\[2mm] m_{Piezo}h_{31}\left(x\right) \\[2mm] m_{Piezo}h_{11}\left(x\right)+\sum\limits_{i=1}^{n}\frac{xw_i}{h_i}\left(\varepsilon_{33,i}^T-\frac{d_{31,i}^2}{s_{11,i}^E}\right) \end{pmatrix}
$$

$$(6.122)$$

7

Network Representation of Piezoelectric Multilayered Bending Actuators

Electromechanical systems consist of interacting electrical, mechanical and acoustic subsystems, that can be described on the basis of circuit representations within the scope of the network theory. By means of the network theory, the entire electromechanical system is characterized in terms of a common circuit representation of different subsystems including their interactions [133]. The systematic development of an electromechanical circuit representation for piezoelectric n-layered beam bending actuators within the scope of the network theory is the content of this chapter. At first, the term of an ideal rod as transducer for translatory and rotatory quantities is introduced providing a basis for fundamental considerations. Within the scope of the network theory, in a next step, the description is extended to the bending deformation of a homogeneous bar dependent on external mechanical quantities.

In order to achieve a description of the dynamic behavior, the mass of a differential beam segment as well as the frictional forces (in the sense of equivalent viscous damping) are taken into account. They allow for the determination of the necessary difference equations explaining the internal structure of the electromechanical circuit representation of a differential beam segment. The bending deformation of a homogeneous beam is described by an inhomogenous differential equation of fourth order in complex form. It can be achieved from the differential equation for flexural vibrations of a multilayered bending actuator by means of the separation ansatz already discussed in the previous chapter. On that base, the bending behavior of an n-layered bending actuator within the scope of the network theory follows. As a result, the beam is represented by a four-port network interconnecting the translatory and rotatory flow and difference quantities respectively. Since the multilayered system consists of piezoelectric layers, the driving of the individual active layers with an electrical voltage allows for an operational mode of the beam bender as an actuator. On the basis of the differential bending behavior of a multilayered actuator segment caused by a driving voltage, the general representation of the electromechanical interconnection of electrical and mechanical quantities results by means of a two-port network. The combination of the two-port

network with the four-port network results in the general electromechanical circuit representation of the piezoelectric multilayer beam bending actuator.

7.1 The Ideal Rod as Transducer for Translatory and Rotatory Quantities

In mechanical systems, quite often translatory motions are transformed into rotatory motions and vice versa. A very simple mechanism, that allows for this task, is the ideal lever with fixed fulcrum (see Fig. 7.1). If a velocity $\underline{v}$ affects the free lever's end, an angular velocity $\underline{\Omega}$ results from. The connection of a rotatory impedance results in a moment $\underline{M}$ and therefore in a force $\underline{F}$ at the free lever's end [134].
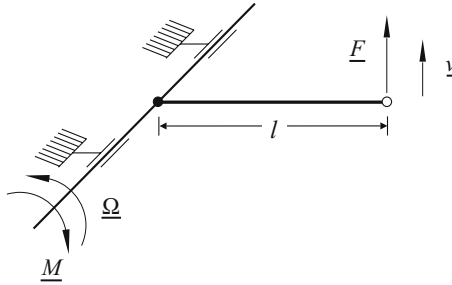
Fig. 7.1. One-sided supported rod as transducer for translatory and rotatory quantities

Small deflections $\left|\underline{\xi}\right| = \left|\frac{\underline{v}}{j\omega}\right| \ll l$ and thus, small angles are to be assumed resulting in the following linear relations:

$$\underline{\Omega} = \frac{\underline{v}}{l} \tag{7.1}$$

and

$$\underline{M} = \underline{F}l \tag{7.2}$$

The translatory and rotatory quantities are interconnected by a two-port network, that has the characteristics of an ideal transformer (see Fig. 7.2).

In the following the model is extended in such a manner, that both ends of the rod are affected by rotatory and translatory quantities. Thus, the previous two-port network is extended to a four-port network as shown in figure 7.3. This element was introduced as new basic element by *Schroth* [135] in conjunction with the analysis of flexural vibrations of rods [136].
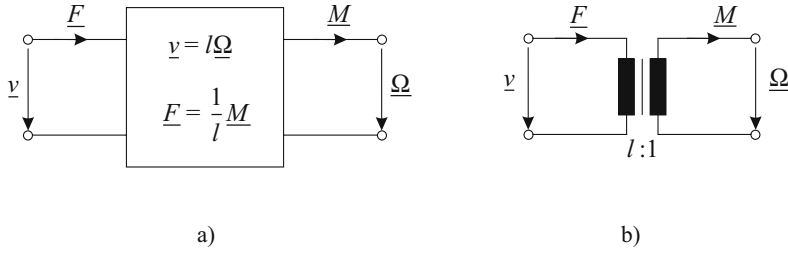
Fig. 7.2. The ideal rod as electromechanical system. - **(a)** two-port network representation; **(b)** ideal transformer
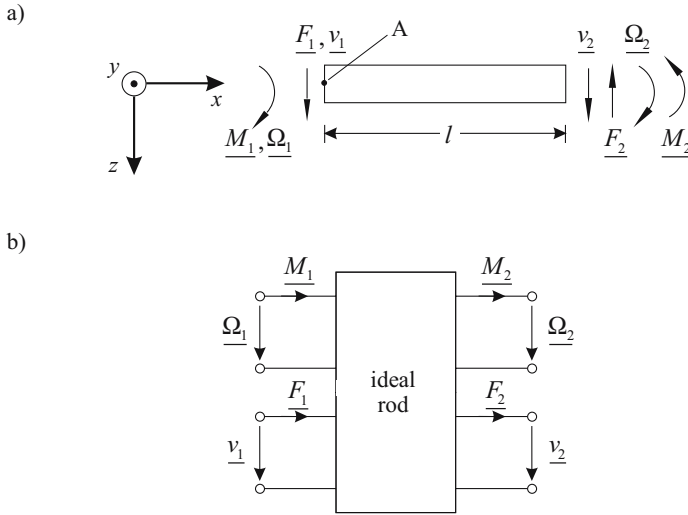
Fig. 7.3. Ideal rod. - **(a)** real arrangement; **(b)** four-port network

In the following, the internal structure of the four-port network is determined by means of kinematic and dynamic conditions.

1. dynamic condition/moment equilibrium around point A:

$$\sum_i \underline{M}_i = 0 \;\Rightarrow\; \underline{M}_1 - \underline{M}_2 - \underline{F}_2 l = 0 \qquad (7.3)$$

2. dynamic condition/force equilibrium:

$$\sum_i \underline{F}_i = 0 \;\Rightarrow\; \underline{F}_1 - \underline{F}_2 = 0 \qquad (7.4)$$

3. stiffness of rod/angular velocity:

$$\underline{\Omega}_1 = \underline{\Omega}_2 = \underline{\Omega} \tag{7.5}$$

4. translatory velocity:

$$\underline{v}_2 - \underline{v}_1 = \underline{\Omega}l \tag{7.6}$$

Taking (7.3) - (7.6) into account, the application of *Kirchhoff's laws* yields the four-port network representation of an ideal rod as shown in figure 7.4.
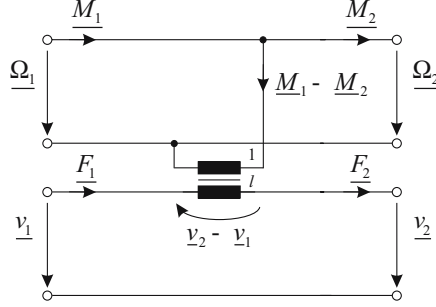
Fig. 7.4. Ideal rod - internal structure of the four-port network

On the basis of the achieved level of knowledge, the considerations are extended to the bending deformation of a homogeneous beam segment.

7.2 Bending of a Differential Beam Segment

In the following, the description of the bending deformation of bars is based on the Euler-Bernoulli hypothesis (see chapter 4.2). Furthermore, only torsional moments develop along the z-axis. Further, it is assumed that the beam length along the x-axis is large compared to the width along the y-axis. Additionally, only a mechanical stress component T_1, depending linearly on z, exists within the beam. In each point of the neutral axis position, the mechanical stress component T_1 results in $T_1 = 0$. Referred to the neutral axis position, a possible stress distribution dependent on the z-coordinate is shown in figure 7.5. The mechanical stress $T_1(z)$ results in

$$T_1(z) = \frac{T_1\left(\frac{h}{2}\right)}{\frac{h}{2}} z. \tag{7.7}$$

Taking equation (4.29) into account, the resulting moment yields in combination with (7.7)
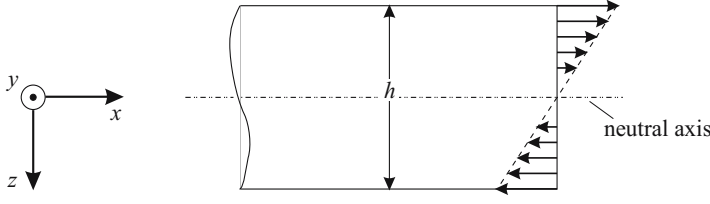
Fig. 7.5. Mechanical stress distribution within a homogeneous beam

$$M = \frac{T_1\left(\frac{h}{2}\right)}{\frac{h}{2}} \underbrace{\iint_A z^2 dA}_{(*)}. \tag{7.8}$$

The expression $(*)$ in (7.8) corresponds to the geometrical moment of inertia I_{yy} around the y-axis, thus it can be written:

$$M = \frac{T_1\left(\frac{h}{2}\right)}{\frac{h}{2}} I_{yy} \tag{7.9}$$

In combination with (4.16), the mechanical strain can be formulated by means of (7.7) as follows:

$$S_1\left(z\right) = \frac{s_{11} T_1\left(\frac{h}{2}\right)}{\frac{h}{2}} z = \frac{S_1\left(\frac{h}{2}\right)}{\frac{h}{2}} z \tag{7.10}$$

In figure 7.6, a differential beam segment of the length Δx in deformation state is illustrated.
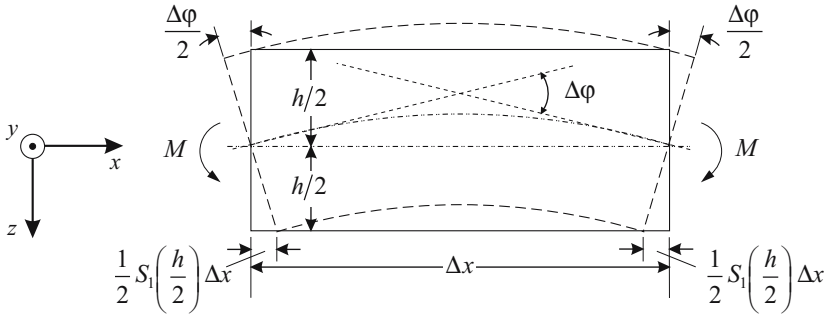
Fig. 7.6. Bending deformation of a differential beam segment

Due to the bending deformation of the differential beam segment according to figure 7.6, the entire change of length Δl at the position $z = h/2$ results in

$$\Delta l = S_1 \left(\frac{h}{2} \right) \Delta x. \tag{7.11}$$

Furthermore, the correlation between bending angle $\Delta\varphi$ and mechanical strain at position $z = h/2$ can be formulated as follows:

$$\Delta\varphi = \frac{S_1 \left(\frac{h}{2} \right) \Delta x}{\frac{h}{2}} \tag{7.12}$$

Concerning a beam segment of length Δx, (7.9) and (7.12) provide the correlation between angle difference $\Delta\varphi$ and moment M:

$$\frac{\Delta\varphi}{M} = \frac{S_1 \left(\frac{h}{2} \right) \Delta x}{T_1 \left(\frac{h}{2} \right) I_{yy}} \tag{7.13}$$

Taking the correlation between the mechanical stress T_1 and the mechanical strain S_1 into account (see eq. 7.10), (7.13) can be reformulated as follows:

$$\frac{\Delta\varphi}{M} = \frac{s_{11}\Delta x}{I_{yy}} = \frac{\Delta x}{EI} = \Delta n_R \tag{7.14}$$

The quantity Δn_R is called *torsional compliance*. Thus, the differential beam segment can be represented by a torsion spring with a torsional compliance Δn_R and by two ideal rods of the length $\Delta x/2$ each, as it is shown in figure 7.7.
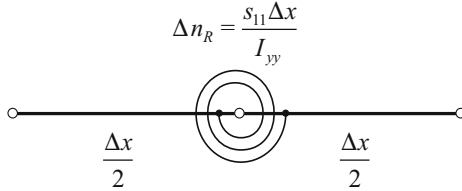
Fig. 7.7. Mechanical model of a differential beam segment

The quantity I_{yy}/s_{11} or EI refers to the flexural rigidity of a homogeneous beam and corresponds to the quantity C defined in equation (4.32), if the number of layers $i = 1$ is assumed. Since the flexural rigidity C in (4.32) is generally formulated for an n-layered beam bender, also the torsional compliance Δn_R can be defined for a multilayered beam bending structure. In order to allow for a universal application of the beam bender model, it is necessary to consider also forces affecting the bending segment along the z-direction in addition to the two moments in y-direction. Indeed, the arising

shear stress causes additional displacements, but due to the small transverse dimensions compared to the length of the beam segment ($w \ll \Delta x$), the additional displacements can be neglected. Assuming this fact, the validity of the model illustrated in figure 7.7 is ensured, even though both ends of the beam segment are affected by forces and moments [137, 138].

7.3 The Differential Beam Segment and Corresponding Correlations

The further modeling is effected on the basis of the mechanical model of a differential beam segment and the developed circuit representation of an ideal rod as transducer for translatory and rotatory quantities. In order to ensure a description of the dynamic behavior, the mass Δm of the differential bending segment and the friction Δr developing in real physical systems are considered. Further, the differential bending segment is affected by a load per unit length $\underline{f}(x)$ along the z-direction. The quantity $\underline{F}(x)$ represents the resulting force consisting of a concentrated force corresponding to the load per unit length and the frictional force affecting the segment at position x. Forces and moments affect both sides of the differential bending segment. Figure 7.8 illustrates the appropriate quantities.
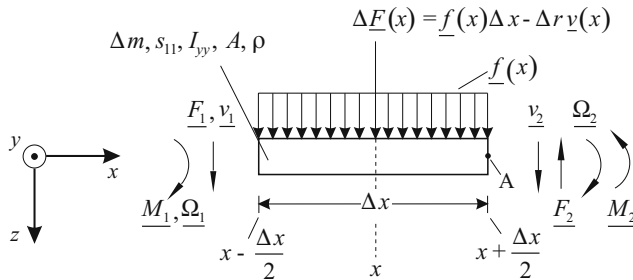
Fig. 7.8. Differential bending segment and consideration of its mass Δm, friction Δr and affecting load per unit length $\underline{f}(x)$

Since the mass Δm and the friction Δr are included into the considerations, the total mass of the bending segment and the affecting frictional force are assumed to be concentrated at position x. The structure of the differential bending segment of the length Δx consists of two ideal rods of the length $\Delta x/2$, that are connected by a moment-free joint and a torsion spring with the torsional compliance Δn_R. The mass and the friction are assumed to affect the joint. The resulting force corresponding to the load per unit length $\underline{f}(x)$ is considered by an additional force source. These considerations result in the

mechanical model of a differential bending segment for the dynamic case, as it is shown in figure 7.9.
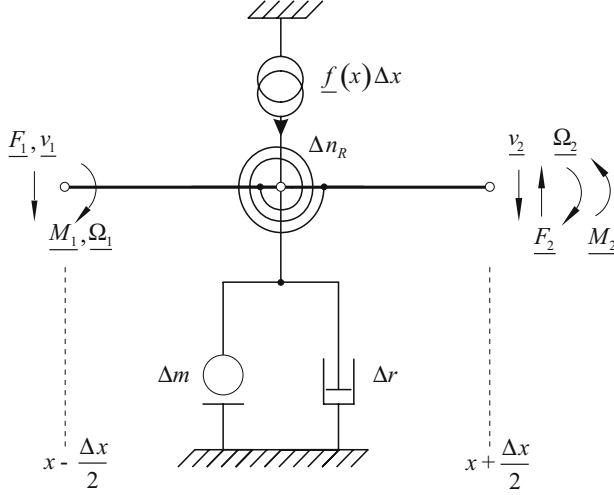
Fig. 7.9. Mechanical model of a bending segment for dynamic considerations

Now both, the general interconnecting equations and the structure of the electromechanical circuit can be derived from the differential bending segment, as it is shown in figure (7.8) and figure (7.9), respectively. Since in the following considerations always complex flow and difference quantities are used, it is necessary to dwell on the analogies between the mechanical quantities Δm, Δr and Δn_R and the corresponding electrical elements in more detail.

1. Mass Δm of a differential bending segment:
   With respect to Newton's second law, a force $\underline{F}$ and a mass element Δm are correlated according to

$$\underline{F} = \Delta m \underline{a}. \tag{7.15}$$

   $\underline{a}$ denotes the acceleration of the mass element Δm. Since the acceleration is equal to the first derivative of velocity $\underline{v}$ with respect to time, (7.15) can be reformulated in complex form:

$$\underline{F} = j\omega \Delta m \underline{v} \tag{7.16}$$

   The *mechanical admittance* $\underline{h}$, which corresponds to the *electrical impedance* $\underline{Z}$, results from the quotient of the difference quantity $\underline{v}$ and the flow quantity $\underline{F}$:

$$\underline{h} = \frac{\underline{v}}{\underline{F}} = \frac{1}{j\omega \Delta m} \tag{7.17}$$

Thus, the mass Δm in the mechanical network corresponds to a capacitance ΔC in the electrical network.

2. Coefficient of friction Δr of a differential bending segment:
The correlation between frictional force $\underline{F}_r$ and coefficient of friction Δr is described by

$$\underline{F}_r = \Delta r \underline{v}. \tag{7.18}$$

The quantity $\underline{v}$ denotes the velocity of the differential bending segment. The *mechanical admittance* $\underline{h}$ yields in accordance with (7.17)

$$\underline{h} = \frac{\underline{v}}{\underline{F}} = \frac{1}{\Delta r}. \tag{7.19}$$

The reciprocal value of the coefficient of friction Δr in the mechanical network corresponds to a resistance ΔR in the electrical network.

3. Torsional compliance Δn_R of a differential bending segment:
The torsional compliance Δn_R is defined by (7.14). The bending moment yields in complex representation

$$\underline{M} = \frac{\Delta \underline{\varphi}}{\Delta n_R}. \tag{7.20}$$

$\Delta \underline{\varphi}$ denotes the bending angle of the differential bending segment. Since the angular velocity $\Delta \underline{\Omega}$ corresponds to the first derivative of bending angle $\Delta \underline{\varphi}$ with respect to time, equation (7.20) can be reformulated as follows:

$$\underline{M} = \frac{\Delta \underline{\Omega}}{j\omega \Delta n_R} \tag{7.21}$$

The *mechanical admittance* $\underline{h}$ results from the quotient of the difference quantity $\Delta \underline{\Omega}$ and the flow quantity $\underline{M}$:

$$\underline{h} = \frac{\Delta \underline{\Omega}}{\underline{M}} = j\omega \Delta n_R \tag{7.22}$$

Thus, the torsional compliance Δn_R in the mechanical network corresponds to an inductance ΔL in the electrical network.

Concerning the translatory and rotatory flow and difference quantities shown in figure (7.8) and figure (7.9), respectively, following conventions are made:

$$\begin{array}{ll}
\underline{M}_1 = \underline{M}\left(x - \frac{\Delta x}{2}\right); & \underline{\Omega}_1 = \underline{\Omega}\left(x - \frac{\Delta x}{2}\right) \\
\underline{M}_2 = \underline{M}\left(x + \frac{\Delta x}{2}\right); & \underline{\Omega}_2 = \underline{\Omega}\left(x + \frac{\Delta x}{2}\right) \\
\\
\underline{F}_1 = \underline{F}\left(x - \frac{\Delta x}{2}\right); & \underline{v}_1 = \underline{v}\left(x - \frac{\Delta x}{2}\right) \\
\underline{F}_2 = \underline{F}\left(x + \frac{\Delta x}{2}\right); & \underline{v}_2 = \underline{v}\left(x + \frac{\Delta x}{2}\right)
\end{array} \tag{7.23}$$

In combination with the mechanical admittances defined in (7.17), (7.19) and (7.22), the general interconnecting equations can be derived describing the differential bending segment and the internal structure of the electromechanical circuit.

1. dynamic condition/force equilibrium:

$$\sum_i \underline{F}_i = j\omega \Delta m \underline{v}(x) \Rightarrow \underline{F}_1 - \underline{F}_2 + \Delta\underline{F}(x) = j\omega \Delta m \underline{v}(x) \qquad (7.24)$$

Taking (7.23) into account, (7.24) yields

$$\underline{F}\left(x - \frac{\Delta x}{2}\right) - \underline{F}\left(x + \frac{\Delta x}{2}\right) + \Delta\underline{F}(x) = j\omega \Delta m \underline{v}(x). \qquad (7.25)$$

2. dynamic condition/moment equilibrium around point A (see Fig. 7.8):

$$\sum_i \underline{M}_i = 0$$

$$\Rightarrow \underline{M}_2 - \underline{M}_1 + \underline{F}_1 \Delta x + [\Delta\underline{F}(x) - j\omega \Delta m \underline{v}(x)]\frac{\Delta x}{2} = 0 \qquad (7.26)$$

Insertion of the quantities in accordance with (7.23) and consideration of equation (7.25) results in the moment equilibrium around point A

$$\underline{M}\left(x - \frac{\Delta x}{2}\right) - \underline{M}\left(x + \frac{\Delta x}{2}\right) = \left[\underline{F}\left(x - \frac{\Delta x}{2}\right) + \underline{F}\left(x + \frac{\Delta x}{2}\right)\right]\frac{\Delta x}{2}. \qquad (7.27)$$

In accordance with figure 7.9 , the differential bending segment exists of two ideal rods of the length $\Delta x/2$ each, which are connected by a torsion spring providing a torsional compliance Δn_R. The knowledge of the internal four-port network structure of an ideal rod (see Fig. 7.4) and the consideration of the equations (7.22), (7.25) and (7.27) finally results in the internal four-port network structure of a differential bending segment for the dynamic case, as it is shown in figure 7.10.
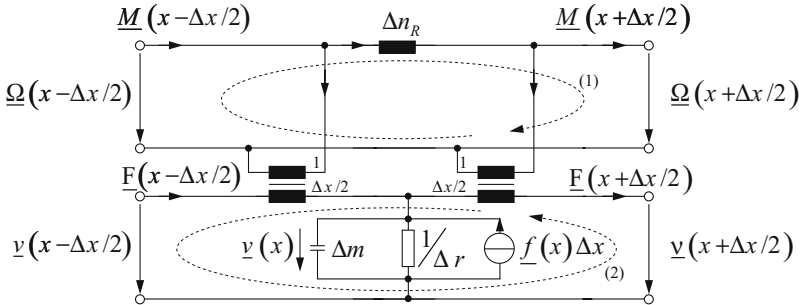
Fig. 7.10. Internal structure of the four-port network of a differential bending segment (dynamic case)

Further, the difference equations concerning the translatory and rotatory velocities $\underline{v}$ and $\underline{\Omega}$ can be derived by means of the internal structure of the four-port network.

Considering $\sum_i \underline{v}_i = 0$, mesh (1) yields:

$$j\omega \Delta n_R \left[\underline{M}\left(x - \frac{\Delta x}{2}\right) - \underline{F}\left(x - \frac{\Delta x}{2}\right) \frac{\Delta x}{2} \right] + \underline{\Omega}\left(x + \frac{\Delta x}{2}\right) = \underline{\Omega}\left(x - \frac{\Delta x}{2}\right) \tag{7.28}$$

Considering $\sum_i \underline{\Omega}_i = 0$, mesh (2) yields:

$$\underline{v}\left(x - \frac{\Delta x}{2}\right) - \underline{v}\left(x + \frac{\Delta x}{2}\right) = -\frac{\Delta x}{2} \left[\underline{\Omega}\left(x - \frac{\Delta x}{2}\right) + \underline{\Omega}\left(x + \frac{\Delta x}{2}\right) \right] \tag{7.29}$$

In combination with the difference equations (7.25), (7.27), (7.28) and (7.29), the complex differential equations can be derived by means of using the limit value. The explicit calculations are presented in appendix K.

In order to determine the differential equation in complex form, also (5.117) can be consulted. With the separation ansatz $\xi(x,t) = \underline{\xi}(x)\,e^{j\omega t}$ and the correlation $\underline{v} = j\omega\underline{\xi}$, the linear, inhomogenous differential equation of fourth order results in

$$\frac{d^4\underline{v}(x)}{dx^4} - \omega^2 \frac{\mu}{C}\underline{v}(x) + j\frac{\omega}{C}r_a\underline{v}(x) = j\frac{\omega}{C}\underline{f}(x). \tag{7.30}$$

7.4 Solution Approach to the Complex Equation of Flexural Vibrations

In order to be able to describe generally the interconnection between the difference quantities $(\underline{v}, \underline{\Omega})$ and the flow quantities $(\underline{F}, \underline{M})$, at first equation (7.30) is solved for a free undamped flexural vibration $(\underline{f}(x) = 0)$. It is supposed, that the flexural rigidity C remains constant over the entire length of the beam bender. Since the eigenfunctions and eigenmodes of the undamped flexural vibration are of interest, the coefficient of friction r_a is neglected at first [120, 121].

In order to determine a solution of the boundary and initial value problem, the separation ansatz

$$\underline{v}(x) = X(x)\,\underline{v} \tag{7.31}$$

is chosen, thus (7.30) can be reformulated according to

$$\frac{\partial^4 X(x)}{\partial x^4} - \frac{\omega^2 \mu}{C}X(x) = 0. \tag{7.32}$$

By analogy with (6.5), equation (7.32) can be formulated as follows:

$$\frac{\partial^4 X(x)}{\partial x^4} - k^4 X(x) = 0 \tag{7.33}$$

The quantity k denotes the wavenumber and has already been defined in (6.6).

The determination of the general solution of the homogeneous differential equation (7.33) results from the Laplace transform in accordance with (6.7) and (6.8) taking the derivative rule into consideration [123]. After following inverse transform, a general solution $X(x)$ is achieved. Furthermore, the first three derivatives of the general solution are evident for the general description. The solutions have already been determined in combination with the dynamic behavior of piezoelectric bending actuators. They can be extracted from (6.9) and (6.14) - (6.16).

The explicit solutions result from the appropriate kinematic boundary conditions of a beam bender. The respective characteristic equations of a beam bender result from the appropriate kinematic boundary conditions. Generally, the characteristic equations are not solvable in analytically closed form. A numerical computation of the appropriate characteristic equations results in m characteristic zeros $k_m l$, where $m = 1, 2, \ldots, \infty$ is valid. m corresponds physically to the appropriate natural propagationable mode X_m. On the basis of the superposition principle, the function $\underline{v}(x)$ yields as superposition of the propagationable modes X_m and the associated complex velocities $\underline{v}_m$ according to (7.31)

$$\underline{v}(x) = \sum_{m=1}^{\infty} X_m(x)\,\underline{v}_m. \tag{7.34}$$
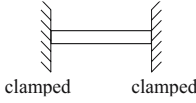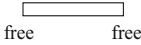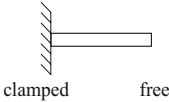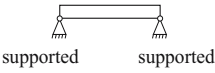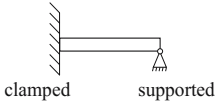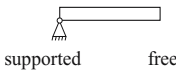
Within the scope of a general description, the usual clampings of a beam bender, the resulting boundary conditions and the appropriate characteristic equations are taken into consideration (see Table 7.1) [139, 140].
In order to implement the usual kinds of clamping of a beam bender (see tab. 7.1) in general form into the formulation of the general solution (7.34), the orthogonality conditions (linear independence) of different eigenmodes have to be considered according to the appropriate kind of clamping. An important result is, that the orthogonality of the eigenmodes is always provided, independent of the kind of clamping.

Thus, if the beam bender is subjected by an external load per unit length $\underline{f}(x)$, the general solution $\underline{v}(x)$ of the differential equation (7.30) can be formulated for arbitrary points x. The proof of the orthogonality of the eigenmodes with respect to the clamping conditions illustrated in Table 7.1 is explicitly presented in appendix L.

Table 7.1. Clampings and boundary conditions for transversal flexural vibrations of an Euler-Bernoulli beam

clamping	boundary conditions	characteristic equation
clamped — clamped	$X_m(0) = X_m(l) = 0$ $X'_m(0) = X'_m(l) = 0$	$\cosh(k_m l)\cos(k_m l) = 1$
free — free	$X''_m(0) = X''_m(l) = 0$ $X'''_m(0) = X'''_m(l) = 0$	$\cosh(k_m l)\cos(k_m l) = 1$
clamped — free	$X_m(0) = X'_m(0) = 0$ $X''_m(l) = X'''_m(l) = 0$	$\cosh(k_m l)\cos(k_m l) = -1$
supported — supported	$X_m(0) = X_m(l) = 0$ $X''_m(0) = X''_m(l) = 0$	$\sin(k_m l) = 0$
clamped — supported	$X_m(0) = X'_m(0) = 0$ $X_m(l) = X''_m(l) = 0$	$\tan(k_m l) - \tanh(k_m l) = 0$
supported — free	$X_m(0) = X''_m(0) = 0$ $X''_m(l) = X'''_m(l) = 0$	$\tan(k_m l) - \tanh(k_m l) = 0$

7.5 General Solution of the Equation for Flexural Vibrations

The inhomogenous differential equation (7.30) is the starting point of following considerations. In combination with (7.34), equation (7.30) can be rewritten in following form:

$$\sum_{m=1}^{\infty} \frac{d^4 X_m}{dx^4} \underline{v}_m - \omega^2 \frac{\mu}{C} \sum_{m=1}^{\infty} X_m \underline{v}_m + j\frac{\omega}{C} r_a \sum_{m=1}^{\infty} X_m \underline{v}_m = j\frac{\omega}{C}\underline{f}(x) \qquad (7.35)$$

Division by $j\frac{\omega}{C}$, multiplication on both sides of (7.35) with dx and X_m as well as integration with respect to the beam length l and following summation yields:

$$\sum_{m=1}^{\infty} \int_0^l \underline{f}(x) X_m dx = \frac{C}{j\omega} \sum_{m=1}^{\infty} \int_0^l \frac{d^4 X_m}{dx^4} X_m \underline{v}_m dx + j\omega\mu \sum_{m=1}^{\infty} \int_0^l X_m^2 \underline{v}_m dx$$

$$+ r_a \sum_{m=1}^{\infty} \int_0^l X_m^2 \underline{v}_m dx \tag{7.36}$$

Taking the orthogonality properties (6.45) and (6.46) into account yields

$$\frac{C\lambda_m}{j\omega} \underline{v}_m + j\omega\mu\underline{v}_m + r_a\underline{v}_m = \frac{\int_0^l \underline{f}(x) X_m dx}{\int_0^l X_m^2 dx}, \tag{7.37}$$

being valid for the mth mode. With the definition (6.32) for the quantity λ_m, equation (7.37) can be rewritten as follows:

$$\underline{v}_m \left[\frac{C(k_m l)^4}{j\omega l^4} + j\omega\mu + r_a \right] = \frac{\int_0^l \underline{f}(x) X_m dx}{\int_0^l X_m^2 dx} \tag{7.38}$$

7.5.1 Reference Values of a Multilayered Beam Bender

In order to achieve a representation of (7.38) within the scope of the network theory, the torsional compliance per unit length n_R' and the translatory reference compliance n_0 are introduced as reference values. Furthermore, the total mass $m = l\mu$ (5.92) and the coefficient of friction $r = r_a l$ (5.105) are also used as reference values.

1. Torsional compliance per unit length n_R':
   In combination with (7.14), the torsional compliance per unit length can be defined as follows:
   $$n_R' = \frac{dn_R}{dx} = \frac{1}{C} \tag{7.39}$$

2. Translatory reference compliance n_0:
   In combination with the torsional compliance per unit length n_R', the translatory reference compliance n_0 is defined as follows:
   $$n_0 = n_R' l^3 = \frac{l^3}{C} \tag{7.40}$$

In order to solve the equation for flexural vibrations within the scope of the network theory, in further considerations reference values are consulted.

7.6 Solution of the Equation of Flexural Vibrations by Means of Reference Values

By means of the defined reference values (5.92), (5.105) and (7.40), equation (7.38) can be reformulated as follows:

$$
\underline{v}_m \left[\frac{1}{j\omega \frac{n_0}{(k_m l)^4}} + j\omega m + r \right] = \frac{l \int_0^l \underline{f}(x) X_m dx}{\int_0^l X_m^2 dx}
\tag{7.41}
$$

The term in brackets on the left side of equation (7.41) shows an analogy to the mechanical impedance $\underline{z}$ of a spring-mass-damper system with one degree of freedom excited by a harmonic force $\underline{F}$ [141]. The mechanical scheme and the appropriate network representation of a spring-mass-damper system are shown in figure 7.11.
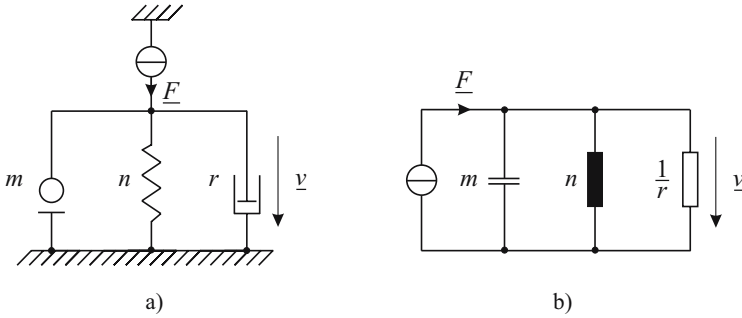
Fig. 7.11. Spring-mass-damper system with one degree of freedom as **(a)** mechanical scheme and **(b)** as electromechanical network representation

On the basis of equation (7.41), the general correlation between the difference quantities $(\underline{v}, \underline{\Omega})$ and the flow quantities $(\underline{F}, \underline{M})$ is derived in the following.

7.7 Admittance Matrix of a Beam Bender

In order to describe the beam bender as an electromechanical system within the scope of the network theory, the correlation between the difference quantities $(\underline{v}, \underline{\Omega})$ and the flow quantities $(\underline{F}, \underline{M})$ is represented by means of a matrix, that is referred to as admittance matrix $\underline{\mathbf{H}}$. The general matrix structure is shown in equation (7.42)

$$
\begin{pmatrix} \underline{v}_1 \\ \underline{\Omega}_1 \\ \underline{v}_2 \\ \underline{\Omega}_2 \end{pmatrix} = \underbrace{\begin{pmatrix} \underline{h}_{11} & \underline{h}_{12} & \underline{h}_{13} & \underline{h}_{14} \\ \underline{h}_{21} & \underline{h}_{22} & \underline{h}_{23} & \underline{h}_{24} \\ \underline{h}_{31} & \underline{h}_{32} & \underline{h}_{33} & \underline{h}_{34} \\ \underline{h}_{41} & \underline{h}_{42} & \underline{h}_{43} & \underline{h}_{44} \end{pmatrix}}_{\equiv \mathbf{H}} \begin{pmatrix} \underline{F}_1 \\ \underline{M}_1 \\ \underline{F}_2 \\ \underline{M}_2 \end{pmatrix}, \tag{7.42}
$$

where following boundary conditions are defined for the difference and flow quantities:

$$
\underline{v}(x)|_{x=0} = \underline{v}_1 \quad \wedge \quad \underline{v}(x)|_{x=l} = \underline{v}_2 \tag{7.43}
$$

$$
\underline{F}(x)|_{x=0} = \underline{F}_1 \quad \wedge \quad \underline{F}(x)|_{x=l} = \underline{F}_2 \tag{7.44}
$$

$$
\underline{\Omega}(x)|_{x=0} = \underline{\Omega}_1 \quad \wedge \quad \underline{\Omega}(x)|_{x=l} = \underline{\Omega}_2 \tag{7.45}
$$

$$
\underline{M}(x)|_{x=0} = \underline{M}_1 \quad \wedge \quad \underline{M}(x)|_{x=l} = \underline{M}_2 \tag{7.46}
$$

For a clearer representation of further calculations, the quantity $\beta_m(\omega)$ is defined:

$$
\frac{l}{\left(\frac{1}{j\omega \frac{n_0}{(k_m l)^4}} + j\omega m + r \right) \int_0^l X_m^2 dx} = \beta_m(\omega) \tag{7.47}
$$

Thus, (7.41) can be represented in more compact form:

$$
\underline{v}_m = \beta_m(\omega) \int_0^l \underline{f}(x) X_m dx \tag{7.48}
$$

7.7.1 Excitation by a Harmonic Force $\underline{F}_1$

By means of the *Dirac delta function* (6.64), the force $\underline{F}_1$ affecting the beam bender at position $x = 0$ can be formulated as load per unit length $\underline{f}(x)$:

$$
\underline{f}(x) = \underline{F}_1 \delta(x) \tag{7.49}
$$

Insertion of (7.49) into (7.48) yields

$$
\underline{v}_m = \underline{F}_1 X_m(0) \beta_m(\omega). \tag{7.50}
$$

In combination with the superposition principle (7.34), the general solution $\underline{v}(x)$ of the differential equation results in

$$\underline{v}(x) = \underline{F}_1 \sum_{m=1}^{\infty} X_m(x) X_m(0) \beta_m(\omega).\tag{7.51}$$

(7.51) yields in combination with (K.10) describing the correlation between the translatory velocity $\underline{v}(x)$ and the angular velocity $\underline{\Omega}(x)$:

$$\underline{\Omega}(x) = \underline{F}_1 \sum_{m=1}^{\infty} \frac{dX_m}{dx}(x) X_m(0) \beta_m(\omega)\tag{7.52}$$

With the boundary conditions defined in (7.43) and (7.45), the matrix elements $\underline{h}_{11}$, $\underline{h}_{21}$, $\underline{h}_{31}$ and $\underline{h}_{41}$ of the admittance matrix $\mathbf{H}$ can be derived:

$$\underline{h}_{11} = \sum_{m=1}^{\infty} X_m^2(0) \beta_m(\omega)\tag{7.53}$$

$$\underline{h}_{21} = \sum_{m=1}^{\infty} \frac{dX_m}{dx}(0) X_m(0) \beta_m(\omega)\tag{7.54}$$

$$\underline{h}_{31} = \sum_{m=1}^{\infty} X_m(l) X_m(0) \beta_m(\omega)\tag{7.55}$$

$$\underline{h}_{41} = \sum_{m=1}^{\infty} \frac{dX_m}{dx}(l) X_m(0) \beta_m(\omega)\tag{7.56}$$

7.7.2 Excitation by a Harmonic Force $\underline{F}_2$

By means of the *Dirac delta function* (6.64), the force $\underline{F}_2$ affecting the beam bender at position $x = l$ can be formulated as load per unit length $\underline{f}(x)$:

$$\underline{f}(x) = \underline{F}_2 \delta(x - l)\tag{7.57}$$

Insertion of (7.57) into equation (7.48) yields

$$\underline{v}_m = \underline{F}_2 X_m(l) \beta_m(\omega).\tag{7.58}$$

The general solution $\underline{v}(x)$ of the differential equation (7.33) results in

$$\underline{v}(x) = \underline{F}_2 \sum_{m=1}^{\infty} X_m(x) X_m(l) \beta_m(\omega).\tag{7.59}$$

Differentiation of the translatory velocity $\underline{v}(x)$ with respect to the length coordinate yields the angular velocity $\underline{\Omega}(x)$ dependent on the the exciting force $\underline{F}_2$:

$$\underline{\Omega}(x) = \underline{F}_2 \sum_{m=1}^{\infty} \frac{dX_m}{dx}(x) X_m(l) \beta_m(\omega) \tag{7.60}$$

With the boundary conditions defined in (7.43) and (7.45), the matrix elements $\underline{h}_{13}$, $\underline{h}_{23}$, $\underline{h}_{33}$ and $\underline{h}_{43}$ of the admittance matrix $\mathbf{H}$ can be derived:

$$\underline{h}_{13} = \sum_{m=1}^{\infty} X_m(0) X_m(l) \beta_m(\omega) \tag{7.61}$$

$$\underline{h}_{23} = \sum_{m=1}^{\infty} \frac{dX_m}{dx}(0) X_m(l) \beta_m(\omega) \tag{7.62}$$

$$\underline{h}_{33} = \sum_{m=1}^{\infty} X_m^2(l) \beta_m(\omega) \tag{7.63}$$

$$\underline{h}_{43} = -\sum_{m=1}^{\infty} \frac{dX_m}{dx}(l) X_m(l) \beta_m(\omega) \tag{7.64}$$

7.7.3 Excitation by a Harmonic Moment $\underline{M}_1$

By means of the derivative of the *Dirac delta function* (6.64), the moment $\underline{M}_1$ affecting the beam bender at position $x = 0$ can be formulated as load per unit length $\underline{f}(x)$:

$$\underline{f}(x) = \underline{M}_1 \frac{d\delta(x)}{dx} \tag{7.65}$$

Applying the differentiation theorem for the Dirac delta function (6.81), (7.48) results in:

$$\underline{v}_m = -\underline{M}_1 \frac{dX_m}{dx}(0) \beta_m(\omega) \tag{7.66}$$

The translatory velocity $\underline{v}(x)$ and the angular velocity $\underline{\Omega}(x)$ are calculated according to

$$\underline{v}(x) = -\underline{M}_1 \sum_{m=1}^{\infty} X_m(x) \frac{dX_m}{dx}(0) \beta_m(\omega) \tag{7.67}$$

and

$$\underline{\Omega}(x) = -\underline{M}_1 \sum_{m=1}^{\infty} \frac{dX_m}{dx}(x) \frac{dX_m}{dx}(0) \beta_m(\omega). \tag{7.68}$$

With the boundary conditions defined in (7.43) and (7.45), the matrix elements $\underline{h}_{12}$, $\underline{h}_{22}$, $\underline{h}_{32}$ and $\underline{h}_{42}$ of the admittance matrix $\mathbf{H}$ can be derived:

$$\underline{h}_{12} = -\sum_{m=1}^{\infty} X_m(0) \frac{dX_m}{dx}(0) \beta_m(\omega) \tag{7.69}$$

$$\underline{h}_{22} = -\sum_{m=1}^{\infty} \left[\frac{dX_m}{dx}(0)\right]^2 \beta_m(\omega) \tag{7.70}$$

$$\underline{h}_{32} = -\sum_{m=1}^{\infty} X_m(l) \frac{dX_m}{dx}(0) \beta_m(\omega) \tag{7.71}$$

$$\underline{h}_{42} = -\sum_{m=1}^{\infty} \frac{dX_m}{dx}(l) \frac{dX_m}{dx}(0) \beta_m(\omega) \tag{7.72}$$

7.7.4 Excitation by a Harmonic Moment $\underline{M}_2$

The moment $\underline{M}_2$ affecting the beam bender at position $x = l$ can be formulated as load per unit length $\underline{f}(x)$:

$$\underline{f}(x) = \underline{M}_2 \frac{d\delta(x-l)}{dx} \tag{7.73}$$

The application of the differentiation theorem for the Dirac delta function (6.81) yields the solution according to (7.48):

$$\underline{v}_m = -\underline{M}_1 \frac{dX_m}{dx}(l) \beta_m(\omega) \tag{7.74}$$

The translatory velocity $\underline{v}(x)$ and the angular velocity $\underline{\Omega}(x)$ are calculated according to

$$\underline{v}(x) = -\underline{M}_2 \sum_{m=1}^{\infty} X_m(x) \frac{dX_m}{dx}(l) \beta_m(\omega) \tag{7.75}$$

and

$$\underline{\Omega}(x) = -\underline{M}_2 \sum_{m=1}^{\infty} \frac{dX_m}{dx}(x) \frac{dX_m}{dx}(l) \beta_m(\omega). \tag{7.76}$$

With the boundary conditions defined in (7.43) and (7.45), the matrix elements $\underline{h}_{14}$, $\underline{h}_{24}$, $\underline{h}_{34}$ and $\underline{h}_{44}$ of the admittance matrix $\mathbf{H}$ can be derived:

$$\underline{h}_{14} = -\sum_{m=1}^{\infty} X_m(0) \frac{dX_m}{dx}(l) \beta_m(\omega) \tag{7.77}$$

$$\underline{h}_{24} = -\sum_{m=1}^{\infty} \frac{dX_m}{dx}(0) \frac{dX_m}{dx}(l) \beta_m(\omega) \tag{7.78}$$

$$\underline{h}_{34} = -\sum_{m=1}^{\infty} X_m(l) \frac{dX_m}{dx}(l) \beta_m(\omega) \tag{7.79}$$

$$\underline{h}_{44} = -\sum_{m=1}^{\infty} \left[\frac{dX_m}{dx}(l)\right]^2 \beta_m(\omega) \tag{7.80}$$

Thus, all matrix $\underline{h}_{ij}$ of the admittance matrix $\underline{\mathbf{H}}$ are defined. Since the individual elements $\underline{h}_{ij}$ include the translatory reference compliance n_0 and the solutions of the characteristic equation $k_m l$, which depend themselves on the flexural rigidity C (4.32) and the mass per unit length μ (5.92), the admittance matrix $\underline{\mathbf{H}}$ is also valid for n-layered beam benders. In order to be able to solve the matrix, the clamping conditions of a beam bender have to be defined. In combination with the general solution of the differential equation and its derivatives, the clamping conditions result in the appropriate characteristic equation. The solution of the appropriate characteristic equation results in the eigenmodes X_m of the beam bender. The interconnection between the difference and flow quantities according to equation (7.42) can be illustrated by means of a general four-port network representation, as it is shown in figure 7.12.
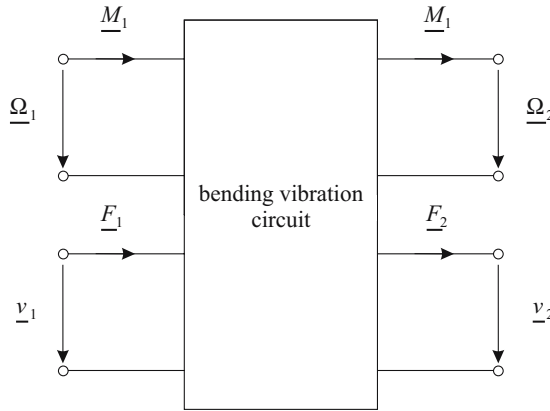
Fig. 7.12. Four-port network representation of a multilayered beam bender

In the following, the multilayered beam bender is assumed to consist of piezo-electric active layers. Further, the individual layers are connected in parallel. Thus, the actuatoric operation of the bending transducer is ensured. In combination with the achieved knowledge of a multilayered beam bender, in the next section, the mechanical system will be extended with respect to an electrical subsystem.

7.8 Transition to the Piezoelectric Multilayer Beam Bending Actuator

The piezoelectric multilayer beam bending actuator as shown in figure 4.5 is the starting point of the following considerations. It is evident, that only

a strain in x-direction would develop, if the system would be driven by a voltage $\underline{u}$. Thus, no rotatory motions are possible. If the layer 1 would be passive, an internal piezoelectric moment would be generated resulting in a bending deformation of the actuator. In order to ensure a general formulation, a segment of a piezoelectric multilayer beam bending actuator in deformation state is considered, as it is shown in figure 7.13.
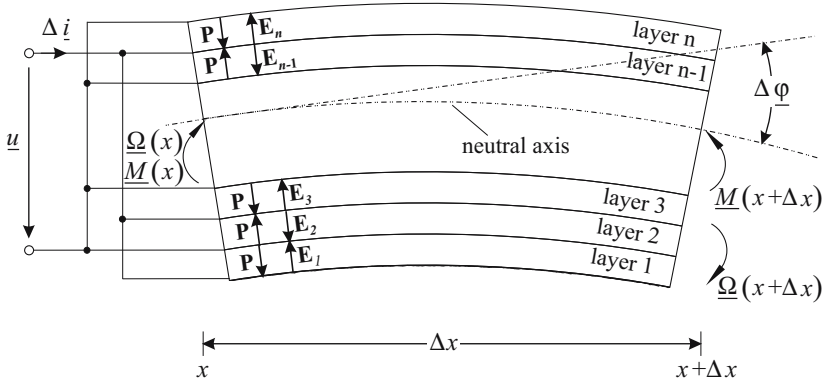
Fig. 7.13. Segment of a piezoelectric multilayer beam bending actuator

The equations of state (5.83) and (5.84) corresponding to the pair of variates $(\mathbf{S}, \mathbf{E})$, that must be satisfied in any point of the material of the piezoelectric multilayer actuator, provide a basis for the modeling. The equations are transformed in such a way, that the strain $\underline{S}_1$ and the electrical displacement $\underline{D}_3$ represent independent quantities. The electrical displacement is defined as follows (see also eq. 4.26):

$$\underline{D}_3 = \varepsilon_{33}^T \underline{E}_3 + d_{31} \underline{T}_1$$

Rearranging with respect to $\underline{E}_3$ results in

$$\underline{E}_3 = \frac{1}{\varepsilon_{33}^T} \underline{D}_3 - \frac{d_{31}}{\varepsilon_{33}^T} \underline{T}_1. \tag{7.81}$$

Insertion of (7.81) into (5.83) yields the mechanical stress

$$\underline{T}_1 = \frac{\varepsilon_{33}^T c_{11}^E}{\varepsilon_{33}^T - d_{31} e_{31}} \underline{S}_1 - \frac{e_{31}}{\varepsilon_{33}^T - d_{31} e_{31}} \underline{D}_3. \tag{7.82}$$

(7.82) can be reformulated in combination with (5.86) and (5.87) describing the correlation between the individual material parameters:

$$\underline{T}_1 = \frac{1}{s_{11}^E \left(1 - \frac{d_{31}^2}{s_{11}^E \varepsilon_{33}^T}\right)} \underline{S}_1 - \frac{d_{31}}{s_{11}^E \varepsilon_{33}^T \left(1 - \frac{d_{31}^2}{s_{11}^E \varepsilon_{33}^T}\right)} \underline{D}_3 \tag{7.83}$$

With the definition of the electromechanical coefficient of coupling

$$k_{31}^2 = \frac{d_{31}^2}{s_{11}^E \varepsilon_{33}^T}, \tag{7.84}$$

the mechanical stress results in

$$\underline{T}_1 = \frac{1}{s_{11}^E \left(1 - k_{31}^2\right)} \underline{S}_1 - \frac{k_{31}^2}{d_{31} \left(1 - k_{31}^2\right)} \underline{D}_3. \tag{7.85}$$

(5.84) is also transformed in such a way, that the strain $\underline{S}_1$ and the electrical displacement $\underline{D}_3$ respresent independent quantities:

$$\underline{E}_3 = -\frac{e_{31}}{\varepsilon_{33}^S} \underline{S}_1 + \frac{1}{\varepsilon_{33}^S} \underline{D}_3 \tag{7.86}$$

In combination with the definitions of the material parameters (5.87) and (5.88), it can finally be written:

$$\underline{E}_3 = -\frac{k_{31}^2}{d_{31} \left(1 - k_{31}^2\right)} \underline{S}_1 + \frac{1}{\varepsilon_{33}^T \left(1 - k_{31}^2\right)} \underline{D}_3 \tag{7.87}$$

In order to ensure the transition to the multilayered actuator, the mechanical stress $\underline{T}_1$ and the electric field $\underline{E}_3$ are defined for the ith layer according to (7.85) and (7.87):

$$\underline{T}_{1,i} = \frac{1}{s_{11,i}^E \left(1 - k_{31,i}^2\right)} \underline{S}_1 - \frac{k_{31,i}^2}{d_{31,i} \left(1 - k_{31,i}^2\right)} \underline{D}_{3,i} \tag{7.88}$$

$$\underline{E}_{3,i} = -\frac{k_{31,i}^2}{d_{31,i} \left(1 - k_{31,i}^2\right)} \underline{S}_1 + \frac{1}{\varepsilon_{33,i}^T \left(1 - k_{31,i}^2\right)} \underline{D}_{3,i} \tag{7.89}$$

In the equations (7.88) and (7.89), the quantities $\underline{T}_{1,i}$ and $\underline{S}_1$ are functions of the coordinate z, whereas $\underline{D}_{3,i}$ does not depend on z due to div $\mathbf{D} = 0$. By means of integration of (7.88) and (7.89) with respect to z, the transition to the integral quantities is achieved.

At first, the independent quantities $\underline{S}_1$ and $\underline{D}_{3,i}$ are rewritten. The strain $\underline{S}_1$ in complex form yields

$$\underline{S}_1 = -z \frac{\Delta\underline{\varphi}}{\Delta x} = -z \frac{\Delta\underline{\Omega}}{j\omega \Delta x} \tag{7.90}$$

according to (4.16). The electrical displacement $\underline{D}_{3,i}$ can be reformulated as follows:

$$\underline{D}_{3,i} = \frac{\Delta\underline{Q}_i}{\Delta A_i} \quad \text{with} \quad \Delta A_i = w_i \Delta x \tag{7.91}$$

Due to the parallel connection, the voltage $\underline{u}$ can be calculated for every individual active layer i:

$$\underline{u} = \int_{h_{i,u}}^{h_{i,o}} \underline{E}_{3,i}\,dz \tag{7.92}$$

Taking the strain (7.90) into account, the insertion of (7.89) into (7.92) and following integration yields the voltage $\underline{u}$:

$$\underline{u} = \frac{k_{31,i}^2 \left(h_{i,o}^2 - h_{i,u}^2\right)}{2d_{31,i}\left(1 - k_{31,i}^2\right)} \frac{\Delta\underline{\Omega}}{j\omega\Delta x} + \frac{h_i}{\varepsilon_{33,i}^T\left(1 - k_{31,i}^2\right)} D_{3,i} \tag{7.93}$$

Rearranging of (7.93) with respect to the electric displacement results in

$$D_{3,i} = -\frac{d_{31,i}\left(h_{i,o}^2 - h_{i,u}^2\right)}{2s_{11,i}^E h_i} \frac{\Delta\underline{\Omega}}{j\omega\Delta x} + \frac{\varepsilon_{33,i}^T\left(1 - k_{31,i}^2\right)}{h_i}\underline{u}. \tag{7.94}$$

Applying *Gauss' theorem*

$$\underline{D}_{3,i}\Delta A_i = \Delta Q_i \tag{7.95}$$

to (7.94) yields the charge within the ith layer. The total charge ΔQ results from the sum of charges within the individual layers:

$$\Delta Q = -\sum_{i=1}^{n} \frac{w_i d_{31,i}\left(h_{i,o}^2 - h_{i,u}^2\right)}{2s_{11,i}^E h_i} \frac{\Delta\underline{\Omega}}{j\omega} + \underline{u}\sum_{i=1}^{n} \frac{w_i\Delta x}{h_i}\varepsilon_{33,i}^T\left(1 - k_{31,i}^2\right) \tag{7.96}$$

With the definition of the current intensity

$$\underline{i} = \dot{\underline{Q}} = j\omega\underline{Q},$$

(7.96) can be formulated as follows:

$$\Delta\underline{i} = -\sum_{i=1}^{n} \frac{w_i d_{31,i}\left(h_{i,o}^2 - h_{i,u}^2\right)}{2s_{11,i}^E h_i}\Delta\underline{\Omega} + j\omega\left[\sum_{i=1}^{n} \frac{w_i\Delta x}{h_i}\varepsilon_{33,i}^T\left(1 - k_{31,i}^2\right)\right]\underline{u} \tag{7.97}$$

At this point it should be noted, that for the left term of equation (7.97) different signs of the piezoelectric constant have to be considered, depending on the orientation of the polarization vector $\mathbf{P}$ and the vector of the electric field $\mathbf{E}$ to each other. In case of an antiparallel orientation of $\mathbf{P}$ and $\mathbf{E}$, $d_{31} < 0$ has to be considered. If $\mathbf{P}$ and $\mathbf{E}$ are in parallel, $d_{31} > 0$ has to be considered. From (7.97), the *gyrator constant* $1/Y$ and the *translatory blocked capacitance* ΔC_b (capacitance in case of a non-bending deformation) result in

$$\frac{1}{Y} = -\sum_{i=1}^{n} \frac{w_i d_{31,i}\left(h_{i,o}^2 - h_{i,u}^2\right)}{2s_{11,i}^E h_i} \tag{7.98}$$

and

$$\Delta C_b = \sum_{i=1}^{n} \frac{w_i \Delta x}{h_i} \varepsilon_{33,i}^{T} \left(1 - k_{31,i}^{2}\right). \tag{7.99}$$

By means of equation (4.29), the bending moment $\underline{M}$ yields in combination with (7.88):

$$\underline{M} = \sum_{i=1}^{n} w_i \int_{h_{i,u}}^{h_{i,o}} \left[\frac{1}{s_{11,i}^{E} \left(1 - k_{31,i}^{2}\right)} \underline{S}_1 - \frac{k_{31,i}^{2}}{d_{31,i} \left(1 - k_{31,i}^{2}\right)} \underline{D}_{3,i} \right] z dz \tag{7.100}$$

In combination with (7.90), after integration equation (7.100) yields

$$\underline{M} = -\frac{1}{3} \sum_{i=1}^{n} \frac{w_i \left(h_{i,o}^{3} - h_{i,u}^{3}\right)}{s_{11,i}^{E} \left(1 - k_{31,i}^{2}\right)} \frac{\Delta \underline{\Omega}}{j\omega \Delta x} - \frac{1}{2} \sum_{i=1}^{n} \frac{k_{31,i}^{2} w_i \left(h_{i,o}^{2} - h_{i,u}^{2}\right)}{d_{31,i} \left(1 - k_{31,i}^{2}\right)} \underline{D}_{3,i}. \tag{7.101}$$

If the electrical displacement in (7.101) is replaced by (7.94), it can be written after some algebraic transformations:

$$\underline{M} = \left(\frac{1}{4} \sum_{i=1}^{n} \frac{w_i k_{31,i}^{2} \left(h_{i,o}^{2} - h_{i,u}^{2}\right)^{2}}{h_i s_{11,i}^{E} \left(1 - k_{31,i}^{2}\right)} - \frac{1}{3} \sum_{i=1}^{n} \frac{w_i \left(h_{i,o}^{3} - h_{i,u}^{3}\right)}{s_{11,i}^{E} \left(1 - k_{31,i}^{2}\right)} \right) \frac{\Delta \underline{\Omega}}{j\omega \Delta x}$$
$$- \frac{1}{2} \sum_{i=1}^{n} \frac{w_i d_{31,i} \left(h_{i,o}^{2} - h_{i,u}^{2}\right)}{s_{11,i}^{E} h_i} \underline{u}. \tag{7.102}$$

In addition to the gyrator constant (7.98), the rotatory short-circuit compliance Δn_{Rk} is achieved from (7.102):

$$\Delta n_{Rk} = \frac{\Delta x}{\frac{1}{4} \sum_{i=1}^{n} \frac{w_i k_{31,i}^{2} \left(h_{i,o}^{2} - h_{i,u}^{2}\right)^{2}}{h_i s_{11,i}^{E} \left(1 - k_{31,i}^{2}\right)} - \frac{1}{3} \sum_{i=1}^{n} \frac{w_i \left(h_{i,o}^{3} - h_{i,u}^{3}\right)}{s_{11,i}^{E} \left(1 - k_{31,i}^{2}\right)}} \tag{7.103}$$

Taking the gyrator constant (7.98), the translatory blocked capacitance (7.99) and the rotatory short-circuit compliance (7.103) into account and considering (7.97) and (7.102), a circuit representation in form of a conductance matrix is achieved [141, 142]:

$$\begin{pmatrix} \Delta \underline{i} \\ \underline{M} \end{pmatrix} = \begin{pmatrix} j\omega \Delta C_b & \frac{1}{Y} \\ \frac{1}{Y} & -\frac{1}{j\omega \Delta n_{Rk}} \end{pmatrix} \begin{pmatrix} \underline{u} \\ \Delta \underline{\Omega} \end{pmatrix} \tag{7.104}$$

The appropriate circuit representation of a piezoelectric bending segment can be immediately derived from the conductance matrix (7.104), as it is illustrated in figure 7.14.
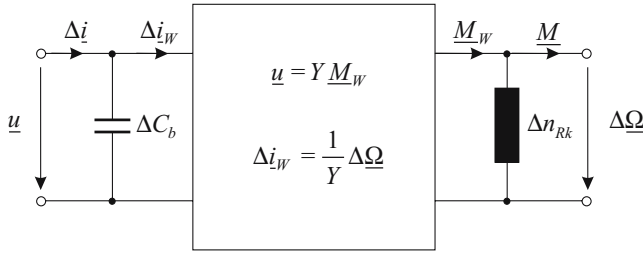
Fig. 7.14. Circuit representation of a piezoelectric bending segment

Since the transducer constant interconnects the mechanical flow and electrical difference quantities and vice versa, the interconnection is also called *gyrator* [143]. If the mechanical circuit representation of the multilayer bending segment according to figure 7.10 is supplemented with the circuit representation of a piezoelectric bending segment, the five-port network representation of a complete piezoelectric multilayered beam segment is achieved, as it is shown in figure 7.15 [5].
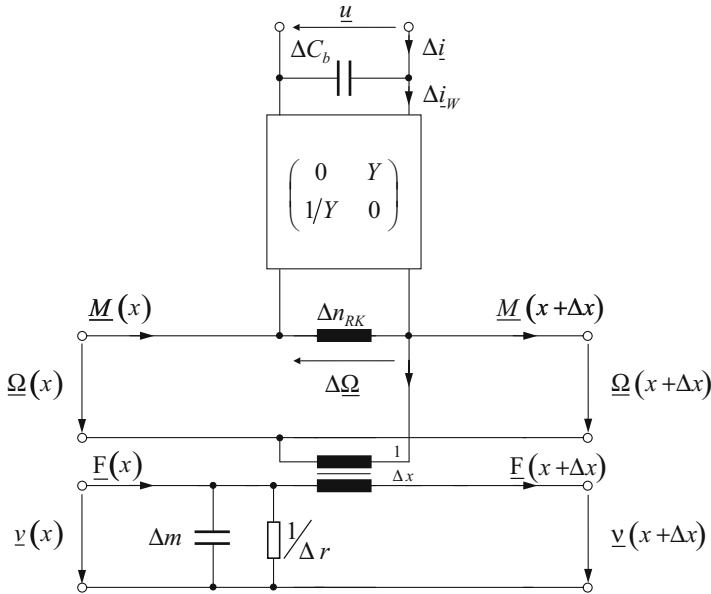
Fig. 7.15. Five-port network representation of a piezoelectric multilayered segment

The difference to the mechanical circuit representation of a multilayer bending segment consisting only of *passive layers* exists in the formulation of the *rotatory short-circuit compliance* Δn_{Rk} (7.103) and the *torsional compliance* Δn_R (7.14). If all layers of the multilayered segment do not have piezoelectric characteristics, the short-circuit compliance Δn_{Rk} is equal to the torsional compliance Δn_R due to $d_{31,i} = 0$ for all $i = 1 \ldots n$. According to the definition of the reference value of the torsional compliance per unit length n'_R (7.39), the flexural rigidity C_k of a segment consisting of piezoelectric layers can be defined by means of the short-circuit compliance per unit length n'_{Rk}:

$$n'_{Rk} = \frac{dn_{Rk}}{dx} = \frac{1}{C_k} \tag{7.105}$$

By connecting the electrical clamps in parallel and by connecting the mechanical four-ports in series, the mechanical five-port network respresentation of the entire beam bending actuator is achieved (see Fig. 7.16).
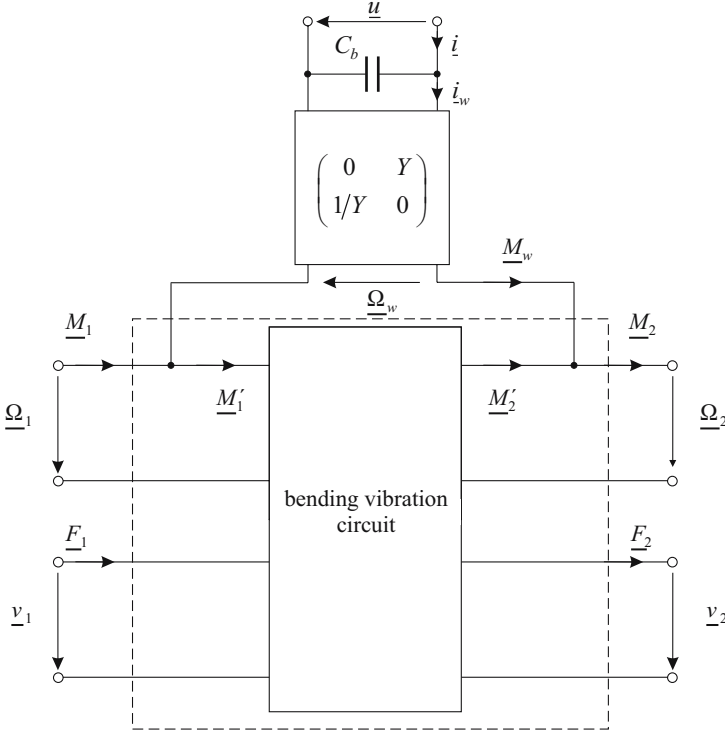
Fig. 7.16. Five-port network representation of the entire beam bending actuator

For the bending vibration circuit with the pairs of clamps $\left(\underline{\Omega}_1, \underline{M}_1'\right)$, $\left(\underline{\Omega}_2, \underline{M}_2'\right)$ and $\left(\underline{v}_1, \underline{F}_1\right)$, $\left(\underline{v}_2, \underline{F}_2\right)$, the admittance matrix $\underline{\mathbf{H}}$ determined in (7.42) is valid, if the moments $\underline{M}_1$, $\underline{M}_2$ are replaced by $\underline{M}_1'$, $\underline{M}_2'$. The following correlations have to be considered:

$$\underline{\Omega}_w = \underline{\Omega}_2 - \underline{\Omega}_1 \tag{7.106}$$

$$\underline{M}_1' = \underline{M}_1 - \underline{M}_w \tag{7.107}$$

$$\underline{M}_2' = \underline{M}_2 - \underline{M}_w \tag{7.108}$$

With the achieved knowledge, in the following section, the electromechanical circuit representation of a *clamped-free* piezoelectric multilayer beam bending actuator will be derived.

7.9 The Clamped-Free Piezoelectric Multimorph

Taking the correlations (7.106) - (7.108) into account, the admittance matrix $\underline{\mathbf{H}}$ is the starting point of further considerations.

$$\begin{pmatrix} \underline{v}_1 \\ \underline{\Omega}_1 \\ \underline{v}_2 \\ \underline{\Omega}_w + \underline{\Omega}_1 \end{pmatrix} = \begin{pmatrix} \underline{h}_{11} & \underline{h}_{12} & \underline{h}_{13} & \underline{h}_{14} \\ \underline{h}_{21} & \underline{h}_{22} & \underline{h}_{23} & \underline{h}_{24} \\ \underline{h}_{31} & \underline{h}_{32} & \underline{h}_{33} & \underline{h}_{34} \\ \underline{h}_{41} & \underline{h}_{42} & \underline{h}_{43} & \underline{h}_{44} \end{pmatrix} \begin{pmatrix} \underline{F}_1 \\ \underline{M}_1 - \underline{M}_w \\ \underline{F}_2 \\ \underline{M}_2 - \underline{M}_w \end{pmatrix} \tag{7.109}$$

In order to determine propagationable modes X_m, the necessary boundary conditions of a clamped-free beam bending actuator listed in Table 7.1 have to be considered:

$$X_m(0) = X_m'(0) = 0 \tag{7.110}$$

$$X_m''(l) = X_m'''(l) = 0 \tag{7.111}$$

The resulting characteristic equation $\cosh\left(k_m l\right) \cos\left(k_m l\right) = -1$ results in the propagationable modes X_m with respect to (6.29):

$$X_m\left(x\right) = \tilde{c}\left(k_m x\right) - \tilde{s}\left(k_m x\right) \frac{\tilde{C}\left(k_m l\right)}{\tilde{S}\left(k_m l\right)} \tag{7.112}$$

With the knowledge of the propagationable eigenmodes of a clamped-free beam bending actuator, all elements $\underline{h}_{ij}$ of the admittance matrix $\underline{\mathbf{H}}$ can
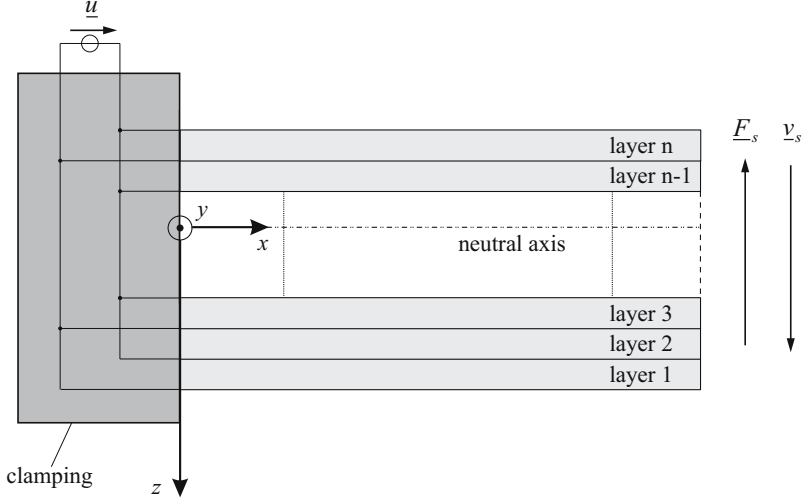
Fig. 7.17. Piezoelectric bending actuator generating mechanical kinetic quantities

be determined explicitly. Since the transducer in the present representation generates mechanical kinetic quantities (see Fig. 7.17), the velocities and forces appearing at the actuator's tip are provided with the index s.

There are no external bending moments affecting the bender's tip ($\underline{M}_2 = 0$). The actuator is driven by a harmonic voltage $\underline{u}$, thus the matrix equation (7.109) can be simplified as follows:

$$\begin{pmatrix} 0 \\ 0 \\ \underline{v}_s \\ \underline{\Omega}_w \end{pmatrix} = \begin{pmatrix} 0 & 0 & 0 & 0 \\ 0 & 0 & 0 & 0 \\ 0 & 0 & \underline{h}_{33} & \underline{h}_{34} \\ 0 & 0 & \underline{h}_{43} & \underline{h}_{44} \end{pmatrix} \begin{pmatrix} \underline{F}_1 \\ \underline{M}_1 - \underline{M}_w \\ \underline{F}_s \\ -\underline{M}_w \end{pmatrix} \tag{7.113}$$

Figure 7.18 illustrates the five-port network reduced to a two-port network **A**.

In combination with the admittance matrix (7.113), the translatory velocity $\underline{v}_s$ and the angular velocity $\underline{\Omega}_w$ can be formulated in dependence of the flow quantities $\underline{F}_s$ and $\underline{M}_w$:

$$\underline{v}_s = \underline{h}_{33}\underline{F}_s - \underline{h}_{34}\underline{M}_w \tag{7.114}$$

$$\underline{\Omega}_w = \underline{h}_{43}\underline{F}_s - \underline{h}_{44}\underline{M}_w \tag{7.115}$$

a)

b)
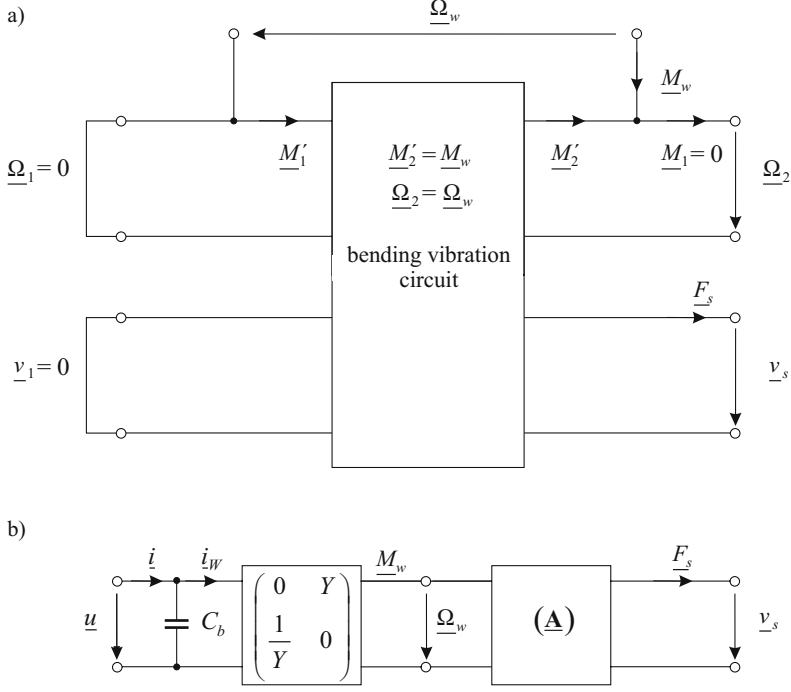
Fig. 7.18. Clamped-free piezoelectric bending actuator. - **(a)** appropriate five-port network representation; **(b)** reduced representation consisting of a piezoelectric transducer and a two-port network ($\underline{\mathbf{A}}$)

After some calculations, the coefficients of the associated two-port network $\underline{\mathbf{A}}$ according to the following matrix equation

$$\begin{pmatrix} \underline{\Omega}_w \\ \underline{M}_w \end{pmatrix} = \begin{pmatrix} \underline{A}_{11} & \underline{A}_{12} \\ \underline{A}_{21} & \underline{A}_{22} \end{pmatrix} \begin{pmatrix} \underline{v}_s \\ \underline{F}_s \end{pmatrix}$$

are achieved in combination with (7.114) and (7.115). The matrix $\underline{\mathbf{A}}$ results in

$$A = \begin{pmatrix} \frac{h_{44}}{h_{34}} & h_{43} - \frac{h_{44}h_{33}}{h_{34}} \\ -\frac{1}{h_{34}} & \frac{h_{33}}{h_{34}} \end{pmatrix}. \tag{7.116}$$

According to figure 7.19, the circuit representation of the two-port network $\underline{\mathbf{A}}$ results from a varied circuit representation with the admittances $\underline{h}_1$ and $\underline{h}_2$ [142].

$$\begin{pmatrix} \underline{A}_{11} & \underline{A}_{12} \\ \underline{A}_{21} & \underline{A}_{22} \end{pmatrix} \quad = \quad \begin{pmatrix} \dfrac{1}{q} & 0 \\ 0 & q \end{pmatrix} \begin{pmatrix} 1 & \underline{h}_2 \\ \dfrac{1}{\underline{h}_1} & 1+\dfrac{\underline{h}_2}{\underline{h}_1} \end{pmatrix}$$
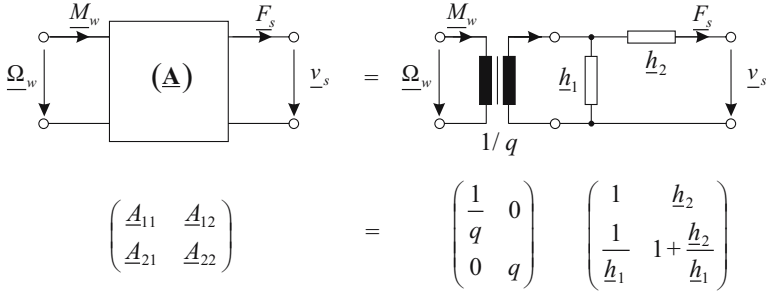
Fig. 7.19. Circuit representation of the mechanical partial two-port network of a piezoelectric bending actuator and the corresponding matrix notation

In combination with (7.116), the transformation ratio q and the admittances $\underline{h}_1$ and $\underline{h}_2$ can be extracted from the circuit representation of the mechanical two-port network (see Fig. 7.19). Matrix multiplication and coefficient comparison yields:

$$q = \frac{\underline{h}_{34}}{\underline{h}_{44}} \tag{7.117}$$

$$\underline{h}_1 = -\frac{\underline{h}_{34}^2}{\underline{h}_{44}} \tag{7.118}$$

$$\underline{h}_2 = \frac{\underline{h}_{34}\underline{h}_{43}}{\underline{h}_{44}} - \underline{h}_{33} \tag{7.119}$$

In the following, the piezoelectric bending actuator is assumed to be exposed to very small external loads, thus the admittance $\underline{h}_2$ can be neglected. In accordance with figure 7.18 b, the reduced two-port network representation of the piezoelectric bending actuator shows the structure illustrated in figure 7.20.
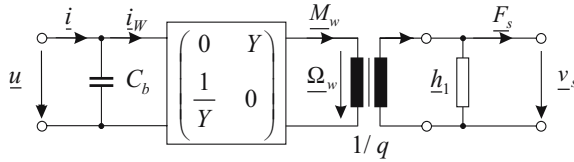
Fig. 7.20. Electromechanical circuit representation of a piezoelectric bending actuator taking the transformation behaviour of rotatory and translatory quantities into consideration

The correlation between the electrical pair of quantities $(\underline{u}, \underline{i}_w)$ and the mechanical pair of quantities $(\underline{v}_s, \underline{F}_s)$ can be derived from the series connection of the gyrator and the mechanical partial two-port network. The gyrator with the gyrator constant Y as well as the transformer with the transformation ratio $1/q$ are combined to a new gyrator $\mathbf{Y}'$ with following structure:

$$\mathbf{Y}' = \begin{pmatrix} 0 & qY \\ \frac{1}{qY} & 0 \end{pmatrix} \tag{7.120}$$

Taking the gyrator matrix (7.120) into account, the electrical and mechanical translatory quantities can be interconnected according to

$$\begin{pmatrix} \underline{u} \\ \underline{i}_w \end{pmatrix} = \begin{pmatrix} 0 & qY \\ \frac{1}{qY} & 0 \end{pmatrix} \begin{pmatrix} 1 & 0 \\ \frac{1}{\underline{h}_1} & 1 \end{pmatrix} \begin{pmatrix} \underline{v}_s \\ \underline{F}_s \end{pmatrix}. \tag{7.121}$$

The matrix equation (7.121) corresponds to the circuit representation of a clamped-free piezoelectric beam bending actuator, as it is shown in figure 7.21.
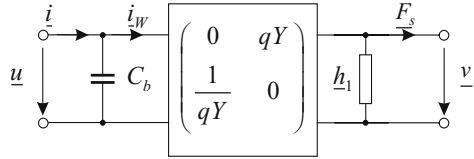
Fig. 7.21. General circuit representation of a clamped-free piezoelectric beam bending actuator affected by small external loads ($\underline{h}_2 = 0$)

By means of the general circuit representation, important knowledge can be achieved concerning the transient characteristics of an n-layered piezoelectric beam bending actuator. At first, the electromechanical circuit representation and the corresponding transfer function of a piezoelectric bending actuator are derived with respect to the fundamental mode. Taking the higher modes into consideration, the circuit representation is extended afterwards. This kind of consideration finally results in the *canonical circuit representation of a piezoelectric multilayered actuator*.

7.9.1 Circuit Representation of a Piezoelectric Multimorph with Respect to the Fundamental Mode

In order to achieve a circuit representation of a clamped-free piezoelectric multilayer beam bending actuator, it is necessary to calculate the admittance

h_1 for the fundamental mode X_1 (see Fig. 7.21) according to equation (7.118). With the definition of the elements h_{34} (7.79) and h_{44} (7.80) of the admittance matrix $\mathbf{H}$ (7.113), from equation (7.118) the admittance h_1 yields with respect to the fundamental mode X_1:

$$h_1 = \frac{X_1^2(l)\left[\frac{dX_1}{dx}(l)\right]^2 \beta_1^2(\omega)}{\left[\frac{dX_1}{dx}(l)\right]^2 \beta_1(\omega)} = X_1^2(l)\beta_1(\omega) \qquad (7.122)$$

Using the definition (7.47) for the quantity $\beta_m(\omega)$, (7.122) can be reformulated:

$$h_1 = \frac{X_1^2(l)}{\left(\frac{1}{j\omega \frac{n_0}{(k_1 l)^4}} + j\omega m + r\right)\int_0^l X_1^2 dx} \qquad (7.123)$$

As it can be shown after some algebraic calculations, for a clamped-free beam bending actuator following equations are valid:

$$X_1^2(l) = 1 \qquad (7.124)$$

and

$$\int_0^l X_1^2 dx = \frac{l}{4} \qquad (7.125)$$

Thus, the admittance h_1 of a piezoelectric bending actuator can be formulated with respect to the fundamental mode as follows:

$$h_1 = \frac{1}{\left(\frac{1}{j\omega \frac{4n_0}{(k_1 l)^4}} + j\omega\frac{m}{4} + \frac{r}{4}\right)} \qquad (7.126)$$

In combination with the general circuit representation of a piezoelectric beam bending actuator illustrated in figure 7.21, the circuit representation valid for the fundamental mode X_1 can be inferred from equation (7.126) (see Fig. 7.22).
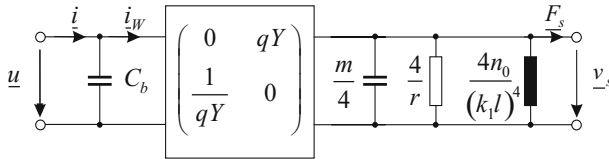
Fig. 7.22. Circuit representation of a piezoelectric bending actuator with respect to the fundamental mode

The circuit representation illustrated in figure 7.22 shows, that 1/4 of the total mass m of the actuator can be assumed to be concentrated at its tip. Also,

$1/4$ of the friction r affecting the bender over its entire length effect on the concentrated mass. With $k_1 l = 1.875$, the translatory reference compliance yields approximately $\frac{1}{3} n_0$. n_0 corresponds to the static reference compliance, which can be determined according to (7.40).

In the next step, the electrical side is transformed to the mechanical side. Since the two-port network in figure 7.22 represents a gyrator, the translatory blocked capacitance C_b on the electrical side corresponds to a compliance n_C on the mechanical side [143]. If it is further assumed, that the electrical driving is done by means of a voltage source, then the voltage source corresponds to a force source after transformation to the mechanical side. If the actuator's tip can perform unhindered motions ($\underline{F}_s = 0$), then following circuit representation is achieved (see Fig. 7.23).

In the figure:

$$F = \frac{u}{qY}$$

$$n_C = C_b Y^2$$
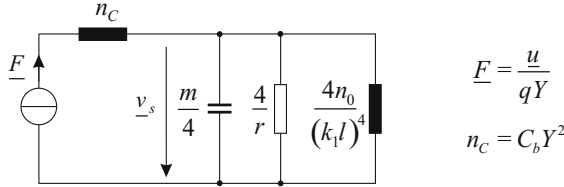
Fig. 7.23. Circuit representation of a piezoelectric beam bending actuator after transformation to the mechanical side

If the actuator is subjected to a harmonic voltage $\underline{u}$, the dynamic behavior can be described by calculation of the frequency response of deflection $\underline{\xi}$. For this, the general correlation

$$\underline{v}_s = \underline{h}_1 \underline{F} \tag{7.127}$$

is considered. In combination with the force $\underline{F}$ formulated in figure 7.23 and with the correlation $\underline{v}_s = j\omega\underline{\xi}$, it can be written

$$j\omega\frac{\underline{\xi}}{\underline{u}} = \frac{\underline{h}_1}{qY} = \frac{1}{qY\,\underline{z}_1}. \tag{7.128}$$

In order to calculate the frequency response, the mechanical impedance $\underline{z}_1$ of the parallel connection consisting of mass, friction and compliance as shown in figure 7.23 is determined. For an easier calculation, following abbreviations are introduced:

$$m^* = \frac{m}{4} \tag{7.129}$$

$$\frac{1}{r^*} = \frac{4}{r} \tag{7.130}$$

$$n^* = \frac{4n_0}{(k_1 l)^4} \tag{7.131}$$

The mechanical impedance results in

$$\underline{z}_1 = \frac{1}{j\omega n^*} \left(1 - \omega^2 m^* n^* + j\omega n^* r^*\right). \tag{7.132}$$

In combination with the natural frequency ω_1 (resonance frequency)

$$\omega_1 = \frac{1}{\sqrt{m^* n^*}} \tag{7.133}$$

and the quality factor Q_1 with respect to the fundamental mode X_1

$$\frac{1}{Q_1} = \omega_1 n^* r^*, \tag{7.134}$$

the impedance $\underline{z}_1$ can be specified in standardized form

$$\underline{z}_1 = \frac{1}{j\omega n^*} \left(1 - \left(\frac{\omega}{\omega_1}\right)^2 + j\frac{\omega}{\omega_1}\frac{1}{Q_1}\right). \tag{7.135}$$

Insertion of (7.135) into (7.128) yields the frequency response of deflection

$$\frac{\underline{\xi}}{\underline{u}} = \frac{n^*}{qY\left(1 - \left(\frac{\omega}{\omega_1}\right)^2 + j\frac{\omega}{\omega_1}\frac{1}{Q_1}\right)}. \tag{7.136}$$

Equation (7.136) corresponds to a lowpass with resonance peak (see. Fig. 7.24) [144].
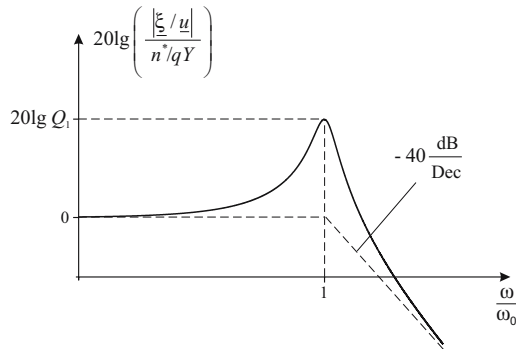
Fig. 7.24. Frequency response of deflection $\underline{\xi}$ caused by a harmonic driving voltage $\underline{u}$

Thus, the deflection characteristics of piezoelectric bending actuators in the fundamental mode can be described as vibrating PT_2-element. In figure 7.24, the frequency response of deflection is illustrated in logarithmic scale. Thus, it is necessary to standardize the ordinate as a dimensionless quantity.

7.9.2 Canonical Circuit Representation of a Piezoelectric Multimorph

In order to achieve a general circuit representation of a piezoelectric multi-layer beam bending actuator taking modes of higher order into account, the definition of the mechanical admittance $\underline{h}_1$ (7.118) is considered. By means of the transformation ratio $1/q$ according to (7.117) and in combination with the definition of the matrix element $\underline{h}_{34}$ according to (7.79), the admittance $\underline{h}_1$ can be reformulated:

$$\underline{h}_1 = -q\underline{h}_{34} = q \sum_{m=1}^{\infty} X_m\left(l\right) \frac{dX_m}{dx}\left(l\right) \beta_m\left(\omega\right) \tag{7.137}$$

Within the scope of the network theory, the sum notation in (7.137) corresponds to a series connection of spring-mass-damper elements connected in parallel resulting in the canonical circuit representation of a piezoelectric multilayer beam bending actuator, as it is illustrated in figure 7.25.
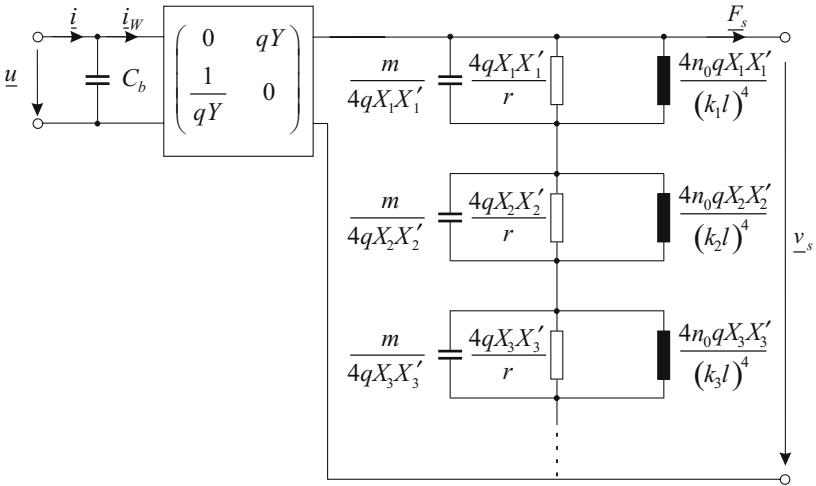
Fig. 7.25. Canonical circuit representation of a piezoelectric multilayer beam bending actuator

By analogy with figure 7.23, in the next step the electrical side is transformed to the mechanical side. In combination with (7.127), the translatory velocity

$\underline{v}_s$ yields with respect to equation (7.137)

$$\underline{v}_s = \frac{\underline{u}}{Y} \sum_{m=1}^{\infty} X_m (l) \frac{dX_m}{dx} (l) \beta_m (\omega) . \tag{7.138}$$

The transformation ratio $1/q$ is not found anymore. If the bending actuator can perform unhindered motions, the circuit representation illustrated in figure 7.26 is achieved.
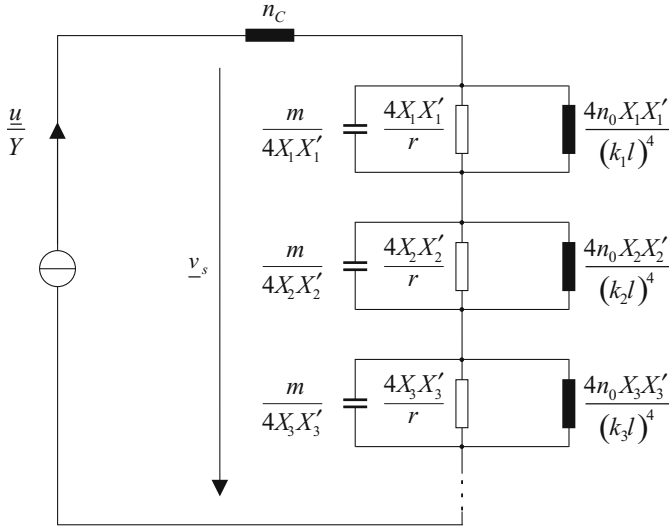
Fig. 7.26. Canonical circuit representation of a piezoelectric multilayer beam bending actuator after transformation to the mechanical side

The expression of the mechanical admittance (7.137) can further be simplified. The respective eigenfunctions X_m and their derivatives X'_m of the clamped-free beam bender according to (7.112) are evaluated at position $x = l$. The computational results are listed in Table 7.2 with respect to the first four eigenmodes.

By means of Table 7.2, the conclusion can be drawn, that for modes of second and higher order following approximation can be made:

$$X_m (l) X'_m (l) \approx k_m \quad \forall m \geq 2 \tag{7.139}$$

and

$$(2m - 1) \frac{\pi}{2} \approx k_m l \quad \forall m \geq 2 \tag{7.140}$$

Table 7.2. Eigenfunction computations with respect to the first four eigenmodes

m	$k_m l$	$X_m(l)$	$X'_m(l)$	$\|X_m(l)\,X'_m(l)\|$
1	1.8751	0.999997	$0.734096k_m$	$0.734093k_m$
2	4.6941	-1.00001	$-1.01847k_m$	$1.01848k_m$
3	7.8548	1.00004	$0.999224k_m$	$0.999267k_m$
4	10.9955	-0.999959	$-1.00003k_m$	$0.999993k_m$

Thus, the admittance $\underline{h}_1$ can be formulated as

$$\underline{h}_1 = qX_1(l)\,X'_1(l)\,\beta_1(\omega) + q\sum_{m=2}^{\infty} \frac{(k_m l)}{l}\beta_m(\omega) \qquad (7.141)$$

or

$$\underline{h}_1 = qX_1(l)\,X'_1(l)\,\beta_1(\omega) + q\sum_{m=2}^{\infty} \frac{(2m-1)\,\pi}{2l}\beta_m(\omega), \qquad (7.142)$$

where the expression $k_m l$ denotes the solutions of the characteristic equation of a clamped-free beam bending actuator. The equations (7.141) and (7.142) allow for minimizing the calculations of the mechanical admittance.

**Measurement Setup and Validation of
Theoretical Aspects**

8

Measurement Setup for Piezoelectric Beam Bending Actuators

For the experimental characterization of piezoelectric bending actuators, a measurement setup has been realized, that will be described in detail in the following chapter. In addition to the description of the measurement setup functionality, it is dwelled on the individual measuring tasks and their experimental realization. In order to arrange the operation of the measurement setup and the respective measuring tasks as effective and simple as possible, a concept for measurement setup automation was elaborated and realized. With the help of the measurement setup, the developed theoretical models and the forecasted statements concerning the static and dynamic behavior of piezoelectric bending actuators can be verified experimentally.

8.1 Measurement Setup

In order to characterize piezoelectric beam bending actuators, the measurement setup as shown in figure 8.1 has been developed and realized [145].
In order to ensure a preferably ideal fixed clamping, the bending actuator is fixed by a rigid restraint. By means of two contact pins integrated into the clamping device, an electrical driving of the actuator is ensured. The top ends of the contact pins have crown-like tips, that foraminate the parasitic oxide films of the bender's copper contact pads, if the bending actuator is clamped. Thus, an electrical contact is always ensured. The contact pins are elastically supported within themselves.

The deflection in z-direction is measured by a high-precision laser triangulator system (Micro Epsilon, type: ILD 2200). The measurement range amounts to 2 mm with a resolution of 0.1 μm. The lower measurement range limit amounts to 24 mm, the upper measurement range limit amounts to 26 mm. The measurement signal of the laser triangulator is used as external reference for deflection measurements of the bending actuator. The laser triangulation belongs to the optical distance measurement methods and is characterized
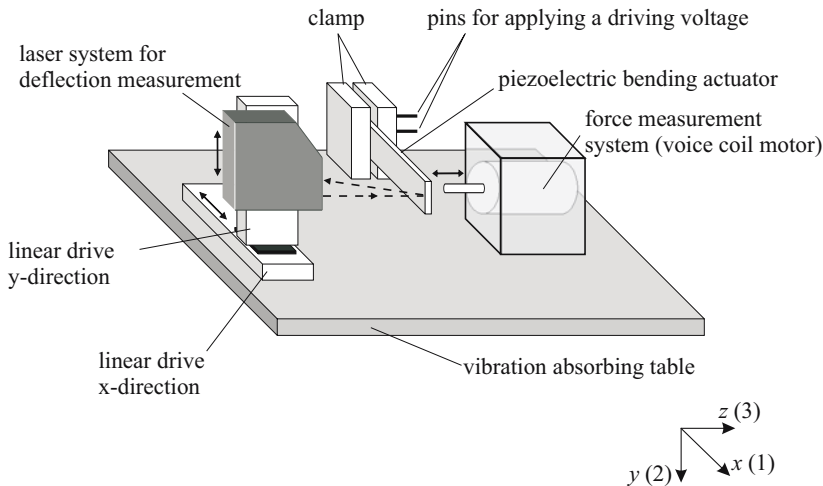
Fig. 8.1. Measurement setup for the experimental characterization of piezoelectric beam bending actuators

by its non-reactive and non-contact properties. The basic structure of a laser triangulator is illustrated in figure 8.2.
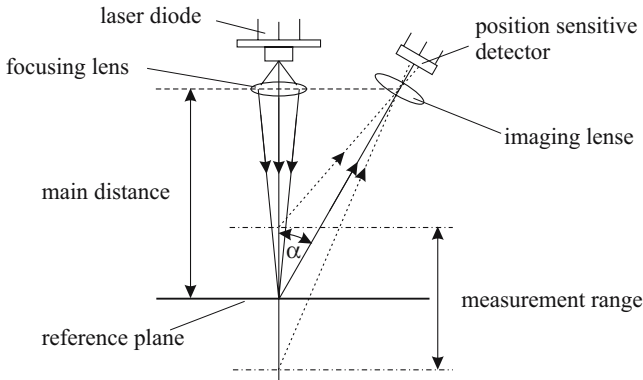
Fig. 8.2. Basic structure of a laser triangulator

By means of a focusing lens, the object, whose distance to the sensor is to be measured, is punctually lit by a light source (laser diode, helium-neon gas laser). By means of an imaging lens, the light spot is mapped into the detector plane with respect to an angle α. However, the triangulation method

will only be applicable, if the light is scattered by the object surface and a part of the scattered light reaches the detector. The position-sensitive detector provides a signal dependent on the position of the mapped light spot, that is a measure for the distance between object surface and sensor [146]. PSDs (Position Sensitive Diodes) or CCDs (Charge Coupled Devices) are used as detectors.

In order to measure at different positions on the surface of the bending actuator, the triangulator can be moved along the x- and y-direction (see Fig. 8.1). The movement is realized by means of two linear drives (MFN series, Newport GmbH), which are characterized by a high resolution and repeat accuracy. The triangulator is attached to the linear drive in y-direction, which is attached itself on the linear drive in x-direction. The moving range of the linear drive in x-direction amounts to 15 mm, the moving range of the linear drive in y-direction amounts to 8 mm. The maximum positioning speed of both linear drives amounts to 0.3 mm/s with respect to maximum position accuracy of 0.055 μm. The smallest moving range amounts to 0.2 μm. The two linear drives are driven by means of a separate controller unit (Newport, type: ESP300). Thus, it is possible to read out and to adjust speeds and positions as absolut and as relative value, respectively.

With the compensating method, forces generated by the bending actuator can be measured by means of a high-accuracy force measurement system (voice coil motor) as shown in figure 8.3.
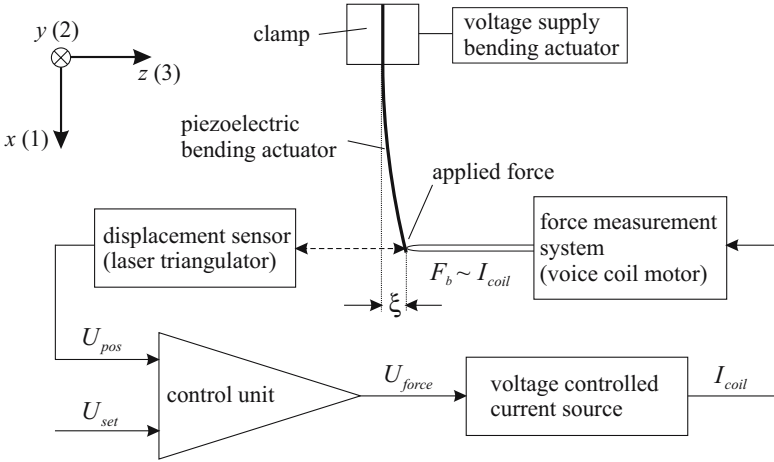
Fig. 8.3. Force measurement principle applied to piezoelectric bending actuators

The force F_b generated by the bending actuator affects a stylus being directly connected with the force measurement system. The force generator provides a force proportional to the quantity F_b to be measured, if it is addressed by a control unit followed by a voltage-controlled current source in such a manner, that the force to be measured is compensated. In order to achieve this, the control unit receives a distance-proportional voltage signal U_{pos} from the laser triangulator detecting the actuator's deflection in z-direction. The distance-proportional voltage signal U_{pos} is compared with a reference U_{set} providing an arbitrary distance, the force compensation is effected. The output of the control unit represents a force signal U_{force} driving the voltage-controlled current source.

The voice coil motor, used as force measurement system, represents a linear electrodynamic actuator consisting of two mechanical main components being movable against each other. The field component consists of a permanent magnet and an iron housing generating a strong, homogeneous magnetic field within a narrow air gap. The coil body, which can move within the air gap, forms the second component of the voice coil motor. The basic structure is illustrated in figure 8.4.
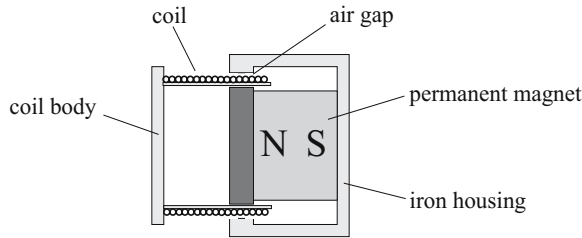
Fig. 8.4. Basic structure of a voice coil motor

If the voice coil motor is driven by a current, a proportional force can be applied to the beam bending actuator. The used voice coil motor (Densitron, type: VM 2671-180) provides a linear operational range of 4 mm with a maximum actuator force of 4 N. By means of a voltage-controlled current source, especially developed for voice coil engines (Mechatronic Systems, Switzerland, type: PowerOTA), the force can be measured with a resolution of 1 mN.

In order to avoid external parasitic vibrations, e.g. building oscillations, the total measurement setup is mounted on a passive vibration absorbing table. In order to exclude temperature effects affecting the measurements, the total measurement setup is placed in an air-conditioned area operating at a constant temperature of 21 °C and a relative air humidity of 50%.

8.2 Automation of Measurement Setup

In order to arrange the operation of the measurement setup and the respective measuring tasks as effective and simple as possible, a concept for measurement setup automation was elaborated and realized [147]. In order to provide the automation, the individual components of the measurement setup like sensors (laser triangulator, capacitive and inductive sensors for tip deflection measurements integrated on the bending actuator) and actuators (piezoelectric bending actuator, linear drives, voice coil motor), are coordinated over interfaces of a measuring system by means of the automation software LabVIEW$^{®}$. Also components, such as function generator, voltage-controlled current source and controller unit, necessary for the control of the sensors and actuators, are coordinated by the appropriate interfaces of the measuring system. The conceptual structure of the measurement setup automation is shown in figure 8.5.
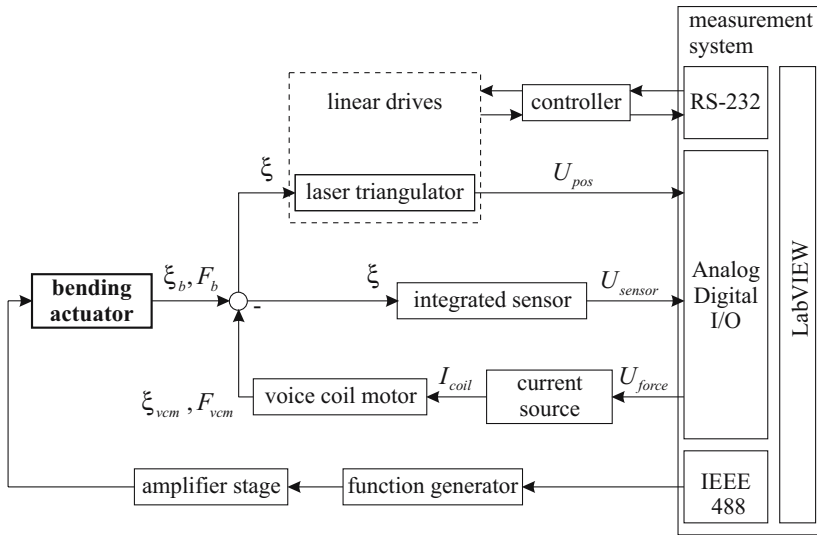
Fig. 8.5. Conceptual structure of an automated measurement setup for piezoelectric bending actuators

An I/O board (analog and digital), a GPIB board (IEEE 488) and a RS-232-interface are used as interfaces. The arrangement and administration of the measuring data as well as their storage in the necessary data format are taken on by LabVIEW$^{®}$. The data analysis is effected with the scientific data analysis software ORIGIN$^{®}$. The advantages of this software tool are on the one hand the large variety of analysis tools, on the other the easy handling of

large data sets limited only by hard disk capacity and main memory of the measuring system.

8.2.1 Stabilization of the Beam Bending Actuator

If the bending actuator is fixed by the clamping, mechanical stresses arise within the bending transducer resulting from the constriction of the gripping jaws. The reduction of the mechanical stresses is achieved by a transient oscillation. The bending actuator is sinusoidally driven (approx. 2 Hz) by a function generator (type: HP 8116 A) followed by an amplifier (Physik Instrumente, type: P-863) resulting in a periodical bending motion of the actuator. Subjecting the individual piezoelectric layers of the bending actuator by a positive voltage has to be provided. Otherwise, tensile stresses ($T > 0$) develop within the individual layers, that cause an irreversible damage of the piezoceramics resulting in a performance loss of the bending actuator. Thus, the alternating voltage is superposed by an offset voltage U_0 corresponding to the amplitude of the alternating voltage (see Fig. 8.6).
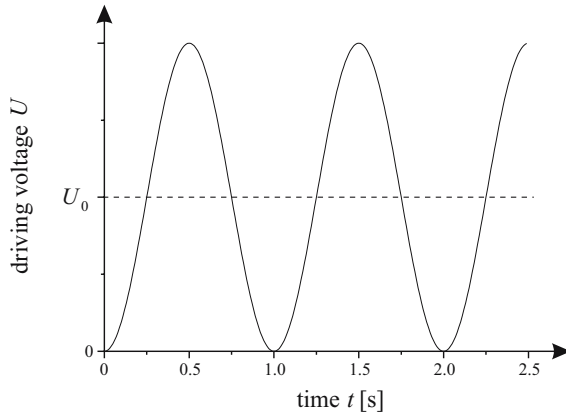
Fig. 8.6. Driving voltage characteristics during transient oscillation

Further, the hysteresis of a piezoelectric bending actuator necessitates a transient oscillation (see Fig. 8.7). After the first deflection of the bending actuator (curve $A - B$), a remanent deflection $\xi \neq 0$ remains, although the driving voltage is equal to zero (curve $B - C$). This is caused by the fact, that only a certain part of domains switches within the ceramics (see Fig. 2.7). In further considerations, the remanent deflection is referred to as reference zero point of deflection ξ. After the transient oscillation, the hysteresis proceeds between the points $B - C$.
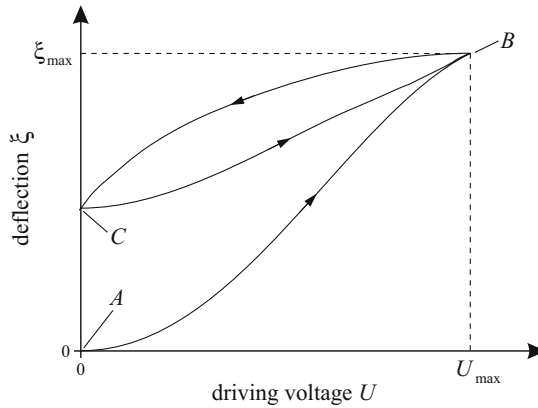
Fig. 8.7. Deflection of a piezoelectric bending actuator during transient oscillation

8.2.2 Electrical Actuation of the Bending Actuator

The control of the piezoelectric bending actuator is provided by both, the external function generator and the I/O board. The function generator is addressed by means of a GPIB board (IEEE 488). In LabVIEW the parameter transfer is realized by means of a VISA protocol (<u>V</u>irtual <u>I</u>nstrument <u>S</u>ystem <u>A</u>rchitecture). Thus, it is possible to transfer parameters such as voltage amplitude, offset voltage, frequency and signal shape (e.g. sine signal, square wave signal), that are necessary for the setting of the function generator. The I/O board possesses two analog outputs. The voltage of each output can be adjusted within a range from $-10\,\text{V}$ to $+10\,\text{V}$ with respect to a resolution of 16 bits. The amplification of the output voltage of the function generator and of the I/O board by the following amplifier amounts approx. 10.2. Thus, a voltage range from $0\,\text{V}$ to $92\,\text{V}$ is provided, that is necessary for the control of the bending actuator.

8.2.3 Deflection Measurement by Means of Triangulation

The used laser triangulator consists of a laser-optical sensor and a controller. The position-sensitive detector consists of a CCD element, which determines the intensity of the diffuse reflection of the modulated light spot on the bending actuator surface in real time. Thus, the sensor has the ability to compensate intensity fluctuations during the measurement data acquisition. The following secondary electronics generates a voltage U_{pos} proportional to the measured deflection ξ. Due to the measurement range from $0\,\text{mm}$ to $2\,\text{mm}$ and a corresponding analog output signal from $0\,\text{V}$ to $+10\,\text{V}$, the transfer coefficient amounts $B = 200\,\mu\text{m/V}$. The analog output signal of the secondary electronics is measured by one of the analog inputs of the I/O board. In LabVIEW, the output signal is multiplied by the transfer coefficient B, thus the

achieved measuring data directly correspond to the deflection of the bending actuator.

8.2.4 Control of the Linear Stages

The control of the linear drives is realized by a controller unit, which is connected with the RS-232 interface of the measuring system. The program modules, that are necessary for communication over the RS-232 interface, are implemented in LabVIEW. The commands being necessary for addressing the controller are provided by the manufacturer in form of a special ASCII syntax. The syntax consists of the number of axis (linear drive) to be controlled, the command to be processed and command-specific values (see Fig. 8.8).

syntax   xx   PA   nn

    number of axis (e.g. 1)

    command (e.g. moving to an absolute position)

    specific value (e.g. 10 mm)
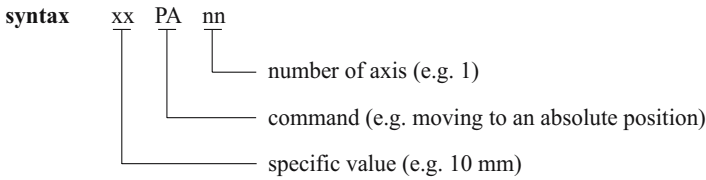
Fig. 8.8. Command syntax for addressing the linear drives' controller unit

In order to allow for the movement of the linear drives for the individual measuring tasks, the commands for enabling (MO = engine on) and disabling (MF = engine off) of the drives, for setting the velocity (VA = set velocity), for setting the target position (Pa = move to absolute position) and for the actual position monitoring (TP = read actual position) are necessary.
If the linear drives are disabled after reaching the target position, an inadvertent adjustment of the measuring position at the control panel of the controller unit is avoided during the measurement. Since the controller needs a certain time for processing the command of the position monitoring, within the program structure a queue time between sending the command and reading out the position value is considered. The experimentally determined queue time amounts to 20 ms. Due to the position data processing time required by LabVIEW and due to the control of other components of the measurement setup, the distance between the individual measuring points yields approx. $2\,\mu$m resulting in 10000 measuring points for a moving distance of 20 mm.

8.2.5 Control of the Voice-Coil-Motor

In order to control the voice coil motor, a voltage-controlled current source operating within a range from -1 A to $+1$ A with a dissolution of 1 mA is used. The control of the current source is effected by a second analog output

of the I/O board. The transfer coefficient of the current source amounts to $B_{S1} = 100\,\text{mA/V}$. Due to the high resolution of the analog output, the current I can be varied in steps of $1\,\text{mA}$. With the monitor output of the current source, the current I, that is proportional to the generated force, can be determined. By means of an analog input of the I/O board, the monitor output voltage is also measured. The transfer coefficient of the monitor output amounts to $B_{S2} = 100\,\text{mA/V}$. Multiplication by the transfer coefficient B_{S2} yields the current I and thus the proportional force F_{vcm} generated by the voice coil motor.

9

Measurements and Analytical Calculations

In the following chapter, different measuring tasks concerning the characterization of the static and dynamic behavior of a clamped-free piezoelectric bending actuator are described in detail. The analytical description of the static and dynamic behavior of piezoelectric multilayer beam bending actuators achieved before is applied to a realized bending actuator. The experimental results are compared to analytical calculations.

9.1 Used Multilayer Beam Bending Structure for Experimental Investigations

For experimental investigations, a monomorph piezoceramic bending transducer in multilayer technology is used, as it is shown in figure 2.13. The bender consists of five active piezoelectric PZT-layers, which are connected in parallel by internal AgPd-electrodes. The piezoceramics is combined with a passive elastic layer system consisting of a carrier and a thermal adjustment layer. Further, the bending actuator consists of a slipping component at its tip, thus deflections and forces caused by bending deformations can be passed on external mechanics.

The used piezoceramics is based on the mass system M 1832 of the company Argillon GmbH and belongs to the class of high-performance single layer ceramics. It is characterized by a piezoelectric constant $d_{33} > 1000\,\text{pm/V}$ in combination with an electric field of $1.0\,\text{kV/mm}$. The thermal adjustment layer provides a compensation of the different thermal coefficients of expansion of the materials, the bending actuator consists of. The thermal adjustment layer consists of a Ni-based alloy ($NiCo$ 2918). The carrier of the bending transducer consists of a unidirectional S2-glassfiber compound [148].

Usually, the electrodes are mutually interconnected, thus an alternating polarity of neighboring layers is ensured (piezoceramic layers connected in parallel). The individual piezoceramic layers are actuated in such a way, that *internal* mechanical tensile stresses T are formed resulting in compressive strains S of

the individual active layers. The cross-sectional structure of the used bending actuator as well as the electrical driving of the individual piezoelectric layers and their polarization directions are illustrated in figure 9.1. The layer sequence as well as the geometrical and material specific parameters of the individual layers, which are necessary for the analytical calculations, are summarized in Table 9.1. Concerning the analytical calculations, the electrodes are not taken into consideration.
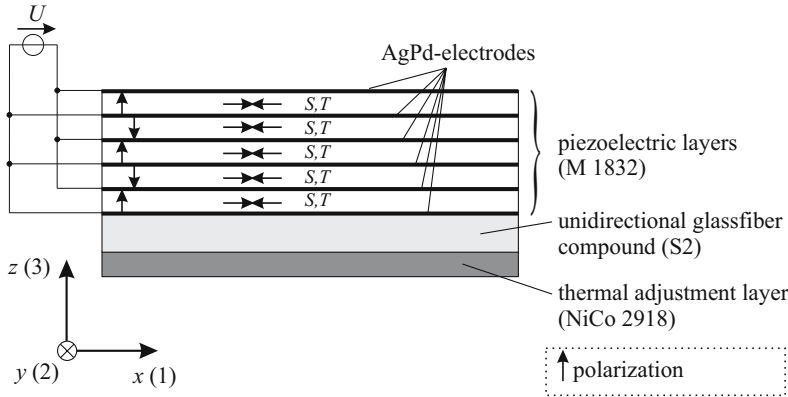
Fig. 9.1. Structure of the piezoelectric multilayer beam bending actuator used for experimental investigations

Table 9.1. Geometrical and material specific parameters of the individual layers

layer i	1	2	$3-7$
material	$NiCo$ 2918	$S2$-glas	M 1832
l_i [mm]		20	
w_i [mm]		8	
h_i [μm]	100	200	5×48
$s_{11,i}^{E}$ [$\cdot 10^{-12} \frac{\text{m}^2}{\text{N}}$]	6.369	17.857	14.144
$d_{31,i}$ [$\cdot 10^{-12} \frac{\text{m}}{\text{V}}$]	—	—	-350
$\varepsilon_{33,i}^{T}$	—	—	4500
ρ_i [$\frac{\text{kg}}{\text{m}^3}$]	8300	1998	8100

Compared to single layer ceramics, the driving voltage can be explicitly minimized by using multilayered piezoceramics. The bending actuator used for the experimental investigations is driven within a voltage range from 0 V to 92 V.

9.2 Static and Quasi-static Measurements

According to the measuring task, the piezoelectric bending actuator is driven by a DC voltage (static measurements) and by a sinusoidal voltage of approx. 100 mHz (quasistatic measurements), respectively. The measurement of hysteresis, the measurement of deflection characteristics, the determination of force-deflection characteristics and the measurements concerning the creep and drift belong to the static and quasistatic measuring tasks. In the following, the individual measuring tasks are described in detail. Analytical calculations based on the achieved results of the theoretical approaches elaborated before are compared to experimental results.

9.2.1 Hysteresis Measurement

An important characteristic of a piezoelectric bending actuator is the deflection ξ of the bender's tip dependent on an alternating driving voltage U. Due to domain processes, for a sufficient low-frequency electric field E and voltage U respectively, a nonlinear and hysteresis-like correlation between the intensive quantity ξ and the extensive quantity E and U respectively exists (see section 2.6). The hysteresis is measured with respect to the reference zero point (tip of the bending actuator). The free bender's length amounts to $x = 20\,\text{mm}$. In order to effect the hysteresis measurement, the bending actuator is driven by a function generator followed by an amplifier for piezoelectric transducers. The measurement setup for hysteresis measurement is shown in figure 9.2.
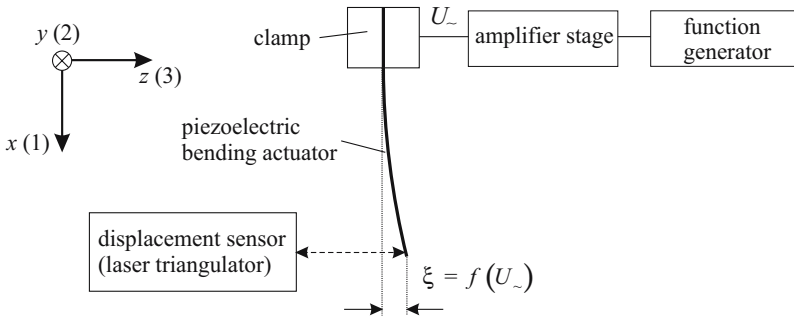
Fig. 9.2. Measurement setup for hysteresis measurement of a piezoelectric beam bending actuator

In order to avoid a discontinous deflection and possibly resulting undesired oscillations, the bending actuator is sinusoidally driven by a voltage with a frequency of $f = 100$ mHz. In order to avoid tensile stress within the piezoceramic layers in x-direction, the alternating voltage is superposed by a DC

offset voltage corresponding to the amplitude of the alternating voltage (see Fig. 8.6). Since the driving voltage, that have to be measured, exceed the measuring range of $10\,\mathrm{V}$ of the I/O board, the measurement setup is extended with a voltage divider network. Its function consists of transforming the voltage range up to $90\,\mathrm{V}$ into the measuring range of the I/O board. The transformed voltage is acquired by one of the analog inputs of the I/O board. In figure 9.3, the measured hysteresis of the bending actuator is shown.
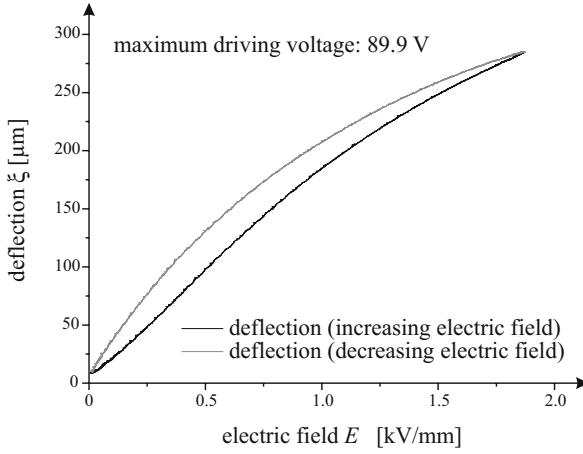
Fig. 9.3. Hysteresis of a piezoelectric bending actuator

From the hysteresis, conclusions can be drawn with respect to the dependence of the piezoelectric constant d_{31} on the driving voltage U and the electric field E, respectively.

Determination of the Piezoelectric Constant d_{31}

The correlation between the deflection ξ and the driving voltage U is described by the matrix element m_{24} of the coupling matrix $\mathbf{M}$ (4.46). In combination with the analytical representation of m_{24} according to (4.130), the deflection ξ yields

$$\xi\left(x\right) = U\frac{m_{Piezo}l^2}{2C}\left[\frac{x}{l}\right]^2. \tag{9.1}$$

The quantity m_{Piezo} has already been defined in equation (4.69). Taking the summation limits of the used monomorph in multilayer technology into consideration, the quantity m_{Piezo} results in

$$m_{Piezo} = \frac{1}{2}\sum_{i=3}^{7}\frac{w_i d_{31,i}}{s_{11,i}h_i}\left[2\overline{z}h_i - 2h_i\sum_{j=1}^{i}h_j + h_i^2\right]. \tag{9.2}$$

The neutral axis position $\overline{z}$ and the flexural rigidity C of the bending actuator result from the equations (4.23) and (4.32). Since all quantities correspond to constant geometrical and material specific parameters, it can be inferred a change of the piezoelectric constant of $d_{31,i}$ from the hysteresis-like deflection ξ in dependence of the driving voltage U. Since all active piezoelectric layers consist of the same piezoceramic material, the piezoelectric constant $d_{31,i} = d_{31}$ can be extracted from the right sum in equation (9.2). In order to calculate the piezoelectric constant d_{31}, equation (9.1) is derived with respect to the driving voltage and afterwards rearranged with respect to d_{31}. Thus, it can generally be written:

$$d_{31} = \frac{4C}{x^2 \sum\limits_{i=3}^{7} \frac{w_i}{s_{11,i} h_i} \left[2\overline{z} h_i - 2h_i \sum\limits_{j=1}^{i} h_j + h_i^2 \right]} \frac{d\xi}{dU} \tag{9.3}$$

By means of the geometrical and material specific parameters listed in Table 9.1, the neutral axis position amounts to $\overline{z} = 231.4 \, \mu m$ and the flexural rigidity amounts to $C = 0.101 \, \mathrm{Nm}^2$. Insertion of the calculated quantities into equation (9.3) yields with respect to the measuring position $x = 20 \, \mathrm{mm}$

$$d_{31} = -9.473 \cdot 10^{-5} \frac{d\xi}{dU}. \tag{9.4}$$

The first derivative of the deflection with respect to the driving voltage results from the measured hysteresis in figure 9.3. In figure 9.4, the dependence of the piezoelectric constant d_{31} on the driving voltage U is illustrated.
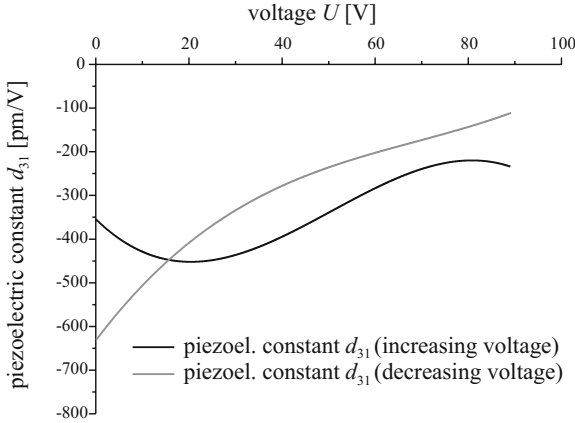
Fig. 9.4. Dependence of the piezoelectric constant d_{31} on the driving voltage U

At this point it should be noted, that the piezoelectric constant d_{31} has been determined within a voltage range from $0 \, \mathrm{V}$ to $89 \, \mathrm{V}$. If a smaller voltage range

is chosen, then hysteresis loops develop, that are mathematically similar to each other. This means, that the represented d_{31}-U-curvature can not simply be transferred to hysteresis loops in smaller voltage ranges. The mean value of the piezoelectric constant derived from measurement data referred to the *increasing* voltage amounts to approx. $-350 \, \text{pm/V}$ and will be used in all further analytical calculations. The important parameters allowing for the calculation of the piezoelectric constant d_{31} and being necessary for the following considerations, are listed in Table 9.2.

Table 9.2. Defining parameters of the piezoelectric constant

$\bar{z}$ $[\mu\text{m}]$	C $[\text{Nm}^2]$	m_{Piezo} $[\text{Nm/kV}]$
231.4	0.010	0.187

9.2.2 Measurement and Analytical Calculation of Bending Curvatures Under Different Excitation Voltages

Within the scope of the static behavior of a piezoelectric bending actuator, the bending curvature characteristics are measured with respect to different driving voltages and are compared to analytical calculations.

The bending curvatures are measured within voltage range of $10 \, \text{V}$ to $90 \, \text{V}$. The measurement setup for the measurement of the bending curvature characteristics is shown in figure 9.5.
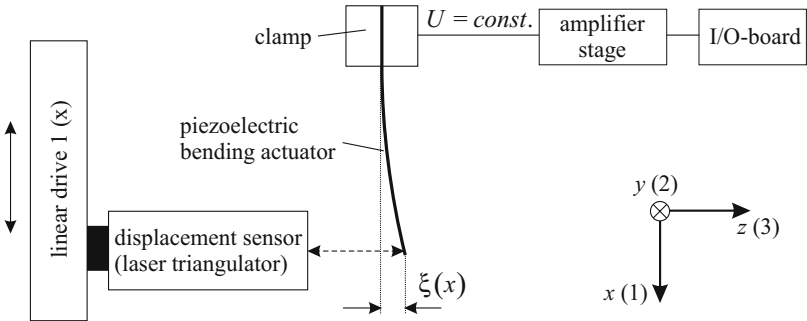
Fig. 9.5. Measurement setup for the experimental investigation of the bending curvature characteristics of a piezoelectric bending actuator

The bending actuator is driven by a constant voltage resulting in a bending deformation. Afterwards, by means of a linear drive, the triangulator is moved

concentrically along the x-direction. For this measurement, the moving speed of the linear drive amounts to 0.005 mm/s in order to achieve a high resolution of the bending curvature characteristics (measuring point distance 2-3 μm).

The analytical calculation of the bending curvature characteristics is effected on the basis of the coupling matrix (4.46) by means of the matrix element $m_{24}(x)$ according to (4.130). Thus, the deflection dependent on the driving voltage can be described as follows:

$$\xi(x) = \frac{m_{Piezo}l^2}{2C}\left(\frac{x}{l}\right)^2 U \tag{9.5}$$

By means of (9.5) it is evident, that the deflection dependent on the driving voltage shows a parabolic characteristic. The piezoelectric moment referred to the driving voltage m_{Piezo} and the flexural rigidity C are calculated by means of the equations (4.69), (4.32) and the parameters listed in Table 9.1. The free length l of the bending actuator used for the experimental investigations amounts to 19.22 mm. The measured bending curvatures dependent on different driving voltages as well as the appropriate analytical calculation results are illustrated in figure 9.6. The experimental investigation is effected for different increasing voltage values.
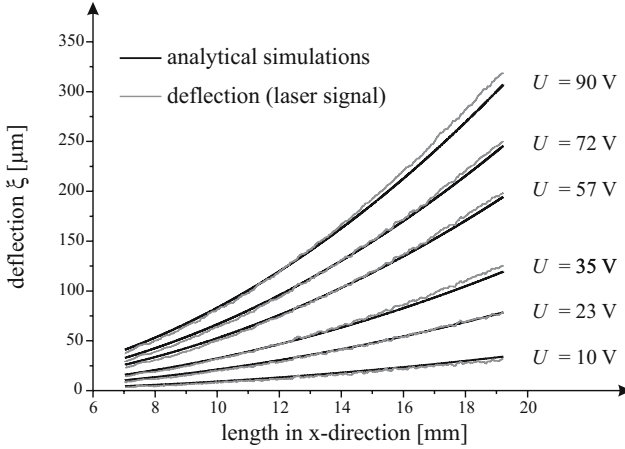

Fig. 9.6. Measured and analytically calculated bending curvatures with respect to different driving voltages

The proportional deviation of the analytical computations compared to the measured bending curvatures amounts approx. to 3.9 %, which justifies the theoretical approaches concerning the static behavior of piezoelectric bending actuators. The deviations are caused by the realized clamping of the bending

actuator. Its compliance becomes apparent more and more with increasing bending deformation of the actuator.

In the next step, the dependence of the bending angle $\alpha(x)$ on different driving voltages as a function of the length coordinate x is to be determined by means of the measurement results of deflection characteristics. The measurement results are compared to analytical calculations. The calculation of the bending angle is effected by means of the matrix element $m_{14}(x)$ of the coupling matrix (4.46) in accordance with (4.130). It can be written:

$$\alpha\left(x\right) = \frac{m_{Piezo}l}{C}\left(\frac{x}{l}\right)U \tag{9.6}$$

In figure 9.7, the bending angles derived from measured bending curvature characteristics are compared to analytical calculations.
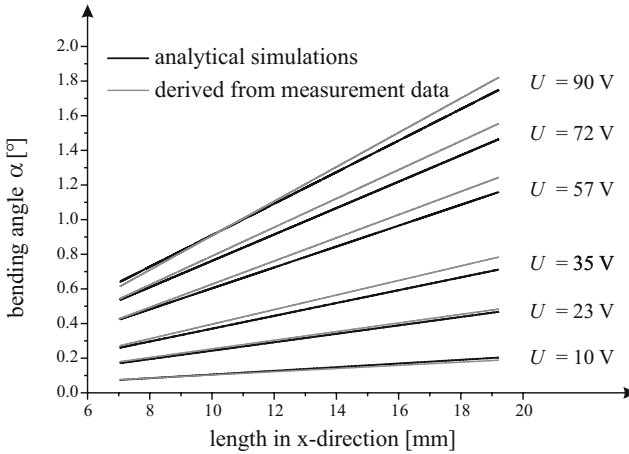
Fig. 9.7. Measured and analytically calculated bending angles with respect to different driving voltages

The measurement results are also in accordance with the analytical approach concerning the static behavior of piezoelectric bending actuators. In the next section it is dwelled on the force-deflection characteristics of piezoelectric bending actuators.

9.2.3 Measurement and Analytical Calculation of Force-Deflection Characteristics

On principle, the deflection of a bending actuator is based on the electrical field (driving voltage) and on external influences like forces, moments and pressure

loads. In this chapter, the resulting deflection ξ of the bender's tip caused by a driving voltage and the external influence of a force F acting perpendicularly against the bending direction of the bender's tip are considered, resulting in the force-deflection characteristics of beam bending actuators. The force acting in negative z-direction is effected by means of a voice coil motor (see section 8.1). The measurement setup for the experimental investigation of force-deflection characteristics is shown in figure 9.8.
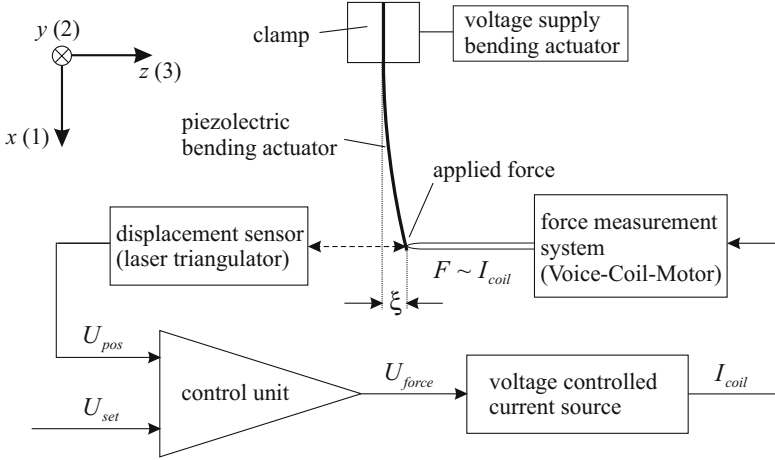
Fig. 9.8. Measurement setup for the experimental investigation of the force-deflection characteristics of a piezoelectric bending actuator

The voice coil motor is driven by a control unit and a following voltage-controlled current source, until the deflection-proportional voltage signal of the laser triangulator U_{pos} coincides with the reference variable U_{set} of the control unit (e.g. $U_{set} = 0$ for $\xi = 0$). As long as a system deviation $U_{set} - U_{pos}$ exists, a deflection-proportional voltage signal U_{force} is generated controlling the current source. The current source generates a coil current I_{coil} proportional to the voltage signal U_{force}. The voice coil motor generates a force F, that is directly proportional to the coil current. The force F can be determined by following equation:

$$F = K_{NI} N I_{coil} \tag{9.7}$$

The quantities K_{NI} and N denote coil parameters given by the manufacturer. K_{NI} corresponds to the force, that can be generated by a current of 1 A per turn, N denotes the turn number of the voice coil motor. The parameters of the voice coil motor amount to $K_{NI} = 0.019\,\text{N/A}$ and $N = 198$, thus the force generated by a current results in:

$$F = 3.762\frac{\text{N}}{\text{A}}I_{coil} \tag{9.8}$$

The analytical calculation of the force-deflection characteristics is effected on the basis of the coupling matrix (4.46) by means of the matrix elements $m_{22}(x)$ and $m_{24}(x)$. The force F affecting the bender's tip $(x = l)$ can be calculated according to

$$F = \frac{1}{m_{22}(l)}\xi(l) - \frac{m_{24}(l)}{m_{22}(l)}U. \tag{9.9}$$

In combination with $m_{22}(x)$ (4.128) and $m_{24}(x)$ (4.130), (9.9) can be reformulated as follows:

$$F = \frac{3C}{l^3}\xi - \frac{m_{Piezo}}{6l}U \tag{9.10}$$

The piezoelectric moment referred to the driving voltage m_{Piezo} and the flexural rigidity C are calculated by means of the equations (4.69), (4.32) and the parameters listed in Table 9.1. The calculated parameters are listed in Table 9.2. The free length l of the bending actuator used for the experimental investigations of the force-deflection characteristics amounts to 20.00 mm. The measured force-deflection characteristics dependent on different driving voltages as well as the appropriate analytical calculation results are illustrated in figure 9.9. The experimental investigation is effected for increasing voltage values.
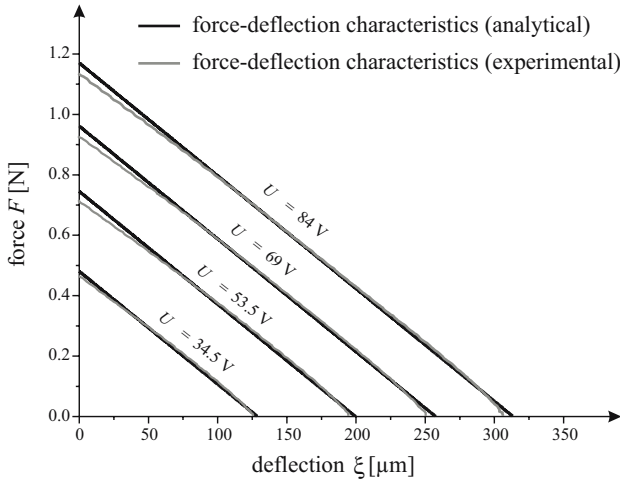
Fig. 9.9. Measured and analytically calculated force-deflection characteristics with respect to different driving voltages

9.2.4 Drift and Creep Measurements

In addition to the hysteresis of piezoelectric bending actuators (see Fig. 9.3), deformation processes dependent on time and temperature arise during a con-

stant load (e.g. constant driving voltage), that are superposed by domain switching processes within piezoceramic materials. These deformation processes are called *creep* [149]. In figure 9.10, this effect is shown by means of deflection ξ as a step response with respect to a voltage step in a transient state.
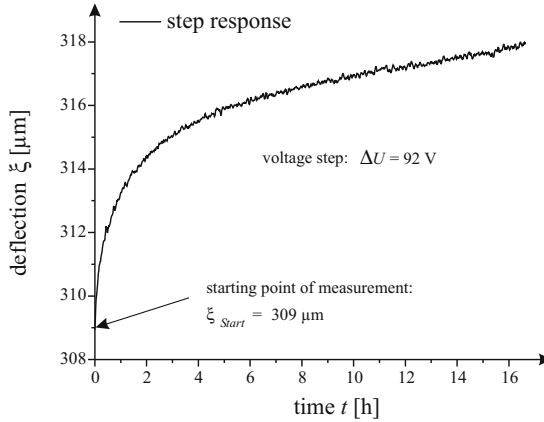
Fig. 9.10. Creep behavior of a piezoelectric bending actuator

The measurement setup for the determination of the creep behavior corresponds to the structure illustrated in figure 9.2. Since creep effects cover a period of several hours, the creep behavior is measured by means of a long-term measurement. The measurement time amounts to approx. 17 h. The deflection is determined at intervals of $\Delta t = 1\,\text{s}$.

The creep behavior is inseparably connected with the hysteresis behavior of piezoceramics also caused by domain processes. A possible reason for the creep can be seen in the fact, that only a part of domains is directly aligned, after the piezoceramics is affected by voltage step. The alignment of the remaining part is delayed by the developing internal electrical field [150].

In summary it may be said, that the employment of piezoelectric beam bending actuators with respect to high-accuracy positioning is limited due to hysteresis and creep effects, that are typical for piezoceramic materials. Only the integration of a high-accuracy sensor for deflection measurements in combination with an appropriate sensor electronics can open new fields of employment of piezoceramic bending actuators within the scope of high-accuracy positioning. Within the scope of the present book, the chapters 10 – 12 deal with the aspect of sensor integration and the associated compensation of hysteresis and creep effects in detail.

9.3 Dynamic Measurements

The differential equation of flexural vibrations is fundamental for the description of the dynamic behavior of piezoelectric bending actuators. The differential equation of flexural vibrations can be derived on the basis of the Hamilton principle (see chapter 5). Concerning the derivation of the differential equation of flexural vibrations, particularly the focus was turned on the consideration of dissipative forces, that dissipate the bending actuator's energy.

The sum of all external and internal frictional forces affecting the bending actuator are combined as *equivalent viscous damping* by means of the coefficient of friction r and the coefficient of friction per unit length r_a, respectively [151]. In order to be able to calculate the dynamic behavior of piezoelectric bending actuators, the knowledge of the coefficient of friction r and r_a is necessary, respectively. The experimental determination of the coefficient of friction is effected by means of the time- and position-dependent representation of the deflection of a clamped-free, subcritically damped beam bender already discussed in chapter 6. Furthermore, the first and second eigenmode of a piezoelectric bending actuator are determined experimentally and compared with analytical calculations. The experimental investigations serve to substantiate experimentally the theoretical drawing ups concerning the eigenmodes discussed in chapter 6.

In a next step, the determined coefficient of friction is implemented into the electromechanical circuit representation of the piezoelectric multilayered actuator. Taking the first two eigenmodes into consideration, the frequency response of the deflection during an electrical control is determined analytically. The experimentally determined transient characteristic is compared to analytical calculations.

9.3.1 Experimental Evaluation of the Coefficient of Friction

The experience has shown, that oscillations of a uniquely excited real physical system decay with time. The reason for this are the dissipative forces (frictional forces), that affect the vibrating system internally and externally. They result in a transition of mechanical energy forms like potential and kinetic energy into thermal energy. In combination with the differential equation of the free damped flexural vibration of a beam bender (see chapter 6)

$$\ddot{\phi}_m + 2\zeta_m\omega_m\dot{\phi}_m + \omega_m^2\phi_m = 0, \tag{9.11}$$

the time- and position-dependent representation of the deflection

$$\phi_m^h(t) = \phi_0 e^{-\omega_m\zeta_m t}\left[\cos\left(\omega_m^d t\right) + \frac{\zeta_m}{\sqrt{1-\zeta_m^2}}\sin\left(\omega_m^d t\right)\right] \tag{9.12}$$

has already been determined analytically as homogeneous solution with respect to the initial conditions $\phi_m^h(0) = \phi_0$ and $\dot{\phi}_m^h(0) = 0$. The quantitiy ϕ_0

corresponds to the amplitude at $t = 0$, ζ_m denotes the attenuation constant, ω_m corresponds to the natural frequency and ω_m^d denotes the frequency of the damped vibration related to the mth eigenmode of the piezoelectric bending actuator. Equation (9.12) represents the waveform of a subcritically damped system ($\zeta < 1$) with a lower frequency ω_m^d (see eq. 6.59). Due to energy losses caused by friction, the oscillation amplitude decreases with $e^{-\omega_m \zeta_m t}$ [152]. In figure 9.11 the waveform of a subcritically damped oscillation is shown.
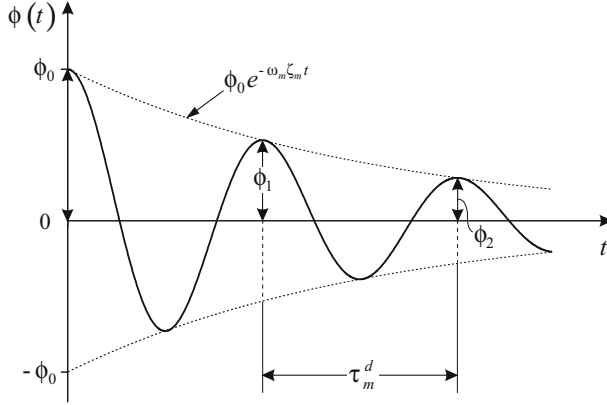
Fig. 9.11. Waveform of a subcritically damped system with the period of oscillation τ_m^d

The period of oscillation τ_m^d (see Fig. 9.11) of a subcritically damped oscillation results from the frequency ω_m^d:

$$\tau_m^d = \frac{2\pi}{\omega_m^d} \tag{9.13}$$

The damping rate can be determined by means of the ratio of the two amplitude maxima ϕ_p and ϕ_{p+q} within q periods of oscillation [153]:

$$\frac{\phi_p}{\phi_{p+q}} = e^{q\omega_m \zeta_m \tau_m^d} = e^{q\Lambda} \tag{9.14}$$

The quantity $\omega_m \zeta_m \tau_m^d$ is called *logaritmic decrement* Λ. In appendix M, equation (9.14) is derived.

The logarithmic decrement allows for the experimental determination of the coefficient of friction of a viscously damped oscillation. Taking the logarithm of (9.14) and taking the correlation (6.51) into account yields

$$\ln\left(\frac{\phi_p}{\phi_{p+q}}\right) = q\Lambda = q\frac{r\tau_m^d}{2m}. \tag{9.15}$$

Equation (9.15) allows for the calculation of the coefficient of friction r according to

$$r = \frac{2m}{q\tau_m^d} \ln\left(\frac{\phi_p}{\phi_{p+q}}\right).$$
(9.16)

The measurement setup shown in figure 9.12 provides the experimental determination of the coefficient of friction.
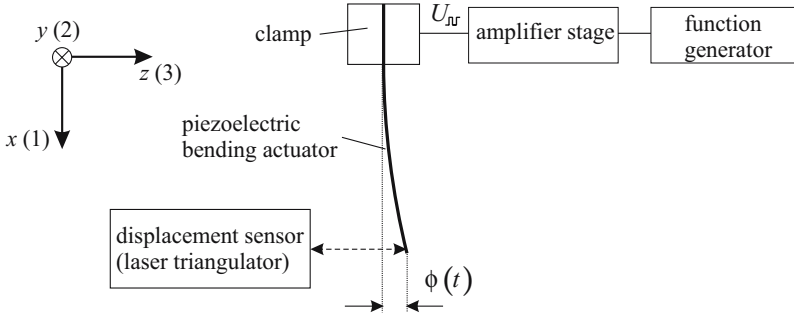
Fig. 9.12. Measurement setup for the experimental determination of the coefficient of friction r of a clamped-free beam bending actuator

By means of a function generator and a following amplifier, the bending actuator is driven by a square wave voltage. The signal frequency amounts to $f = 7\,\text{Hz}$. The maximum voltage level amounts to $U_{High} = 50\,\text{V}$, the minimum voltage level amounts to $U_{Low} = 0\,\text{V}$. Since the coefficient of friction r is determined by means of the waveform $\phi(t)$ of the free subcritically damped oscillation, the deflection characteristics of the bending actuator during the voltage step from U_{High} to U_{Low} is important. In figure 9.13, the waveforms of both, the square wave signal and the damped oscillation of the bending actuator are illustrated.

In order to determine experimentally the coefficient of friction r, the amplitude maxima $\phi_p = \phi_1$ and $\phi_{p+q} = \phi_2$ are chosen (see Fig. 9.13). In Table 9.3 the necessary defining parameters are listed.

Table 9.3. Defining parameters of the coefficient of friction (per unit length)

$\phi_1\,[\mu\text{m}]$	$\phi_2\,[\mu\text{m}]$	q	$\tau_1^d\,[\text{ms}]$	$m\,[\text{g}]$	$l\,[\text{mm}]$
-59.20	-10.45	20	0.973	0.442	17.4

Using the correlation (9.16) in combination with the defining parameters listed in Table 9.3 yields the experimentally determined coefficient of friction r and
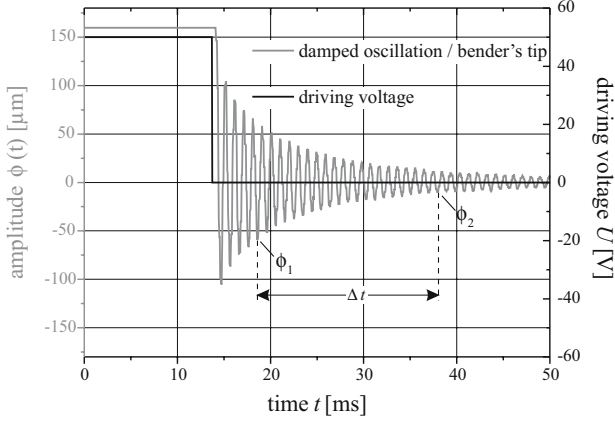
Fig. 9.13. Betriebsspannung und dazugehöriger Driving voltage signal and appropriate waveform of the damped oscillation of a piezoelectric bending actuator – measured at the bender's tip

the coefficient of friction per unit length r_a, respectively:

$$r = 0.078 \ \frac{\text{Ns}}{\text{m}} \qquad \text{and} \qquad r_a = 4.528 \ \frac{\text{Ns}}{\text{m}^2} \qquad (9.17)$$

9.3.2 Measurement and Analytical Calculation of the First and Second Eigenmode

Concerning the analytical description of the dynamic behavior of a clamped-free piezoelectric bending actuator, it has already been dwelled on the propagationable eigenmodes of the vibrating system. Since the eigenmodes are also implemented into the electromechanical circuit representation of a bending actuator, it is necessary to confirm experimentally the development of the eigenmodes. In the following, the first two eigenmodes of the bending actuator shown in figure 9.1 are determined experimentally and compared to analytical calculations. The measurement setup for the experimental investigation of the eigenmodes is shown in figure 9.14.

Concerning the experimental determination of the eigenmodes, it has to be paid attention on the avoidance of tensile stresses affecting the piezoelectric layers of the bending actuator in case of flexural vibrations. Tensile stresses can lead to an irreversible damage within the piezoceramics, thus the actuator's performance is lost. Therefore, the bending actuator is not driven by a pure alternating voltage. Instead, the actuator is driven by a positive offset voltage u_{Offset}, thus the active piezoelectric layers are affected by a mechanical compressive stress. If the offset voltage is superposed by a low alternating voltage, the actuator performs periodical oscillations around the
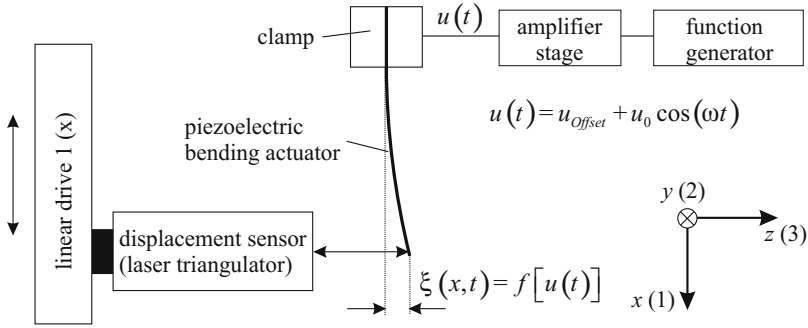
Fig. 9.14. Measurement setup for the experimental investigation of the eigenmodes of a clamped-free bending actuator

static deflection $\xi_{stat}(x) = f(u_{Offset}) > 0$ corresponding the x-coordinate. The condition

$$\xi(x,t) > 0 \quad \forall x, t \in \{0 \le x \le l \ \wedge \ t \ge 0\} \tag{9.18}$$

has to be provided. Nevertheless, in order to represent the eigenmodes with respect to the zero line of the actuator ($\xi = 0$), at first, the bending curvature is measured along the x-axis by means of the triangulator, after the actuator was affected by the offset voltage u_{Offset}. The measured bending curvature serves as zero point reference for later data evaluation. Afterwards, the bending actuator is put into periodical flexural vibrations by means of a superposed alternating voltage. The time-dependent deflections $\xi(x,t)$ are measured along the x-axis, then their difference to the zero point reference is determined. The offset voltage chosen for the measurements amounts to $u_{Offset} = 45.9 \, \text{V}$.

The standardized deflection of the bending actuator and the appropriate eigenmode $X_1(x)$ and $X_2(x)$ are shown in the figures 9.15 and 9.16. The analytical calculation of the eigenmodes is effected in accordance with equation (6.29) in combination with Table 9.4.

Table 9.4. Defining parameters for the first and second eigenmode

l [μm]	C [Nm^2]	m [g]	k_1 [m^{-1}]	k_2 [m^{-1}]	f_1 [kHz]	f_2 [kHz]
17.3	0.010	0.439	108.38	271.34	1.179	7.392

In order to determine the first two eigenmodes, the frequencies of the alternating voltage signal $f_{meas1} = 1.1 \, \text{kHz}$ and $f_{meas2} = 7.1 \, \text{kHz}$ are chosen.
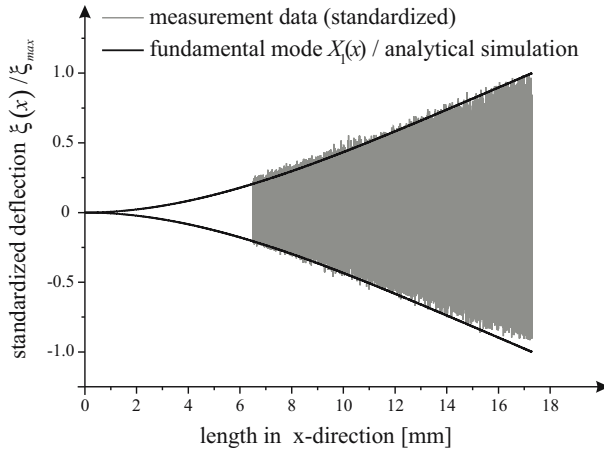
Fig. 9.15. Analytically calculated eigenmode $X_1 (x)$ and standardized measurement data of a clamped-free piezoelectric bending actuator
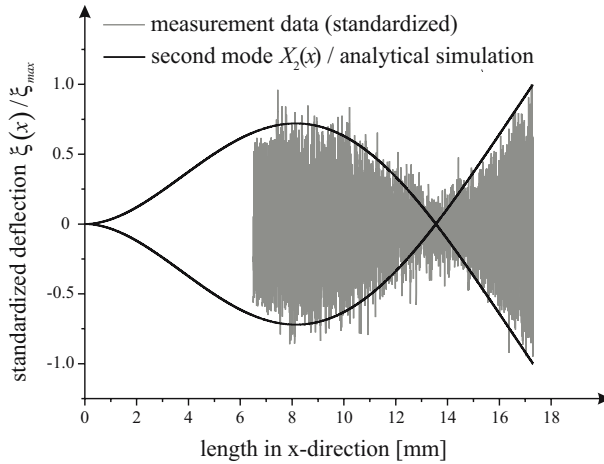
Fig. 9.16. Analytically calculated eigenmode $X_2 (x)$ and standardized measurement data of a clamped-free piezoelectric bending actuator

They are chosen somewhat below the natural frequencies of the appropriate eigenmodes, thus an operation in resonance is impossible. Since the amplifier stage following the function generator shows a frequency dependent behavior, for both measurements the amplitude of the alternating voltage signal is adjusted manually to $u_0 = 5\,\mathrm{V}$ by means of an oscilloscope. Due to the structure of the measurement setup, the triangulator can not be moved up

to the clamping $(x = 0)$, thus the measurements are effected from the initial position $x_0 = 6.5\,\mathrm{mm}$.

In chapter 6, by means of the dynamic admittance matrix $\mathbf{H}$, the correlation between the extensive dynamic quantities and the intensive dynamic quantities dependent on the bender's length variable x has been represented in closed form analysis. In the following, the maxima of deflection $\xi(x,t)$ of the first two eigenmodes are calculated with respect to an alternating driving voltage amplitude of $u_0 = 5\,\mathrm{V}$. The analytical calculations are compared to achieved measurement results. The correlation between the deflection $\xi(x,t)$ and the driving voltage $u(t)$ is described by means of the matrix element $h_{24}(x)$ of the the dynamic admittance matrix $\mathbf{H}$ (see eq. 6.100). It can generally be written:

$$\xi(x,t) = -\left(\frac{4m_{Piezo}}{l^2\mu}\sum_{m=1}^{\infty} X_m(x)\,\frac{k_m l\,\alpha_M(k_m l)}{\omega_m^2\sqrt{(1-\eta_m^2)^2 + (2\zeta_m\eta_m)^2}}\right)$$
$$\cdot u_0\cos(\omega t - \Psi) \tag{9.19}$$

Since the maxima of deflection are of interest, the alternating signal part in (9.19) can be neglected. Thus, the fundamental mode $X_1(x)$ yields with respect to (6.51)

$$\xi_{\mathrm{max},1}(x) = -\frac{4m_{Piezo}}{l^2\mu}\,\frac{X_1(x)\,k_1 l\,\alpha_M(k_1 l)}{\omega_1^2\sqrt{(1-\eta_1^2)^2 + \left(2\frac{r_a}{\omega_1\mu}\eta_1\right)^2}}u_0. \tag{9.20}$$

The amplitudes of the second eigenmode result from (9.19):

$$\xi_{\mathrm{max},2}(x) = -\frac{4m_{Piezo}}{l^2\mu}\sum_{m=1}^{2}\frac{X_m(x)\,k_m l\,\alpha_M(k_m l)}{\omega_m^2\sqrt{(1-\eta_m^2)^2 + \left(2\frac{r_a}{\omega_m\mu}\eta_m\right)^2}}u_0. \tag{9.21}$$

The mass per unit length μ, the natural frequency ω_m, the eigenmode $X_m(x)$, the frequency ratio η_m, the factor $\alpha_M(k_m l)$ and the piezoelectric moment referred to the driving voltage m_{Piezo} are calculated by means of the equations (5.92), (6.25), (6.29), (6.71), (6.83) (6.96), the characteristic zeros and the defining parameters listed in Table 6.1 and 9.1 and by means of the derived parameters listed in Table 9.2 and 9.4. On the basis of the free damped oscillation, the coefficient of friction r_a has already been determined and amounts to $r_a = 4.528\,\mathrm{Ns/m^2}$. The measured deflections of the bending actuator and the appropriate analytical calculations are shown in the figures 9.17 and 9.18. The analytical calculation of the first two eigenmodes is effected on the basis of the equations (9.20) and (9.21).

The achieved measurement results show a very good coincidence with the analytical calculations based on the dynamic admittance matrix $\mathbf{H}(x)$. In the next step, the transient characteristics of a bending actuator is investigated.
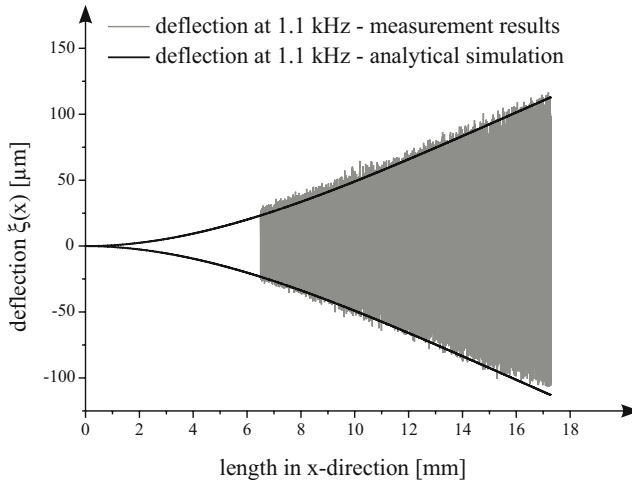
Fig. 9.17. Measured and calculated deflection characteristics of the fundamental mode of a clamped-free piezoelectric bending actuator
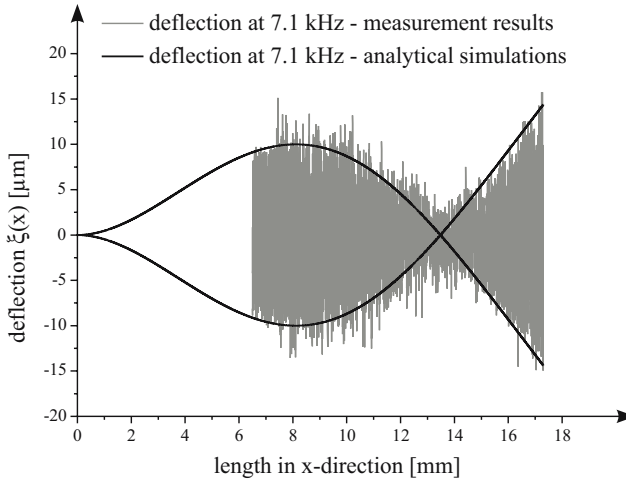
Fig. 9.18. Measured and calculated deflection characteristics of the second eigenmode of a clamped-free piezoelectric bending actuator

9.3.3 Measurement and Analytical Calculation of the Transfer Function

In the following, the canonical circuit representation of a clamped-free piezoelectric multilayer beam bending actuator developed in chapter 7 is verified

experimentally. The actuator used for the experimental investigations is illustrated in figure 9.1.

Generally, the experimental determination of the transient characteristics of dynamic systems is effected by means of so-called *test functions*. Descriptive and easily realizable test functions like the *impulse function*, the *step function*, the *ramp function* or a *harmonic function* are chosen as input $x_e(t)$ of the system. Simultanously, the time dependent behavior of the output $x_a(t)$ is recorded in response to the chosen input $x_e(t)$ (see Fig. 9.19). The output characteristic is representative for the transient characteristics of the system [154]. It is merely a matter of advisability, which test function is chosen as input. If a system is affected by different test functions, the information of the respective response functions are equivalent.
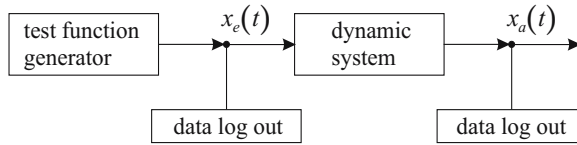
Fig. 9.19. Experimental data aquisition concerning the transient characteristics of a dynamic system

In order to determine the transient characteristic of the bending actuator, a harmonic function (sine function) is chosen as test function. The time dependent behavior of the bending actuator can be described for all frequencies between zero and infinite by the allocation of changes of the output to temporally sinusoidal changes of the input in transient state. If a sinusoidal oscillation with frequency ω is supplied, after a transient time, the output $x_a(t)$ also performs a harmonic oscillation with the same frequency ω. However, the amplitude and the phase of the output generally vary. If the ratio of output and input is formed in the transient state for all frequencies between $0 < \omega < \infty$, the transfer function $\underline{B}(\omega)$ of the system is achieved [155]:

$$\underline{B}(\omega) = \underline{B} = \frac{\underline{x_a}}{\underline{x_e}} \tag{9.22}$$

As test function generator, a network analyzer (Agilent 35670A) is used. The measuring chain consists of an amplifier stage, the bending actuator and a laser triangulator. The measuring arrangement is shown in figure 9.20 [156]. The measurement of the deflection ξ is effected at the actuator's tip $(x = l)$. The free length of the actuator amounts to $l = 19.2\,\mathrm{mm}$. The investigated frequency range extends from $20\,\mathrm{Hz}$ to $10\,\mathrm{kHz}$. The transfer function $\underline{B}_0$ of the measuring chain consists of the transfer function $\underline{B}_1$ of the amplifier stage, the bending actuator $\underline{B}_2$ and the laser triangulators $\underline{B}_3$. It can be written:
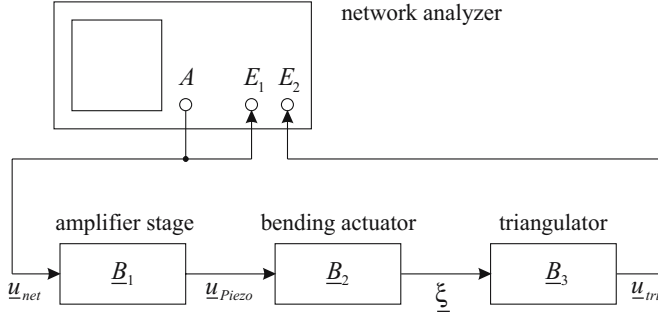
Fig. 9.20. Measuring chain for the experimental verification of the canonical circuit representation of a clamped-free piezoelectric multilayer beam bending actuator

$$\underline{B}_0 = \underline{B}_1 \cdot \underline{B}_2 \cdot \underline{B}_3 \tag{9.23}$$

According to the input and output illustrated in figure 9.20, the transfer function (9.23) can be reformulated:

$$\underline{B}_0 = \frac{\underline{u}_{Piezo}}{\underline{u}_{net}} \cdot \frac{\underline{\xi}}{\underline{u}_{Piezo}} \cdot \frac{\underline{u}_{tri}}{\underline{\xi}} = \frac{\underline{u}_{tri}}{\underline{u}_{net}} \tag{9.24}$$

The measured transient characteristic $\underline{B}_0$ of the entire measuring chain is illustrated in figure 9.21. Within the investigated frequency range, the first and the second resonant frequency can be identified.
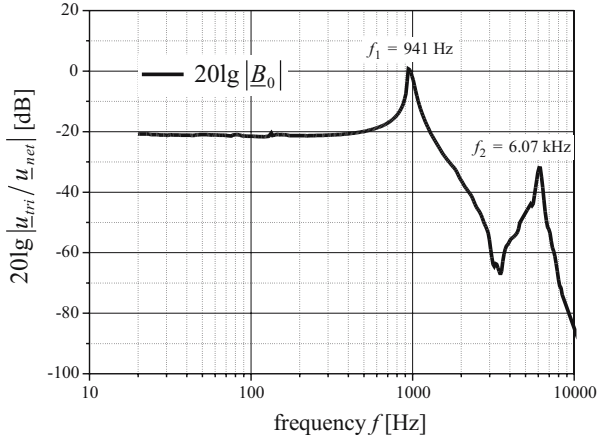
Fig. 9.21. Measured transfer function $\underline{B}_0$ of the measuring chain within a frequency range from 20 Hz to 10 kHz

In order to calculate the total transfer function $\underline{B}_0$ in closed form analysis, the transfer functions $\underline{B}_1$, $\underline{B}_2$ and $\underline{B}_3$ of the individual measuring chain elements have to be available in closed form analysis.

The transient characteristics $\underline{B}_3$ of the laser triangulators is constant within the investigated frequency range $(f_{\max} = 10\,\text{kHz})$ and amounts to $\underline{B}_3 = 5 \cdot 10^3\,\text{V/m}$ according to the manufacturer's data sheet. Since the transient characteristics of the amplifier stage was unknown, $\underline{B}_1$ had to be determined. The measured transient characteristic of the amplifier stage is shown in figure 9.22. Here, for the approximation of the transient characteristic, a polynomal of 9th order was used.
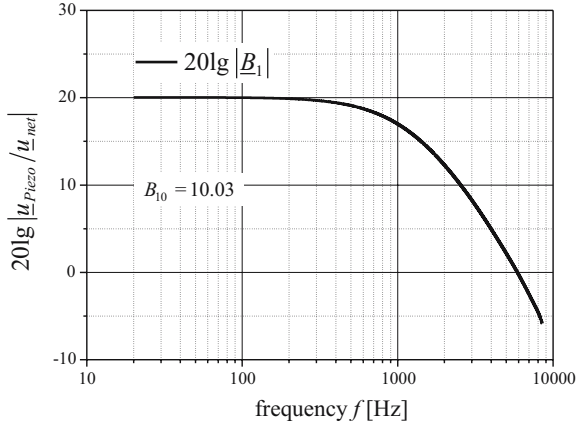
Fig. 9.22. Transfer function $\underline{B}_1$ of the amplifier stage - for frequencies $f < 300\,\text{Hz}$ a constant amplification factor of $B_{10} = 10,03$ is identified

The transfer function $\underline{B}_2$ of the bending actuator is determined on the basis of the mechanical admittance $\underline{h}_1$ (7.137). Since two resonant frequencies appear within the investigated frequency range (see Fig. 9.21), the calculation of the mechanical admittance $\underline{h}_1$ is effected for the first two eigenmodes $X_1(l)$ and $X_2(l)$. The correlation between deflection $\underline{\xi}$ and driving voltage $\underline{u} = \underline{u}_{Piezo}$ according to (7.128) yields the transfer function $\underline{B}_2$ in closed form analysis:

$$\frac{\underline{\xi}}{\underline{u}_{Piezo}} = \frac{\underline{h}_1}{j\omega qY} = \underline{B}_2 \tag{9.25}$$

Insertion of (7.137) into (9.25) results in

$$\frac{\underline{\xi}}{\underline{u}_{Piezo}} = \frac{1}{j\omega Y} \sum_{m=1}^{2} X_m(l) X'_m(l) \beta_m(\omega). \tag{9.26}$$

In combination with (7.47) defining the quantity $\beta_m(\omega)$, equation (9.26) can be reformulated, taking (7.124) and (7.125) into account:

$$\frac{\underline{\xi}}{\underline{u}_{Piezo}} = \frac{1}{j\omega Y} \sum_{m=1}^{2} \frac{X_m(l) X'_m(l)}{\frac{1}{j\omega n_m} + j\omega m^* + r^*} \tag{9.27}$$

In (9.27), the following abbreviations are introduced:

$$n_m = \frac{4n_0}{(k_m l)^4} \tag{9.28}$$

$$m^* = \frac{m}{4} \tag{9.29}$$

$$r^* = \frac{r}{4} \tag{9.30}$$

Taking the natural frequency ω_m according to (6.25) and the Q-factor of the particular eigenmode according to

$$\frac{1}{Q_m} = \omega_m n_m r^* = \frac{rl}{(k_m l)^2} \sqrt{\frac{1}{C\mu}} \tag{9.31}$$

into account, the mechanical impedance $\underline{z}_1$ in the denominator of the summation term in (9.27) can be formulated in standardized form:

$$\frac{\underline{\xi}}{\underline{u}_{Piezo}} = \frac{1}{Y} \sum_{m=1}^{2} \frac{n_m X_m(l) X'_m(l)}{1 - \left(\frac{\omega}{\omega_m}\right)^2 + j\frac{\omega}{\omega_m}\frac{1}{Q_m}} \tag{9.32}$$

After some algebraic calculations, (9.32) results in

$$\frac{\underline{\xi}}{\underline{u}_{Piezo}} = \frac{1}{Y} \sum_{m=1}^{2} \frac{n_m X_m(l) X'_m(l)}{\left[1 - \left(\frac{\omega}{\omega_m}\right)^2\right]^2 + \left[\frac{\omega}{\omega_m}\frac{1}{Q_m}\right]^2} \left[1 - \left(\frac{\omega}{\omega_m}\right)^2 + j\frac{\omega}{\omega_m}\frac{1}{Q_m}\right]. \tag{9.33}$$

At this point, the total transfer function $\underline{B}_0$ can be calculated in closed form analysis. In order to provide a logarithmic representation of the transfer function, it necessitates the supply of dimensionless quantities and the formation of the absolut value. (9.23) results in

$$20\lg|\underline{B}_0| = 20\lg|\underline{B}_1| + 20\lg\left|\frac{\underline{B}_3\underline{\xi}}{\underline{u}_{Piezo}}\right|, \tag{9.34}$$

where (9.33) has to be inserted into (9.34). The natural frequency ω_m, the propagationable eigenmodes $X_m(x)$ and their derivatives, the gyrator constant Y, the compliance n_m and the Q-factor Q_m are calculated by means of

the equations (6.25), (6.29), (7.98), (9.28) (9.31) and the characteristic zeros and the defining parameters listed in Table 6.1 and 9.1. On the basis of the free damped oscillation, the coefficient of friction r has already been determined and amounts to $r = 0.078 \, \text{Ns/m}$. The measured transfer function $\underline{B}_0$ and the appropriate analytical calculations are shown in figure 9.23 within a frequency range from 20 Hz to 10 kHz.
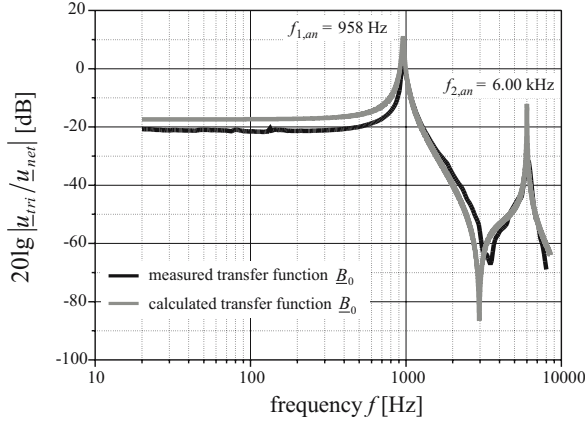
Fig. 9.23. Measured and simulated transfer function $\underline{B}_0$, calculated on the basis of the canonical circuit representation of a clamped-free piezoelectric multilayer beam bending actuator

The measurement results show a very good coincidence with the analytical calculations. Thus, the conclusion can be drawn, that the developed canonical circuit representation of a clamped-free piezoelectric bending actuator can be consulted for its description within the scope of the network theory.

**Sensor Integration for Tip Deflection
Measurements**

10

Piezoelectric Beam Bending Actuator with Integrated Sensor

Due to the piezoelectric effect, which interconnects electrical and mechanical quantities, piezoceramics can be used in different application areas, both as actuator and as sensor. Applications can be found in almost all fields of electrical engineering, mechanical engineering, acoustics, automation, automotive, health care and in countless further application areas of industry and daily life. Piezoceramic compacts, piezoceramic actuators and sensors as well as complex units and systems are used [2, 3]. The development of high-effective and low-cost piezoceramic materials optimized for technical applications allowed for a multiplicity of technical solutions for piezoceramic actuators and sensors. The so-called high-effective mass systems provide maximum gain at only $1\,kV/mm$ resulting in a material strain of approx. 2 ppm. Therefore, high-effective piezoceramics show very large piezoelectric coefficients d_{iq} representing the ratio between strain and electric field. Inherent hysteresis, drift and creep characteristics are a disadvantage of high-effective piezoceramic materials. Therefore, piezoceramic bending actuators consisting of high-effective piezoceramics are only suitable for a limited extent, as far as high-accuracy positioning is concerned [157].

For applications, that require precise switching and exact position control, measures have to be taken for the compensation of the inherent piezoelectric effects such as creep and hysteresis and the compensation of external varying mechanical loads and vibrations. By means of a sensor integrated into the bending actuator and an appropriate sensor electronics, the disturbing effects can be detected. The implementation of such a sensor-actuator system into a closed-loop control allows for a compensation of negative effects, thus high-efficient piezoceramics can be used for high-accuracy positioning.

Within the scope of the federal german research project EPIETEC (Effektive piezokeramische Multilayer-Technologie für integrierte Niedervolt-Piezobieger), a new pneumatic micro valve has been realized. The heart of the micro

valve is a smart piezoelectric low voltage multilayer bending actuator with an integrated sensor for tip deflection measurements.

10.1 Smart Pneumatic Micro Valve

Piezoelectric pneumatic valves used in automation as pilot valves or proportional pressure warning valves are state-of-the-art. The structure and the operating mode of a piezoelectric pilot valve are illustrated in figure 10.1. In the off-state, the valve nozzle is opened, in the on-state, the deflected bending actuator closes the valve nozzle and the pneumatic flow is interrupted. The two valve positions "closed" and "opend" corresponding to the "on-state" and the "off-state" characterize a pneumatic pilot valve [158].
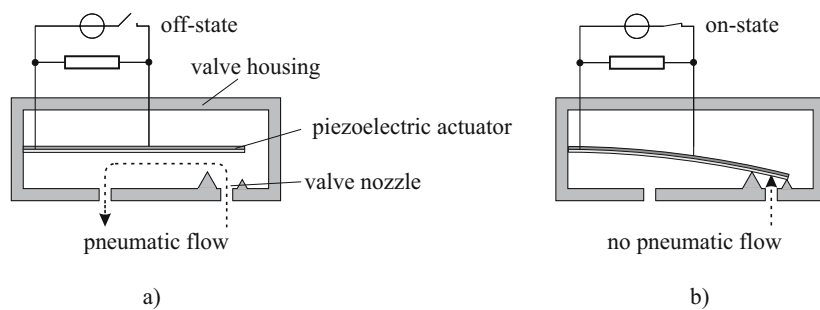
Fig. 10.1. Structure and operating mode of a piezoelectric pneumatic pilot valve. - **(a)** off-state; **(b)** on-state

By contrast, the pneumatic flow of a proportional valve is controlled by the adjustment of the driving voltage of the piezoelectric bending actuator. However the repeatability with the same actual value has to be regarded problematically. Due to hysteresis and relaxation effects, a distinct allocation between bending actuator deflection and driving voltage is not possible [159, 160].

Nowadays, a controlled operating of the bending actuator is only possible with the help of external sensor signals, e.g. by means of pressure sensors arranged in the complete system. The indirect position sensing of the actuator on the basis of an external signal, e.g. a pressure signal, complicates a fast and effective control. Due to their complex structure, such piezoelectric proportional valves are relatively voluminous. Typical geometrical dimensions are: width 30 mm, depth 44 mm and height 65 mm.

Furthermore, pneumatic valve units are used at locations spatially separated from the actual mechanical components of the automation. The spatial separation is necessary, in order to allow for a decoupling of the pneumatic valve

units of the mechanical influences such as oscillations and vibrations of technical applications. The long pneumatic shifting travel, when the valve position is changed, is one of the fundamental disadvantages of the mechanical decouplingb [161].

In order to realize a controlled pneumatic automation, the use of fast proportional valves is indispensable implying their direct integration in the industrial application. Thus, long pneumatic switching times can be avoided. However, this results in exposuring the valves to oscillations and vibrations of the appropriate application. In order to control the pneumatic flow independently of external vibrations and piezoelectric effects such as hysteresis, drift and creep, it necessitates a sensor technology and an appropriate sensor electronics. Due to the direct functional integration of this new kind of pneumatic proportional pilot valves into the industrial application, their miniaturization has to be provided. It is focused on a width of 10 mm, a height of 8 mm and a length of 14 mm resulting in a reduction of the previous valve volume (more than 98%).

10.2 Sensor Requirements

By means of a sensor integrated into the bending actuator or the valve housing, tip deflections, the forces affecting the bender's tip and external vibrations affecting the valve housing are to be detected. The force affecting the bender's tip corresponds to the pressure applied by the compressed air during inflow. The conceptional structure of a piezoelectric pneumatic proportional valve with an integrated force/deflection sensor is shown in figure 10.2.
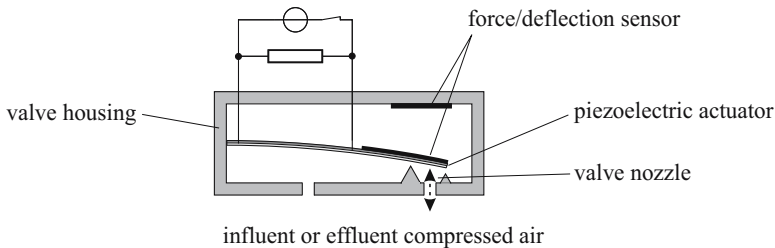
Fig. 10.2. Conceptional structure of a piezoelectric pneumatic proportional valve with an integrated force/deflection sensor

The main focus of the present book is laid on the integrated sensor for *tip deflection measurements*. In order to realize the concept of a piezoelectric pneumatic proportional valve, as it is shown in figure 10.2, the sensor requirements for tip deflection measurements have to be defined. The sensor

requirements for the compensation of hysteresis, creep and drift effects of the piezoelectric bending actuator shown in figure 9.1 are listed in Table 10.1.

Table 10.1. Sensor requirements

measuring range	$0\dots350\,\mu\mathrm{m}$
resolution	$3.5\,\mu\mathrm{m}$
temperature range	$-10\,^{\circ}\mathrm{C}\dots+60\,^{\circ}\mathrm{C}$
cutoff frequency	$350\,\mathrm{Hz}$
long term stability	permanent resolution has to be ensured

Taking the sensor requirements into account, within in the scope of the federal research project EPIETEC, a lot of possible sensor concepts have been elaborated. Here, the systems integration came to the fore, in order to ensure the miniaturization of piezoelectric proportional valves. In scientific literature, a multiplicity of publications concerning piezoelectric actuators with integrated sensors can be found [38–65]. In order to estimate quantitatively the expected sensor signals, calculations have been performed for the considered sensor principles [162]. Finally, the attention was turned to the *capacitive* and *inductive* sensor principle. A detailed representation of the short-listed sensor principles suitable for tip deflection measurements as well as their quantitative signal estimation are presented in appendix N.

The doctoral thesis of A. J. Schmid [67], written within the federal german research project EPIETEC mentioned above, describes the conceptual draw up, development and realization of an economical sensor for detecting forces and deflections based on a *capacitive strain sensor*. Thus, in this book a detailed and separate presentation is abandoned, instead a summarized overview will be given in the next chapter. This book focuses on the one hand on the realization of a sensor electronics for capacitive strain sensors on the other hand on the development and realization of an inductive proximity sensor in combination with a high-accuracy electronic circuit for tip deflection measurements.

11

Tip Deflection Measurement - Capacitive Sensor Principle

A multiplicity of new applications within the field of high-accuracy positioning could be made accessible for piezoceramic bending actuators, if typical effects like hysteresis, creep and drift as well as mechanical and thermal relaxation could be compensated. An aim of the book is the representation of a developed sensor electronics of an integrated capacitive strain sensor for tip deflection measurements. The implementation of the sensor and the appropriate sensor electronics into a closed loop allows for a high-accuracy positioning of a bending actuator independent of inherent piezoelectric effects.

11.1 Sensor Positioning

On the basis of the theoretical model of the static behavior of piezoelectric multilayer beam bending actuators developed in chapter 4, conclusions can be drawn with respect to deflection, blocking force, bending profile, mechanical stress and strain of a bending actuator. The bending deformation is caused by internal piezoelectric moments and by externally affecting quantities like forces, moments and pressure loads. A constant deflection of the bending actuator independent of variable external forces affecting the bender's tip is the base of considerations concerning the sensor integration. In order to maintain a constant operating point, the electric field (driving voltage) is adapted to external forces. Due to the different electrical field strengths in combination with the variable external forces, different bending curvature characteristics, bends and mechanical strains are expected [163]. Figure 11.1 shows different bending curvatures at a constant operating point of $100\,\mu$m with respect to varying external forces affecting the bender's tip.

It is evident, that the bending curvature characteristic is defined by the individual combination of the electrical field E (driving voltage) and the external force F. The higher the external force working against the deflection of the bending actuator is, the higher the electric field has to be, in order to maintain a constant deflection. By means of the increase of the electric field strength and
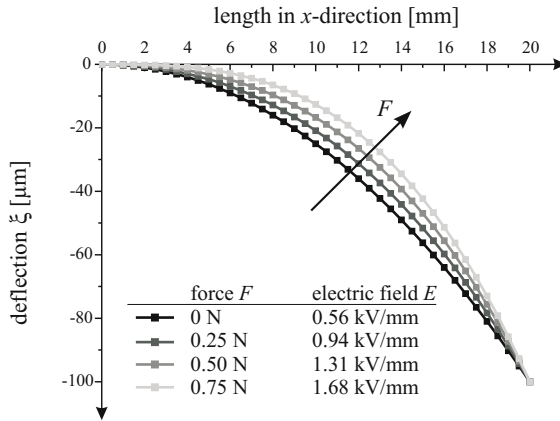
Fig. 11.1. Different bending curvatures at a constant operating point by variation of the external force F and the electric field E

the external force, internal and external moments increase. Thus, a stronger deflection in the middle section of the actuator develops.

The associated strains within the actuator cross section to the bending curvature characteristics shown in figure 11.1 are illustrated in figure 11.2. In the representation of the strains within the actuator cross section two lines can be identified, the strains intersect. The intersection line of the strains in longitudinal direction of the actuator (x-axis) characterizes the main inertia axis. The main inertia axis is identical with the neutral axis of the multilayered beam bending actuator. Along this axis, neither strains nor compressions are found during a bending deformation. Furthermore, an intersection line of strains can be identified in transverse direction (z-axis). Thus, at a constant distance from the clamping ($x = 0$) and the main inertia axis of the actuator, around a fixed point the strains are independent of external loads and applied electric fields [164].

Taking the identified strains within the actuator cross section into consideration, the optimal position of a strain sensor can be determined. On the one hand, the strains increase with increasing distance from the neutral axis, as it is shown in illustration 11.2. Thus, for a strain sensor a maximum sensor signal is expected, if it is attached on the upper or lower surface of the bending actuator. A point of constant strain exists independently of the external force affecting the bender's tip (approx. 1/3 of the free length measured from the clamping). A foil capacitor is applied symmetrically around the point of constant strain (see Fig. 11.3).

In the simplest case, the foil capacitor consists of two planar Cu-electrodes with an intermediate dielectric on polymer basis. If the actuator performs a bending movement, the mechanical strain or compression of the actuator sur-

force F	electric field E
0 N	0.56 kV/mm
0.25 N	0.94 kV/mm
0.50 N	1.31 kV/mm
0.75 N	1.68 kV/mm
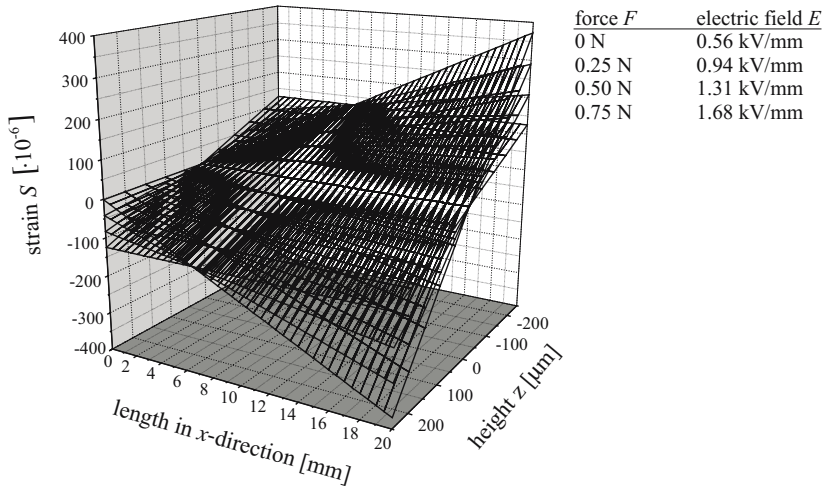
Fig. 11.2. Mechanical strain within the actuator cross section at a constant operating point by variation of the electric field E and the external force F
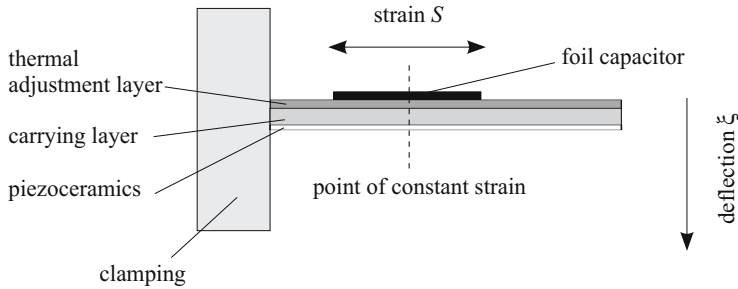
Fig. 11.3. Foil capacitor applied symmetrically around the point of constant strain

face will be transferred to the capacitor. Due to the assumed volume constancy of the foil capacitor, the electrode gap changes. The resulting capacitance change is a measure for the actuator's tip deflection [165]. Due to the very small strains on the actuator surface $\left(S \approx 10^{-4}\right)$ and the associated small capacitance changes (fF-range), it is necessary to develop a special sensor electronics, that is able to transform the capacitance changes into utilizable electrical output signals. In appendix O, different methods for measurement of small capacitances with high resolution are discussed in more detail. They provide a basis for the realization of a high-accuracy senor electronics, that is discussed in the next section.

11.2 Sensor Electronics for Capacitive Strain Sensors

The following section dwells on the realized sensor electronics for capacitive strain sensors. The sensor electronics is based on the "direct method" presented in appendix O. The "direct method" is the most interesting variant with respect to circuit complexity and accuracy of measurement. In order to provide the necessary resolution with a nominal capacitance of approx. 300 pF, the circuit variant "direct method" has to be extended. Thus, the tip deflection hysteresis of the sensor-actuator-system can be measured with the developed high-accuracy sensor electronics.

11.2.1 Electronic Circuit

In order to provide the later application of the sensor electronics in a closed loop, the circuit is developed with respect to the *capacitance change* ΔC_x of the foil capacitors. Figure 11.4 shows the block diagram of the realized sensor electronics for capacitive strain sensors.
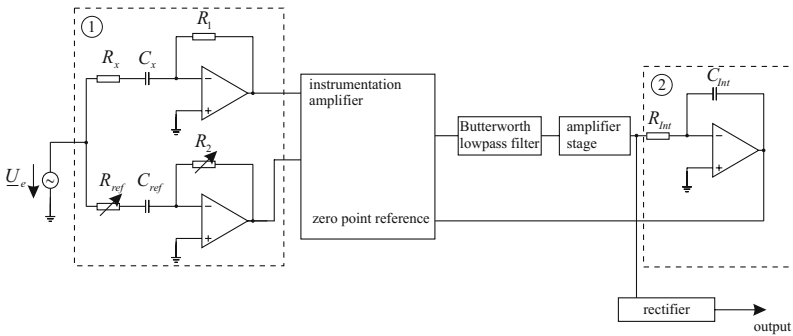
Fig. 11.4. Block diagram of the electronic circuit: 1) the suppression of parasitic capacitances at the input and balancing circuit; 2) automatic DC offset compensation

The input of the circuit is based on the "direct method", presented in section 11.2, which is suitable for suppressing parasitic capacitances effectively. The capacitance change of the foil capacitor C_x is measured in combination with a reference capacitance C_{ref}. The reference capacitance is somewhere in the order of the nominal capacitance of the foil capacitor.

After the instrumentation amplifier, a Butterworth lowpass filter and a further amplifier stage, the difference signal passes an integrator in order to determine the temperature- and time-dependent DC offsets of the used operational amplifiers. The DC offset of the processed signal is fed back to the

instrumentation amplifier as zero point reference. Thus, an automatic DC offset compensation is realized [166].

Input Circuit

The used foil capacitors have a nominal capacitance of 30 pF to 300 pF. Due to the bending deformations of the piezoelectric bending actuator in the μm-range and thus the small surface strains, the capacitance changes are expected to be in the fF-range. In order to measure these small capacitance changes, it is necessary to focus on parasitic capacitances, that can be somewhere in the same order as the capacitance changes to be measured and thus affect the measurement significantly. In order to suppress the parasitic capacitances effectively, the input of the electronic circuit is realized as shown in figure 11.5.
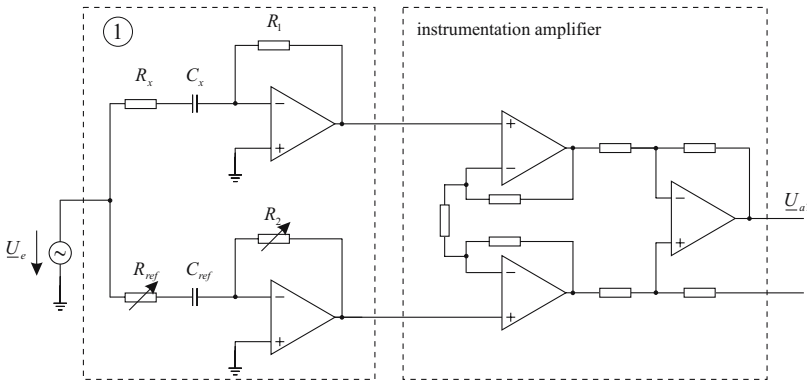
Fig. 11.5. Differential amplifier for suppressing parasitic capacitances and following instrumentation amplifier

By means of the potentiometers R_{ref} and R_2, the output signal of the reference capacitance C_{ref} can be adjusted in phase and amplitude to the output signal of the unstressed foil capacitor C_{x0} (no bending deformation of the actuator). Thus, the difference of both signals can be tuned to zero.

The instrumentation amplifier charges the input sources by infinite input resistances. Due to the preceding balance zero of both signals, the amplifier stage can be realized with a high gain factor. This fact accompanies a high sensitivity simultanously.

The output signal $\underline{U}_{a1}$ of the instrumentation amplifier yields with the gain factor A_1 of the input circuit (derivation see appendix P)

$$\underline{U}_{a1} = j\omega\underline{U}_e A_1 \left[\frac{R_1 C_{x0} - R_2 C_{ref} + j\omega C_{x0} C_{ref}\left(R_{ref}R_1 - R_x R_2\right)}{1 - \omega^2 R_x R_{ref} C_{x0} C_{ref} + j\omega\left(R_x C_{x0} + R_{ref} C_{ref}\right)}\right]. \quad (11.1)$$

Using resistances in the kΩ-range and capacitors in the pF-range at frequencies around 200 kHz, the output signal results with respect to $\omega R_{ref} C_{ref} \ll 1$ in

$$\underline{U}_{a1} = j\omega\underline{U}_e A_1 \left[\frac{R_1 C_{x0} - R_2 C_{ref} + j\omega C_{x0} C_{ref}\left(R_{ref}R_1 - R_x R_2\right)}{1 + j\omega\left(R_x C_{x0} + R_{ref} C_{ref}\right)}\right]. \quad (11.2)$$

The balancing conditions for the output signal ($\underline{U}_{a1} = 0$) are equal to

$$R_2 = \frac{R_1 C_{x0}}{C_{ref}} \quad \text{and} \quad R_{ref} = \frac{R_x C_{x0}}{C_{ref}}. \quad (11.3)$$

If the bending actuator performs a bending deformation, the capacitance of the foil capacitor changes with ΔC_x:

$$C_x = C_{x0} + \Delta C_x \quad (11.4)$$

Thus, from (11.2) the output signal yields

$$\underline{U}_{a1} = \frac{j\omega\underline{U}_e A_1 R_1 \Delta C_x}{1 + j\omega R_x\left(2C_{x0} + \Delta C_x\right)} \approx \omega\underline{U}_e A_1 R_1 \Delta C_x \exp\left(j\phi\right) \quad (11.5)$$

with

$$\phi = \frac{\pi}{2} - \arctan\left[\omega R_x\left(2C_{x0} + \Delta C_x\right)\right]. \quad (11.6)$$

Butterworth Lowpass Filter and Amplifier Stage

A Butterworth lowpass filter of second order is added to the amplifier stage. The cutoff frequency of the Butterworth lowpass filter amounts to $f_{meas} = 200$ kHz and corresponds to the frequency, the electronic circuit is driven with (see Fig. 11.6).

The Butterworth lowpass filter is necessary for the suppression of high frequency error signals, that can appear after generating the difference signal $\underline{U}_{a1}$ and cause a saturation of the following amplifier stage due to voltage overload. The transfer function of a lowpass filter of second order can be described by following equation

$$A\left(s_n\right) = \frac{A_0}{1 + a_1 s_n + b_1 s_n^2}, \quad (11.7)$$

with the coefficients $a_1 = \sqrt{2}$, $b_1 = 1$ and the standardized frequency $s_n = j\Omega_n = j\omega/\omega_0$, where ω_0 corresponds to the cutoff frequency.
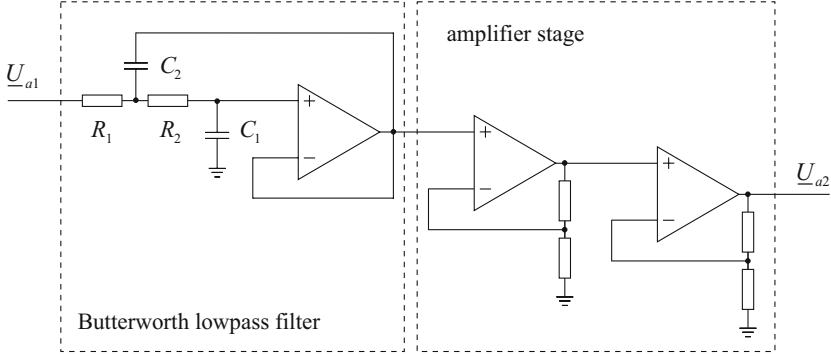
Fig. 11.6. Butterworth lowpass filter for the suppression of high frequency error signals and following amplifier stage

The lowpass filter is followed by an amplifier stage consisting of two noninverting operational amplifiers. With the total gain factor A_2, the output signal $\underline{U}_{a2}$ results in

$$\underline{U}_{a2} = \omega \underline{U}_e A_1 A_2 R_1 \Delta C_x \frac{A_0}{1 + a_1 j \Omega_n - b_1 \Omega_n^2}\, \mathrm{e}^{j\phi} \,. \qquad (11.8)$$

In order to ensure an A/D-conversion, the output signal $\underline{U}_{a2}$ is rectified.

Rectifier

The realized rectifier in figure 11.7 corresponds to a full-wave rectifier with grounded output [167].
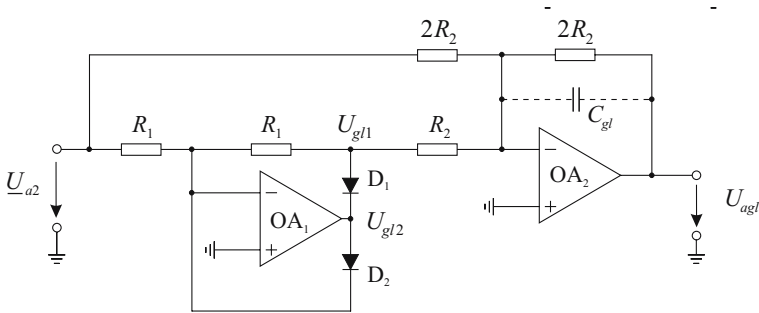
Fig. 11.7. Full-wave rectifier with grounded output

At first, the mechanism of OA_1 is described. For a positive input voltage, the operational amplifier OA_1 works as an inverting amplifier. Thus, the output

voltage U_{gl2} is negative and the diode D_1 is conductive, while the diode D_2 is non-conductive. Thus, it can be written $U_{gl1} = -U_{a2}$. If the input voltage is negative, U_{gl2} becomes positive and the diode D_1 is non-conductive, while the diode D_2 is conductive and thus the amplifier is negatively fed back. It prevents an overmodulation of the amplifier OA_1. U_{gl2} is equal to zero. Since D_1 is non-conductive, U_{gl1} is also equal to zero. In summary, it can be written:

$$U_{gl1}(t) = \begin{cases} -U_{a2}(t) & \text{for } U_{a2} \geq 0 \\ 0 & \text{for } U_{a2} \leq 0 \end{cases} \tag{11.9}$$

Thus, the operational amplifier OA_1 works as *inverting half-wave rectifier*.

The operation amplifier OA_2 extends the circuit to a full-wave rectifier. It forms the expression:

$$U_{agl}(t) = -\left[U_{a2}(t) + 2U_{gl1}(t)\right] \tag{11.10}$$

In combination with (11.9), it follows:

$$U_{agl}(t) = \begin{cases} U_{a2}(t) & \text{for } U_{a2} \geq 0 \\ -U_{a2}(t) & \text{for } U_{a2} \leq 0 \end{cases} \tag{11.11}$$

(11.11) represents the desired function of a full-wave rectifier. With the capacitor C_{gl}, the operational amplifier OA_2 can be extended to a lowpass of first order. If its cutoff frequency is chosen low compared to the lowest signal frequency, a pure DC voltage is measured at the ouput. In order to keep the dead time with the transition of one diode to the other as small as possible, a high slew rate of the operation amplifier OV_1 has to be ensured.

The rectified signal U_{agl} can be expressed by following equation

$$U_{agl} = \left|\overline{\underline{U}_{a2}}\right| = \left|\Re\left\{\frac{\omega R_1 A_1 A_2 \underline{U}_e \Delta C_x}{\sqrt{\left(1 - b_1 \Omega_n^2\right)^2 + a_1^2 \Omega_n^2}} \, e^{j\left[-\arctan\frac{(1-b_1 \Omega_n^2)}{a_1 \Omega_n} + \phi + \omega t\right]}\right\}\right|, \tag{11.12}$$

where $\left|\overline{U_{a2}}\right|$ denotes the absolute mean value with respect to one period T. For the used Butterworth lowpass filter with $\omega = \omega_0$ it can be written

$$U_{agl} = \frac{\omega R_1 A_{tot} \hat{U}_e}{\sqrt{2}} \Delta C_x \cdot \left|\cos\left(\phi + \omega t\right)\right|$$
$$= \frac{\omega R_1 A_{tot} \hat{U}_e}{\sqrt{2}} \Delta C_x \cdot \frac{2}{\pi}, \tag{11.13}$$

where A_{tot} denotes the total gain factor of the complete electronic circuit. The temperature- and time-dependent DC offsets of the individual operational amplifiers of the instrumentation amplifier, the low-pass filter and the amplifier stage represent a problem. The complete DC offset can cause serious problems due to the high gain factor $A_{tot} > 1000$ leading to a DC offset in the Volt range. In order to avoid this effect, an automatic DC offset compensation has been implemented into the electronic circuit.

DC Offset Compensation

In order to realize the DC offset compensation an integrator has been implemented after the amplifier stage and fed back to the instrumentation amplifier. The output signal of the integrator U_{DC} is now the zero reference for the instrumentation amplifier. In figure 11.8 the complete circuit without rectifier is shown.
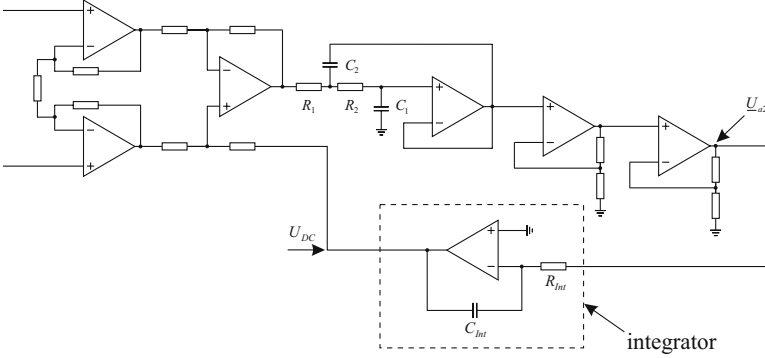
Fig. 11.8. Implemented integrator for DC offset compensation

The output signal U_{DC} of the integrator results in:

$$U_{DC} = -\frac{1}{R_{Int}C_{Int}} \int_0^t U_{a2}\left(\tilde{t}\right) d\tilde{t} + U_{0Int} \tag{11.14}$$

U_{0Int} denotes the DC offset of the integrator. With a cosine shape of the gained voltage signal $U_{a2}(t)$, the DC signal generated by the integrator yields

$$U_{DC} = -\frac{1}{R_{Int}C_{Int}} \int_0^t \left[\hat{U}_{a2} \cos\left(\omega\tilde{t} + \phi\right) + U_{0Inst} + U_{0Filt} + U_{0Ampl}\right] d\tilde{t}$$

$$+ U_{0Int}. \tag{11.15}$$

U_{0Inst}, U_{0Filt} and U_{0Ampl} correspond to the DC offsets of the instrumentation amplifier, the low-pass filter and the amplifier stage. After passing a transient time $t = R_{Int}C_{Int}$, the remaining DC offset of the output signal can be calculated according to

$$U_{offset} = -\frac{\hat{U}_{a2}}{\omega R_{Int}C_{Int}} \sin\left(\omega t + \phi\right) + U_{0Int}. \tag{11.16}$$

In combination with the cutoff frequency of the lowpass filter ω_0, the output signal of the rectifier is equal to

$$U_{agl} = \frac{\sqrt{2}\omega_0 R_1 A_{tot}\hat{U}_e}{\pi}\Delta C_x \left(1 - \frac{1}{\omega_0 R_{Int}C_{Int}}\right) + U_{0Gl} + U_{0Int} \qquad (11.17)$$

Thus, the output signal of the sensor electronics only depends on the DC offsets of the integrator and the rectifier. Furthermore, the output signal U_{agl} of the rectifier is a linear function of the capacitance change ΔC_x.

11.2.2 Static Sensor Performance and Uncertainty of Measurement

With respect to a frequency $f = 200\,\text{kHz}$, a feedback resistor $R_1 = 10\,\text{k}\Omega$, a total gain factor $A_{tot} = 1760$, an integrator time constant $R_{Int}C_{Int} = 1\,\text{s}$ and a voltage amplitude $\hat{U}_e = 2.5\,\text{V}$, the ideal sensor characteristics is calculated, as it is illustrated in figure 11.9. The DC offsets of the integrator and the rectifier have not been taken into account, since they do not influence the transfer coefficient B_C, only a parallel shifting of the sensor characteristics along the axis of ordinates would appear.
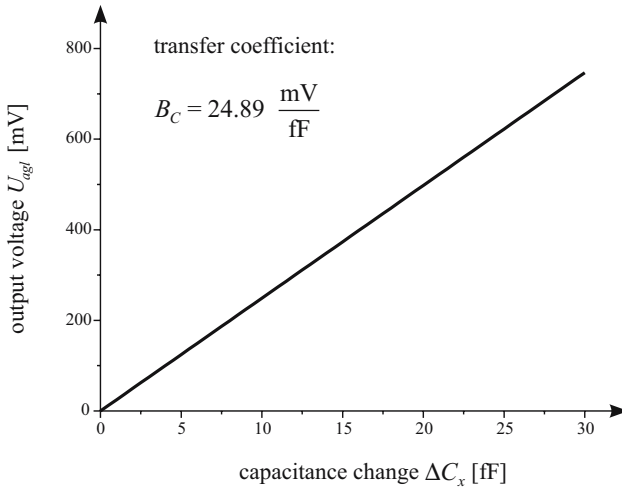
Fig. 11.9. Ideal static sensor characteristics

In the following, the effects of signal variations with respect to both, the amplitude and the frequency, are considered. From (11.17), the output voltage U_{agl} results in

$$U_{agl} = \frac{\sqrt{2}\omega R_1 A_{tot}\hat{U}_e \Delta C_x}{\pi}.$$ (11.18)

If R_{Int} and C_{Int} are chosen appropriately, the error caused by the automatic offset compensation is very small and can therefore be neglected. Furthermore, the individual offset voltages and their drift characteristics are neglected. Taking the total differential of (11.18) yields [168]:

$$\Delta U_{agl} = \left| \frac{\partial U_{agl}}{\partial \hat{U}_e} \Delta \hat{U}_e \right| + \left| \frac{\partial U_{agl}}{\partial \omega} \Delta \omega \right|$$

$$= \left| \frac{\sqrt{2}\omega R_1 A_{tot}\Delta C_x}{\pi} \Delta \hat{U}_e \right| + \left| \frac{\sqrt{2}R_1 A_{tot}\hat{U}_e \Delta C_x}{\pi} \Delta \omega \right|$$ (11.19)

An example for the sensitivity to variations in the measurement signal is to be given. Assuming a signal frequency $f = 200\,\text{kHz}$, a signal amplitude $\hat{U}_e = 2.5\,\text{V}$, a total gain factor $A_{tot} = 1760$ and a capacitance change $\Delta C_x = 30\,\text{pF}$, (11.19) results in

$$\Delta U_{agl} = 0.29 \cdot \Delta \hat{U}_e + 3.73 \frac{\mu\text{V}}{\text{Hz}} \cdot \Delta \omega$$ (11.20)

(11.20) shows, that the sensor electronics responds more sensitively to variations in the signal amplitude than to variations in the signal frequency. Thus, the amplitude stability of the chosen function generator is of great importance.

11.2.3 Measurement Results

In the following, measurement results are presented concerning the realized sensor-actuator-system in combination with the developed sensor electronics.

Hysteresis Measurement

The tip deflection has been measured in accordance with the measurement setup shown in figure 9.2. The deflection measurement by means of the laser triangulator provides a comparison and bench mark for the capacitive sensor and the developed sensor electronics. Figure 11.10 shows the tip deflection ξ versus the electric field E (driving voltage). The measurement shows the ability of the capacitive strain sensor in combination with the developed sensor electronics to detect the hysteresis being typical for bending actuators.

Linearity Error and Hysteresis Error

The ideal static sensor characteristic is defined by a straight line with a gradient characterized by the transfer coefficient B_0 (see Fig. 11.9). A linear correlation exists between the output signal U_{agl} and the physical measurement
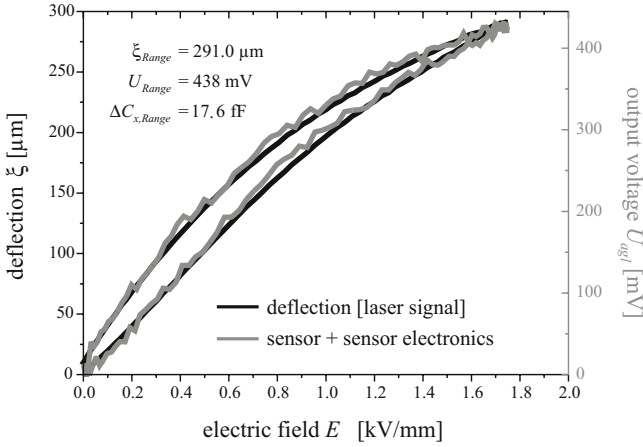
Fig. 11.10. Beam deflection ξ and sensor signal U_{agl} showing the deflection hysteresis versus applied electric field E

value ΔC_x and ξ, respectively. The real static characteristics of capacitive strain sensors is characterized by bias and random deviations from the ideal output signal curvature characteristics (see Fig. 11.11).
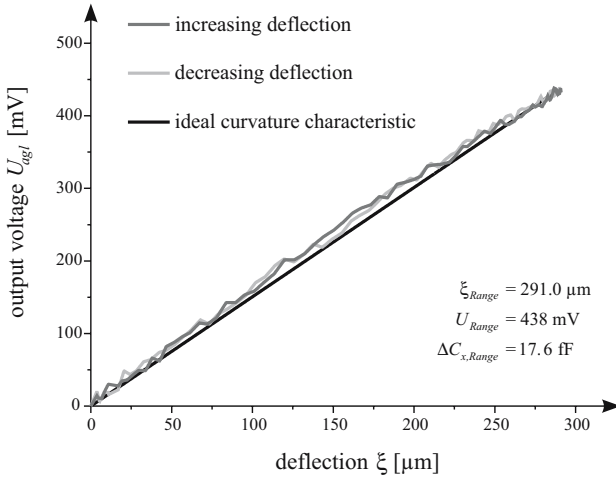
Fig. 11.11. Ideal static sensor characteristics (desired characteristic curve) and real static sensor characteristics (terminal-based conformity)

It is evident, that the experimental results confirm the theoretical prediction of the linear correlation between sensor electronics signal U_{agl} and capacitance change ΔC_x and deflection ξ, respectively. The transfer coefficient B_0 of the sensor system amounts to $B_0 = 1.50\,\text{mV}/\mu\text{m}$.

The reasons for the deviations from the ideal transient characteristics go back to the sensor's physical transformation principle, the influence of manufacturing tolerances, the influences of the assembly technology as well as the sensor electronics. The linearity error F_{Lin} and the hysteresis error F_{Hys} can be derived from the maximum values of the deviations. Both types of errors belong to the class of bias errors. The linearity error characterizes the deviation of the real sensor characteristics from the ideal one, the hysteresis error characterizes the maximum deviation of the error curvature with respect to a loading and an unloading of the sensor system [169]. In order to determine the linearity and hysteresis error of the sensor system, the measuring data in figure 11.11 are used. Here a terminal-based conformity is assumed [170]. The maximum difference between the sensor electronics signal and the desired characteristic curve related to the nominal value of the sensor electronics signal ($U_{Range} = 438\,\text{mV}$) yields a linearity error $F_{Lin} = 4.92\%$ (see Fig. 11.12a).

The hysteresis error results from the maximum difference between the sensor electronics signal with respect to an increasing and decreasing deflection related to the nominal value of the sensor electronics signal. Evaluation of the measurement data in figure 11.11 yields a hysteresis error $F_{Hys} = -3.19\%$ (see Fig. 11.12b).
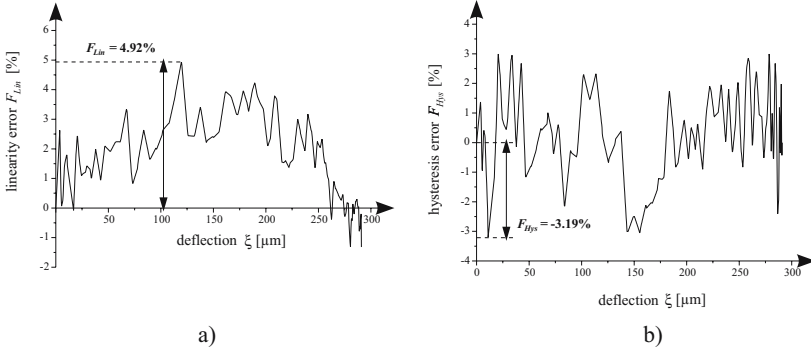
Fig. 11.12. (a) Linearity error and **(b)** hysteresis error of the capacitive displacement sensor.

The linearity and hysteresis error result in the static total error F_G of the sensor system according to

$$F_G = \sqrt{F_{Lin}^2 + F_{Hys}^2}. \tag{11.21}$$

The combination of a capacitive strain sensor with the developed sensor electronics results in a total error $F_G = 5.86\%$ corresponding to a maximum deviation of $\Delta\xi = 17.1\,\mu m$ and $\Delta C_x = 1.0\,fF$ between the real and ideal static curvature characteristics, respectively. It should be noted, that the linearity errors can be further minimized by means of a suitable secondary electronics.

12

Tip Deflection Measurement - Inductive Sensor Principle

The very small capacitance changes of the capacitive distance sensor presented in chapter 11 represent a disadvantage. The requirements to the sensor electronics of the capacitive sensor are enormous, as far as resolution and electromagnetic shielding are concerned. Thus, this sensor principle is only suitable for an integrated sensor-actuator-system under certain circumstances.

Within the scope of the federal research project EPIETEC, the conceptional development of a second distance sensor was pursued. The function of the favored distance sensor is based on an inductive, non-contact measurement principle. Compared to the capacitive sensor, on the one hand the inductive sensor shows a very high inductance change, on the other hand the size of the sensor in combination with the sensor electronics allows for the use in applications, where small dimensions of a sensing system are needed.

In the following, it is dwelled on the operational mode and the realization of an inductive proximity sensor in combination with a high-accuracy sensor electronics. Particularly, the characterization of the inductive sensor with respect to its static and dynamic transient characteristics is in the focus of attention.

12.1 Measurement Setup and Basic Structure of the Inductive Proximity Sensor

The measurement setup of the non-contact inductive proximity sensor for tip deflection measurements is shown in figure 12.1.

The non-contact inductive proximity sensor consists of a microelectronic circuit realized as an ASIC (Application Specific Integrated Circuit), courtesy of the EPFL (Switzerland). Two external 3D-microcoils are connected to the ASIC. One coil acts as sensing coil, the other one provides a reference. The sensing coil is connected to the integrated oscillator 1. Its resonant frequency f_1 changes during an approach of the actuator's tip (see Fig. 12.2).
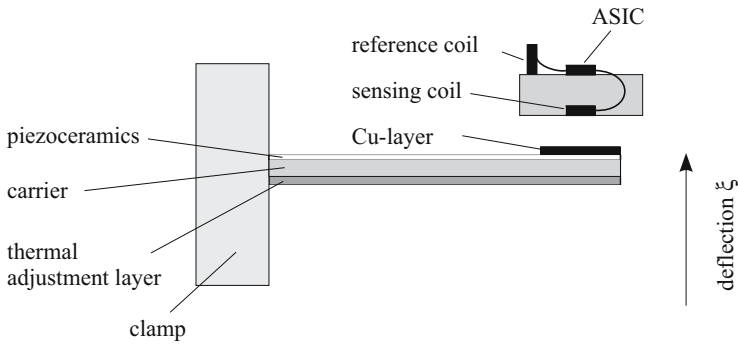
Fig. 12.1. Miniaturized non-contact inductive proximity sensor to detect the tip deflection of a piezoelectric bending actuator
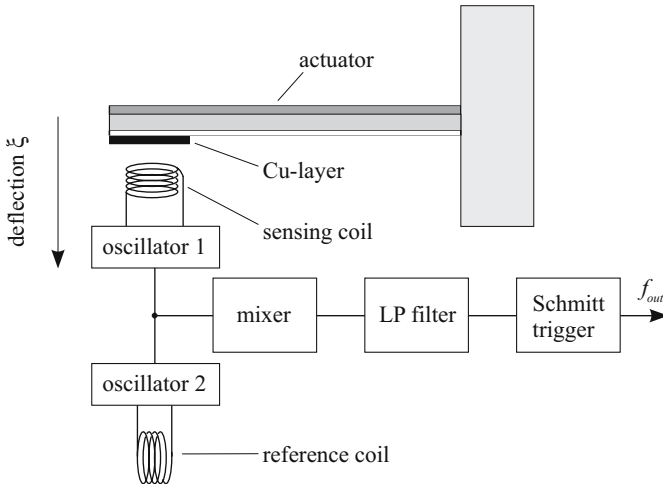
Fig. 12.2. Schematics of the inductive proximity sensor electronics to detect the tip deflection of a beam bending actuator

If the sensing coil is driven by an alternating current i_1, an alternating magnetic field will be generated. In its turn, it causes eddy currents within the Cu-layer generating magnetic fields, that counteract the external magnetic field (*Lenz's law*). As a consequence, the external magnetic field decreases resulting in a decrease ΔL_1 of the inductance L_1 of the sensing coil. Thus, the changing resonant frequency of the oscillator 1 is a measure for the deflection ξ of the beam bender's tip. The reference coil is connected to the integrated oscillator 2 and is arranged in such a manner, that it can not be influenced by the Cu-layer. With its constant inductance L_2, the reference coil provides the generation of the reference frequency f_2. By means of the mixer, the difference

$|f_1 - f_2|$ and the sum $|f_1 + f_2|$ of both frequency signals are evaluated and passed on the following lowpass filter. The lowpass filter suppresses the deterministically caused higher-frequency signals. The following Schmitt trigger provides a shaping of the difference of both frequency signals, thus the output signal f_{out} is available in binary form (TTL level) [171, 172].

12.2 Functioning of the Inductive Proximity Sensor

Both oscillator circuits consist of an integrated capacitance C as well as an active cell maintaining the oscillation. The sensing and reference coil complete the respective L-C-resonant circuit. In both resonant circuits, the capacitance C can be assumed to be equal. The resonant frequency of an L-C-resonant circuit is generally defined by

$$f_0 = \frac{1}{2\pi\sqrt{LC}}. \tag{12.1}$$

Thus, the frequency f_2 of the resonant circuit 2 is specified by the reference coil L_2:

$$f_2 = \frac{1}{2\pi\sqrt{L_2 C}} \tag{12.2}$$

If a conductive material approaches the sensing coil, eddy currents are generated within this material, that weaken the alternating magnetic field of the measuring coil. Thus, the effective inductance $L_e = L_1 - \Delta L_1$ of the sensing coil decreases and the oscillator's resonant frequency increases from f_1 up to

$$f_e = \frac{1}{2\pi\sqrt{L_e C}} = \frac{1}{2\pi\sqrt{(L_1 - \Delta L_1)C}} = f_1\sqrt{\frac{L_1}{L_1 - \Delta L_1}}. \tag{12.3}$$

The general correlation between the relative frequency change and the relative inductance change concerning the oscillator 1 results in combination with $f_e = f_1 + \Delta f_1$ and by taking of the total differential in

$$\left|\frac{\Delta f_1}{f_1}\right| = \left|\frac{\left|\frac{\partial f_1}{\partial L_1}\right|\Delta L_1}{f_1}\right| = \frac{1}{2}\left|\frac{\Delta L_1}{L_1}\right|. \tag{12.4}$$

Since the relative inductance change ΔL_1 can amount up to -30% during approximation of a conductive material from a distance of several centimeters to almost contact with miniaturized planar coils, the maximum relative frequency change can amount $+15\%$ with respect to (12.4). The mixer (see Fig. 12.2) evaluates the difference of the two frequencies f_e and f_2. In order to achieve a reliable and a non-disturbed signal on TTL level, the difference signal is filtered by a lowpass filter and shaped by a Schmitt trigger. Thus, the output frequency results in

$$f_{out} = |f_e - f_2|. \tag{12.5}$$

Dependent on the relative inductance change concerning the oscillator 1, the relative change of the output frequency yields in combination with (12.5)

$$\left| \frac{\Delta f_{out}}{f_{out}} \right| = \left| \frac{\left| \frac{\partial f_{out}}{\partial L_1} \right|_{\Delta L_1 = 0} \Delta L_1}{f_{out}} \right| = \frac{1}{2} \underbrace{\left| \frac{\Delta L_1}{L_1} \right|}_{\longrightarrow 15\%} \underbrace{\left| \frac{\sqrt{L_2}}{\sqrt{L_1} - \sqrt{L_2}} \right|}_{\gg 1}. \tag{12.6}$$

Equation (12.6) shows, that a very high relative change of the output frequency can be achieved, if both nominal inductances of the sensing and reference coil are nearly equal, although the change of the inductance L_1 and thus, the distance change between the sensing coil and the conductive layer can be very small. This aspect constitutes the choice of an inductive proximity sensor for high-accuracy tip deflection measurements of a piezoelectric bending actuator. In further considerations, two 3D-microcoils with the nominal inductances $L_1 = 7.62\,\mu H$ (sensing coil) and $L_2 = 8.30\,\mu H$ (reference coil) are used. By means of a high precision LCR-meter (type: HP 4284A), the nominal inductances were determined with respect to a frequency of $f_{meas} = 1\,MHz$.

12.2.1 Output Signal Performance

If the piezoelectric bending actuator is in the *non-deflection state* ($\xi = 0$), then the output frequency of the sensor electronics amounts to $f_{out} = 360\,kHz$. A thin copper sheet ($d = 48\,\mu m$) is applied to the bender's tip (see Fig. 12.2). Copper shows a relative permeability of $\mu_r = 1$ and a high conductivity $\left(\kappa_{Cu} = 56.18 \cdot 10^6\,S\,m^{-1} \right)$ [173, 174]. Thus, it is ensured, that ohmic losses are very small within the layer. The choice of the copper sheet thickness is based on the fact, that with arising resonant frequencies of the two oscillators ($f_1 \approx f_2 \approx 17\,MHz$), the eddy current is displaced to the surface of the copper layer (*skin effect*).

In order to constrict the formation of the eddy currents as few as possible, the thickness of the metallic layer should amount to approx. a triple of the *equivalent conductive layer thickness*, which can be generally calculated in following way [175]:

$$\delta = \frac{1}{\sqrt{\pi f \mu_0 \mu_r \kappa}} \tag{12.7}$$

In case of the arising resonant frequency of the oscillator 1, the equivalent conductive layer thickness of the copper sheet amounts to $\delta \approx 16\,\mu m$.

If the applied copper layer approaches the sensing coil up to almost contact, the output frequency increases up to $f_{out} = 660\,kHz$. For the following consideration, the dependence of the output frequency on the distance x between the

sensing coil and the copper layer is assumed to be linear. This does not correspond to the reality, however, the understanding and the representation are simplified. Futhermore, the bending actuator is to be driven with a sinusoidal voltage of the frequency $f_{mod} = 2\,\text{kHz}$. The driving voltage is superposed by a DC offset, thus the bending actuator never deflects over its rest position into the upper area shown in figure 12.2. The time-dependent deflection characteristic of the bender's tip is illustrated in figure 12.3. Here, nonlinearities and hysteresis effects are neglected. The maximum deflection is assumed to be $300\,\mu\text{m}$ corresponding to the contact between sensing coil and copper sheet.
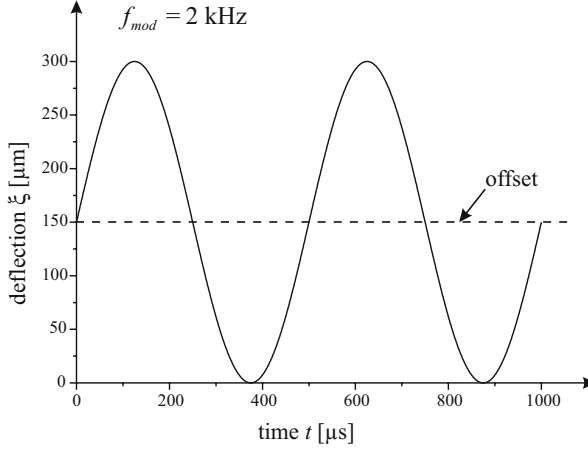
Fig. 12.3. Calculated deflection ξ of the bending actuator with respect to a sinusoidal voltage of the frequency $f_{mod} = 2\,\text{kHz}$

If the bender is in rest position ($\xi = 0$), f_{out} is assumed to be minimal, thus $360\,\text{kHz}$, for maximum deflection f_{out} is assumed to be maximal, thus $660\,\text{kHz}$. Due to the sinusoidal deflection characteristics of the bending actuator and the correlated sinusoidal distance change between the sensing coil and copper layer, the output frequency of the ASIC also shows a sinusoidal variation in time, if nonlinearities and hysteresis effects are neglected. The output signal is composed of a carrier frequency signal $f_T = 510\,\text{kHz}$ (offset deflection of the bending actuator) and an alternating frequency signal with the amplitude $\Delta f_T = 150\,\text{kHz}$ caused by the modulation frequency f_{mod} of the sinusoidal tip movement:

$$f_{out}(t) = \Delta f_T \sin(2\pi f_{mod} t) + f_T \tag{12.8}$$

The time-dependent characteristic of the output frequency is illustrated in figure 12.4. Now, the phase signal $\varphi_{out}(t)$ of the non-contact inductive proximity sensor is considered. In order to represent its time-dependent characteristic, the angular frequency $\omega_{out}(t) = 2\pi f_{out}(t)$ has to be integrated with respect
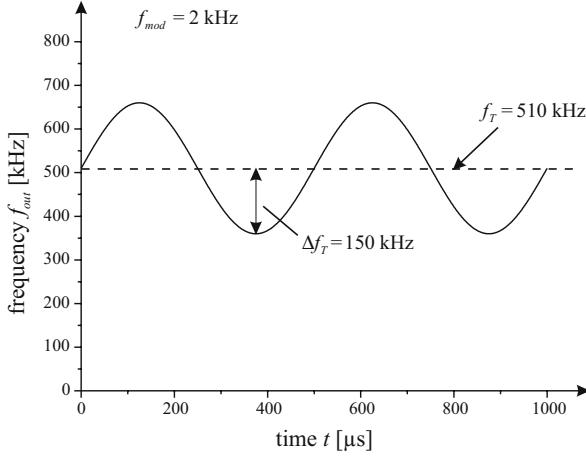
Fig. 12.4. Calculated output frequency f_{out} of the ASIC influenced by the 2 kHz oscillation of the bender's tip

to time t. At time $t = 0$, $\varphi_{out}(t = 0) = 0$ is assumed. It can be written:

$$\varphi_{out}(t) = \int_{o}^{t} \omega_{out}(t') \, dt'$$

$$\Leftrightarrow \varphi_{out}(t) = 2\pi \int_{o}^{t} (\Delta f_T \sin(2\pi f_{mod} t') + f_T) \, dt'$$

$$\Leftrightarrow \varphi_{out}(t) = \frac{\Delta f_T}{f_{mod}} [1 - \cos(2\pi f_{mod} t)] + 2\pi f_T t \qquad (12.9)$$

The time-dependent phase signal is shown in figure 12.5.

The phase signal is shaped by the integrated Schmitt trigger. Thus, a square wave signal on TTL level is generated, that can be calculated according to

$$U_{out} = 2.5 \, \text{V} \, \text{sign} [\sin(\varphi_{out})] + 2.5 \, \text{V}.$$

For the purpose of a better representation, in figure 12.6 the frequency modulated TTL signal is shown in a smaller time interval $0 \leq t \leq 100 \, \mu s$. The frequency modulated voltage signal, that can be read in and evaluated, represents a measure for the tip deflection ξ of the bending actuator.
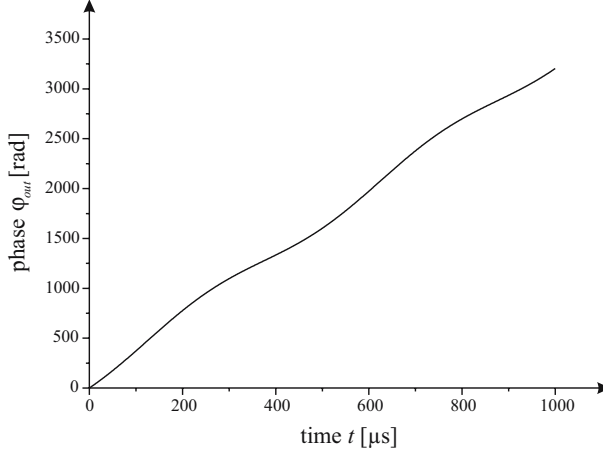
Fig. 12.5. Calculated phase angle $\varphi_{out}(t)$ as a function of time assuming $\varphi_{out}(t=0)=0$
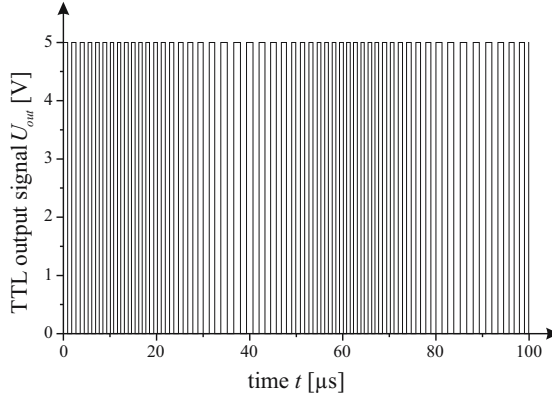
Fig. 12.6. Calculated TTL output signal

12.3 Equivalent Network Representation

The equivalent network of a sensing coil close to a conductive layer is illustrated in figure 12.7a [176].

It is assumed, that the layer the eddy current i_s flows in, can be represented as a series connection of the inductance L_s and the resistance R_s. The sensing coil is represented by the inductance L_1 and the resistance R_1. Due to the coupling between both L-R-circuits, an alternate circuit representation is to be achieved, which allows for the representation of the arising effective inductance
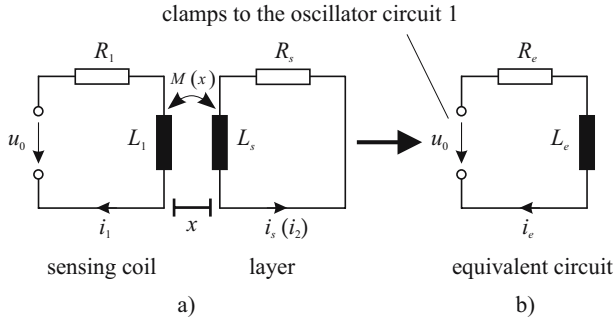
Fig. 12.7. Inductive interaction between sensing coil and conductive layer. - (a) interconnection by means of the distance-dependent mutual inductance $M(x)$ (transformer); (b) equivalent circuit representation.

L_e as a function of the distance x between sensing coil and conductive layer (see Fig. 12.7b).

In order to describe the inductive interaction between the conductive layer and the sensing coil, the equivalent circuit representation of a transformer without iron core is considered (see Fig. 12.8).
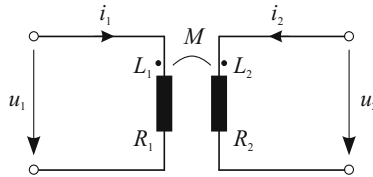
Fig. 12.8. General circuit representation of a transformer without iron core with coils wound in the same direction

If two coils with N_1 and N_2 turns are considered, the following pair of equations can be formulated for the two meshes of the circuit in figure 12.8, taking Lenz's law into account:

$$-u_1 + i_1 R_1 = -N_1 \frac{d\Phi_1}{dt} \tag{12.10}$$

$$-u_2 + i_2 R_2 = -N_2 \frac{d\Phi_2}{dt} \tag{12.11}$$

The quantities Φ_1 and Φ_2 correspond to the magnetic flux correlated with coil 1 and 2, respectively [177]. The respective fluxes are proportional to the currents i_1 and i_2:

$$N_1 \Phi_1 = L_1 i_1 + M i_2 \tag{12.12}$$

$$N_2 \Phi_2 = L_2 i_2 + M i_1 \tag{12.13}$$

In the equations (12.12) and (12.13) the quantities L_1 and L_2 denote the self-inductances, the quantity M denotes the mutual inductance. Taking (12.12) and (12.13) into consideration, the equations (12.10) and (12.11) can be re-formulated:

$$-u_1 + i_1 R_1 = -L_1 \frac{di_1}{dt} - M \frac{di_2}{dt} \tag{12.14}$$

$$-u_2 + i_2 R_2 = -L_2 \frac{di_2}{dt} - M \frac{di_1}{dt} \tag{12.15}$$

In the following, the correlation formulated in the equations (12.14) and (12.15) is applied to the equivalent circuit representation shown in figure 12.7a. Following analogies are achieved:

$$u_1 = u_0, \quad i_1 = i_1, \quad i_2 = i_s, \quad u_2 = 0 \tag{12.16}$$

(12.14) and (12.15) can be reformulated according to

$$u_0 = i_1 R_1 + L_1 \frac{di_1}{dt} + M \frac{di_s}{dt} \tag{12.17}$$

$$0 = i_s R_s + L_s \frac{di_s}{dt} + M \frac{di_1}{dt}. \tag{12.18}$$

In case of a stady state of the currents and voltages, the complex root mean square values result in:

$$\underline{U}_0 = (R_1 + j\omega L_1)\,\underline{I}_1 + j\omega M \underline{I}_s \tag{12.19}$$

$$0 = (R_s + j\omega L_s)\,\underline{I}_s + j\omega M \underline{I}_1 \tag{12.20}$$

Rearranging of (12.20) with respect to the eddy current $\underline{I}_s$ and following insertion into (12.19) yields the potential difference at the clamps of the ASIC's oscillator 1

$$\underline{U}_0 = \underline{I}_1 \left[R_1 + \frac{\omega^2 M^2}{R_s^2 + \omega^2 L_s^2} R_s + j\omega \left(L_1 - L_s \frac{\omega^2 M^2}{R_s^2 + \omega^2 L_s^2} \right) \right]. \tag{12.21}$$

Assuming a good conductivity of the layer $\left(R_s^2 \ll \omega^2 L_s^2 \right)$ applied to the bender's tip, (12.21) can be simplified:

$$\underline{U}_0 = \underline{I}_1 \left[R_1 + \frac{M^2}{L_s^2} R_s + j\omega \left(L_1 - \frac{M^2}{L_s} \right) \right] = \underline{I}_1 \left(R_e + j\omega L_e \right) \tag{12.22}$$

Thus, the equivalent resistance R_e and the equivalent inductance L_e of the equivalent network in figure 12.7b are known.

By means of the definition of the coefficient of coupling [178]

$$k\left(x\right) = \frac{M\left(x\right)}{\sqrt{L_1 L_s}}, \tag{12.23}$$

the mutual inductance can be formulated as a function of distance x between the bender's tip and sensing coil. Thus, the equivalent quantities R_e and L_e are also dependent on the distance x according to

$$R_e\left(x\right) = R_1 + R_s \frac{L_1}{L_s} k^2\left(x\right) \tag{12.24}$$

and

$$L_e\left(x\right) = L_1 \left[1 - k^2\left(x\right)\right]. \tag{12.25}$$

With respect to (12.25), the relative inductance change yields

$$\frac{L_1 - L_e\left(x\right)}{L_1} = \frac{\Delta L_1}{L_1} = k^2\left(x\right). \tag{12.26}$$

Furthermore, with respect to (12.1), the basic inductance L_1 $(x \longrightarrow \infty)$ is correlated with the frequency f_1 of the oscillator 1:

$$L_1 = \frac{1}{4\pi^2 f_1^2 C} \tag{12.27}$$

Similarly, the effective inductance yields

$$L_e\left(x\right) = \frac{1}{4\pi^2 f_e^2\left(x\right) C}. \tag{12.28}$$

Thus, (12.26) can be reformulated:

$$\frac{\Delta L_1}{L_1} = 1 - \left(\frac{f_1}{f_e\left(x\right)}\right)^2 \tag{12.29}$$

Since the frequencies f_1 and $f_e(x)$ can be measured, the relative inductance change and thus the coefficient of coupling $k\left(x\right)$ can be determined experimentally. However, at this point it is a question, whether the experimentally achieved data concerning the distance-dependent relative inductance change can also be achieved by an analytical formulation. In the following section, the physical fundamentals of the available inductive proximity sensor are discussed in detail. They provide a basis for the description of the distance-dependent relative inductance change in closed form analysis. In a following section, the analytical calculations are compared to experimental results.

12.4 Inductance of a Circular Loop Influenced by a Conductive Layer

The arrangement of a circular loop opposite to a conductive layer as shown in figure 12.9 is the starting point of following considerations. With respect to the origin of the coordinate system, the circular loop is parallel to the surface layer in distance $z = -d$. The represented arrangement is axially symmetric, thus in the following, it is described by means of cylindrical coordinates (r, θ, z).
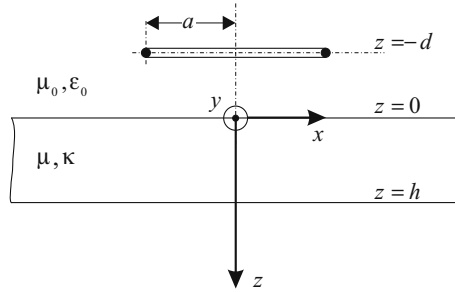
Fig. 12.9. Arrangement of a circular loop opposite to a conductive layer (side view)

With respect to Maxwell's equations for time-variable fields, the electric field **E** generates a magnetic field **H** by means of the conduction and displacement current. On its part, the magnetic field **H** generates an electric field by means of induction. Thus, electric and magnetic fields are connected with each other [179]. For the physical description of the arrangement illustrated in figure 12.9, the vector of the magnetic field strength $\mathbf{H}(\mathbf{r}, t)$ is of interest.

12.4.1 Solution Approach

The fundamental describing Maxwell equations are:

$$\operatorname{curl} \mathbf{E}(\mathbf{r}, t) = -\frac{\partial \mathbf{B}(\mathbf{r}, t)}{\partial t} \tag{12.30}$$

$$\operatorname{curl} \mathbf{H}(\mathbf{r}, t) = \frac{\partial \mathbf{D}(\mathbf{r}, t)}{\partial t} + \mathbf{J}(\mathbf{r}, t) \tag{12.31}$$

Taking the material-specific relations for the electric displacement $\mathbf{D}(\mathbf{r}, t)$, the current density $\mathbf{J}(\mathbf{r}, t)$ and the magnetic induction $\mathbf{B}(\mathbf{r}, t)$ in accordance with

$$\mathbf{D}(\mathbf{r}, t) = \varepsilon \mathbf{E}(\mathbf{r}, t) \tag{12.32}$$

$$\mathbf{J}(\mathbf{r}, t) = \kappa \mathbf{E}(\mathbf{r}, t) \tag{12.33}$$

and

$$\mathbf{B}\left(\mathbf{r},t\right) = \mu\mathbf{H}\left(\mathbf{r},t\right) \tag{12.34}$$

into account, yields:

$$\operatorname{curl}\mathbf{E}\left(\mathbf{r},t\right) = -\mu\frac{\partial\mathbf{H}\left(\mathbf{r},t\right)}{\partial t} \tag{12.35}$$

$$\operatorname{curl}\mathbf{H}\left(\mathbf{r},t\right) = \varepsilon\frac{\partial\mathbf{E}\left(\mathbf{r},t\right)}{\partial t} + \kappa\mathbf{E}\left(\mathbf{r},t\right) \tag{12.36}$$

In (12.35) and (12.36), it is assumed, that the permittivity ε, the conductivity κ and the permeability μ exhibit a time-independent, isotropic behavior. The application of the vector operation "curl" to equation (12.36) and following insertion of (12.35) yields:

$$\operatorname{curl}\operatorname{curl}\mathbf{H}\left(\mathbf{r},t\right) = -\varepsilon\mu\frac{\partial^2\mathbf{H}\left(\mathbf{r},t\right)}{\partial t^2} - \kappa\mu\frac{\partial\mathbf{H}\left(\mathbf{r},t\right)}{\partial t} \tag{12.37}$$

With respect to the calculation rules of vector analysis, it can generally be written [180]:

$$\operatorname{curl}\operatorname{curl}\mathbf{X} = \operatorname{grad}\operatorname{div}\mathbf{X} - \Delta\mathbf{X} \tag{12.38}$$

Thus, (12.37) can be reformulated:

$$\operatorname{grad}\operatorname{div}\mathbf{H}\left(\mathbf{r},t\right) - \Delta\mathbf{H}\left(\mathbf{r},t\right) = -\varepsilon\mu\frac{\partial^2\mathbf{H}\left(\mathbf{r},t\right)}{\partial t^2} - \kappa\mu\frac{\partial\mathbf{H}\left(\mathbf{r},t\right)}{\partial t} \tag{12.39}$$

Taking the fact into account, that there is no source of the magnetic field ($\operatorname{div}\mathbf{H}\left(\mathbf{r},t\right) = 0$), equation (12.39) can be simplified:

$$\Delta\mathbf{H}\left(\mathbf{r},t\right) - \varepsilon\mu\frac{\partial^2\mathbf{H}\left(\mathbf{r},t\right)}{\partial t^2} - \kappa\mu\frac{\partial\mathbf{H}\left(\mathbf{r},t\right)}{\partial t} = \mathbf{0} \tag{12.40}$$

By means of equation (12.40), for the the metallic semi-infinite space ($\varepsilon = 0$, μ, κ) and the medium air ($\varepsilon = \varepsilon_0$, $\mu = \mu_0$, $\kappa = 0$), the following differential equations can be derived:

$$\Delta\mathbf{H}\left(\mathbf{r},t\right) - \kappa\mu\frac{\partial\mathbf{H}\left(\mathbf{r},t\right)}{\partial t} = \mathbf{0} \qquad\qquad \text{metal} \tag{12.41}$$

$$\Delta\mathbf{H}\left(\mathbf{r},t\right) - \varepsilon_0\mu_0\frac{\partial^2\mathbf{H}\left(\mathbf{r},t\right)}{\partial t^2} = \mathbf{0} \qquad\qquad \text{air} \tag{12.42}$$

The expressions (12.41) and (12.42) represent the electromagnetic skin and wave equation concerning the magnetic field in metal and air, respectively. Since cylindrical coordinates are used, the Laplacian operator Δ has to be formulated explicitly [181].

Furthermore, if the angle independence of the magnetic field ($\partial\mathbf{H}\left(\mathbf{r},t\right)/\partial\theta = 0$)

resulting from symmetry characteristics is taken into consideration, the necessary differential equations of the z-component of the magnetic field result in their final formulation [182]:

$$\frac{1}{r}\frac{\partial}{\partial r}\left(r\frac{\partial H_z}{\partial r}\right) + \frac{\partial^2 H_z}{\partial z^2} - \kappa\mu\frac{\partial H_z}{\partial t} = 0 \qquad\qquad \text{metal} \quad (12.43)$$

$$\frac{1}{r}\frac{\partial}{\partial r}\left(r\frac{\partial H_z}{\partial r}\right) + \frac{\partial^2 H_z}{\partial z^2} - \varepsilon_0\mu_0\frac{\partial^2 H_z}{\partial t^2} = 0 \qquad\qquad \text{air} \qquad (12.44)$$

Assuming an alternating current $\underline{I}(t) = \underline{I}\,e^{j\omega t}$ in the circular loop, an alternating magnetic field is generated, too. The general solution for the alternating magnetic field within the conductive layer is achieved by means of separation of variables:

$$\underline{H}_z(r,z,t) = e^{j\omega t}\int_0^\infty J_0(ur)\left[\underline{A}_1\,e^{-z\sqrt{u^2+j\omega\kappa\mu}} + \underline{A}_2\,e^{z\sqrt{u^2+j\omega\kappa\mu}}\right]du \quad (12.45)$$

The quantity $\underline{H}_z(r,z,t)$ represents the complex time function of the z-component of the magnetic field. Later on, the quantities $\underline{A}_1$ and $\underline{A}_2$ are solved by means of corresponding boundary conditions. The function $J_0(ur)$ denotes the Bessel function of first kind and order zero [183]. In appendix Q, the derivation of the solution (12.45) is represented in detail .

The general solution for the alternating magnetic field in the air is similar to (12.45), while the term $j\omega\kappa\mu$ has to be replaced by the term $-\varepsilon_0\mu_0\omega^2$. Due to the arising oscillation frequency (oscillator 1) of $f \approx 17\,\text{MHz}$ of the available inductive proximity sensor, compared to the considered range of u the term $-\varepsilon_0\mu_0\omega^2$ can be neglected. Thus, the alternating magnetic field in the air is formulated in following way:

$$\underline{H}_z(r,z,t) = e^{j\omega t}\int_0^\infty J_0(ur)\left[\underline{B}_1\,e^{-zu} + \underline{B}_2\,e^{zu}\right]du \qquad (12.46)$$

12.4.2 Magnetic Field of a Circular Loop

The magnetic field of a circular loop in the plane $z = -d$ (see Fig. 12.9) caused by an alternating current $\underline{I}(t) = \underline{I}\,e^{j\omega t}$ can be described by analogy with equation (12.46) [182].

$$\underline{H}_z(r,z,t) = e^{j\omega t}\int_0^\infty \underline{B}_1\,e^{-zu}\,J_0(ur)\,du \qquad (z > -d), \qquad (12.47)$$

where

$$\underline{B}_1 = \frac{1}{2} a u \underline{I} \, \mathrm{e}^{-ud} \, J_1 \left(ua \right) \qquad (12.48)$$

is valid and the quantities a and J_1 denote the coil radius and the Bessel function of the first kind of order one. For the derivation of (12.47) and (12.48), it is referred to appendix R. From (12.47), the magnetic field in the plane of the circular loop results for $z = -d$ in

$$\underline{H}_{coil} = \underline{H}_z \left(r, z = -d, t \right) = \mathrm{e}^{j\omega t} \int_0^\infty \underline{B}_1 \, \mathrm{e}^{ud} \, J_0 \left(ur \right) du. \qquad (12.49)$$

Later on, (12.49) will be used.

12.4.3 Influence of a Conductive Layer

In order to investigate the influence of a conductive layer of thickness h on a circular loop, it is assumed, that the upper and lower surface of the conductive layer are formed by the two planes at $z = 0$ and $z = h$ (see Fig. 12.9). In order to consider the influence on the the space $z < 0$, the magnetic field of the circular loop (12.47) has to be modified by an additional term. Thus, it is ensured, that the analytical formulation corresponds to the general form in equation (12.46) and moreover, the part of the additional magnetic field is zero for $z \to -\infty$. Thus, the magnetic field between the circular loop and the conductive layer can be described by

$$\underline{H}'_z \left(r, z, t \right) = \mathrm{e}^{j\omega t} \int_0^\infty J_0 \left(ur \right) \left[\underline{B}_1 \, \mathrm{e}^{-zu} + \underline{B}_2 \, \mathrm{e}^{zu} \right] du \qquad \left(-d < z < 0 \right),$$

$$(12.50)$$

where $\underline{B}_1$ is already defined by equation (12.48). $\underline{B}_2$ has to be determined.

Within the conductive layer, the description of the magnetic field results from equation (12.45). If

$$k = \frac{\omega \kappa \mu}{u^2} \qquad (12.51)$$

is defined, (12.45) results in

$$\underline{H}'_z \left(r, z, t \right) = \mathrm{e}^{j\omega t} \int_0^\infty J_0 \left(ur \right) \left[\underline{A}_1 \, \mathrm{e}^{-uz\sqrt{1+jk}} + \underline{A}_2 \, \mathrm{e}^{uz\sqrt{1+jk}} \right] du \qquad \left(0 < z < h \right).$$

$$(12.52)$$

The magnetic field outside the layer $(z > h)$ can be described similarly to the expression (12.46). However, the positive exponential term has to be excluded:

$$\underline{H}'_z \left(r, z, t \right) = \mathrm{e}^{j\omega t} \int_0^\infty \underline{C}_1 \, \mathrm{e}^{-zu} \, J_0 \left(ur \right) du \qquad \left(z > h \right) \qquad (12.53)$$

In order to determine the four unknown quantities $\underline{B}_2$, $\underline{A}_1$, $\underline{A}_2$ and $\underline{C}_1$, the continuity characteristics of the normal component B_n of the magnetic induction and the discontinuity characteristics of the normal component H_n of the magnetic field are consulted with respect to the two boundary surfaces of the conductive layer at $z = 0$, $z = h$ and $r = 0$, i.e.

$$B_{n1} = B_{n2} \tag{12.54}$$

and

$$\frac{dH_{n1}}{dz} = \frac{dH_{n2}}{dz}. \tag{12.55}$$

Following system of equations is achieved:

$$\mu_0 \left(\underline{B}_1 + \underline{B}_2 \right) = \mu \left(\underline{A}_1 + \underline{A}_2 \right) \tag{12.56}$$

$$\underline{B}_1 - \underline{B}_2 = \sqrt{1 + jk} \left(\underline{A}_1 - \underline{A}_2 \right) \tag{12.57}$$

$$\mu \left(\underline{A}_1 \, e^{-uh\sqrt{1+jk}} + \underline{A}_2 \, e^{uh\sqrt{1+jk}} \right) = \mu_0 \underline{C}_1 \, e^{-uh} \tag{12.58}$$

$$\sqrt{1 + jk} \left(\underline{A}_1 \, e^{-uh\sqrt{1+jk}} - \underline{A}_2 \, e^{uh\sqrt{1+jk}} \right) = \underline{C}_1 \, e^{-uh} \tag{12.59}$$

Since the magnetic field between the circular loop and the conductive layer is of interest, the quantity $\underline{B}_2$ in equation has to be determined. Eliminating of $\underline{A}_1$, $\underline{A}_2$ and $\underline{C}_1$ yields

$$\frac{\underline{B}_2}{\underline{B}_1} = \frac{[\mu - \mu_0 \left(1 + jk \right)] \sinh \left(uh\sqrt{1 + jk} \right)}{[\mu + \mu_0 \left(1 + jk \right)] \sinh \left(uh\sqrt{1 + jk} \right) + 2\mu\mu_0 \sqrt{1 + jk} \cosh \left(uh\sqrt{1 + jk} \right)}. \tag{12.60}$$

The axial component of the magnetic field within the plane of the circular loop $(z = -d)$ in presence of the conductive layer yields with (12.50)

$$\underline{H}'_{coil} = \underline{H}'_z \left(r, z = -d, t \right) = e^{j\omega t} \int_0^\infty J_0 \left(ur \right) \left[\underline{B}_1 \, e^{ud} + \underline{B}_2 \, e^{-ud} \right] du, \tag{12.61}$$

where $\underline{B}_1$ und $\underline{B}_2$ are defined by (12.48) and (12.60).

12.4.4 Relative Inductance Change of a Circular Loop in Presence of a Conductive Layer

On the basis of the definition for the magnetic flux within the plane of the circular loop in accordance with

$$\underline{\Phi}_{coil} = 2\pi\mu_0 \int_0^a \underline{H}_{coil} r \, dr, \tag{12.62}$$

a conductive layer influences the magnetic field of the coil H_{coil} resulting in a change of the magnetic flux:

$$\Delta\underline{\Phi} = \underline{\Phi}_{coil} - \underline{\Phi}'_{coil} = 2\pi\mu_0 \int_0^a \left(\underline{H}_{coil} - \underline{H}'_{coil}\right) r \, dr \tag{12.63}$$

Insertion of the equations (12.49) and (12.61) into (12.63) yields the change of the magnetic flux at position $z = -d$

$$\Delta\underline{\Phi} = -2\pi\mu_0 \, e^{j\omega t} \int_0^\infty \int_0^a J_0\left(ur\right) \underline{B}_2 \, e^{-ud} \, r \, dr du \tag{12.64}$$

and

$$\Delta\underline{\Phi} = -2\pi\mu_0 \, e^{j\omega t} \int_0^\infty \int_0^a \frac{\underline{B}_2}{\underline{B}_1} J_0\left(ur\right) \underline{B}_1 \, e^{-ud} \, r \, dr du, \tag{12.65}$$

respectively.

Insertion of definition (12.48) for $\underline{B}_1$ into (12.65) results in

$$\Delta\underline{\Phi} = -\pi\mu_0 a \underline{I} \, e^{j\omega t} \int_0^\infty \int_0^a \frac{\underline{B}_2}{\underline{B}_1} J_1\left(ua\right) e^{-2ud} \, ur J_0\left(ur\right) \, dr du. \tag{12.66}$$

The evaluation of the inner integral yields [184]

$$\int_0^a ur J_0\left(ur\right) \, dr = a J_1\left(ua\right), \tag{12.67}$$

thus, (12.66) can be written in following form:

$$\Delta\underline{\Phi} = -\pi\mu_0 a^2 \underline{I} \, e^{j\omega t} \int_0^\infty \frac{\underline{B}_2}{\underline{B}_1} \, e^{-2ud} \, J_1^2\left(ua\right) \, du \tag{12.68}$$

Due to the change of the magnetic flux, a voltage $\Delta\underline{U}$ is induced resulting in

$$\Delta\underline{U} = \frac{d\Delta\underline{\Phi}}{dt} = j\omega \Delta\underline{\Phi}. \tag{12.69}$$

Insertion of (12.68) into (12.69) yields the impedance change $\Delta \underline{Z}$:

$$\frac{\Delta \underline{U}(t)}{\underline{I} e^{j\omega t}} = \Delta \underline{Z} = \Delta R + j\omega \Delta L = -j\omega\pi\mu_0 a^2 \int_0^\infty \frac{\underline{B_2}}{\underline{B_1}} e^{-2ud} J_1^2 (ua) \, du \quad (12.70)$$

An idealized, free circular loop with small wire radius r compared to the loop radius a, with the number of turns 1 has an inductance, that can be represented in following form [182, 185]:

$$L_0 = \frac{\pi a \mu_0}{2} \tag{12.71}$$

Thus, from (12.70) follows

$$\frac{\Delta L}{L_0} + \frac{\Delta R}{j\omega L_0} = -2a \int_0^\infty \frac{\underline{B_2}}{\underline{B_1}} e^{-2ud} J_1^2 (ua) \, du. \tag{12.72}$$

Introducing the dimensionless variable

$$z^* = 2ud, \tag{12.73}$$

(12.72) can be written as

$$\frac{\Delta L}{L_0} + \frac{\Delta R}{j\omega L_0} = -\frac{a}{d} \int_0^\infty \frac{\underline{B_2}}{\underline{B_1}} e^{-z^*} J_1^2 \left(\frac{az^*}{2d}\right) dz^*. \tag{12.74}$$

By analogy with the left side of (12.74), the quotient of the two integration constants $\underline{B_1}$ and $\underline{B_2}$ has to be formulated as a complex number

$$\frac{\underline{B_1}}{\underline{B_2}} = \alpha(z^*) + j\beta(z^*). \tag{12.75}$$

In order to calculate the real part $\alpha(z^*)$ and the imaginary part $\beta(z^*)$, it necessitates a representation of the complex root $\sqrt{1+jk}$ in equation (12.60) as a complex number by means of the relationship [186]

$$2\sqrt{1+jk} = \lambda + j\nu. \tag{12.76}$$

Since the representation of the quotient in equation (12.60) as a complex number in the form (12.75) comes along with an enormous mathematical calculation complexity, the software package Mathematica was used. Furthermore, the relative inductance change in (12.74) is of interest, thus a representation of $\beta(z^*)$ in equation (12.75) is set aside.

In combination with (12.60), (12.75) and (12.76), the fundamentals for the calculation of the relative inductance change of a circular loop in presence of a conductive layer are finally achieved:

$$\frac{\Delta L}{L_0} = -\frac{a}{d} \int_0^\infty e^{-z^*} J_1^2 \left(\frac{az^*}{2d} \right) \alpha \left(z^* \right) dz^*, \tag{12.77}$$

where

$$\alpha \left(z^* \right) = -\frac{k}{D} \left[k \cosh \left(\frac{\lambda h z^*}{2d} \right) + \nu \sinh \left(\frac{\lambda h z^*}{2d} \right) \right]$$
$$+ \frac{k}{D} \left[k \cos \left(\frac{\nu h z^*}{2d} \right) + \lambda \sin \left(\frac{\nu h z^*}{2d} \right) \right] \tag{12.78}$$

with

$$D = \lambda^2 \left(1 + \frac{\lambda^2}{4} \right) \cosh \left(\frac{\lambda h z^*}{2d} \right) + \lambda^3 \sinh \left(\frac{\lambda h z^*}{2d} \right)$$
$$+ \nu^2 \left(1 - \frac{\nu^2}{4} \right) \cos \left(\frac{\nu h z^*}{2d} \right) - \nu^3 \sin \left(\frac{\nu h z^*}{2d} \right), \tag{12.79}$$

$$\frac{\lambda^2}{2} = \sqrt{1 + k^2} + 1, \qquad \frac{\nu^2}{2} = \sqrt{1 + k^2} - 1 \tag{12.80}$$

and (see also eq. 12.51)

$$k = \frac{8\pi d^2 f \mu_0 \kappa}{\left(z^* \right)^2} \tag{12.81}$$

It should be noted, that equation (12.77) is not solvable in closed form analysis, thus a numeric integration has to be considered.

12.5 Measurement Results

Following section dwells on the experimental characterization of the piezoelectric bending actuator in combination with the non-contact inductive proximity sensor. At first, the relative inductance change of the sensing coil in presence of a conductive Cu-layer applied to the bender's tip is experimentally determined as a function of the distance x. The measurement results are compared to analytical calculations based on the fundamental equation (12.77). A determination of the coefficient of coupling $k \left(x \right)$ defined in section 12.3 directly follows.

Furthermore, the characterization of the inductive proximity sensor concerning its static and dynamic transient characteristics within the sensor-actuator-system represents a main focus.
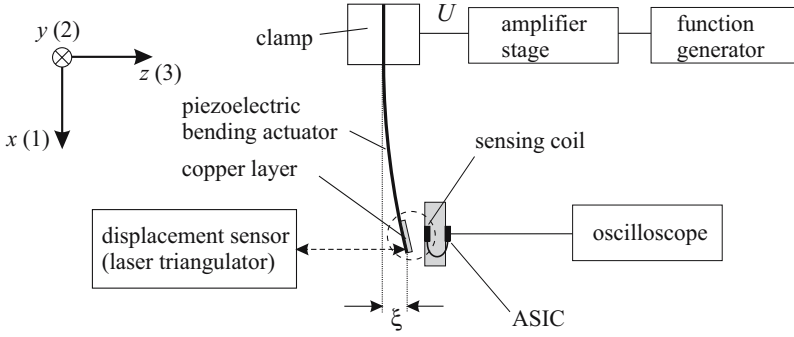
Fig. 12.10. Measurement setup for the experimental determination of the relative inductance change of the sensing coil dependent on the tip deflection ξ of a piezoelectric bending actuator

12.5.1 Relative Inductance Change of the Sensing Coil with Respect to a Conductive Copper Layer

In order to determine the relative inductance change of the sensing coil with respect to the conductive copper layer, the measurement setup, as it is shown in figure 12.10, is used.

Since the geometry of the arrangement plays a decisive role concerning the analytical calculations, the circle sector scetched in figure 12.10 is represented in higher magnification in the following figure 12.11 showing the non-deflection and deflection state of the piezoelectric bending actuator. Here, x_0 denotes the maximum distance between the upper side of the copper layer and the central position of the sensing coil for the non-deflection state of the bending actuator, x denotes the distance between the upper side of the copper layer and the central position of the sensing coil for the deflection state of the bending actuator, ξ_{max} correspond to the maximum deflection of the bending actuator, b corresponds to the distance between the front edges of the coil and the ceramic carrier, a denotes the coil radius, l corresponds to the coil length and d_{air} denotes the air gap between the ceramics carrier and the copper layer at maximum deflection.

The physical dimensions of the quantities ξ_{max}, b, a, l and d_{air} being necessary for the analytical calculations of the relative inductance change of the sensing coil in presence of the conductive copper layer are listed in Table 12.1.

Taking figure 12.11 into consideration, following correlation can be formulated for the deflection state of the bending actuator:

$$\xi_{max} + d_{air} + b + \frac{l}{2} = x_0 \qquad (12.82)$$

Furthermore, for an arbitrary deflection $0 < \xi < \xi_{max}$, it can be written

a) non-deflection state   b) deflection state
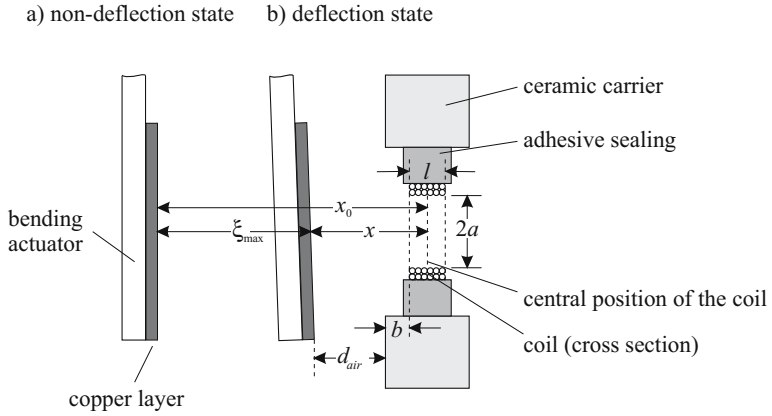
Fig. 12.11. Geometrical dimensions of the sensor-actuator-system. - **(a)** non-deflection state; **(b)** deflection state of the piezoelectric bending actuator

Table 12.1. Relevant geometrical quantities being necessary for the calculation of the relative inductance change of the sensing coil in presence of a conductive copper layer

ξ_{max} [μm]	b [μm]	a [μm]	l [μm]	d_{air} [μm]
329.6	341.2	513.0	600.0	15.0

$$\xi + x = x_0, \tag{12.83}$$

thus, the distance x between the copper layer and the central position of the sensing coil can be calculated by insertion of (12.83) into (12.82):

$$x = \xi_{max} + d_{air} + b + \frac{l}{2} - \xi \tag{12.84}$$

Taking the equations (12.77) - (12.81) in section 12.4.4 into consideration, the relative inductance change is analytically calculated. Here, the variable d in the equations (12.77) - (12.79) and (12.81) has to be replaced by the variable x in accordance with equation (12.84).

Equation (12.26) in section 12.3 is the starting point for the experimental characterization of the relative inductance change:

$$\frac{\Delta L_1}{L_1} = 1 - \left(\frac{f_1}{f_e(x)}\right)^2 \tag{12.85}$$

Equation (12.85) shows, that both, the knowledge of the frequency f_1 of the uninfluenced coil ($x \longrightarrow \infty$) and the frequency $f_e(x)$ of the coil affected by
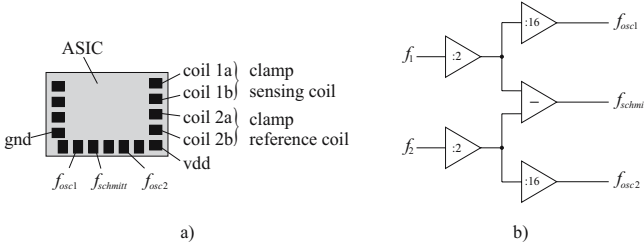
Fig. 12.12. ASIC of the inductive proximity sensor. - **(a)** pin assignment; **(b)** correlation between the frequency signals f_{osc1}, f_{osc2} and $f_{schmitt}$ and the frequencies of the oscillators 1 and 2 within the ASIC

the copper layer in distance x is necessary. Thus, in the following, the pin assignment of the ASIC shown in figure 12.12a is considered [187].

The sensing coil is connected to `coil 1a` and `coil 1b`. The reference coil is connected to `coil 2a` and `coil 2b`. f_{osc1}, f_{osc2} and $f_{schmitt}$ denote the output frequencies of the oscillator 1 and 2 as well as the output signal f_{out} after passing the Schmitt trigger shown in figure 12.2. In accordance with figure 12.12b, the frequency signals f_{osc1}, f_{osc2} und $f_{schmitt}$ are generated on the basis of the resonant frequencies f_1 and f_2 of the two oscillators 1 and 2 [188].

Since with respect to (12.85) the relative inductance change of the sensing coil can be determined by means of the ratio between f_1 of the uninfluenced oscillator 1 and the frequency $f_e(x)$ of the influenced oscillator, the measuring of the output signal f_{osc1} is sufficient. At room temperature, the resonant frequency f_1 of the *uninfluenced* oscillator 1 (absence of the conductive copper layer) yields in combination with $f_{osc1} = 552\,\text{kHz}$ (see Fig. 12.12b)

$$f_1 = 32\, f_{osc1} = 17.644\,\text{MHz}. \tag{12.86}$$

In section 12.2.1, the skin depth δ of the copper layer has already been determined on the basis of (12.86) (see also eq. 12.7). Similarly, the determination of the frequency $f_e(x)$ of the sensing coil affected by the copper layer results from

$$f_e(x) = 32\, f_{osc1}(x), \tag{12.87}$$

thus, the relative inductance change can be derived from (12.85):

$$\frac{\Delta L_1}{L_1} = 1 - \left(\frac{f_{osc1}}{f_{osc1}(x)} \right)^2 \tag{12.88}$$

The frequency measurements concerning f_{osc1} and $f_{osc1}(x)$ are effected by means of an oscilloscope (type: Agilent 54621A). Figure 12.13 shows the experimentally determined and analytically calculated relative inductance change

of the sensor-actuator-system as a function of the distance between copper layer and central position of the coil.
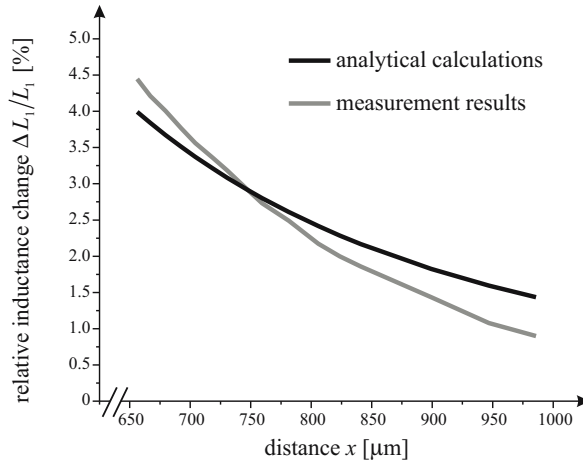
Fig. 12.13. Experimentally determined and analytically calculated relative inductance change of the sensor-actuator-system as a function of the distance x between copper layer and central position of the coil

Figure 12.13 shows a good coincidence between the measurement results and the analytical calculations. It can be recognized, that the relative inductance change increases with decreasing distance x, since the eddy currents induced in the copper layer have an increasing reaction to the magnetic field generated by the coil. On the one hand, the differences between the measurement values and the analytical calculations are caused by the coil geometry deverging from an ideal circular loop. On the other hand, in the derivation of the fundamental equation (12.77) does not consider the layers of the bending actuator below the copper layer. Furthermore, the copper layer represents a conductive, spatially limited semi-infinite space. Also this aspect is not integrated into the derivation of the fundamental equation (12.77). Also the fact, that the copper layer is not aligned coplanary to the sensing coil during a bending deformation of the actuator, has not been taken into account.

From the relative inductance change of the sensing coil in the presence of the copper layer according to equation (12.26), conclusions can be drawn with respect to the dependence of the coefficient of coupling $k(x)$ on the distance x. In figure 12.14, the experimentally determined and analytically calculated coefficient of coupling is represented as a function of distance x. Since the distance x is directly correlated with the deflection ξ of the bending actuator with respect to equation (12.84), the relative inductance change of the sensing

coil can also be represented as a function of the deflection of the bending actuator (see Fig. 12.15).
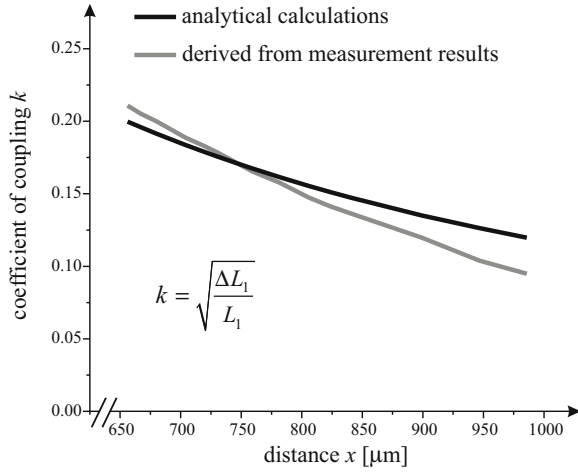
Fig. 12.14. Experimentally determined and analytically calculated coefficient of coupling $k(x)$ as a function of distance x between sensing coil and copper layer
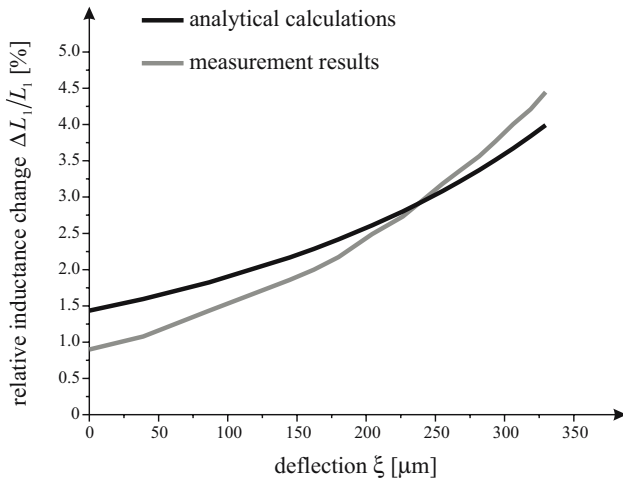
Fig. 12.15. Relative inductance change of the sensing coil as a function of the actuator's tip deflection ξ

12.5.2 Performance of the Inductive Proximity Sensor

In order to investigate experimentally the static and dynamic transient characteristics of the inductive proximity sensor, the measurement setup, as it is shown in figure 12.16, is used.
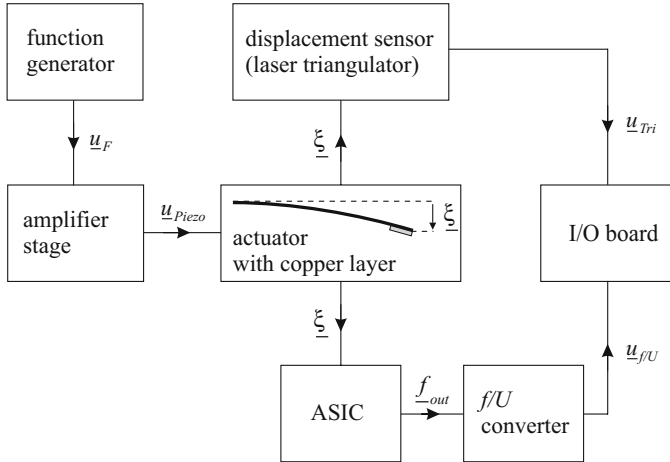
Fig. 12.16. Measurement setup for the determination of the static and dynamic transient characteristics of the inductive proximity sensor

The amplifier stage following the function generator generates the voltage $\underline{u}_{Piezo}$, the bending actuator is driven with. By the ASIC, the distance $\underline{x}$ between the copper layer applied to the bender's tip and the sensing coil and thus the deflection $\underline{\xi}$ of the bending actuator (see eq. 12.83) is transformed to a frequency signal $\underline{f}_{out}$. Then the frequency signal is converted to a voltage signal $\underline{u}_{f/U}$ by a frequency-to-voltage converter (type: AD650) and afterwards read in by an I/O-board. The measuring chain extracted from figure 12.16 and illustrated in figure 12.17 is of interest.

The transfer functions denoted in the block diagram are defined as follows:

$$\underline{B}_1 = \frac{\underline{\xi}}{\underline{u}_{Piezo}} \tag{12.89}$$

$$\underline{B}_2 = \frac{\underline{f}_{out}}{\underline{\xi}} \tag{12.90}$$

$$\underline{B}_3 = \frac{\underline{u}_{f/U}}{\underline{f}_{out}} \tag{12.91}$$

$$\underline{B}_4 = \underline{B}_2 \cdot \underline{B}_3 = \frac{\underline{u}_{f/U}}{\underline{\xi}} \tag{12.92}$$
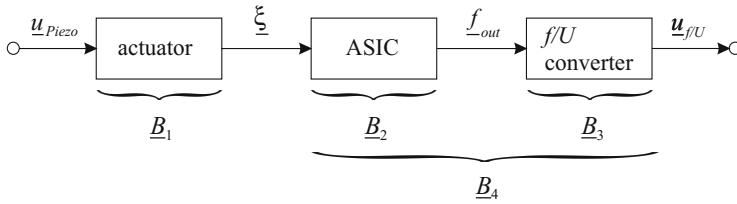
Fig. 12.17. Measuring chain for the characterization of the inductive proximity sensor

The transfer function of the bending actuator $\underline{B}_1$ has already been discussed in section 9.3.3 and therefore it is well-known in its analytical and experimentally determined form. Here the two transfer functions $\underline{B}_2$ and $\underline{B}_4$ are in the main focus. The transfer function $\underline{B}_4$ can be determined by variation of the driving frequency and amplitude of the output signal $\underline{u}_{Piezo}$ of the amplifier stage. Simultaneously, both the deflection signal $\underline{\xi}$ and $\underline{u}_{f/U}$ are recorded by the measurement system. However, in order to be able to determine the transfer function $\underline{B}_2$ of the ASIC, the transient characteristics of the frequency-to-voltage converter $\underline{B}_3$ has to be determined.

Characteristics of the f/U converter

In figure 12.18, the measuring chain for the determination of the *static* characteristic of the frequency-to-voltage converter is illustrated.
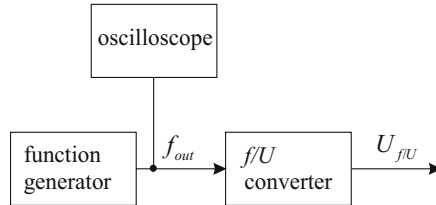
Fig. 12.18. Measuring chain for the determination of the static characteristic of the frequency-to-voltage converter

As already described in section 12.2.1, for the non-deflection state of the bending actuator, the output frequency of the sensor electronics amounts to $f_{out} = 360\,\text{kHz}$. In case of maximum deflection ($\xi \approx 300\,\mu\text{m}$), the maximum frequency change of the ASIC amounts to $\Delta f_{out} = 300\,\text{kHz}$. In order to determine the static characteristics, the input frequency is increased from $360\,\text{kHz}$ up to $660\,\text{kHz}$ in $10\,\text{kHz}$-steps. Thereby, the generation of the input frequencies is realized by means of a frequency generator (type: HP 8116A). In order to

consider a possible error of the frequency display of the frequency generator, the respective adjusted frequencies are additionally measured by means of an oscilloscope (type: Agilent 54621A). In figure 12.19, the static characteristic of the frequency-to-voltage converter is illustrated.
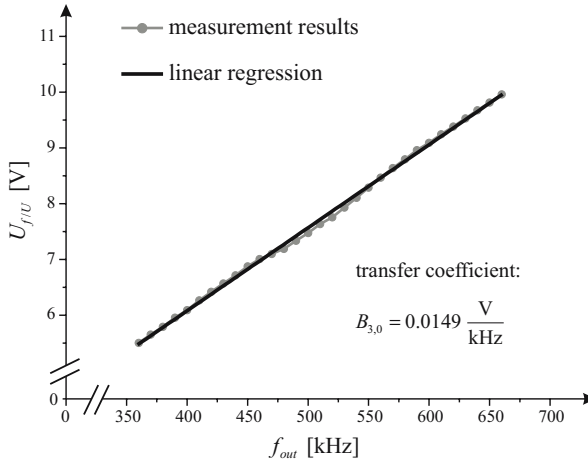
Fig. 12.19. Static characteristic of the frequency-to-voltage converter

In order to be able to determine the *dynamic* transient characteristics $\underline{B}_3$, the measurement setup shown in figure 12.18 is modified (see Fig. 12.20).
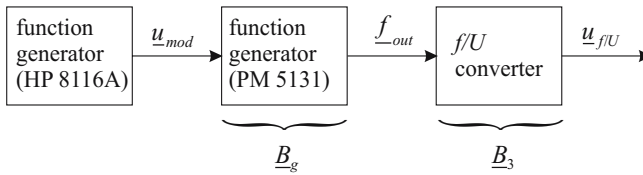
Fig. 12.20. Modified measuring chaine for the determination of the dynamic transient characteristics of the frequency-to-voltage converter

Here, it is necessary to modulate a carrier frequency f_T with a fixed frequency deviation Δf_T within a defined frequency band (see Fig. 12.4). In order to generate the lower frequency f_u of the frequency band, a frequency generator (type: PM 5131) is used. It allows for the manual adjustment of the lower frequency f_u. Now, the lower frequency is chosen in such a way, that it corresponds to the ASIC's output frequency f_{out} , when the bending actuator is *not*

deflected. The chosen signal shape at the output of the PM 5131 corresponds to a square wave signal (TTL level). As already mentioned in section 12.2.1, the output frequency of the sensor electronics amounts to $f_{out} = 360\,\mathrm{kHz}$ for the non-deflection state of the bending actuator, thus this value is adjusted for f_u at the PM 5131. The double frequency deviation $2\Delta f_T$ of 300 kHz corresponds to the ASIC's maximum frequency change Δf_{out} for maximum deflection of the bending actuator ($\xi \approx 300\,\mu\mathrm{m}$). The double frequency deviation is defined by the peak-to-peak value $\underline{u}_{mod,ss}$ of the sine signal generated by a second function generator (type: HP 8116A) and applied to the input of the PM 5131. The maximum amplitude $\underline{u}_{mod}$ of the modulation signal determines the maximum frequency of the output signal $\underline{f}_{out}$ of the PM 5131. The modulating frequency f_{mod} is determined by the frequency of the signal applied to the sweep input of the PM 5131.

Then, the modulated frequency signal $\underline{f}_{out}$ at the output of the PM 5131 is applied to the input of the frequency-to-voltage converter. For every series of measurements, the modulating frequencies are defined from 10 Hz up to 20 kHz in well defined frequency steps. For every modulation frequency, the value of maximum amplitude $\underline{u}_{f/U}$ at the output of the frequency-to-voltage converter is logged. The dynamic transient characteristics $\underline{B}_3$ can be determined according to figure 12.20. It can be written:

$$\underline{B}_3 = \frac{\underline{u}_{f/U}}{\underline{u}_{mod}} \cdot \frac{1}{\underline{B}_g}, \tag{12.93}$$

where the quantity $\underline{B}_g$ denotes the transfer function of the frequency generator PM 5131 (see Fig. 12.21).
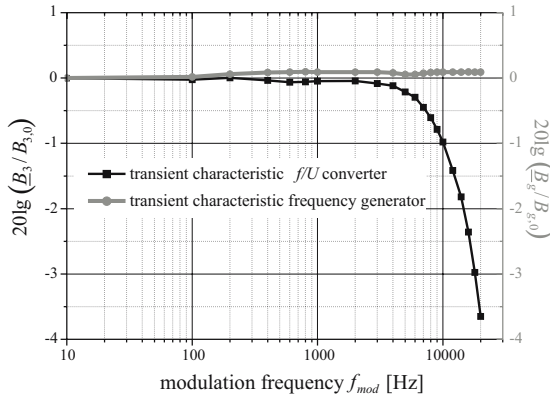
Fig. 12.21. Standardized transient characteristics of the frequency-to-voltage converter and the frequency generator (PM 5131)

The standardized transfer functions $\underline{B}_3$ and $\underline{B}_g$ dependent on the modulating frequency f_{mod} are shown in figure 12.21. The transient characteristic $\underline{B}_g$ of the frequency generator is almost independent on the frequency up to $f_{mod} = 20\,\mathrm{kHz}$. Furthermore, figure 12.21 shows, that the cutoff frequency of the transient characteristic of the frequency-to-voltage converter amounts to $f_{mod} \approx 20\,\mathrm{kHz}$. Since the following measurements for the determination of the transient characteristic of the ASIC and frequency-to-voltage converter combination (determination of $\underline{B}_4$, see Fig. 12.17) are effected on the basis of harmonic tip deflections within a frequency range of $100\,\mathrm{mHz} < f < 10\,\mathrm{kHz}$, due to the constant transient characteristic of the frequency-to-voltage converter within the considered frequency range conclusion can be drawn with respect to the transient characteristic $\underline{B}_2$ of the inductive proximity sensor.

Static Behavior

Figure 12.22 shows the static behavior of the output $u_{f/U}$ dependent on the increasing and decreasing deflection ξ of the bender's tip.
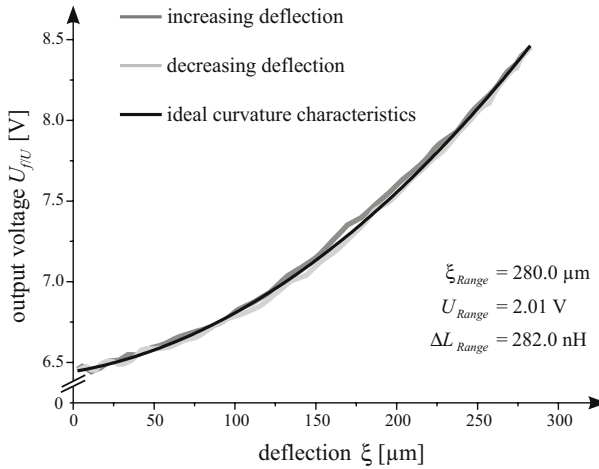
Fig. 12.22. Ideal and real static sensor characteristics of the inductive proximity sensor in combination with the frequency-to-voltage converter

In order to determine the static characteristics, the bending actuator is driven by a sinusoidal voltage with the frequency $f = 100\,\mathrm{mHz}$. The tip deflection ξ and the output voltage of the frequency-to-voltage converter $U_{f/U}$ are logged simultaneously. The appropriate measurement setup is shown in figure 12.16.

As ideal characteristic curvature, a polynomial of second order was chosen. It is evident, that the ideal and real static characteristics of the inductive approximation sensor technology differ from each other.

As already mentioned in section 11.2.3, the deviations from the ideal transient characteristics are caused by the sensor's physical transformation principle, the influence of manufacturing tolerances, the influences of the assembly technology as well as the sensor electronics. The linearity error F_{Lin} and the hysteresis error F_{Hys} can be derived from the maximum values of the deviations. Both types of errors belong to the class of bias errors. In order to determine the linearity and hysteresis error of the inductive proximity sensor, the measuring data in figure 12.22 are used. Here, a terminal-based conformity is assumed. The maximum difference between the sensor electronics signal and the ideal curvature characteristic related to the nominal value of the sensor electronics signal ($U_{Range} = 2.01\,\text{V}$) yields a linearity error $F_{Lin} = 1.41\%$ (see Fig. 12.23a).

The hysteresis error results from the maximum difference between the sensor electronics signal with respect to an increasing and decreasing deflection related to the nominal value of the sensor electronics signal. Evaluation of the measurement data in figure 12.22 yields a hysteresis error $F_{Hys} = 4.60\%$ (see Fig. 12.23b).

a)   b)
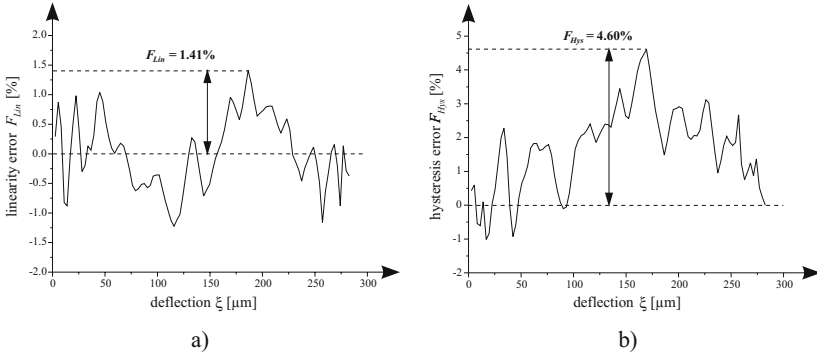
Fig. 12.23. **(a)** Linearity error and **(b)** hysteresis error of the inductive proximity sensor

The linearity and hysteresis error result in the static total error $F_G = 4.81\%$ of the inductive proximity sensor according to (11.21). It should be noted, that linearity errors can be further minimized by means of a suitable secondary electronics.

Since it is an aim to detect the hysteresis of the piezoelectric bending actuator by means of the integrated proximity sensor, the tip deflection has been measured in accordance with the measurement setup shown in figure 12.16. The

deflection measurement by means of the laser triangulator provides a comparison and bench mark for the inductive proximity sensor in combination with the frequency-to-voltage converter. Figure 12.24 shows the tip deflection ξ versus the electric field E (driving voltage). The measurement shows the ability of the inductive proximity sensor in combination with the appropriate sensor electronics to detect the hysteresis being typical for bending actuators.
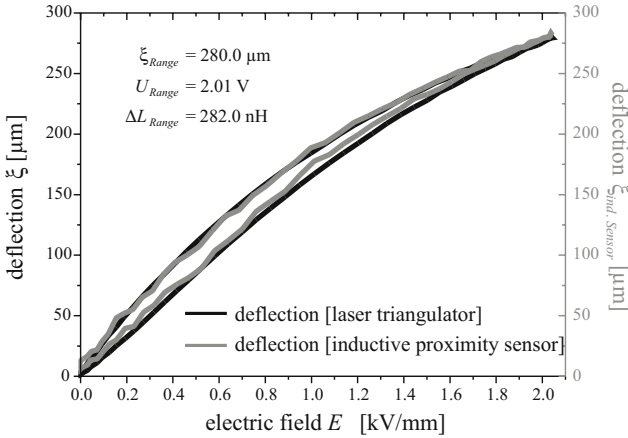
Fig. 12.24. Beam deflection ξ and inductive sensor signal $\xi_{ind.\ Sensor}$ showing the deflection hysteresis versus applied electric field E

Dynamic Performance

In order to determine the dynamic transient characteristics $\underline{B}_4$ of the inductive proximity sensor in combination with the frequency-to-voltage converter (see Fig. 12.17), the bender is driven with a harmonic voltage within a frequency range of $100\,\mathrm{mHz} < f < 10\,\mathrm{kHz}$ with respect to well defined frequency steps. Concerning the measurement, it has to be ensured, that the bender's tip always moves within a deflection range of $0 < \xi < 300\,\mu\mathrm{m}$ (see Fig. 12.11). Thus, the resonances regarding the first and second vibrational mode are avoided (see Fig. 9.21, section 9.3.3). This is realized in such a way, that the amplitude of the driving voltage generated by the amplifier stage is readjusted in such a manner, that the actuator's developing resonances do not exceed the defined deflection range.

The static characteristics of the inductive proximity sensor in combination with the frequency-to-voltage converter illustrated in figure 12.22 shows a *nonlinear* correlation between the electrical output quantity $\underline{u}_{f/U}$ and the physical measuring quantity $\underline{\xi}$. Therefore, the sensor must not be considered as *linear time-invariant* system (LTI system), since the superposition of two

input signals $\xi_1(t) + \xi_2(t)$ does not correspond to the superposition of the associated output signals $u_{f/U,1}(t) + u_{f/U,2}(t)$ [189].

However, in order to use the complex transfer function $\underline{B}$, generally defined for LTI systems, the transfer function $\underline{B}_4$ is formulated according to

$$\underline{B}_4 = \frac{\underline{u}_N}{\underline{\mu}_N} = \frac{\underline{u}_{f/U,\mathrm{max}} - \underline{u}_{f/U,0}}{\underline{\xi}_{\mathrm{max}} - \underline{\xi}_0}, \tag{12.94}$$

where $\underline{u}_N$ and $\underline{\mu}_N$ denote the nominal voltage and the nominal measured quantity of the inductive proximity sensor in combination with the frequency-to-voltage converter with respect to the considered frequency f.

Figure 12.25 shows the experimentally determined transfer characteristic $\underline{B}_4$ in standardized form.
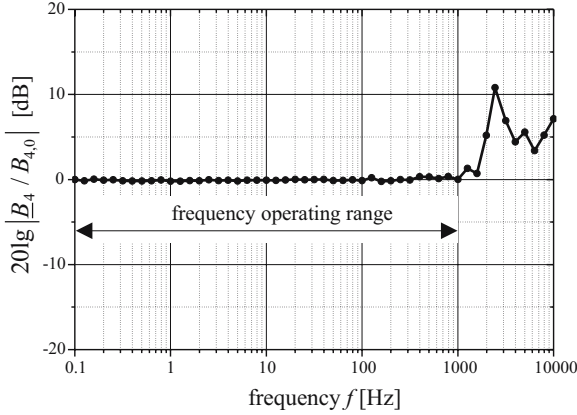
Fig. 12.25. Transfer characteristic of the inductive proximity sensor in combination with the frequency-to-voltage converter

Due to the constant response characteristic $\underline{B}_3$ of the frequency-to-voltage converter within the considered frequency range $100\,\mathrm{mHz} < f < 10\,\mathrm{kHz}$ (see Fig. 12.21), the transfer function $\underline{B}_4$ and the ASIC's transfer function $\underline{B}_2$ are identical. Figure 12.25 shows, that the frequency operating range extends to an upper frequency $f = 1\,\mathrm{kHz}$.

The measurement shows the ability of the inductive proximity sensor in combination with a piezoelectric bending actuator to detect the hysteresis being typical for bending actuators. Thus, inherent creep and drift effects, that arise in the static operation mode, can be detected. A further advantage of the realized non-contact proximity sensor is on the one hand the high relative inductance change. On the other hand, the size of the sensor in combination with

the sensor electronics allows for the use in applications where small dimensions of a sensing system are needed. Particularly, the dynamic transient characteristic of the inductive proximity sensor should be emphasized. Its frequency operating range of $100\,\text{mHz} < f < 1\,\text{kHz}$ easily satisfies the requirements to the cutoff frequency listed in Table 10.1. Thus, it is able to detect external vibrations, which can be compensated by means of an integration into a closed loop.

13

Conclusion

The book can be divided into two main emphasis. The mechanical and electromechanical modeling of an n-layered piezoelectric bending structure represents the first emphasis. The models provide the derivation of the static and dynamic characteristics for arbitrary points over the entire length of any kind of clamped-free piezoelectric bending actuators. The second emphasis dwells on the development and realization of a new bending actuator in multilayer technology with different integrated sensors for tip deflection measurements, independent of externally affecting loads.

13.1 Summary and Results

The description of the strain and stress conditions as well as the elastic behavior of a piezoelectric crystal structure provide a basis for the analytical description of the static and dynamic behavior of n-layered bending actuators. With this knowledge, the constitutive equations of state corresponding to the respective application can be derived. With the help of the constitutive equations the electrical enthalpy is deduced by means of Legendre's transformation. The electrical enthalpy is indispensable for the formulation of the dynamic behavior of piezoelectric bending actuators.

The static behavior of piezoelectric multilayer beam bending actuators has been formulated in closed form analysis. Here, Bernoulli's hypothesis of bending theory provides a basis. In combination with the fundamental laws of elastostatics, the calculation of the neutral axis position is effected. The neutral axis position incorporates the general formulation of the total flexural rigidity of the multilayered system and the description of the internal piezoelectric moment and represents a central quantity in all further considerations.

In combination with the linear equations of state, the energy density of the elastic deformation and the electrical energy density result in the total stored

energy of a bending actuator. With the principle of minimum total potential energy, for the first time the combining equations between extensive affecting quantities such as forces, bending moments, pressure loads and electrical driving voltages and the resulting intensive quantities like deflections, bending angles, volume displacements and electrical charges have been derived for arbitrary points over the entire length of the actuator in closed form analysis. The combining equations are presented in form of a matrix, that allows for a universal representation of the static behavior of n-layered bending actuators.

With the developed model, also the characteristics of piezoelectric bending actuators in the actuator's cross section can be determined. It allows for the calculation of the mechanical stresses and strains in the actuator's cross section caused by externally affecting mechanical and electrical quantities.

With respect to thermodynamic considerations, from Hamilton's principle the describing differential equations of piezoelectric multilayer beam bending actuators have been derived in concentrated form. In the book, for the first time the Lagrange formalism has been developed for piezoelectric multilayered bending actuators considering dissipative forces, which extract energy from an oscillating system. On the basis of Rayleigh's dissipation function and in the sense of the equivalent viscous damping, the internal and external frictional forces have been integrated into Lagrange's formalism resulting in the modified Hamilton principle. The application of the modified Hamilton principle to the electrical enthalpy mentioned before results in the differential equation system describing the dynamics of a piezoelectric multilayer beam bending actuator in concentrated form.

The achieved differential equation system is used for the description of the time-harmonic, dynamic behavior of n-layered piezoelectric bending actuators. By analogy with the static description, in the present book, the correlation between the external dynamic quantities like forces, moments, pressure loads and driving voltages and the resulting dynamic quantities such as deflections, bending angles, volume displacements and electrical charges is represented for arbitrary points over the entire length of the actuator by means of a dynamic admittance matrix in closed from analysis. The method of separation of variables precedes the general formulation. In combination with the characteristic equation for clamped-free bending actuators, it allows for the calculation of the temporal and spatial characteristics of the fundamental mode and the modes of higher order, which are considered in the formulation of the dynamic admittance matrix.

Furthermore, in the book the systematic development of a general circuit representation of multilayered bending actuators has been elaborated within the scope of the network theory. Particularly, the frictional forces, arising with bending vibrations, are considered in the sense of the equivalent viscous damping. Moreover, the arising modes of higher order are considered by

means of the method of separation. Thus, a descriptive circuit representation of mechanically interacting quantities such as masses, coefficients of friction and compliances and also their interconnection with respect to the appropriate vibrational modes is achieved. The achieved circuit representation extends the theory of electromechanical systems in a way, that has never been shown before.

For the experimental characterization of piezoelectric bending actuators, a measurement setup has been developed and realized. The functionality of the automated measurement setup allows for the experimental verification of the developed theoretical models concerning the static and dynamic behavior in combination with a realized beam bender. It has been shown, that the analytical calculations concerning a monomorph bending actuator in multilayer technology agree in a remarkable and outstanding way with real measurement data. This fact supports the validity of the general analytical description of n-layered bending actuators and its applicability to specific real bending actuator types.

The development and realization of a sensor for tip deflection measurements integrated into the bending actuator represents the second emphasis of the book. On the basis of a comprehensive collection of different sensor principles, a capacitive and inductive sensor principle have been chosen.

The functional principle of a capacitive strain sensor is represented. The evaluation of the strain characteristics of the multilayered bending actuator provides a basis for the integration of the strain sensor into the actuator. The evaluation is effected on the basis of the achieved combining equations concerning the static behavior of piezoelectric bending actuators. The determination of the tip deflection independent of externally affecting forces is substantial for the integration of the sensor into the actuator.

Based on the calculated strain characteristics within the cross-sectional area of multilayered bending actuators, a point of constant strain perpendicularly to the bender's length axis could be identified with respect to a constant tip deflection. For the determination of the tip deflection, the strain sensor has been applied symmetrically around the point of constant strain. The integration of the strain information yields a value, that is proportional to the tip deflection and independent of externally affecting forces.

Due to the very small strains on the actuator surface and the associated small capacitance changes, a special sensor electronics has been developed, which is able to transform the small capacitance changes in the fF-range to an electric output signal, that can easily be handled. The circuit has been developed in such a way, that the capacitance change of the strain sensor is measured with respect to a constant reference capacitance. After passing an

instrumentation amplifier, the difference signal is applied to a Butterworth lowpass filter followed by an amplifier stage. An integrator circuit following the amplifier stage allows for the determination of the temperature- and time-dependent DC offsets of the used operational amplifiers. The DC offset of the processed signal is fed back to the instrumentation amplifier as zero point reference. Thus, an automatic DC offset compensation is realized.

The experimental characterization of the realized sensor-actuator-system show the ability of the capacitive strain sensor in combination with the developed sensor electronics to detect hysteresis being typical for bending actuators.

In addition to the realization of high-accuracy sensor electronics for capacitive strain sensors a miniaturized non-contact inductive proximity sensor based on eddy current effects has been developed and realized.

The non-contact inductive proximity sensor consists of a microelectronic circuit realized as an ASIC. Two external 3D-microcoils are connected to the ASIC. One coil acts as sensing coil, the other one provides a reference. A conductive copper layer is applied to the actuator's tip. During approximation of the bender's tip towards the sensing coil driven by an alternating current, a magnetic alternating field will be generated. In its turn, it causes eddy currents within the Cu-layer generating magnetic fields, that counteract the external magnetic field of the sensing coil. As a consequence, the external magnetic field decreases resulting in a decrease of the inductance of the sensing coil. The sensing coil is connected to an integrated oscillator circuit of the ASIC. Its resonant frequency changes during approximation of the actuator's tip. Thus, the changing resonant frequency of the oscillator circuit is a measure for the inductance change of the sensing coil and the deflection of the beam bender's tip, respectively.

The reference coil is connected to a second oscillator and is arranged in such a manner, that it can not be influenced by the Cu-layer. With its constant inductance, the reference coil provides the generation of the reference frequency. By means of a mixer, the difference and the sum of both frequency signals are evaluated and passed on the following lowpass filter. The lowpass filter suppresses the deterministically caused higher-frequency signals. The following Schmitt trigger provides a shaping of the difference of both frequency signals, thus the output signal is available as TTL signal.

In order to determine analytically the relative inductance change as a function of the beam bender's tip deflection, an electrodynamical approach has been formulated, that verifies experimental measurement results in an outstanding way. By means of the theoretical formulation, a deep physical understanding of the mechanism of the inductive proximity sensor based on eddy current effects is given at the same time.

The measurement results show the ability of the inductive proximity sensor in combination with a piezoelectric bending actuator to detect hysteresis being typical for bending actuators. Thus, also the inherent creep and drift effects being found in the static operation mode can be detected. A further advantage of the realized non-contact proximity sensor is on the one hand the high relative inductance change. On the other hand, the size of the sensor in combination with the sensor electronics allows for the use in applications where small dimensions of a sensing system are needed. Particularly, the dynamic transient characteristics of the inductive proximity sensor should be emphasized. Its frequency operating range satisfies the requirements to the cutoff frequency of 1 kHz. Thus, the realized inductive proximity sensor is suitable for static, quasistatic and dynamic applications.

13.2 Outlook

The experimental results corroborate the developed theoretical approaches regarding the static and dynamic behavior of n-layered bending actuators in an outstanding way. Due to the general formulation, the calculation of the performance and the characteristics of concrete bending structures is enabled. Thus, it is possible to influence purposefully their performance by variation of geometrical, elastomechanical and electromechanical parameters. A powerful and all-purpose analysis and design tool is at scientist's and engineer's disposal.

It has to be allowed for the fact, that the material parameters of piezoceramic materials like piezoelectric coefficients, coefficients of compliances, moduli of elasticity, piezoelectric moduli and permittivities show a nonlinear behavior at high electric fields. An implementation of nonlinear material properties into the developed models is possible. If very short bending structures are considered, the developed approaches must be modified in such a way, that transverse effects influencing the bending deformations have to be considered.

With respect to the realized sensors for tip deflection measurements, the measurement results show, that applications of such smart sensor-actuator-systems are possible in fields, piezoelectric systems have never been used before.

The implementation into a closed loop allows for the compensation of internal and external loads affecting the deflection of piezoceramic bending actuators. Thereby, the influences can be very different, e.g. external forces, moments and pressure loads affecting the bending actuator, temperature fluctuations, vibrations of technical applications, hysteresis effects of piezoceramics, clamping conditions, thermal and mechanical relaxation, drift, failure of individual

piezoelectric layers, aging of piezoceramics as well as environmental conditions.

In addition to technical applications like pneumatic micro valves with piezoelectric actuators, also a lot of applications can be identified within the fields of adaptronics, mechatronics as well as measurement and sensor technology. The functionality of all technical applications featuring piezoelectric bending actuators can be extended in combination with an integrated sensor for tip deflection measurements. Their implementation into an appropriate closed loop allows for the compensation of external loads.

But also technical applications like high-accuracy positioning, piezoelectric bending actuators are to be used for, profit from an integrated sensor. The deflection of piezoelectric actuators can be controlled independently of the hysteresis of piezoelectric materials. Due to the fact, that the developed inductive proximity sensor is suitable for static, quasistatic and dynamic measurements, new application fields can be made accessible for piezoelectric bending actuators, where a high-accuracy and high-dynamic control is needed.

Part V

Appendix

A

Work Done by Stresses Acting on an Infinitesimal Volume Element

In order to calculate the mechanical work performed for the deformation of an infinitesimal volume element, figure 3.3 in section 3.1 is considered. It represents the volume element in its undeformed and deformed configuration in the x-y plane. The displacement of the midpoint of side $A'D'$ results from the notations in figure 3.3:

$$u_{A'D'} = u + \frac{1}{2}\frac{\partial u}{\partial y}dy \tag{A.1}$$

The work done by the mechanical stress T_{xx} results in combination with equation (A.1) in:

$$dW_{T_{xx}}^{(1)} = -T_{xx}d\left(u + \frac{1}{2}\frac{\partial u}{\partial y}dy\right)dydz \tag{A.2}$$

Taking the midpoint displacements of the sides $B'C'$, $A'B'$ and $D'C'$ caused by the accordingly resulting mechanical stresses (see Fig. 3.2 in sect. 3.1) into account and including the body force f_x, provide the total done work dW_{x_1} in x-direction:

$$
\begin{aligned}
dW_{x_1} = &-T_{xx}d\left(u + \frac{1}{2}\frac{\partial u}{\partial y}dy\right)dydz \\
&+ \left(T_{xx} + \frac{\partial T_{xx}}{\partial x}dx\right)d\left(u + \frac{\partial u}{\partial x}dx + \frac{1}{2}\frac{\partial u}{\partial y}dy\right)dydz \\
&- T_{xy}d\left(u + \frac{1}{2}\frac{\partial u}{\partial x}dx\right)dxdz \\
&+ \left(T_{xy} + \frac{\partial T_{xy}}{\partial y}dy\right)d\left(u + \frac{\partial u}{\partial y}dy + \frac{1}{2}\frac{\partial u}{\partial x}dx\right)dxdz \\
&+ f_x d\left(u + \frac{1}{2}\frac{\partial u}{\partial y}dy + \frac{1}{2}\frac{\partial u}{\partial x}dx\right)dxdydz
\end{aligned} \tag{A.3}
$$

Expansion and rearranging equation (A.3) yields:

$$dW_{x_1} = T_{xx}d\left(\frac{\partial u}{\partial x}\right)dxdydz$$

$$+\frac{\partial T_{xx}}{\partial x}d\left(u + \frac{\partial u}{\partial x}dx + \frac{1}{2}\frac{\partial u}{\partial y}dy\right)dxdydz$$

$$+T_{xy}d\left(\frac{\partial u}{\partial y}\right)dxdydz$$

$$+\frac{\partial T_{xy}}{\partial y}d\left(u + \frac{\partial u}{\partial y}dy + \frac{1}{2}\frac{\partial u}{\partial x}dx\right)dxdydz$$

$$+f_xd\left(u + \frac{1}{2}\frac{\partial u}{\partial y}dy + \frac{1}{2}\frac{\partial u}{\partial x}dx\right)dxdydz \tag{A.4}$$

Furthermore, the following correlation is used:

$$d\left(\frac{\partial u}{\partial x}\right) = dS_{xx} \tag{A.5}$$

The variable S_{xx} denotes the strain in x-direction with respect to the mechanical *axial stress* T_{xx} acting in the same direction. Insertion of (A.5) in (A.4) in combination with $dxdydz = dV$ yields the work done by mechanical stresses acting in x-direction:

$$dW_{x_1} = \left[\left(\frac{\partial T_{xx}}{\partial x} + \frac{\partial T_{xy}}{\partial y} + f_x\right)du + \left(\frac{\partial T_{xx}}{\partial x} + \frac{1}{2}\frac{\partial T_{xy}}{\partial y} + \frac{1}{2}f_x\right)dS_{xx}dx\right.$$

$$+\left(\frac{1}{2}\frac{\partial T_{xx}}{\partial x} + \frac{\partial T_{xy}}{\partial y} + \frac{1}{2}f_x\right)d\left(\frac{\partial u}{\partial y}\right)dy$$

$$\left.+T_{xx}dS_{xx} + T_{xy}d\left(\frac{\partial u}{\partial y}\right)\right]dV \tag{A.6}$$

The first term in equation (A.6) represents the equilibrium of forces for the static case and is omitted due to $\sum_i \mathbf{F}_i = \mathbf{0}$. The second and third term are multiplied by the differentials dx and dy and can therefore be neglected. Thus, equation (A.6) results in:

$$dW_{x_1} = \left[T_{xx}dS_{xx} + T_{xy}d\left(\frac{\partial u}{\partial y}\right)\right]dV \tag{A.7}$$

Similarly, the work done by mechanical stresses acting in y-direction results in:

$$dW_{x_2} = \left[T_{yy}dS_{yy} + T_{xy}d\left(\frac{\partial v}{\partial x}\right)\right]dV \tag{A.8}$$

The total work in the x-y plane done by the mechanical stresses results from summation of (A.7) and (A.8)

$$dW_x = [T_{xx}dS_{xx} + T_{yy}dS_{yy} + 2T_{xy}S_{xy}] \, dV, \tag{A.9}$$

where following correlation for the transverse strain S_{xy} is used in equation (A.9):

$$S_{xy} = \frac{1}{2}\left(\frac{\partial u}{\partial y} + \frac{\partial v}{\partial x}\right) \tag{A.10}$$

Considering the y-z plane, the work done by mechanical stresses acting in y-direction yields:

$$dW_y = [T_{zz}dS_{zz} + 2T_{yz}dS_{yz}] \, dV \tag{A.11}$$

The term $T_{yy}dS_{yy}$ is omitted, because it is already taken into account by equation (A.9).

Considering the x-z plane, the work done by mechanical stresses acting in z-direction yields:

$$dW_z = [2T_{zx}dS_{zx}] \, dV \tag{A.12}$$

The terms $T_{xx}dS_{xx}$ and $T_{zz}dS_{zz}$ are omitted, because they are already taken into account by the equations (A.9) and (A.11).

Thus, the total work dW_m necessary for the deformation of the infinitesimal volume element dV is equal to the sum of the equations (A.9), (A.11) and (A.12):

$$\begin{aligned} dW_m = (&T_{xx}dS_{xx} + T_{yy}dS_{yy} + T_{zz}dS_{zz} + T_{xy}dS_{xy} \\ &+2T_{xy}dS_{xy} + 2T_{yz}dS_{yz} + 2T_{xz}dS_{xz}) \, dV \end{aligned} \tag{A.13}$$

B

Derivation of the Coupling Matrix Elements

B.1 Multilayer Beam Bender Subjected to an External Static Moment

If the beam bender's tip is affected by an external bending moment M, the minimum of total potential energy Π can be calculated according to

$$\frac{\partial \Pi}{\partial a_i} = \int_0^l \frac{\partial}{\partial a_i} \left(\frac{\partial^2 \xi}{\partial x^2}\right) \left[C\left(\frac{\partial^2 \xi}{\partial x^2}\right) - M_{Piezo}\right] dx - M\frac{\partial}{\partial a_i} \left(\frac{\partial \xi}{\partial x}\right)\Bigg|_{x=l} = 0. \tag{B.1}$$

In combination with the ansatz function

$$\xi(x) = \sum_{j=1}^k a_j \xi_j(x), \tag{B.2}$$

the first and second derivative result in:

$$\frac{\partial \xi}{\partial x} = \sum_{j=2}^k j a_j x^{j-1} \tag{B.3}$$

$$\frac{\partial^2 \xi}{\partial x^2} = \sum_{j=2}^k j(j-1) a_j x^{j-2} \tag{B.4}$$

According to (B.3) and (B.4), the partial derivations with respect to the coefficients a_i result in:

$$\frac{\partial}{\partial a_i} \left(\frac{\partial \xi}{\partial x}\right)\Bigg|_{x=l} = i l^{i-1} \tag{B.5}$$

$$\frac{\partial}{\partial a_i} \left(\frac{\partial^2 \xi}{\partial x^2}\right) = i(i-1) x^{i-2} \tag{B.6}$$

Insertion of (B.4), (B.5) and (B.6) into (B.1) yields:

$$\int_0^l i\,(i-1)\,x^{i-2}\left[C\sum_{j=2}^{k} j\,(j-1)\,a_j x^{j-2} - M_{Piezo}\right]dx - Mil^{i-1} = 0 \quad \text{(B.7)}$$

Integration of (B.7) yields after some algebraic rearranging:

$$\Leftrightarrow (i-1)\sum_{j=2}^{k}\frac{j\,(j-1)}{j+i-3}a_j l^{j-2} = \underbrace{\frac{M}{C}}_{\equiv\nu} + \underbrace{\frac{M_{Piezo}}{C}}_{\equiv\tau} \quad \text{(B.8)}$$

Equation (B.8) represents a linear system of equations, the coefficients a_j of the ansatz function $\xi(x)$ can be derived from. In order to set up the linear system of equations, $k = 4$ is chosen.

Following linear system of equations is determined:

$$\begin{pmatrix} 2 & 3l & 4l^2 \\ 2 & 4l & 6l^2 \\ 2 & \frac{9}{2}l & \frac{36}{5}l^2 \end{pmatrix}\begin{pmatrix} a_2 \\ a_3 \\ a_4 \end{pmatrix} = \begin{pmatrix} \nu+\tau \\ \nu+\tau \\ \nu+\tau \end{pmatrix} \quad \text{(B.9)}$$

The evaluation of (B.9) yields the following solutions for the individual coefficients a_j:

$$a_2 = \tfrac{1}{2}\,(\nu+\tau); \; a_3 = 0; \; a_4 = 0$$

Thus, the ansatz function $\xi(x)$ results in:

$$\xi(x) = a_2 x^2$$

$$\Rightarrow \xi(x) = \frac{\nu}{2}x^2 + \frac{\tau}{2}x^2$$

$$\Rightarrow \xi(x) = \frac{M}{2C}x^2 + \frac{M_{Piezo}}{2C}x^2 \quad \text{(B.10)}$$

Using the relationship (4.33) concerning the piezoelectric moment, the ansatz function $\xi(x)$ can be formulated in following way:

$$\xi(x) = \frac{M}{2C}x^2 + \frac{1}{2C}\sum_{i=1}^{n}\frac{w_i d_{31,i}}{2s_{11,i}}E_{3,i}\left[2\bar{z}h_i - 2h_i\sum_{j=1}^{i}h_j + h_i^2\right]x^2 \quad \text{(B.11)}$$

Furthermore, it is assumed, that all active layers are driven with the same voltage U. Thus, (B.11) results in:

$$\xi\left(x\right) = M\frac{x^2}{2C}$$

$$+ U\left[\frac{1}{2C}\underbrace{\left(\sum_{i=1}^{n}\frac{w_i d_{31,i}}{2s_{11,i}h_i}\left[2\bar{z}h_i - 2h_i\sum_{j=1}^{i}h_j + h_i^2\right]\right)}_{\equiv m_{Piezo}}x^2\right]$$

$$\tag{B.12}$$

The quantity m_{Piezo} represents the piezoelectric moment referred to the driving voltage U. It can generally be written:

$$M_{Piezo} = m_{Piezo}U \tag{B.13}$$

Thus, equation (B.10) can be formulated as follows:

$$\xi\left(x\right) = M\frac{x^2}{2C} + U\frac{m_{Piezo}x^2}{2C} \tag{B.14}$$

Thereby, the deflection $\xi\left(x\right)$ in equation (B.14) can be represented as a function dependent on the extensive quantities M and U as well as on the length coordinate x of the bending actuator. Thus, the matrix elements $m_{21}\left(x\right)$ and $m_{24}\left(x\right)$ of the coupling matrix $\mathbf{M}$ (see eq. 4.46, section 4.6) are known.

The standardization on the bending actuator length l yields:

$$m_{21}\left(x\right) = \frac{l^2}{2C}\left(\frac{x}{l}\right)^2 \tag{B.15}$$

$$m_{24}\left(x\right) = \frac{m_{Piezo}l^2}{2C}\left(\frac{x}{l}\right)^2 \tag{B.16}$$

The derivative of the ansatz function $\xi\left(x\right)$ with respect to the length coordinate x yields the bending angle for small deflections $\tan\alpha\left(x\right) \approx \alpha\left(x\right) = d\xi/dx$.

$$\alpha\left(x\right) = M\frac{x}{C} + U\frac{m_{Piezo}x}{C} \tag{B.17}$$

The elements $m_{11}\left(x\right)$ and $m_{14}\left(x\right)$ of the coupling matrix $\mathbf{M}$ standardized on the actuator length l are equal to:

$$m_{11}\left(x\right) = \frac{l}{C}\left(\frac{x}{l}\right) \tag{B.18}$$

$$m_{14}\left(x\right) = \frac{m_{Piezo}l}{C}\left(\frac{x}{l}\right) \tag{B.19}$$

The volume displacement $V(x)$ is calculated by means of integration of equation (B.14) according to

$$V(x) = \int_0^x \int_0^w \xi(x')\,dx'\,dy \qquad , \text{where } w = \max\{w_i\,\forall i\,|1 \leq i \leq n\}. \quad \text{(B.20)}$$

Thus, the volume displacement results in

$$V(x) = w \int_0^x \left[M\frac{x'^2}{2C} + U\frac{m_{Piezo}x'^2}{2C} \right] dx'$$

$$\Leftrightarrow V(x) = M\frac{wx^3}{6C} + U\frac{m_{Piezo}wx^3}{6C} \quad \text{(B.21)}$$

The matrix elements $m_{31}(x)$ and $m_{34}(x)$ are equal to:

$$m_{31}(x) = \frac{wl^3}{6C}\left(\frac{x}{l}\right)^3 \quad \text{(B.22)}$$

$$m_{34}(x) = \frac{m_{Piezo}wl^3}{6C}\left(\frac{x}{l}\right)^3 \quad \text{(B.23)}$$

B.2 Multilayer Beam Bender Subjected to an External Static Force

If the beam bender's tip is affected by an external force F, the minimum of total potential energy Π can be calculated according to

$$\int_0^l \frac{\partial}{\partial a_i}\left(\frac{\partial^2 \xi}{\partial x^2}\right)\left[C\left(\frac{\partial^2 \xi}{\partial x^2}\right) - M_{Piezo}\right]dx - F\frac{\partial \xi}{\partial a_i}\bigg|_{x=l} = 0. \quad \text{(B.24)}$$

In combination with the ansatz function (B.2), the partial derivations with respect to the coefficients a_i result in:

$$\frac{\partial}{\partial a_i}\left(\frac{\partial^2 \xi}{\partial x^2}\right) = i(i-1)x^{i-2} \quad \text{(B.25)}$$

$$\frac{\partial \xi}{\partial a_i}\bigg|_{x=l} = l^i \quad \text{(B.26)}$$

Insertion of (B.25), (B.26) and (B.4) into (B.24) yields:

$$\int_0^l i(i-1)x'^{i-2}\left[C\sum_{j=2}^k j(j-1)a_j x^{j-2} - M_{Piezo}\right]dx - Fl^i = 0 \quad \text{(B.27)}$$

Integration of (B.27) yields after some algebraic rearranging:

$$i(i-1) \sum_{j=2}^{k} \frac{j(j-1)}{j+i-3} a_j l^{j-2} = \underbrace{\frac{Fl}{C}}_{\equiv \nu} + i \underbrace{\frac{M_{Piezo}}{C}}_{\equiv \tau} \tag{B.28}$$

In order to set up the linear system of equations, $k = 4$ is chosen. Further it should be noted, that $j \leq i \leq k$.

Following linear system of equations is determined:

$$\begin{pmatrix} 4 & 6l & 8l^2 \\ 6 & 12l & 18l^2 \\ 8 & 18l & \frac{144}{5}l^2 \end{pmatrix} \begin{pmatrix} a_2 \\ a_3 \\ a_4 \end{pmatrix} = \begin{pmatrix} \nu + 2\tau \\ \nu + 3\tau \\ \nu + 4\tau \end{pmatrix} \tag{B.29}$$

The evaluation of (B.29) yields the following solutions for the individual coefficients a_j:

$$a_2 = \tfrac{1}{2}(\nu + \tau); \ a_3 = -\tfrac{1}{6l}\nu; \ a_4 = 0$$

Thus, the ansatz function $\xi(x)$ results in:

$$\xi(x) = a_2 x^2 + a_3 x^3$$

$$\Rightarrow \xi(x) = \frac{\nu}{2} x^2 + \frac{\tau}{2} x^2 - \frac{\nu}{6l} x^3$$

$$\Rightarrow \xi(x) = \frac{Fl}{2C} x^2 - \frac{F}{6C} x^3 + \frac{M_{Piezo}}{2C} x^2 \tag{B.30}$$

Taking equation (B.13) into consideration, the ansatz function $\xi(x)$ standardized on the bending actuator length l can be formulated in following way:

$$\xi(x) = \frac{Fl^3}{2C}\left(\frac{x}{l}\right)^2 - \frac{Fl^3}{6C}\left(\frac{x}{l}\right)^3 + U\frac{m_{Piezo}l^2}{2C}\left(\frac{x}{l}\right)^2$$

$$\Leftrightarrow \xi(x) = F\frac{l^3}{6C}\left[3\left(\frac{x}{l}\right)^2 - \left(\frac{x}{l}\right)^3\right] + U\frac{m_{Piezo}l^2}{2C}\left(\frac{x}{l}\right)^2 \tag{B.31}$$

The deflection $\xi(x)$ in equation (B.31) can be represented as a function dependent on the extensive quantities F and U as well as on the length coordinate x of the bending actuator. Thus, the matrix element $m_{22}(x)$ of the coupling matrix $\mathbf{M}$ (see eq. 4.46, section 4.6) is known. The matrix element $m_{24}(x)$ has already been formulated in equation (B.16).

The matrix element $m_{22}(x)$ is equal to:

$$m_{22}(x) = \frac{l^3}{6C}\left[3\left(\frac{x}{l}\right)^2 - \left(\frac{x}{l}\right)^3\right] \tag{B.32}$$

The bending angle α can be derived from (B.31) according to:

$$\alpha(x) = F\frac{l^2}{2C}\left[2\left(\frac{x}{l}\right) - \left(\frac{x}{l}\right)^2\right] + U\frac{m_{Piezo}l}{C}\left(\frac{x}{l}\right) \tag{B.33}$$

Thus, the matrix element $m_{12}(x)$ results in:

$$m_{12}(x) = \frac{l^2}{2C}\left[2\left(\frac{x}{l}\right) - \left(\frac{x}{l}\right)^2\right] \tag{B.34}$$

The volume displacement $V(x)$ is calculated by means of integration of equation (B.20) and yields:

$$V(x) = w\int_0^x \left[F\frac{l^3}{6C}\left[3\left(\frac{x'}{l}\right)^2 - \left(\frac{x'}{l}\right)^3\right] + U\frac{m_{Piezo}l^2}{2C}\left(\frac{x'}{l}\right)^2\right]dx'$$

$$\Rightarrow V(x) = F\frac{wl^4}{24C}\left[4\left(\frac{x}{l}\right)^3 - \left(\frac{x}{l}\right)^4\right] + U\frac{m_{Piezo}wl^3}{6C}\left(\frac{x}{l}\right)^3 \tag{B.35}$$

The matrix element $m_{32}(x)$ is equal to:

$$m_{32}(x) = \frac{wl^4}{24C}\left[4\left(\frac{x}{l}\right)^3 - \left(\frac{x}{l}\right)^4\right] \tag{B.36}$$

B.3 Multilayer Beam Bender Subjected to a Uniform Pressure Load

If the lower side of the beam bender is affected by a uniform pressure load p, the integral minimum of total potential energy Π can be calculated according to

$$\int_0^l \frac{\partial}{\partial a_i}\left(\frac{\partial^2\xi}{\partial x^2}\right)\left[C\left(\frac{\partial^2\xi}{\partial x^2}\right) - M_{Piezo}\right]dx - pw\int_0^l \frac{\partial\xi}{\partial a_i}dx = 0. \tag{B.37}$$

In combination with the ansatz function (B.2), the partial derivations with respect to the coefficients a_i result in:

$$\frac{\partial}{\partial a_i}\left(\frac{\partial^2\xi}{\partial x^2}\right) = i(i-1)x^{i-2} \tag{B.38}$$

$$\frac{\partial\xi}{\partial a_i} = x^i \tag{B.39}$$

Insertion of (B.4), (B.38) and (B.39) into (B.37) yields:

$$\int_0^l i\,(i-1)\,x^{i-2} \left[C\sum_{j=2}^k j\,(j-1)\,a_j x^{j-2} - M_{Piezo} \right] dx - pw\int_0^l x^i dx = 0$$

$$\Leftrightarrow i\,(i^2-1)\sum_{j=2}^k \frac{j\,(j-1)}{j+i-3}a_j l^{j-2} = \underbrace{\frac{pwl^2}{C}}_{\equiv\nu} + i\,(i+1)\underbrace{\frac{M_{Piezo}}{C}}_{\equiv\tau} \tag{B.40}$$

In order to set up the linear system of equations, $k=4$ is chosen. Further it should be noted, that $j \le i \le k$.

Following linear system of equations is determined:

$$\begin{pmatrix} 12 & 18l & 24l^2 \\ 24 & 48l & 72l^2 \\ 40 & 90l & 144l^2 \end{pmatrix} \begin{pmatrix} a_2 \\ a_3 \\ a_4 \end{pmatrix} = \begin{pmatrix} \nu+6\tau \\ \nu+12\tau \\ \nu+20\tau \end{pmatrix} \tag{B.41}$$

The evaluation of (B.41) yields the following solutions for the individual coefficients a_j:

$$a_2 = \tfrac{1}{4}\,(\nu+2\tau); \; a_3 = -\tfrac{1}{6l}\nu; \; a_4 = \tfrac{1}{24l^2}\nu$$

Thus, the ansatz function $\xi\,(x)$ results in:

$$\xi\,(x) = a_2 x^2 + a_3 x^3 + a_4 x^4$$

$$\Rightarrow \xi\,(x) = \frac{\nu}{4}x^2 + \frac{\tau}{2}x^2 - \frac{\nu}{6l}x^3 + \frac{\nu}{24l^2}x^4$$

$$\Rightarrow \xi\,(x) = \frac{pwl^2}{4C}x^2 - \frac{pwl}{6C}x^3 + \frac{pw}{24C}x^4 + \frac{M_{Piezo}}{2C}x^2 \tag{B.42}$$

Taking equation (B.13) into consideration, the ansatz function $\xi\,(x)$ standardized on the bending actuator length l can be formulated in following way:

$$\xi\,(x) = p\frac{wl^4}{24C}\left[6\left(\frac{x}{l}\right)^2 - 4\left(\frac{x}{l}\right)^3 + \left(\frac{x}{l}\right)^4 \right] + U\frac{m_{Piezo}l^2}{2C}\left(\frac{x}{l}\right)^2 \tag{B.43}$$

The deflection $\xi\,(x)$ in equation (B.43) can be represented as a function dependent on the extensive quantities p and U as well as on the length coordinate x of the bending actuator. Thus, the matrix element $m_{23}\,(x)$ of the coupling matrix $\mathbf{M}$ (see eq. 4.46, section 4.6) is known.

The matrix element $m_{23}(x)$ is equal to:

$$m_{23}(x) = \frac{wl^4}{24C}\left[6\left(\frac{x}{l}\right)^2 - 4\left(\frac{x}{l}\right)^3 + \left(\frac{x}{l}\right)^4\right] \tag{B.44}$$

The bending angle α can be derived from (B.43) according to:

$$\alpha(x) = p\frac{wl^3}{6C}\left[3\left(\frac{x}{l}\right) - 3\left(\frac{x}{l}\right)^2 + 4\left(\frac{x}{l}\right)^3\right] + U\frac{m_{Piezo}l}{C}\left(\frac{x}{l}\right) \tag{B.45}$$

Thus, the matrix element $m_{13}(x)$ results in:

$$m_{13}(x) = \frac{wl^3}{6C}\left[3\left(\frac{x}{l}\right) - 3\left(\frac{x}{l}\right)^2 + 4\left(\frac{x}{l}\right)^3\right] \tag{B.46}$$

The volume displacement $V(x)$ is calculated by means of integration of equation (B.20) and yields:

$$V(x) = w\int_0^x \frac{pwl^4}{24C}\left[6\left(\frac{x'}{l}\right)^2 - 4\left(\frac{x'}{l}\right)^3 + \left(\frac{x'}{l}\right)^4\right]dx'$$

$$+ w\int_0^x U\frac{m_{Piezo}l^2}{2C}\left(\frac{x'}{l}\right)^2 dx'$$

$$\Rightarrow V(x) = p\frac{w^2l^5}{120C}\left[10\left(\frac{x}{l}\right)^3 - 5\left(\frac{x}{l}\right)^4 + \left(\frac{x}{l}\right)^5\right]$$

$$+ U\frac{m_{Piezo}wl^3}{6C}\left(\frac{x}{l}\right)^3 \tag{B.47}$$

The matrix element $m_{33}(x)$ is equal to:

$$m_{33}(x) = \frac{w^2l^5}{120C}\left[10\left(\frac{x}{l}\right)^3 - 5\left(\frac{x}{l}\right)^4 + \left(\frac{x}{l}\right)^5\right] \tag{B.48}$$

B.4 Electrical Charge Generated by the Extensive Parameters

In this section, the matrix elements $m_{41}(x)$, $m_{42}(x)$, $m_{43}(x)$ and $m_{44}(x)$ of the coupling matrix $\mathbf{M}$ will be derived. The starting point of following considerations is the total stored energy within the bending actuator (see eq. 4.45, section 4.5.2). Taking the boundary condition into account, that all active layers are driven with the same voltage $U_{3,i} = U$, equation (4.45) can be formulated in following way:

$$W_{tot} = \frac{1}{2} \sum_{i=1}^{n} \int_{0}^{l} \left[\frac{\varepsilon_{33,i}^{T} w_i}{h_i} U^2 \right] dx - \frac{1}{2} \sum_{i=1}^{n} \int_{0}^{l} \left[\frac{d_{31,i}^2 w_i}{s_{11,i}^{E} h_i} U^2 \right] dx$$

$$+ \int_{0}^{l} \frac{M_{Piezo}^2}{2C} dx + \int_{0}^{l} \left[\frac{M^2}{2C} + \frac{M M_{Piezo}}{C} \right] dx \tag{B.49}$$

According to the definition of the quantity M_{Piezo} in (4.33), the quantity m_{Piezo} will be defined:

$$M_{Piezo} = \underbrace{\sum_{i=1}^{n} \frac{d_{31,i} w_i}{2 s_{11,i} h_i} \left[2\bar{z} h_i - 2 h_i \sum_{j=1}^{i} h_j + h_i^2 \right]}_{m_{Piezo}} U = m_{Piezo} U \tag{B.50}$$

Using equation (B.50) yields:

$$\frac{M_{Piezo}^2}{2C} = U^2 \frac{m_{Piezo}^2}{2C} \tag{B.51}$$

The term

$$\frac{m_{Piezo}^2}{2C}$$

physically corresponds to a capacitance per unit length (unit: $1\,\text{F/m}$). In order to formulate the total potential energy Π, the driving voltage U combining the charge Q_i and the capacitance C_i of the ith layer of the piezoelectric multilayer beam bending actuator is considered.

For the ith layer, it can be written

$$U = \frac{Q_i}{C_i}, \tag{B.52}$$

from which follows

$$U = \frac{\sum_{i=1}^{n} Q_i}{\sum_{i=1}^{n} C_i} = \frac{Q_{tot}(x)}{C_{tot}(x)}. \tag{B.53}$$

Furthermore, the general correlations

$$C_{tot} = \frac{\partial Q_{tot}}{\partial U} \quad \text{and} \quad Q_{tot} = \frac{\partial W_{tot}}{\partial U}$$

are valid resulting in:

$$C_{tot} = \frac{\partial^2 W_{tot}}{\partial U^2} \tag{B.54}$$

Now, equation (B.49) can be formulated using the definition (B.50):

$$W_{tot}(x) = \frac{1}{2}\sum_{i=1}^{n}\int_0^x \left[\frac{\varepsilon_{33,i}^T w_i}{h_i}U^2\right]dx' - \frac{1}{2}\sum_{i=1}^{n}\int_0^x \left[\frac{d_{31,i}^2 w_i}{s_{11,i}^E h_i}U^2\right]dx'$$

$$+U^2\int_0^x \frac{m_{Piezo}^2}{2C}dx' + \int_0^x \left[\frac{M^2}{2C} + \frac{MM_{Piezo}}{C}\right]dx' \qquad (B.55)$$

Double partial derivation of (B.55) with respect to U yields:

$$\frac{\partial^2 W_{tot}(x)}{\partial U^2} = x\sum_{i=1}^{n}\frac{\varepsilon_{33,i}^T w_i}{h_i} - x\sum_{i=1}^{n}\frac{d_{31,i}^2 w_i}{s_{11,i}^E h_i} + x\frac{m_{Piezo}^2}{C}$$

$$\Leftrightarrow \frac{\partial^2 W_{tot}(x)}{\partial U^2} = x\left[\sum_{i=1}^{n}\frac{\varepsilon_{33,i}^T w_i}{h_i} - \sum_{i=1}^{n}\frac{d_{31,i}^2 w_i}{s_{11,i}^E h_i} + \frac{m_{Piezo}^2}{C}\right] \qquad (B.56)$$

In combination with the definition of the capacitance per unit length

$$C'_{Piezo} = \sum_{i=1}^{n}\frac{\varepsilon_{33,i}^T w_i}{h_i} - \sum_{i=1}^{n}\frac{d_{31,i}^2 w_i}{s_{11,i}^E h_i} + \frac{m_{Piezo}^2}{C}, \qquad (B.57)$$

it follows with respect to (B.56) and (B.54):

$$\frac{\partial^2 W_{tot}(x)}{\partial U^2} = C'_{Piezo}x = C_{tot} \qquad (B.58)$$

The formation of the derivative

$$U = \frac{\partial Q}{\partial C_{tot}}$$

yields in combination with equation (B.58):

$$U = \frac{1}{C'_{Piezo}}\frac{\partial Q}{\partial x} \qquad (B.59)$$

The total stored energy (B.55) can be defined in following form including (B.13) and (B.58):

$$W_{tot} = \sum_{i=1}^{n}\int_0^l \frac{U^2}{2}\left[\frac{\varepsilon_{33,i}^T w_i}{h_i} - \frac{d_{31,i}^2 w_i}{s_{11,i}^E h_i} + \frac{m_{Piezo}^2}{C}\right]dx$$

$$+\int_0^l \frac{M^2}{2C}dx + \int_0^l \frac{MM_{Piezo}}{C}dx$$

$$\Leftrightarrow W_{tot} = \int_0^l \frac{U^2}{2}C'_{Piezo}dx + \int_0^l \frac{M^2}{2C}dx + \int_0^l \frac{MU}{C}m_{Piezo}dx \qquad (B.60)$$

If now equation (B.59) is considered, the total energy W_{tot} is defined in its final form:

$$W_{tot} = \int_0^l \frac{1}{2C'_{Piezo}} \left(\frac{\partial Q}{\partial x}\right)^2 dx + \int_0^l \frac{M^2}{2C} dx + \int_0^l \frac{M}{C} \frac{m_{Piezo}}{C'_{Piezo}} \left(\frac{\partial Q}{\partial x}\right) dx \quad (B.61)$$

In order to be able to formulate the total potential energy, the final value work W_a performed by the extensive quantity U has to be determined.

It can generally be written:

$$dW_a = U dQ$$

$$\Rightarrow W_a = \int_0^{Q_{tot}} U dQ \quad (B.62)$$

Applying the total differential to $dQ = dQ(x)$ yields:

$$dQ = \left(\frac{\partial Q}{\partial x}\right) dx \quad (B.63)$$

Insertion of (B.63) into (B.62) and taking the new integral limits into account, the final value work W_a is equal to:

$$W_a = U \int_0^l \left(\frac{\partial Q}{\partial x}\right) dx \quad (B.64)$$

Finally, the total potential energy Π can be formulated using (B.61) and (B.64):

$$\Pi = \frac{1}{2C'_{Piezo}} \int_0^l \left(\frac{\partial Q}{\partial x}\right)^2 dx + \frac{M}{C} \frac{m_{Piezo}}{C'_{Piezo}} \int_0^l \left(\frac{\partial Q}{\partial x}\right) dx + \int_0^l \frac{M^2}{2C} dx$$

$$-U \int_0^l \left(\frac{\partial Q}{\partial x}\right) dx \quad (B.65)$$

According to the Ritz method, following ansatz function

$$Q(x) = \sum_{j=1}^k a_j x^j \quad (B.66)$$

is chosen. Insertion of (B.66) into (B.65) and following partial derivation with respect to the coefficients a_i for $j \le i \le k$ yields the integral minimum of

the total potential energy Π. With respect to the necessary condition for the existence of a minimum, it follows:

$$\frac{\partial \Pi}{\partial a_i} = 0$$

$$\Leftrightarrow \frac{1}{C'_{Piezo}} \int_0^l \frac{\partial}{\partial a_i} \left(\frac{\partial Q}{\partial x}\right) \left[\left(\frac{\partial Q}{\partial x}\right) + \frac{M}{C} m_{Piezo}\right] dx - U \int_0^l \frac{\partial}{\partial a_i} \left(\frac{\partial Q}{\partial x}\right) dx = 0$$

$$(B.67)$$

Furthermore, it follows from the ansatz function (B.66):

$$\frac{\partial Q}{\partial x} = \sum_{j=1}^k j a_j x^{j-1} \tag{B.68}$$

The partial derivative with respect to the general coefficient a_i yields in combination with (B.68):

$$\frac{\partial}{\partial a_i} \left(\frac{\partial Q}{\partial x}\right) = i x^{i-1} \tag{B.69}$$

B.4.1 External Static Moment

Insertion of (B.68) and (B.69) into equation (B.65) yields:

$$\frac{1}{C'_{Piezo}} \int_0^l i x^{i-1} \left[\sum_{j=1}^k j a_j x^{j-1} + \frac{M}{C} m_{Piezo}\right] dx - U \int_0^l i x^{i-1} dx = 0$$

$$\Leftrightarrow i \sum_{j=1}^k \frac{j}{j+i-1} a_j l^{j-1} = \underbrace{U C'_{Piezo}}_{\equiv \nu} - \underbrace{\frac{M m_{Piezo}}{C}}_{\equiv \tau} \tag{B.70}$$

In order to set up the linear system of equations, $k = 3$ is chosen. Furthermore, $j \leq i \leq k$ is considered.

Thus, the following linear system of equations can be formulated according to:

$$\begin{pmatrix} 1 & l & l^2 \\ 1 & \frac{4}{3}l & \frac{3}{2}l^2 \\ 1 & \frac{3}{2}l & \frac{9}{5}l^2 \end{pmatrix} \begin{pmatrix} a_1 \\ a_2 \\ a_3 \end{pmatrix} = \begin{pmatrix} \nu - \tau \\ \nu - \tau \\ \nu - \tau \end{pmatrix} \tag{B.71}$$

The evaluation of the linear system of equations (B.71) yields the nontrivial solution for the individual coefficients a_j:

$$a_1 = \nu - \tau; \; a_2 = 0; \; a_3 = 0$$

Thus, the ansatz function $Q(x)$ results in:

$$Q(x) = a_1 x$$

$$\Rightarrow Q(x) = \nu x - \tau x$$

$$\Rightarrow Q(x) = UC'_{Piezo} x - \frac{M m_{Piezo}}{C} x$$

$$\Leftrightarrow Q(x) = -\frac{M m_{Piezo}}{C} x$$
$$+ U \left[\sum_{i=1}^{n} \frac{w_i}{h_i} \left(\varepsilon_{33,i}^{T} - \frac{d_{31,i}^2}{s_{11,i}^E} \right) + \frac{m_{Piezo}^2}{C} \right] x \qquad (B.72)$$

The bracket term after the summation sign can be summarized according to

$$\varepsilon_{33,i}^{S} = \varepsilon_{33,i}^{T} - \frac{d_{31,i}^2}{s_{11,i}^E}. \qquad (B.73)$$

The ansatz function standardized on the bending actuator length l yields:

$$Q(x) = -\frac{M m_{Piezo} l}{C} \left(\frac{x}{l} \right) + U \left[\sum_{i=1}^{n} \frac{\varepsilon_{33,i}^{S} w_i l}{h_i} + \frac{m_{Piezo}^2}{C} l \right] \left(\frac{x}{l} \right) \qquad (B.74)$$

The charge $Q(x)$ in equation (B.74) can be represented as a function dependent on the extensive quantities M and U as well as on the length coordinate x of the bending actuator. Thus, the matrix elements $m_{41}(x)$ and $m_{44}(x)$ of the coupling matrix $\mathbf{M}$ (see eq. 4.46, section 4.6) are known.

The matrix elements $m_{41}(x)$ and $m_{44}(x)$ are equal to:

$$m_{41}(x) = -\frac{m_{Piezo} l}{C} \left(\frac{x}{l} \right) \qquad (B.75)$$

$$m_{44}(x) = \left[\sum_{i=1}^{n} \frac{\varepsilon_{33,i}^{S} w_i l}{h_i} + \frac{m_{Piezo}^2}{C} l \right] \left(\frac{x}{l} \right) \qquad (B.76)$$

B.4.2 External Static Force

Subjecting the beam bending actuator to an external static force F perpendicularly to the tip (see Fig. 4.5, section 4.6) results in an internal bending moment M. In order to calculate the internal bending moment, the definition
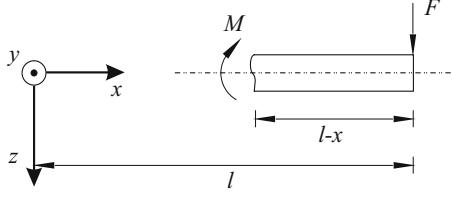
Fig. B.1. Correlation between the external force F and the internal bending moment M

of the sectional quantities is considered. Figure B.1 illustrates the correlation between the external force F and the internal bending moment M.

Considering the equilibrium condition $\sum_i M_i = 0$, the internal bending moment M results in:

$$M = -F\left(l - x\right) \tag{B.77}$$

Thus, according to (B.67) and using (B.77), the integral minimum of the total potential energy results in:

$$\frac{1}{C'_{Piezo}} \int_0^l \frac{\partial}{\partial a_i}\left(\frac{\partial Q}{\partial x}\right)\left[\left(\frac{\partial Q}{\partial x}\right) - \frac{F\left(l-x\right)}{C}m_{Piezo}\right] dx = U \int_0^l \frac{\partial}{\partial a_i}\left(\frac{\partial Q}{\partial x}\right) dx \tag{B.78}$$

Insertion of (B.68) and (B.69) into equation (B.78) yields:

$$\frac{1}{C'_{Piezo}} \int_0^l ix^{i-1}\left[\sum_{j=1}^k ja_j x^{j-1} - \frac{F\left(l-x\right)}{C}m_{Piezo}\right] dx - U \int_0^l ix^{i-1}dx = 0$$

$$\Leftrightarrow i\sum_{j=1}^k \frac{j}{j+i-1}a_j l^{j-1} = \underbrace{UC'_{Piezo}}_{\equiv \nu} + \frac{1}{(i+1)}\underbrace{\frac{Fm_{Piezo}l}{C}}_{\equiv \tau} \tag{B.79}$$

In order to set up the linear system of equations, $k = 3$ is chosen. Furthermore, $j \leq i \leq k$ is considered.

Thus, the following linear system of equations can be formulated:

$$\begin{pmatrix} 1 & l & l^2 \\ 1 & \frac{4}{3}l & \frac{3}{2}l^2 \\ 1 & \frac{3}{2}l & \frac{9}{5}l^2 \end{pmatrix} \begin{pmatrix} a_1 \\ a_2 \\ a_3 \end{pmatrix} = \begin{pmatrix} \nu + \frac{1}{2}\tau \\ \nu + \frac{1}{3}\tau \\ \nu + \frac{1}{4}\tau \end{pmatrix} \tag{B.80}$$

The evaluation of the linear system of equations (B.80) yields the nontrivial solution for the individual coefficients a_j:

$$a_1 = \nu + \tau; \; a_2 = -\frac{1}{2l}\tau; \; a_3 = 0$$

Thus, the ansatz function Q(x) results in:

$$Q(x) = a_1 x + a_2 x^2$$

$$\Rightarrow Q(x) = \nu x + \tau x - \frac{1}{2l}\tau x^2$$

$$\Rightarrow Q(x) = U C'_{Piezo} x + \frac{F m_{Piezo} l}{C} x - \frac{F m_{Piezo}}{2C} x^2$$

The ansatz function standardized on the bending actuator length l yields in combination with (B.73):

$$Q(x) = \frac{F m_{Piezo} l^2}{2C} \left[2\left(\frac{x}{l}\right) - \left(\frac{x}{l}\right)^2 \right] + U \left[\sum_{i=1}^{n} \frac{\varepsilon_{33,i}^{S} w_i l}{h_i} + \frac{m_{Piezo}^2}{C} l \right] \left(\frac{x}{l}\right)$$

(B.81)

The charge $Q(x)$ in equation (B.81) can be represented as a function dependent on the extensive quantities F and U as well as on the length coordinate x of the bending actuator. Thus, the matrix element $m_{42}(x)$ of the coupling matrix $\mathbf{M}$ (see eq. 4.46, section 4.6) is known. The matrix element $m_{44}(x)$ has already been determined before.

The matrix element $m_{42}(x)$ is equal to:

$$m_{42}(x) = \frac{m_{Piezo} l^2}{2C} \left[2\left(\frac{x}{l}\right) - \left(\frac{x}{l}\right)^2 \right]$$

(B.82)

B.4.3 External Uniform Pressure Load

Subjecting the beam bending actuator to an external uniform pressure load p perpendicularly to the x-y plane (see Fig. 4.5, section 4.6) results also in an internal bending moment M. Figure B.2 shows the correlation between the external pressure load p and the internal bending moment M. Considering the width w of the bending actuator, the resulting force F_{res} caused by the uniform pressure load p is equal to:

$$F_{res} = pw(l - x)$$

(B.83)

Taking the equilibrium condition $\sum_i M_i = 0$ into account, the internal bending moment M results in:
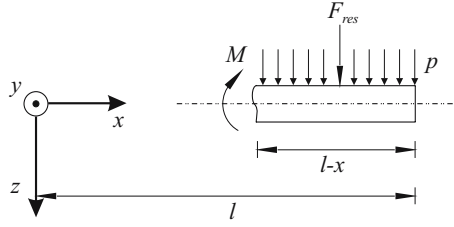
Fig. B.2. Correlation between the external pressure load p and the internal bending moment M

$$M = -F_{res}\frac{(l - x)}{2}$$

$$\Rightarrow M = -pw\frac{(l - x)^2}{2} \tag{B.84}$$

Thus, according to (B.67) and using (B.84), the integral minimum of the total potential energy results in:

$$\frac{1}{C'_{Piezo}}\int_0^l \frac{\partial}{\partial a_i}\left(\frac{\partial Q}{\partial x}\right)\left[\left(\frac{\partial Q}{\partial x}\right) - \frac{pwm_{Piezo}}{2C}(l - x)^2\right]dx = U\int_0^l \frac{\partial}{\partial a_i}\left(\frac{\partial Q}{\partial x}\right)dx \tag{B.85}$$

Insertion of (B.68) and (B.69) into equation (B.85) yields:

$$\frac{1}{C'_{Piezo}}\int_0^l ix^{i-1}\left[\sum_{j=1}^k ja_j x^{j-1} - \frac{pwm_{Piezo}}{2C}(l - x)^2\right]dx = U\int_0^l ix^{i-1}dx$$

$$\Leftrightarrow i\sum_{j=1}^k \frac{j}{j + i - 1}a_j l^{j-1} = \underbrace{UC'_{Piezo}}_{\equiv \nu} + \frac{1}{(i + 1)(i + 2)}\underbrace{\frac{pwm_{Piezo}l^2}{C}}_{\equiv \tau} \tag{B.86}$$

In order to set up the linear system of equations, $k = 3$ is chosen. Furthermore, $j \leq i \leq k$ is considered.

Thus, the following linear system of equations can be formulated:

$$\begin{pmatrix} 1 & l & l^2 \\ 1 & \frac{4}{3}l & \frac{3}{2}l^2 \\ 1 & \frac{3}{2}l & \frac{9}{5}l^2 \end{pmatrix}\begin{pmatrix} a_1 \\ a_2 \\ a_3 \end{pmatrix} = \begin{pmatrix} \nu + \frac{1}{6}\tau \\ \nu + \frac{1}{12}\tau \\ \nu + \frac{1}{20}\tau \end{pmatrix} \tag{B.87}$$

The evaluation of the linear system of equations (B.87) yields the nontrivial solution for the individual coefficients a_j:

$$a_1 = \nu + \tfrac{1}{2}\tau;\ a_2 = -\tfrac{1}{2l}\tau;\ a_3 = \tfrac{1}{6l^2}\tau$$

Thus, the ansatz function $Q(x)$ results in:

$$Q(x) = a_1 x + a_2 x^2 + a_3 x^3$$

$$\Rightarrow Q(x) = \nu x + \frac{\tau}{2}x - \frac{\tau}{2l}x^2 + \frac{\tau}{6l^2}x^3$$

$$\Rightarrow Q(x) = UC'_{Piezo}x + \frac{pwm_{Piezo}l^2}{2C}x - \frac{pwm_{Piezo}l}{2C}x^2 + \frac{pwm_{Piezo}}{6C}x^3$$

The ansatz function standardized on the bending actuator length l yields in combination with (B.73):

$$Q(x) = \frac{pwm_{Piezo}l^3}{6C}\left[3\left(\frac{x}{l}\right) - 3\left(\frac{x}{l}\right)^2 + \left(\frac{x}{l}\right)^3\right]$$

$$+U\left[\sum_{i=1}^{n}\frac{\varepsilon_{33,i}^S w_i l}{h_i} + \frac{m_{Piezo}^2}{C}l\right]\left(\frac{x}{l}\right) \tag{B.88}$$

The charge $Q(x)$ in equation (4.126) can be represented as a function dependent on the extensive quantities p and U as well as on the length coordinate x of the bending actuator. Thus, the matrix element $m_{43}(x)$ of the coupling matrix $\mathbf{M}$ (see eq. 4.46, section 4.6) is known.

The matrix element $m_{43}(x)$ is equal to:

$$m_{43}(x) = \frac{wm_{Piezo}l^3}{6C}\left[3\left(\frac{x}{l}\right) - 3\left(\frac{x}{l}\right)^2 + \left(\frac{x}{l}\right)^3\right] \tag{B.89}$$

At this point, all matrix elements of the coupling matrix $\mathbf{M}$ are formulated in an analytically closed form.

C

Mechanical Potential and Kinetic Energy

In the following, the potential V being founded on the electrical enthalpy H_e and the total kinetic energy T of a piezoelectric multilayer beam bending actuator are deduced. Thereby, the electrical enthalpy represents a thermodynamic potential corresponding to an energy density.

The potential V is equal to

$$V = \tilde{H}_e \tag{C.1}$$

with

$$\tilde{H}_e = \iiint_V H_e dV. \tag{C.2}$$

Thus, the potential V results in:

$$V = \tilde{H}_e = \iiint_V H_e dV \tag{C.3}$$

For an n-layered system the individual layers have to be taken into account. The potential of the ith layer yields in accordance with (C.3):

$$V_i = \tilde{H}_{e,i} = \iiint_{V_i} H_{e,i} dV_i \tag{C.4}$$

Using the equations (C.2) and (C.4) results in the total potential:

$$V = \sum_{i=1}^{n} \tilde{H}_{e,i} = \sum_{i=1}^{n} \iiint_{V_i} H_{e,i} dV_i \tag{C.5}$$

For the kinetic energy T_i of the ith layer, it can be written (see eq. 5.24, section 5.3):

$$dT_i = dm_i \frac{\mathbf{v}_i^2}{2}$$

$$\Leftrightarrow dT_i = \frac{1}{2}\rho_i \mathbf{v}_i^2 dV_i$$

$$\Leftrightarrow dT_i = \frac{1}{2}\rho_i \left(\frac{\partial \xi(x,t)}{\partial t}\right)^2 dV_i$$

$$\Rightarrow T_i = \iiint_{V_i} \frac{1}{2}\rho_i \left(\frac{\partial \xi(x,t)}{\partial t}\right)^2 dV_i \tag{C.6}$$

The quantity $\xi(x,t)$ denotes the deflection in z-direction (see Fig. 4.6, section 4.6).

The total kinetic energy of an n-layered system results from the sum of the kinetic energies of each individual layer according to

$$T = \sum_{i=1}^{n} T_i$$

in

$$T = \sum_{i=1}^{n} \iiint_{V_i} \frac{1}{2}\rho_i \left(\frac{\partial \xi(x,t)}{\partial t}\right)^2 dV_i. \tag{C.7}$$

D

Derivation of the Electrical Enthalpy

The electrical enthalpy is equal to (see eq. 3.61, section 3.3.3):

$$H_e = \frac{1}{2}c_{pq}^E S_q S_p - e_{ip}E_i S_p - \frac{1}{2}\varepsilon_{ik}^S E_k E_i \tag{D.1}$$

With the Einstein sum convention, the electrical enthalpy can also be formulated as follows:

$$H_e = \sum_{p=1}^{6}\sum_{q=1}^{6}\frac{1}{2}c_{pq}^E S_q S_p - \sum_{i=1}^{3}\sum_{p=1}^{6}e_{ip}E_i S_p - \sum_{i=1}^{3}\sum_{k=1}^{3}\frac{1}{2}\varepsilon_{ik}^S E_k E_i \tag{D.2}$$

The active layers of the considered bending actuators consist of the ferroelectric ceramic material PZT. With the matrices of the material coefficients (see eq. 3.67 - 3.71, section 3.3.3), equation (D.2) results in:

$$H_e = \frac{1}{2}c_{11}^E S_1^2 + c_{12}^E S_1 S_2 + c_{13}^E S_1 S_3 + \frac{1}{2}c_{22}^E S_2^2 + c_{23}^E S_2 S_3$$

$$+ \frac{1}{2}c_{33}^E S_3^2 + \frac{1}{2}c_{44}^E S_4^2 + \frac{1}{2}c_{55}^E S_5^2 + \frac{1}{2}c_{66}^E S_6^2$$

$$- e_{31}E_3 S_1 - e_{32}E_3 S_2 - e_{33}E_3 S_3 - e_{24}E_2 S_4 - e_{15}E_1 S_5$$

$$- \frac{1}{2}\varepsilon_{11}^S E_1^2 - \frac{1}{2}\varepsilon_{22}^S E_2^2 - \frac{1}{2}\varepsilon_{33}^S E_3^2 \tag{D.3}$$

The following boundary conditions are specified:

1. There is only an electric field **E** along the z-direction, thus

$$E_1 = E_2 = 0 \tag{D.4}$$

2. No strain in y-direction and no torsion in z-direction develop.

$$S_2 = \ldots = S_6 = 0 \tag{D.5}$$

With the boundary conditions specified above, equation (D.3) can be simplified according to:

$$H_e = \frac{1}{2}c_{11}^E S_1^2 - e_{31}E_3 S_1 - \frac{1}{2}\varepsilon_{33}^S E_3^2 \tag{D.6}$$

E

Correlation Between Material Parameters

In order to determine the correlation between the material parameters, the constitutive equations of state (see eq. 3.57, 3.58, 3.59 and 3.60, section 3.3.3) corresponding to the pairs of variates $(\mathbf{T}, \mathbf{E})$ and $(\mathbf{S}, \mathbf{E})$ are considered:

$$D_3 = \varepsilon_{33}^T E_3 + d_{31} T_1 \tag{E.1}$$

$$S_1 = d_{31} E_3 + s_{11}^E T_1 \tag{E.2}$$

and

$$T_1 = c_{11}^E S_1 - e_{31} E_3 \tag{E.3}$$

$$D_3 = e_{31} S_1 + \varepsilon_{33}^S E_3 \tag{E.4}$$

Insertion of equation (E.3) into (E.2) yields:

$$S_1 + s_{11}^E e_{31} E_3 = s_{11}^E c_{11}^E S_1 + d_{31} E_3 \tag{E.5}$$

The comparison of the coefficients on the left and the right side of (E.5) yields the following correlations:

$$c_{11}^E = \frac{1}{s_{11}^E} \tag{E.6}$$

and

$$e_{31} = \frac{d_{31}}{s_{11}^E} \tag{E.7}$$

In combination with (E.3), from the equations (E.1) and (E.4) follows:

$$\varepsilon_{33}^T E_3 + d_{31} c_{11}^E S_1 - d_{31} e_{31} E_3 = e_{31} S_1 + \varepsilon_{33}^S E_3$$

$$\Leftrightarrow d_{31} c_{11}^E S_1 + \left(\varepsilon_{33}^T - d_{31} e_{31}\right) E_3 = e_{31} S_1 + \varepsilon_{33}^S E_3 \tag{E.8}$$

The comparison of coefficients yields in combination with (E.7):

$$\varepsilon_{33}^{S} = \varepsilon_{33}^{T} - \frac{d_{31}^{2}}{s_{11}^{E}} \tag{E.9}$$

Equation (E.9) has already been used concerning the description of the static behavior (see eq. 4.114, section 4.9.4).

F

Work Done by Extensive Dynamic Quantities

F.1 Work Done by a Force

A force F affecting a beam bender's tip perpendicularly to its main inertia axis causes a deflection ξ of the bender's tip. The work done by the force F with respect to the ith layer yields:

$$W_{i,F} = \int_\xi F_i d\xi \tag{F.1}$$

The work done by the force F with respect to the n-layered system results in

$$W_F = \sum_{i=1}^{n} W_{i,F}, \tag{F.2}$$

thus, the total work can be defined in following way:

$$W_F = \sum_{i=1}^{n} \int_\xi F_i d\xi \tag{F.3}$$

The affecting force F causes a shear force f_A in the y-z-plane. Taking figure F.1 into account, the shear force f_A results in

$$f_A = \frac{dF_i}{dA_i}. \tag{F.4}$$

In combination with (F.4), F_i can be formulated:

$$F_i = \iint_{A_i} f_A dA_i \tag{F.5}$$

Insertion of (F.5) into (F.3) yields
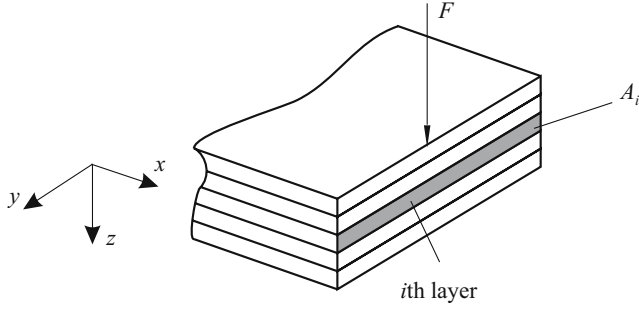
Fig. F.1. Beam bending actuator subjected by an external force F

$$W_F = \sum_{i=1}^{n} \iiint_{V_i} f_A d\xi dA_i. \tag{F.6}$$

Since ξ is a function of the length coordinate x, the application of the total differential results in

$$d\xi = \frac{\partial \xi}{\partial x} dx. \tag{F.7}$$

Thus, the work done by the force F can be defined as a volume integral:

$$W_F = \sum_{i=1}^{n} \int_{h_{i,u}}^{h_{i,o}} \int_{0}^{w_i} \int_{0}^{l} f_A \left(\frac{\partial \xi}{\partial x} \right) dx dy dz \tag{F.8}$$

F.2 Work Done by a Moment

A moment M affecting the bender's tip is energetically correlated with the resulting bending angle $\alpha = \partial \xi / \partial x$. Thus, a total work W_M can defined by analogy with an affecting force. It can be written:

$$W_M = -\sum_{i=1}^{n} \int_{\alpha} M_i d \left(\frac{\partial \xi}{\partial x} \right) \tag{F.9}$$

The affecting moment M related to the y-z-plane can be defined in following way:

$$m_A = \frac{dM_i}{dA_i} \tag{F.10}$$

M_i results from (F.10):

$$M_i = \iint_{A_i} m_A dA_i \tag{F.11}$$

Insertion of (F.11) into (F.9) yields:

$$W_M = -\sum_{i=1}^{n} \int_{z_i} \int_{y_i} \int_{\alpha} m_A d\left(\frac{\partial \xi}{\partial x}\right) dA_i \tag{F.12}$$

Since α is a function of the length coordinate x, the application of the total differential results in $d\alpha$:

$$d\alpha = d\left(\frac{\partial \xi}{\partial x}\right) = \frac{\partial\left(\frac{\partial \xi}{\partial x}\right)}{\partial x} dx = \left(\frac{\partial^2 \xi}{\partial x^2}\right) dx \tag{F.13}$$

Thus, the work done by the moment M can be represented in integral form:

$$W_M = -\sum_{i=1}^{n} \int_{h_{i,u}}^{h_{i,o}} \int_{0}^{w_i} \int_{0}^{l} m_A \left(\frac{\partial^2 \xi}{\partial x^2}\right) dx dy dz \tag{F.14}$$

F.3 Work Done by a Driving Voltage

An applied electrical voltage U causes a change of charge dQ. The performed electrical work W_U in the ith layer is equal to:

$$dW_{u,i} = dQ_i U \tag{F.15}$$

By means of the integral representation of the charge Q_i

$$\oint_{\partial V_i} \mathbf{D}\left(\mathbf{r}\right) \cdot d\mathbf{A}_i = \iint_{A_i} \sigma_A dA_i = Q_i, \tag{F.16}$$

it can be written:

$$dQ_i = \sigma_A dA_i \tag{F.17}$$

dA_i denotes a two dimensional element in the x-y-plane. Insertion of (F.17) into (F.15) and following summation with respect to all layers yields the total energy

$$W_U = -\sum_{i=1}^{n} \int_{U} \int_{y_i} \int_{x_i} \sigma_A dx dy dU. \tag{F.18}$$

Due to $U = U\left(z\right)$, the application of the total differential results in:

$$dU = \left(\frac{\partial U}{\partial z}\right) dz \tag{F.19}$$

Thus, from (F.18) follows

$$W_U = -\sum_{i=1}^{n} \int_{h_{i,u}}^{h_{i,o}} \int_{0}^{w_i} \int_{0}^{l} \sigma_A \left(\frac{\partial U}{\partial z}\right) dx\, dy\, dz. \qquad (F.20)$$

The minus sign in (F.20) results from the fact, that the part of the electrical energy of the electrical enthalpy H_e always has a sign different from the sign of the internal energy density.

G

On the Variation of the Lagrange Function

The Lagrange function L of a piezoelectric beam bending actuator is equal to:

$$L = \frac{1}{2}\mu \int_0^l \left(\frac{\partial \xi}{\partial t}\right)^2 dx - \frac{1}{2}C \int_0^l \left(\frac{\partial^2 \xi}{\partial x^2}\right)^2 dx$$

$$-\frac{1}{2}\sum_{i=1}^n \frac{d_{31,i}}{s_{11,i}^E} w_i \left[h_{i,o}^2 - h_{i,u}^2\right] \int_0^l E_{3,i} \left(\frac{\partial^2 \xi}{\partial x^2}\right) dx$$

$$+\sum_{i=1}^n \frac{1}{2}\varepsilon_{33,i}^S h_i w_i \int_0^l E_{3,i}^2 dx. \tag{G.1}$$

From equation (G.1), it is getting obviously, that

$$L = L\left(\frac{\partial \xi}{\partial t}, \frac{\partial^2 \xi}{\partial x^2}, E_{3,i}\right). \tag{G.2}$$

In accordance with the definition of the total differential, the application of the functional δ to (G.2) yields:

$$\delta L = \frac{\partial L}{\partial \left(\frac{\partial \xi}{\partial t}\right)} \delta\left(\frac{\partial \xi}{\partial t}\right) + \frac{\partial L}{\partial \left(\frac{\partial^2 \xi}{\partial x^2}\right)} \delta\left(\frac{\partial^2 \xi}{\partial x^2}\right) + \frac{\partial L}{\partial E_{3,i}} \delta E_{3,i} \tag{G.3}$$

Applying of equation (G.3) to (G.1) results in:

$$\delta L = \mu \int_0^l \left(\frac{\partial \xi}{\partial t}\right) \delta\left(\frac{\partial \xi}{\partial t}\right) dx - C \int_0^l \left(\frac{\partial^2 \xi}{\partial x^2}\right) \delta\left(\frac{\partial^2 \xi}{\partial x^2}\right) dx$$

$$-\frac{1}{2}\sum_{i=1}^n \frac{d_{31,i}}{s_{11,i}^E} w_i \left[h_{i,o}^2 - h_{i,u}^2\right] \int_0^l E_{3,i} \delta\left(\frac{\partial^2 \xi}{\partial x^2}\right) dx$$

$$-\frac{1}{2}\sum_{i=1}^{n}\frac{d_{31,i}}{s_{11,i}^{E}}w_{i}\left[h_{i,o}^{2}-h_{i,u}^{2}\right]\int_{0}^{l}\left(\frac{\partial^{2}\xi}{\partial x^{2}}\right)\delta E_{3,i}dx$$

$$+\sum_{i=1}^{n}\varepsilon_{33,i}^{S}h_{i}w_{i}\int_{0}^{l}E_{3,i}\delta E_{3,i}dx \tag{G.4}$$

Moreover, summarizing the terms in (G.4) yields:

$$\delta L=\mu\int_{0}^{l}\left(\frac{\partial\xi}{\partial t}\right)\delta\left(\frac{\partial\xi}{\partial t}\right)dx$$

$$-\int_{0}^{l}\left[C\left(\frac{\partial^{2}\xi}{\partial x^{2}}\right)+\underbrace{\frac{1}{2}\sum_{i=1}^{n}\frac{d_{31,i}}{s_{11,i}^{E}}w_{i}\left[h_{i,o}^{2}-h_{i,u}^{2}\right]E_{3,i}}_{(*)}\right]\delta\left(\frac{\partial^{2}\xi}{\partial x^{2}}\right)dx$$

$$+\int_{0}^{l}\left[\underbrace{\sum_{i=1}^{n}\varepsilon_{33,i}^{S}h_{i}w_{i}E_{3,i}-\frac{1}{2}\sum_{i=1}^{n}\frac{d_{31,i}}{s_{11,i}^{E}}w_{i}\left[h_{i,o}^{2}-h_{i,u}^{2}\right]\left(\frac{\partial^{2}\xi}{\partial x^{2}}\right)}_{(**)}\right]\delta E_{3,i}dx$$

$$\tag{G.5}$$

The term $(*)$ in equation (G.5) corresponds to the piezoelectric moment M_{Piezo} (see eq. 4.33, section 4.4). With the definition of the material parameter e_{31} (see eq. 5.87, section 5.7) and with

$$S_{1}=-z\left(\frac{\partial^{2}\xi}{\partial x^{2}}\right), \tag{G.6}$$

the second term $(**)$ can be summarized as follows:

$$(**)=\sum_{i=1}^{n}\varepsilon_{33,i}^{S}h_{i}w_{i}E_{3,i}-\frac{1}{2}\sum_{i=1}^{n}\frac{d_{31,i}}{s_{11,i}^{E}}w_{i}\left[h_{i,o}^{2}-h_{i,u}^{2}\right]\left(\frac{\partial^{2}\xi}{\partial x^{2}}\right)$$

$$=\sum_{i=1}^{n}\int_{h_{i,u}}^{h_{i,o}}w_{i}\left[\varepsilon_{33,i}^{S}E_{3,i}-e_{31,i}z\left(\frac{\partial^{2}\xi}{\partial x^{2}}\right)\right]dz$$

$$=\sum_{i=1}^{n}\int_{h_{i,u}}^{h_{i,o}}w_{i}\left[\varepsilon_{33,i}^{S}E_{3,i}+e_{3,i}S_{1\,i}\right]dz \tag{G.7}$$

The term in brackets in (G.7) corresponds to the displacement D_3 (see eq. 5.84, section 5.7). Thus, $(**)$ can be reformulated according to

$$(**) = \sum_{i=1}^{n} \int_{h_{i,u}}^{h_{i,o}} w_i D_{3,i} dz. \tag{G.8}$$

Thus, (G.5) can be simplified:

$$\delta L = \mu \int_0^l \left(\frac{\partial \xi}{\partial t}\right) \delta \left(\frac{\partial \xi}{\partial t}\right) dx - \int_0^l C \left(\frac{\partial^2 \xi}{\partial x^2}\right) \delta \left(\frac{\partial^2 \xi}{\partial x^2}\right) dx$$

$$- \int_0^l M_{Piezo} \delta \left(\frac{\partial^2 \xi}{\partial x^2}\right) dx + \sum_{i=1}^{n} \int_{h_{i,u}}^{h_{i,o}} \int_0^l w_i D_{3,i} \delta E_{3,i} dx dz \tag{G.9}$$

In accordance with the Hamilton principle, equation (G.9) is integrated with respect to the time variable t between the limits of integration t_1 and t_2 resulting in:

$$\int_{t_1}^{t_2} \delta L dt = \int_{t_1}^{t_2} \left[\mu \int_0^l \underbrace{\left(\frac{\partial \xi}{\partial t}\right) \delta \left(\frac{\partial \xi}{\partial t}\right)}_{(1)} dx - C \int_0^l \underbrace{\left(\frac{\partial^2 \xi}{\partial x^2}\right) \delta \left(\frac{\partial^2 \xi}{\partial x^2}\right)}_{(2)} dx \right.$$

$$\left. - \int_0^l M_{Piezo} \underbrace{\delta \left(\frac{\partial^2 \xi}{\partial x^2}\right)}_{(3)} dx + \sum_{i=1}^{n} \int_{h_{i,u}}^{h_{i,o}} \int_0^l \underbrace{w_i D_{3,i} \delta E_{3,i}}_{(4)} dz dx \right] dt$$

$$\tag{G.10}$$

In order to connect equation (G.10) with the integral of action of the externally performed work $\int_{t_1}^{t_2} \delta W dt$ (5.72), the terms (1), (2), (3) and (4) in (G.10) are simplified by means of integration by parts.

1. Simplification of term (1):
   By applying the integration by parts with respect to the limits of integration t_1 and t_2, term (1) can be reformulated in the following way:

$$\int_{t_1}^{t_2} \left(\frac{\partial \xi}{\partial t}\right) \delta \left(\frac{\partial \xi}{\partial t}\right) dt = \left(\frac{\partial \xi}{\partial t}\right) \delta \xi \Big|_{t_1}^{t_2} - \int_{t_1}^{t_2} \left(\frac{\partial^2 \xi}{\partial t^2}\right) \delta \xi dt \tag{G.11}$$

Since t_1 and t_2 are fixed and the function $\xi(t)$ is not varied at the integral limits, (G.11) is simplified as follows:

$$\int_{t_1}^{t_2} \left(\frac{\partial \xi}{\partial t}\right) \delta \left(\frac{\partial \xi}{\partial t}\right) dt = -\int_{t_1}^{t_2} \left(\frac{\partial^2 \xi}{\partial t^2}\right) \delta \xi dt \qquad \text{(G.12)}$$

2. Simplification of term (2):
   Indefinite integration by parts yields for the second term:

$$\int \left(\frac{\partial^2 \xi}{\partial x^2}\right) \delta \left(\frac{\partial^2 \xi}{\partial x^2}\right) dx = \left(\frac{\partial^2 \xi}{\partial x^2}\right) \delta \left(\frac{\partial \xi}{\partial x}\right) - \underbrace{\int \left(\frac{\partial^3 \xi}{\partial x^3}\right) \delta \left(\frac{\partial \xi}{\partial x}\right) dx}_{(*)}$$

$$\text{(G.13)}$$

Second integration by parts yields for $(*)$ in (G.13):

$$\int \left(\frac{\partial^3 \xi}{\partial x^3}\right) \delta \left(\frac{\partial \xi}{\partial x}\right) dx = \left(\frac{\partial^3 \xi}{\partial x^3}\right) \delta \xi - \int \left(\frac{\partial^4 \xi}{\partial x^4}\right) \delta \xi dx \qquad \text{(G.14)}$$

Insertion of (G.14) into (G.13) results in:

$$\int \left(\frac{\partial^2 \xi}{\partial x^2}\right) \delta \left(\frac{\partial^2 \xi}{\partial x^2}\right) dx = \left(\frac{\partial^2 \xi}{\partial x^2}\right) \delta \left(\frac{\partial \xi}{\partial x}\right) - \left(\frac{\partial^3 \xi}{\partial x^3}\right) \delta \xi + \int \left(\frac{\partial^4 \xi}{\partial x^4}\right) \delta \xi dx$$

$$\text{(G.15)}$$

3. Simplification of term (3):
   Term (3) can be reformulated by means of indefinite integration by parts.

$$\int \delta \left(\frac{\partial^2 \xi}{\partial x^2}\right) dx = \delta \left(\frac{\partial \xi}{\partial x}\right) \qquad \text{(G.16)}$$

4. Simplification of term (4):
   In combination with equation (3.19), term (4) can be formulated as follows:

$$\int D_3 \delta E_3 dz = -\int D_3 \delta \left(\frac{dU}{dz}\right) dz \qquad \text{(G.17)}$$

Thus, it can be written by means of integration by parts:

$$\int D_3 \delta E_3 dz = \int \frac{dD}{dz} \delta U dz - D_3 \delta U \qquad \text{(G.18)}$$

Taking the equations (G.12), (G.15), (G.16) and (G.18) into consideration, the integral of action of the Lagrange function finally results in:

$$\int_{t_1}^{t_2} \delta L dt = \int_{t_1}^{t_2} \left[-\mu \int_0^l \left(\frac{\partial^2 \xi}{\partial t^2} \right) \delta \xi dx - C \int_0^l \left(\frac{\partial^4 \xi}{\partial x^4} \right) \delta \xi dx \right.$$

$$- C \left(\frac{\partial^2 \xi}{\partial x^2} \right) \delta \left(\frac{\partial \xi}{\partial x} \right) \Big|_0^l + C \left(\frac{\partial^3 \xi}{\partial x^3} \right) \delta \xi \Big|_0^l - M_{Piezo} \delta \left(\frac{\partial \xi}{\partial x} \right) \Big|_0^l$$

$$\left. + \sum_{i=1}^n \int_{h_{i,u}}^{h_{i,o}} \int_0^l w_i \frac{dD_{3,i}}{dz} \delta U dx dz - \sum_{i=1}^n w_i \int_0^l D_{3,i} \delta U \Big|_{h_{i,u}}^{h_{i,o}} dx \right] dt$$

$$(G.19)$$

H

On the Variation of the Work Done by Extensive Quantities

The integral of action of the work W performed at the system can be written in following form:

$$\int_{t_1}^{t_2} \delta W = \int_{t_1}^{t_2} \left[\underbrace{\sum_{i=1}^{n} F_i \int_0^l \delta \left(\frac{\partial \xi}{\partial x} \right) dx - \sum_{i=1}^{n} M_i \int_0^l \delta \left(\frac{\partial^2 \xi}{\partial x^2} \right) dx}_{(1)} + \underbrace{pw \int_0^l \delta \xi dx}_{(2)} \right.$$

$$- \int_0^l r_a \left(\frac{\partial \xi}{\partial t} \right) \delta \xi dx - \sum_{i=1}^{n} w_i \underbrace{\int_0^l \int_{h_{i,u}}^{h_{i,o}} \sigma_A \delta \left(\frac{\partial U}{\partial z} \right) dz \, dx}_{(3)}$$

$$\left. - \int_0^l r_a \underbrace{\xi \delta \left(\frac{\partial \xi}{\partial t} \right) dx}_{(4)} \right] dt \tag{H.1}$$

In (H.1) the terms (1), (2), (3) and (4) are simplified by means of integration by parts.

1. Simplification of term (1):
   Using the indefinite integration by parts yields:

$$\int \delta \left(\frac{\partial \xi}{\partial x} \right) dx = \delta \xi \tag{H.2}$$

2. Simplification of term (2):
   The second term yields by means of indefinite integration by parts:

$$\int \delta \left(\frac{\partial^2 \xi}{\partial x^2} \right) dx = \delta \left(\frac{\partial \xi}{\partial x} \right) \tag{H.3}$$

3. Simplification of term (3):
   By means of integration by parts it can be written:

$$\int \sigma_A \delta \left(\frac{\partial U}{\partial z} \right) dz = \sigma_A \delta U \tag{H.4}$$

4. Simplification of term (4):
   The integration by parts within in the limits of integration t_1 and t_2 results in:

$$\int_{t_1}^{t_2} \delta \left(\frac{\partial \xi}{\partial t} \right) dt = \delta \xi |_{t_1}^{t_2}$$

Since t_1 and t_2 are fixed and the function $\xi(t)$ is not varied at the integration limits, it can be written

$$\int_{t_1}^{t_2} \delta \left(\frac{\partial \xi}{\partial t} \right) dt = 0. \tag{H.5}$$

Taking the equations (H.2) - (H.5) into account, the integral of action of the external work W finally results in:

$$\int_{t_1}^{t_2} \delta W \, dt = \int_{t_1}^{t_2} \left[F \delta \xi |_0^l - M \delta \left(\frac{\partial \xi}{\partial x} \right) \Big|_0^l + pw \int_0^l \delta \xi \, dx \right.$$

$$\left. - \int_0^l r_a \left(\frac{\partial \xi}{\partial t} \right) \delta \xi \, dx - \sum_{i=1}^n w_i \int_0^l \sigma_A \delta U |_{h_{i,u}}^{h_{i,o}} \, dx \right] dt \tag{H.6}$$

I

On the Excitation by a Periodic Force

The calculation of the expression

$$\frac{X_m\left(l\right)}{\int\limits_0^l X_m^2 \, dx} \tag{I.1}$$

can only be solved with great mathematical effort, thus the software package Mathematica® is used for calculations. In combination with the eigenmodes (6.29) of the clamped-free beam bender and the Rayleigh functions (6.10) - (6.13), it can be written:

$$\frac{X_m\left(l\right)}{\int\limits_0^l X_m^2} = \frac{4}{l}\underbrace{\left[\frac{\cosh\left(k_m l\right)\sin\left(k_m l\right) - \cos\left(k_m l\right)\sinh\left(k_m l\right)}{\sin\left(k_m l\right) + \sinh\left(k_m l\right)}\right]}_{\equiv \alpha_F\left(k_m l\right)} = \frac{4}{l}\alpha_F\left(k_m l\right) \tag{I.2}$$

By means of the characteristic equation for clamped-free beam benders

$$1 + \cos\left(k_m l\right)\cosh\left(k_m l\right) = 0 \quad \Leftrightarrow \quad \cosh\left(k_m l\right) = -\frac{1}{\cos\left(k_m l\right)} \tag{I.3}$$

and in combination with the relationship for hyperbolic functions [190]

$$\cosh^2\left(k_m l\right) - \sinh^2\left(k_m l\right) = 1, \tag{I.4}$$

the quantity $\alpha_F\left(k_m l\right)$ in equation (I.2) can be reformulated in following way:

$$\alpha_F\left(k_m l\right) = \frac{-\frac{1}{\cos\left(k_m l\right)}\sin\left(k_m l\right) - \cos\left(k_m l\right)\sqrt{\cosh^2\left(k_m l\right) - 1}}{\sin\left(k_m l\right) + \sqrt{\cosh^2\left(k_m l\right) - 1}} \tag{I.5}$$

Applying the relationship (I.3) to equation (I.5) results in

$$\alpha_F\left(k_m l\right) = \frac{-\frac{1}{\cos\left(k_m l\right)}\sin\left(k_m l\right) - \cos\left(k_m l\right)\sqrt{\frac{1}{\cos^2\left(k_m l\right)} - 1}}{\sin\left(k_m l\right) + \sqrt{\frac{1}{\cos^2\left(k_m l\right)} - 1}}$$

$$\Leftrightarrow \alpha_F\left(k_m l\right) = \frac{-\frac{1}{\cos\left(k_m l\right)}\sin\left(k_m l\right) - \sqrt{1 - \cos^2\left(k_m l\right)}}{\sin\left(k_m l\right) + \frac{1}{\cos\left(k_m l\right)}\sqrt{1 - \cos^2\left(k_m l\right)}}. \tag{I.6}$$

With the relationship

$$\sin^2\left(k_m l\right) + \cos^2\left(k_m l\right) = 1 \tag{I.7}$$

finally follows

$$\alpha_F\left(k_m l\right) = \frac{-\frac{1}{\cos\left(k_m l\right)}\sin\left(k_m l\right) \mp \sin\left(k_m l\right)}{\sin\left(k_m l\right) \pm \frac{1}{\cos\left(k_m l\right)}\sin\left(k_m l\right)} \tag{I.8}$$

or

$$\alpha_F\left(k_m l\right) = 1 \quad \vee \quad \alpha_F\left(k_m l\right) = -1. \tag{I.9}$$

J

Particular Solution of the Differential Equation for Flexural Vibrations

The inhomogenous differential equation of a beam bender excited by a periodic force F affecting the beam bender's tip in z-direction is equal to

$$2\zeta_m\omega_m\dot{\phi}_m + \omega_m^2\phi_m = \frac{4F\alpha_1\left(k_ml\right)}{l\mu}\cos\left(\Omega t\right). \tag{J.1}$$

In order to solve (J.1), the ansatz function

$$\phi_m^p\left(t\right) = A_m\cos\left(\Omega t\right) + B_m\sin\left(\Omega t\right) \tag{J.2}$$

is chosen.

Insertion of the ansatz function into equation (J.1) yields the constants A_m and B_m:

$$A_m = \frac{4F\,\alpha_F\left(k_ml\right)}{l\mu}\frac{\omega_m^2 - \Omega^2}{\left(\omega_m^2 - \Omega^2\right)^2 + \left(2\zeta_m\omega_m\Omega\right)^2} \tag{J.3}$$

$$B_m = \frac{4F\,\alpha_F\left(k_ml\right)}{l\mu}\frac{2\zeta_m\omega_m\Omega}{\left(\omega_m^2 - \Omega^2\right)^2 + \left(2\zeta_m\omega_m\Omega\right)^2} \tag{J.4}$$

With the abbreviations

$$\eta_m = \frac{\Omega}{\omega_m} \tag{J.5}$$

(dimensionless ratio of the excitation frequency and the frequency of the free, undamped oscillation) and

$$S_m = \frac{4F\,\alpha_F\left(k_ml\right)}{l\mu\omega_m^2}, \tag{J.6}$$

the constants A_m and B_m can also be expressed as

$$A_m = S_m \frac{1 - \eta_m^2}{\left(1 - \eta_m^2\right)^2 + \left(2\zeta_m\eta_m\right)^2} \tag{J.7}$$

$$B_m = S_m \frac{2\zeta_m\eta_m}{\left(1 - \eta_m^2\right)^2 + \left(2\zeta_m\eta_m\right)^2} \tag{J.8}$$

For a better understanding of the particular solution $\phi_m^p(t)$, the achieved solution is reformulated as follows:

$$\phi_m^p(t) = a_m \cos\left(\Omega t - \Psi\right) \tag{J.9}$$

By means of the theorem of the cosine

$$\cos\left(\alpha \pm \beta\right) = \cos\left(\alpha\right)\cos\left(\beta\right) \mp \sin\left(\alpha\right)\sin\left(\beta\right), \tag{J.10}$$

(J.9) can be written in the following form:

$$\phi_m^p(t) = a_m \cos\left(\Omega t\right)\cos\left(\Psi\right) + a_m \sin\left(\Omega t\right)\sin\left(\Psi\right) \tag{J.11}$$

A comparison of (J.11) with (J.2) yields:

$$A_m = a_m \cos\left(\Psi\right) \tag{J.12}$$

$$B_m = a_m \sin\left(\Psi\right) \tag{J.13}$$

Thus, the resulting amplitude

$$a_m = \frac{S_m}{\sqrt{\left(1 - \eta_m^2\right)^2 + \left(2\zeta_m\eta_m\right)^2}} \tag{J.14}$$

and the phase angle Ψ according to

$$\tan\left(\Psi\right) = \frac{2\zeta_m\eta_m}{1 - \eta_m^2} \tag{J.15}$$

can be calculated.

K

Transition to the Differential Equations in Complex Form

The difference equations (7.25) - (7.29) represent the starting point for the determination of the complex differential equations for flexural vibrations.

1. Force differential equation:
   The difference equation for force equilibrium (7.25) results in

$$\underline{F}\left(x + \frac{\Delta x}{2}\right) - \underline{F}\left(x - \frac{\Delta x}{2}\right) = \Delta\underline{F}(x) - j\omega\Delta m\underline{v}(x).$$ (K.1)

Following multiplication with $1/\Delta x$ yields

$$\frac{\underline{F}\left(x + \frac{\Delta x}{2}\right) - \underline{F}\left(x - \frac{\Delta x}{2}\right)}{\Delta x} = \frac{\underline{f}(x)\,\Delta x}{\Delta x} - j\omega\frac{\Delta m}{\Delta x}\underline{v}(x) - \frac{r\underline{v}(x)}{\Delta x}.$$ (K.2)

The quotients $\Delta m/\Delta x$ and $\Delta r/\Delta x$ denote the mass per unit length μ (see eq. 5.92, section 5.7) and the coefficient of friction per unit length r_a (see eq. 5.105, section 5.8), respectively. The quantity $\underline{f}(x)$ denotes the load per unit length. Following formation of the limit value

$$\lim_{\Delta x \to 0} \frac{\underline{F}\left(x + \frac{\Delta x}{2}\right) - \underline{F}\left(x - \frac{\Delta x}{2}\right)}{\Delta x} = \underline{f}(x) - j\omega\mu\underline{v}(x) - r_a\underline{v}(x)$$

yields

$$\frac{d\underline{F}(x)}{dx} = \underline{f}(x) - j\omega\mu\underline{v}(x) - r_a\underline{v}(x).$$ (K.3)

2. Moment differential equation:
   The difference equation for the moment equilibrium (7.27) can be transformed to the following difference quotient:

$$\frac{\underline{M}\left(x + \frac{\Delta x}{2}\right) - \underline{M}\left(x - \frac{\Delta x}{2}\right)}{\Delta x} = -\frac{1}{2}\left[\underline{F}\left(x - \frac{\Delta x}{2}\right) + \underline{F}\left(x + \frac{\Delta x}{2}\right)\right]$$ (K.4)

Further, (K.4) can be reformulated according to

$$\frac{\underline{M}\left(x + \frac{\Delta x}{2}\right) - \underline{M}\left(x - \frac{\Delta x}{2}\right)}{\Delta x} = -\underline{F}\left(x + \epsilon\Delta x\right), \qquad \text{(K.5)}$$

where $\epsilon \in \mathbb{R}$. By means of limit value formation in accordance with

$$\lim_{\Delta x \to 0} \frac{\underline{M}\left(x + \frac{\Delta x}{2}\right) - \underline{M}\left(x - \frac{\Delta x}{2}\right)}{\Delta x} = -\lim_{\Delta x \to 0} \underline{F}\left(x + \epsilon\Delta x\right),$$

the differential correlation between the complex flow quantities $\underline{M}$ and $\underline{F}$ is achieved according to

$$\frac{d\underline{M}\left(x\right)}{dx} = -\underline{F}\left(x\right). \qquad \text{(K.6)}$$

3. Angular velocity differential equation:
   Equation (7.28) can be written as difference quotient

$$\frac{\underline{\Omega}\left(x + \frac{\Delta x}{2}\right) - \underline{\Omega}\left(x - \frac{\Delta x}{2}\right)}{\Delta x} = -j\omega\frac{s_{11}}{I_{yy}}\underline{M}\left(x - \frac{\Delta x}{2}\right)$$

$$+j\omega\frac{s_{11}\Delta x}{2I_{yy}}\underline{F}\left(x - \frac{\Delta x}{2}\right) \qquad \text{(K.7)}$$

The limit value formation of

$$\lim_{\Delta x \to 0} \frac{\underline{\Omega}\left(x + \frac{\Delta x}{2}\right) - \underline{\Omega}\left(x - \frac{\Delta x}{2}\right)}{\Delta x}$$

yields in combination with the definition of the torsional compliance (see eq. 7.14, section 7.2) the following differential equation:

$$\frac{d\underline{\Omega}\left(x\right)}{dx} = -j\omega\frac{s_{11}}{I_{yy}}\underline{M}\left(x\right) = -j\omega\frac{\underline{M}\left(x\right)}{EI} = -j\omega\frac{\underline{M}\left(x\right)}{C} \qquad \text{(K.8)}$$

4. Translatory velocity differential equation:
   At least, equation (7.29) is transformed to the difference quotient

$$\frac{\underline{v}\left(x + \frac{\Delta x}{2}\right) - \underline{v}\left(x - \frac{\Delta x}{2}\right)}{\Delta x} = \underline{\Omega}\left(x + \epsilon\Delta x\right), \qquad \text{(K.9)}$$

from which the following differential equation after formation of the limit value is achieved:

$$\frac{d\underline{v}\left(x\right)}{dx} = \underline{\Omega}\left(x\right) \qquad \text{(K.10)}$$

The four differential equations (K.3), (K.6), (K.8) and (K.10) yield by means of stepwise differentiation:

$$\frac{d\underline{v}(x)}{dx} = \underline{\Omega}(x)$$

$$\Rightarrow \frac{d^2\underline{v}(x)}{dx^2} = \frac{d\underline{\Omega}(x)}{dx} = -j\omega\frac{\underline{M}(x)}{C}$$

$$\Rightarrow \frac{d^3\underline{v}(x)}{dx^3} = -j\frac{\omega}{C}\frac{d\underline{M}(x)}{dx} = j\frac{\omega}{C}\underline{F}(x)$$

$$\Rightarrow \frac{d^4\underline{v}(x)}{dx^4} = j\frac{\omega}{C}\frac{d\underline{F}(x)}{dx} = j\frac{\omega}{C}\left[\underline{f}(x) - j\omega\mu\underline{v}(x) - r_a\underline{v}(x)\right] \quad \text{(K.11)}$$

After some algebraic manipulations the linear, inhomogenous differential equation of fourth order in complex form is achieved:

$$\frac{d^4\underline{v}(x)}{dx^4} - \omega^2\frac{\mu}{C}\underline{v}(x) + j\frac{\omega}{C}r_a\underline{v}(x) = j\frac{\omega}{C}\underline{f}(x) \quad \text{(K.12)}$$

The differential equation (K.12) in complex form is identical to the non-complex differential equation for flexural vibrations (see eq. 5.117, section 5.11). The identity is achieved by means of the separation ansatz $\xi(x,t) = \underline{\xi}(x)e^{j\omega t}$ and the correlation $\underline{v} = j\omega\underline{\xi}$.

L

Orthogonality of Different Boundary Conditions

In order to proof the orthogonality of the eigenmodes, the clampings and boundary conditions for flexural vibrations of an Euler-Bernoulli beam shown in Table L.1 are taken into account.

By analogy with the clamped-free beam bender, equation (7.33) is rewritten as follows:

$$\frac{\partial^4 X_m}{\partial x^4} = \lambda_m X_m \tag{L.1}$$

with

$$\lambda_m = k_m^4 = \frac{\omega_m^2}{C} \mu \tag{L.2}$$

Equation (L.1) represents an eigenvalue problem, which is characterized by the fact, that the fourth derivative of the eigenfunction X_m corresponds to the product of the eigenfunction and its eigenvalue λ_m. In order to analyze the orthogonality properties (linear independence) of the eigenfunctions, different modes m and p are assumed:

$$\frac{\partial^4 X_m}{\partial x^4} = \lambda_m X_m \tag{L.3}$$
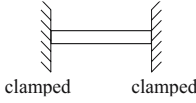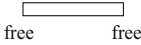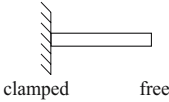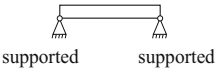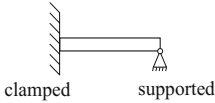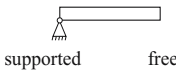
$$\frac{\partial^4 X_p}{\partial x^4} = \lambda_p X_p \tag{L.4}$$

Multiplication of (L.3) with X_p, multiplication of (L.4) with X_m and following integration with respect to the beam length l yields:

$$\int_0^l \frac{\partial^4 X_m}{\partial x^4} X_p dx = \lambda_m \int_0^l X_m X_p dx \tag{L.5}$$

$$\int_0^l \frac{\partial^4 X_p}{\partial x^4} X_m dx = \lambda_p \int_0^l X_m X_p dx \tag{L.6}$$

Table L.1. Clampings and boundary conditions for transversal flexural vibrations of an Euler-Bernoulli beam

clamping	boundary conditions	characteristic equation
clamped — clamped	$X_m(0) = X_m(l) = 0$ $X'_m(0) = X'_m(l) = 0$	$\cosh(k_m l)\cos(k_m l) = 1$
free — free	$X''_m(0) = X''_m(l) = 0$ $X'''_m(0) = X'''_m(l) = 0$	$\cosh(k_m l)\cos(k_m l) = 1$
clamped — free	$X_m(0) = X'_m(0) = 0$ $X''_m(l) = X'''_m(l) = 0$	$\cosh(k_m l)\cos(k_m l) = -1$
supported — supported	$X_m(0) = X_m(l) = 0$ $X''_m(0) = X''_m(l) = 0$	$\sin(k_m l) = 0$
clamped — supported	$X_m(0) = X'_m(0) = 0$ $X_m(l) = X''_m(l) = 0$	$\tan(k_m l) - \tanh(k_m l) = 0$
supported — free	$X_m(0) = X''_m(0) = 0$ $X''_m(l) = X'''_m(l) = 0$	$\tan(k_m l) - \tanh(k_m l) = 0$

Integration of the left side of (L.5) and (L.6), respectively yields by means of double integration by parts:

$$\frac{d^3 X_m}{dx^3} X_p \bigg|_0^l - \frac{d^2 X_m}{dx^2}\frac{dX_p}{dx}\bigg|_0^l - \int_0^l \frac{d^2 X_m}{dx^2}\frac{d^2 X_p}{dx^2}dx = \lambda_m \int_0^l X_m X_p dx \quad \text{(L.7)}$$

$$\frac{d^3 X_p}{dx^3} X_m \bigg|_0^l - \frac{d^2 X_p}{dx^2}\frac{dX_m}{dx}\bigg|_0^l - \int_0^l \frac{d^2 X_m}{dx^2}\frac{d^2 X_p}{dx^2}dx = \lambda_p \int_0^l X_m X_p dx \quad \text{(L.8)}$$

Taking the boundary conditions illustrated in Table L.1 and the equations (L.7) and (L.8) into consideration, for *any kind of clamping*, the same general correlation can be defined:

$$-\int_0^l \frac{d^2 X_m}{dx^2}\frac{d^2 X_p}{dx^2}dx = \lambda_m \int_0^l X_m X_p dx \tag{L.9}$$

$$-\int_0^l \frac{d^2 X_m}{dx^2}\frac{d^2 X_p}{dx^2}dx = \lambda_p \int_0^l X_m X_p dx. \tag{L.10}$$

Following difference formation of (L.9) and (L.10) yields

$$(\lambda_m - \lambda_p)\int_0^l X_m X_p dx = 0. \tag{L.11}$$

Due to $\lambda_m \neq \lambda_p$ for $m \neq p$, equation (L.11) is only satisfied in general, if following equation is valid:

$$\int_0^l X_m X_p dx = 0 \tag{L.12}$$

Furthermore, the insertion of (6.42) into (L.5) and (L.9) results in:

$$\int_0^l \frac{\partial^4 X_m}{\partial x^4}X_p dx = 0 \tag{L.13}$$

$$\int_0^l \frac{d^2 X_m}{dx^2}\frac{d^2 X_p}{dx^2}dx = 0 \tag{L.14}$$

The equations (L.12) - (L.14) demonstrate the orthogonality properties for flexural vibrations arising on a bending beam, indepedent of the kind of clamping. If $m = p$ is valid, from equation (L.12) follows

$$\int_0^l X_m^2 dx = \alpha_m, \tag{L.15}$$

where the quantity α_m denotes an arbitrary constant. Thus, from (L.5) and (L.9) follows:

$$\int_0^l \frac{\partial^4 X_m}{\partial x^4}X_m dx = \int_0^l \left(\frac{d^2 X_m}{dx^2}\right)^2 dx = \lambda_m \alpha_m = k_m^4 \alpha_m = \left(\frac{\omega_m^2}{C}\mu\right)\alpha_m. \tag{L.16}$$

With this knowledge the general solution $\underline{v}(x)$ of the complex differential equation (see eq. 7.30, section 7.3) can be determined at arbitrary points x of the beam bender affected by an external line load $\underline{f}(x)$, independent of the kind of clamping.

M

Logarithmic Decrement

The time- and position-dependent representation of the deflection of a sub-critically damped system can be described by the homogeneous solution with respect to the initial conditions $\phi_m^h(0) = \phi_0$ and $\dot{\phi}_m^h(0) = 0$:

$$\phi_m^h(t) = \phi_0\, e^{-\omega_m \zeta_m t} \left[\cos\left(\omega_m^d t\right) + \frac{\zeta_m}{\sqrt{1 - \zeta_m^2}} \sin\left(\omega_m^d t\right)\right] \tag{M.1}$$

After q periods of oscillation it can be written with the period τ_m^d of the damped oscillation (M.1)

$$\phi_m^h\left(t + q\tau_m^d\right) = \phi_0\, e^{-\omega_m \zeta_m \left(t + q\tau_m^d\right)}$$
$$\cdot \left[\cos\left(\omega_m^d\left(t + q\tau_m^d\right)\right) + \frac{\zeta_m}{\sqrt{1 - \zeta_m^2}} \sin\left(\omega_m^d\left(t + q\tau_m^d\right)\right)\right]. \tag{M.2}$$

Rearranging yields

$$\phi_m^h\left(t + q\tau_m^d\right) = \phi_0\, e^{-\omega_m \zeta_m t}\, e^{-q\omega_m \zeta_m \tau_m^d}$$
$$\cdot \left[\cos\left(\omega_m^d t + q\omega_m^d \tau_m^d\right) + \frac{\zeta_m}{\sqrt{1 - \zeta_m^2}} \sin\left(\omega_m^d t + q\omega_m^d \tau_m^d\right)\right]. \tag{M.3}$$

Due to

$$\omega_m^d \tau_m^d = 2\pi \tag{M.4}$$

and due to the periodicity of the cosine and sine function, (M.3) results in

$$\phi_m^h \left(t + q\tau_m^d\right) = \phi_0 \, \mathrm{e}^{-\omega_m \zeta_m t} \, \mathrm{e}^{-q\omega_m \zeta_m \tau_m^d} \left[\cos\left(\omega_m^d t\right) + \frac{\zeta_m}{\sqrt{1 - \zeta_m^2}} \sin\left(\omega_m^d t\right)\right].$$

$$(\mathrm{M.5})$$

From (M.1) and (M.5), the ratio of deflections within an interval of q periods of oscillation can be calculated according to

$$\frac{\phi_m^h\,(t)}{\phi_m^h\left(t + q\tau_m^d\right)} = \frac{\phi_p}{\phi_{p+q}} = \mathrm{e}^{q\omega_m \zeta_m \tau_m^d} = \mathrm{e}^{q\Lambda}\,. \qquad (\mathrm{M.6})$$

The quantity $\omega_m \zeta_m \tau_m^d$ is called logarithmic decrement Λ. The correlation (M.6) allows for the experimental determination of the coefficient of friction r of a viscously damped flexural vibration.

N

Favored Sensor Principles and Sensor Signal Estimation

Within the scope of the federal german research project EPIETEC (Effektive piezokeramische Multilayer-Technologie für integrierte Niedervolt-Piezobieger), a comprehensive sensor principle collection for tip deflection measurements has been elaborated and subjected to several evaluation steps. Following sensor principles were short-listed:

- resistive sensor principle
- capacitive sensor principle
- inductive sensor principle
- piezoelectric sensor principle

In the following, calculations are effected with respect to the sensor principles specified above, in order to determine the measuring effect, that can be expected. By means of the bending actuator illustrated in figure N.1, in combination with its geometrical and material parameters listed in Table 9.1, section 9.1, calculations are effected with respect to the sensor principles mentioned above.

The bending actuator is to be driven by a DC voltage U in such a manner, that a deflection of $\xi_{\max} = -100\,\mu\text{m}$ in negative z-direction is achieved. If the actuator would deflect in positive z-direction, the individual piezoelectric layers would affected by tensile stresses, resulting in an irreversible damage of the piezoceramics (see section 2.6). In order to calculate the deflection, the matrix element $m_{24}(x)$ of the coupling matrix $\mathbf{M}$ (see eq. 4.130, section 4.10) has to be considered. Thus, the deflection results in

$$\xi(x) = m_{24}(x)\,U. \tag{N.1}$$

By means of the parameters listed in Table 9.1, the necessary driving voltage results in $U = 27,07\,\text{V}$. For the resistive, capacitive and piezoelectric sensor principles, the strain and compression of the outer surfaces are the important quantities. Thus, the expected strains and compressions of the outer surfaces are calculated by means of equation (4.16) in section 4.3 assuming a maximum
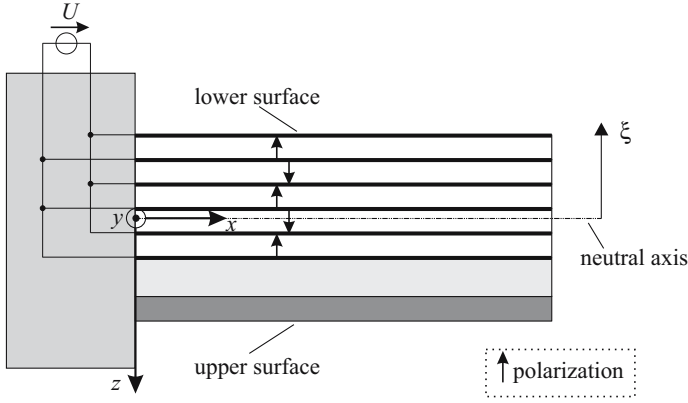
Fig. N.1. Deflection of a bending actuator in negative z-direction caused by a driving voltage U

tip deflection of $\xi_{\max} = -100\,\mu$m. Using the definition of the bend κ^0 (4.34), the strain $S_1\,(z)$ can be calculated according to

$$S_1\,(z) = -z\frac{U m_{Piezo}}{C}. \tag{N.2}$$

The calculated strain on the upper surface (surface in positive z-direction) of the used bending actuator amounts to $S_u = 115.7 \cdot 10^{-6}$, the strain on the lower surface amounts to $S_l = -154.3 \cdot 10^{-6}$. To simplify matters, the strain and compression on the upper and lower surface are assumed to be equal in further considerations. Therefore, the absolut mean value from S_u and S_l is formed resulting in $\overline{|S|} =: \overline{S} = 135 \cdot 10^{-6}$. This value is used for the estimation of the expected measuring effect concerning the resistive, capacitive and piezoelectric sensor principle.

N.1 Resisitive Distance Sensors

The basis of the resistive distance sensor is represented by the elastic deformation of a solid, in the present case the bending deformation of the piezoelectric bending actuator caused by a driving voltage U. If a conductor is applied on the upper and lower surface of the bending actuator, a bending deformation will affect the conductor's resistance. Since the derivation of the relative resistance change dR/R of an uniaxial stressed electrical conductor would go beyond the scope of the present book, it is referred to further reading books [191, 192]. Generally, the relative resistance change of a conductive material can be described by the fundamental relationship

$$\frac{dR}{R} = \left(2 - \frac{d\,(N_e\mu_e)}{N_e\mu_e\overline{S}}\right)\overline{S} := k\overline{S} \tag{N.3}$$

with the k-factor

$$k := 2 - \frac{d\,(N_e \mu_e)}{N_e \mu_e \overline{S}},\tag{N.4}$$

where the quantities N and μ denote the amount of carrier and the carrier mobility within a space volume of a conductive solid. The k-factor is a measure for the sensitivity of the strain measurement and consists of a *geometric constant* term and a *material* term, that describes the effect of the mechanical strain on the amount of carrier N and the carrier mobility μ. For metals, the material term can be neglected. However semiconductor materials and ceramic materials show a dependence on the material term ($k \gg 2$).

In practice, the conductor is commonly realized as thin layer (*strain gage*), that is attached to a deformation element by means of a layer insulation. In the particular case, it has to be attended to a preferably unchanged transfer of the bending deformation to the strain gage. With respect to equation (N.3), the strain transferred by the bending actuator to the resistor gage causes a measurable resistance change. Following resistor gages are the main representatives [193]:

1. Metallic strain gages
2. Semiconductor strain gages

In the following, both gage types are considered in more detail.

N.1.1 Metallic Strain Gages

The k-factor (N.4) of metallic strain gages is defined by the geometric term [194]:

$$k \approx 2 \tag{N.5}$$

Since the strains of the strain gage should be restricted to the elastic range, usually a value of 0.1% may not be exceeded with materials with distinct yield strength [191]. Taking this fact into account results in a relative resistance change, that is usually smaller than 10^{-3}. In order to consider the influence of lead resistance as well as an effective temperature compensation with balanced temperature coefficients of resistance, the metallic strain gage is often used in a *Wheatstone bridge*. The Wheatstone bridge allows for a high-accuracy measurement of small relative resistance changes of strain gages.

In order to estimate the expected measuring signal, two metallic strain gages are assumed to be attached on the upper and lower surface of the bending actuator shown in figure N.1. The evaluation is effected by means of a full bridge as illustrated in figure N.2.
The illustrated full bridge corresponds to an arrangement, the resistances R_2 and R_3 are attached to the upper surface (tensile stress) and R_1 and R_4 are attached to the lower surface (compressive stress) of the bending actuator.
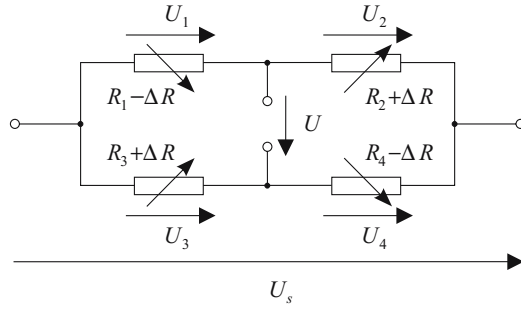
Fig. N.2. Full bridge

With respect to figure N.2, the ratio between the bridge voltage U and the supply voltage U_s generally yields

$$\frac{U}{U_s} = \frac{R_2 + \Delta R}{R_1 + R_2} - \frac{R_4 - \Delta R}{R_3 + R_4}. \tag{N.6}$$

Assuming $R_1 = R_2 = R_3 = R_4 = R$, equation (N.6) yields in combination with (N.3) and (N.5)

$$\frac{U}{U_s} = \frac{\Delta R}{R} = k\overline{S}. \tag{N.7}$$

The advantage of the full bridge is founded on the linear correlation between bridge voltage U and average strain $\overline{S}$. The expected relative resistance change results in combination with an average strain $\overline{S} = 135 \cdot 10^{-6}$ in

$$\frac{U}{U_s} = \frac{\Delta R}{R} = 0.27 \cdot 10^{-3}. \tag{N.8}$$

An instrumentation amplifier following the bridge section of the full bridge allows for the detection of the mechanical strain $\overline{S}$ and thus, the deflection ξ of the bending actuator.

N.1.2 Semiconductor Strain Gages

Compared to metallic strain gages, the k-factor of semiconductor strain gages is primarily determined by the material term being larger than the geometric term resulting in a strain sensitivity, that is much larger than 2. The measuring effect is based on the piezoresistive effect in semiconductors (germanium, silicon). The piezoresistive effect is ascribed to the dependence of the band structure on elastic lattice deformations caused by external mechanical stresses [195].

The k-factors of commercial p-type semiconductors range from $+110$ to $+130$, the k-factors of n-type semiconductors range from -80 to -100. However, it is

not possible to describe completely the relative resistance change dependent on the strain by means of the k-factor. In fact the relative resistance change shows parabolic characteristics. With respect to an average strain $\overline{S} = 135 \cdot 10^{-6}$ and room temperature $T_0 = 300\,\mathrm{K}$, on the basis of the equations (N.9) and (N.11) following estimations for the relative resistance change of p- and n-doped silicon are made [196].

1. p-doped silicon:

$$\left(\frac{\Delta R}{R}\right)_{T_0} = 119.5\,\overline{S} + 4000\,\overline{S}^2 \tag{N.9}$$

$$\Rightarrow \left(\frac{\Delta R}{R}\right)_{T_0} = 16.1 \cdot 10^{-3} + 0.1 \cdot 10^{-3} = 16.2 \cdot 10^{-3} \tag{N.10}$$

2. n-doped silicon:

$$\left(\frac{\Delta R}{R}\right)_{T_0} = -110\,\overline{S} + 10000\,\overline{S}^2 \tag{N.11}$$

$$\Rightarrow \left(\frac{\Delta R}{R}\right)_{T_0} = -14.9 \cdot 10^{-3} + 0.2 \cdot 10^{-3} = 14.7 \cdot 10^{-3} \tag{N.12}$$

Compared to metallic strain gages, the estimations show a much higher relative resistance change of semiconductors. However, the k-factor is affected adversely by its temperature dependency, that can generally be described according to

$$\frac{\Delta R}{R} = 119.5\,\overline{S}\left(\frac{T_0}{T}\right) + 4000\,\overline{S}^2\left(\frac{T_0}{T}\right)^2. \tag{N.13}$$

If the temperature rises from $T_0 = 300\,\mathrm{K}$ to $T_1 = 331\,\mathrm{K}$ and a maximum tip deflection $\xi_{\mathrm{max}} = -100\,\mu\mathrm{m}$ is assumed, the sensitivity $\Delta R/R$ of a semiconductor strain gage attached to the bending actuator will decrease from $16.2 \cdot 10^{-3}$ to $14.7 \cdot 10^{-3}$ corresponding to a percentage change of approx. 10%. Further disadvantages of semiconductor strain gages are:

- Semiconductor strain gages are considerably more expensive than metallic strain gages.
- The compensation of temperature-dependent disturbing influences is very difficult.
- The brittleness of semiconductor materials causes a more difficult handling.

Due to the disadvantages specified above, it is advised, not to employ semiconductor strain gages in combination with piezoelectric bending actuators.

N.2 Capacitive Distance Sensors

The mechanical strain arising on the upper and lower surface of the actuator during a bending deformation is to be measured by an applied capacitor. Two different capacitor types are considered:

1. Electrodes with intermediate dielectric applied to the upper and lower surface.
2. Interdigital structures applied to the upper and lower surface.

In the following, the relative capacitance change of both capacitor types caused by a bending deformation is estimated.

N.2.1 All over Covering Electrodes (double-sided)

A layer sequence consisting of electrode-dielectric-electrode is applied to the upper and lower surface of the bending actuator (see Fig. N.3).
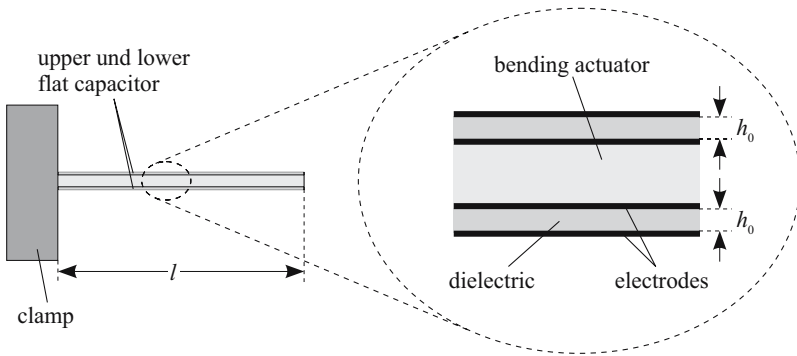
Fig. N.3. Strain and compression of flat capacitors applied to the upper and lower surface of a bending actuator

In order to estimate the relative capacitance change, the width b and the volume V_0 of the dielectric are assumed to remain constant. Furthermore, the width b and length l of the two capacitors correspond to the actuator's width and length (see tab. 9.1, section 9.1).

At first, that capacitor is considered, which is attached on the upper surface of the actuator affected by the mechanical strain $\overline{S}$ caused by bending deformation. Due to the mechanical strain, the origin length l of the capacitor extends to l_1, whereas the electrode gap is reduced from h_0 to h_1. The geometrical correlations are illustrated in figure N.4.
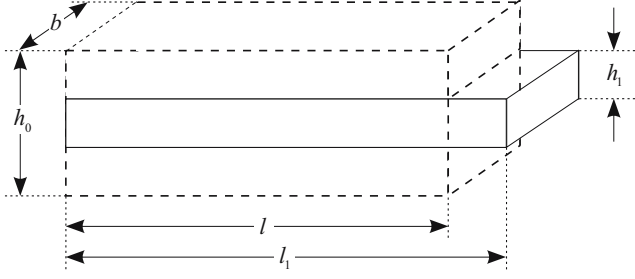
Fig. N.4. Geometry of the dielectric before and after the extension

The volume of the dielectric in the non-deformed state yields:

$$V_0 = bh_0 l \tag{N.14}$$

After an extension, the volume of the dielectric on the upper surface results in

$$V_1 \overset{!}{=} V_0 = bh_1 l \left(1 + \overline{S}\right). \tag{N.15}$$

Thus, the thickness h_1 results from (N.14) and (N.15):

$$h_1 = \frac{h_0}{1 + \overline{S}} \tag{N.16}$$

The capacitance change caused by the extension of the dielectric on the upper surface can be determined as follows:

$$C_1 = \varepsilon \frac{bl_1}{h_1} = \varepsilon \underbrace{\frac{bl}{h_0}}_{\equiv C_0} \left(1 + \overline{S}\right)^2 \approx C_0 \left(1 + 2\overline{S}\right) \tag{N.17}$$

The quantity C_0 represents the nominal capacitance (non-deformed state). By analogy with the extension of the dielectric on the actuator's upper surface, the dielectric on the lower surface is compressed. The capacitance resulting from the compression yields according to equation (N.17)

$$C_2 = \varepsilon \frac{bl_1}{h_1} = \frac{bl}{h_0} \left(1 - \overline{S}\right)^2 \approx C_0 \left(1 - 2\overline{S}\right). \tag{N.18}$$

The relative capacitance change can be determined by means of (N.17) and (N.18):

$$\frac{\Delta C}{C_0} = \frac{C_1 - C_2}{C_0} \approx 4\overline{S} \tag{N.19}$$

Taking the average strain $\overline{S} = 135 \cdot 10^{-6}$ into account, (N.19) yields

$$\frac{\Delta C}{C_0} \approx 0.54 \cdot 10^{-3}. \tag{N.20}$$

The capacitance C_0 in the non-deformed state is decisive for the absolute capacitance change ΔC. The absolute capacitance change is represented in Table N.1 with respect to two different dielectrics (polyimide, PZT). The chosen thicknesses h_0 are based on realizable values for polyimide and PZT layers, respectively.

Table N.1. Absolute capacitance change with respect to different dielectrics

dielectrics	ε_r	h_0 [μm]	C_0 [nF]	ΔC [pF]
polyimide	3.4	1	4.8	2.6
PZT	4500	20	318.7	172.1

Table N.1 shows, that the nominal capacitance C_0 may not be chosen too small, in order to achieve a large capacitance change ΔC. The smaller the capacitance changes are, the more complex the realization of an appropriate sensor electronics will be (resolution, electromagnetic shielding).

N.2.2 Interdigital Electrodes (double-sided)

In the following, a capacitor in form of *interdigital structures* is considered. The inderdigital structures consist of a two-layered system, i.e. dielectric and electrode. The interdigital structure applied to the upper and lower surface of the bending actuator is shown in figure N.5.

a)   b)
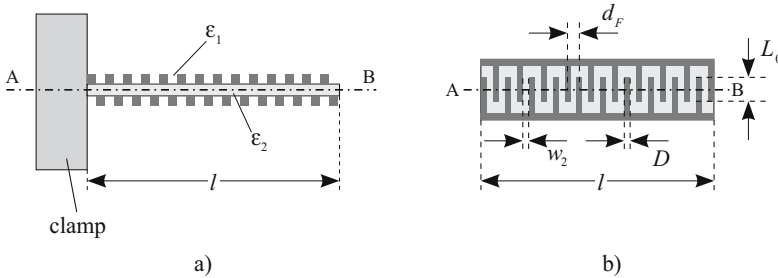
Fig. N.5. Capacitive displacement sensor. - **(a)** Arrangement of an interdigital structure on the upper and lower surface of the actuator (side view); **(b)** Geometry of the interdigital structure (top view).

The geometrical quantities L_0, d_F, w_2 and D denote the overlap of the finger structures, the interdigital period, the gap length and the finger width. The

total capacitance C_T of the interdigital structure yields with the number of the interdigital periods N_F (finger pairs)

$$C_T = C'_F N_F L_0, \tag{N.21}$$

where the capacitance per unit length C'_F of one interdigital period can be formulated as a function of the finger width D and the interdigital period d_F according to [197]

$$C'_F = \varepsilon_0 \varepsilon_{eff} \left[2.94 \left(\frac{D}{d_F} \right)^2 + 0.488 \left(\frac{D}{d_F} \right) + 1.07 \right]. \tag{N.22}$$

Taking figure N.5 into account, the dielectric of the interdigital electrodes is represented on the one hand by air ($\varepsilon_r = 1$) and on the other hand by the top layer of the PZT ceramics ($\varepsilon_r = \varepsilon_2$). In combination with the effective permittivity

$$\varepsilon_{eff} = \frac{1}{2} (\varepsilon_2 + 1), \tag{N.23}$$

the capacitance per unit length in (N.22) can be formulated as follows:

$$C'_F = \frac{\varepsilon_0}{2} (\varepsilon_2 + 1) \left[2.94 \left(\frac{D}{d_F} \right)^2 + 0.488 \left(\frac{D}{d_F} \right) + 1.07 \right] \tag{N.24}$$

If the gap length and the finger width are assumed to be equal, it follows

$$\frac{D}{d_F} = \frac{1}{2}. \tag{N.25}$$

Thus, the expression (N.24) can be simplified:

$$C'_F \approx \varepsilon_0 (\varepsilon_2 + 1) \tag{N.26}$$

In order to calculate the total capacitance C_T in equation (N.21), the knowledge of the quantity N_F is necessary. Taking figure N.5 into consideration, the free length l can be expressed by means of the interdigital structure geometry:

$$l = N_F D + (N_F - 1) w_2 \tag{N.27}$$

Thus, the quantity N_F can be determined:

$$N_F = \frac{l + w_2}{D + w_2} \tag{N.28}$$

Taking the assumption of an equal gap length and finger width into consideration, the number of interdigital periods results in

$$N_F = \frac{l}{2D} + \frac{1}{2}. \tag{N.29}$$

Insertion of (N.26) and (N.29) into (N.21) results in the nominal capacitance

$$C_T = \varepsilon_0 \left(\varepsilon_2 + 1\right) \left(\frac{l}{2D} + \frac{1}{2}\right) L_0. \tag{N.30}$$

At first, the interdigital structure applied to the upper surface of the actuator is considered. It is affected by the mechanical strain $\overline{S}$ caused by the bending deformation. The mechanical strain causes an extension of the interdigital period d_F according to

$$d_{F,1} = d_F \left(1 + \overline{S}\right) = \left(D + w_2\right) \left(1 + \overline{S}\right). \tag{N.31}$$

If the gap length and finger width are assumed to be equal, equation (N.31) results in

$$\frac{D}{d_{F,1}} = \frac{1}{2\left(1 + \overline{S}\right)}. \tag{N.32}$$

Insertion of (N.32) into (N.24) and taking equation (N.21) into consideration, the capacitance resulting from the bending deformation yields

$$C_{T,1} = \frac{\varepsilon_0}{2} \left(\varepsilon_2 + 1\right) \left[2.94 \left(\frac{1}{2\left(1 + \overline{S}\right)}\right)^2 + 0.488 \left(\frac{1}{2\left(1 + \overline{S}\right)}\right) + 1.07\right] N_F L_0. \tag{N.33}$$

By analogy with the extension of the dielectric ε_2 applied on the upper surface of the actuator, the dielectric applied on the lower surface is compressed. In accordance with equation (N.33), the capacitance yields

$$C_{T,2} = \frac{\varepsilon_0}{2} \left(\varepsilon_2 + 1\right) \left[2.94 \left(\frac{1}{2\left(1 - \overline{S}\right)}\right)^2 + 0.488 \left(\frac{1}{2\left(1 - \overline{S}\right)}\right) + 1.07\right] N_F L_0. \tag{N.34}$$

With respect to the approximations $\left(1 \pm \overline{S}\right)^2 \approx 1 \pm 2\overline{S}$ and $1 - \overline{S}^2 \approx 1$, the equations (N.30), (N.33) and (N.34) allow for the calculation of the relative capacitance change:

$$\frac{\Delta C}{C_T} = \frac{C_{T,2} - C_{T,1}}{C_T} \approx 1.714\,\overline{S} \tag{N.35}$$

The relative capacitance change, that can be expected, yields in combination with the average strain $\overline{S} = 135 \cdot 10^{-6}$

$$\frac{\Delta C}{C_T} \approx 0.23 \cdot 10^{-3}. \tag{N.36}$$

The capacitance C_T in the non-deformed state is decisive for the absolute capacitance change ΔC. In Table N.2, the absolute capacitance change is represented with respect to two different dielectrics (polyimide, PZT). A finger overlap of $L_0 = 5\,\text{mm}$, a finger width of $D = 20\,\mu\text{m}$ and a free length of $l = 20\,\text{mm}$ were chosen for the calculations. With respect to equation (N.29), the number of interdigital periods amounts to $N_F = 500$.

Table N.2. Absolute capacitance change of an interdigital structure with respect to different dielectrics

dielectrics	ε_2	C_T [nF]	ΔC [pF]
polyimide	3.4	0.097	0.02
PZT	4500	99.6	23.1

Compared to the first capacitor type, the relative capacitance change of the interdigital structure is smaller. Using an interdigital structure as capacitive displacement sensor, Table N.2 shows, that the capacitance changes ΔC are in the pF- and fF-range, respectively. This fact necessitates an enormous effort in the development and realization of an appropriate sensor electronics. In order to realize an interdigital structure, also the technological requirements may not be neglected (PVD, sputtering techniques, masking techniques).

N.3 Piezoelectric Distance Sensor

In the following, a passive piezoelectric layer of thickness h_p is assumed to be applied to the lower surface of the bending actuator. A deflection ξ in negative z-direction causes a compression S_1 in x-direction affecting the passive piezoelectric layer. The arrangement is shown in figure N.6.

The deflection ξ of the bending actuator in negative z-direction results in a compression S_1 in x-direction. This causes a charge displacement in z-direction within the passive piezoelectric layer, that can be measured as potential difference ΔU by means of a charge amplifier.

In order to estimate the potential difference ΔU, the following piezoelectric constitutive equations are taken into consideration:

$$S_1 = s_{11}^E T_1 + d_{31} E_3 \tag{N.37}$$

$$D_3 = d_{31} T_1 + \varepsilon_{33}^T E_3 \tag{N.38}$$

Since there is no *external* electric field affecting the piezoelectric sensor layer, the electrical displacement D_3 has to become zero due to the conservation of energy. Thus, from (N.38) the mechanical stress T_1 results in:
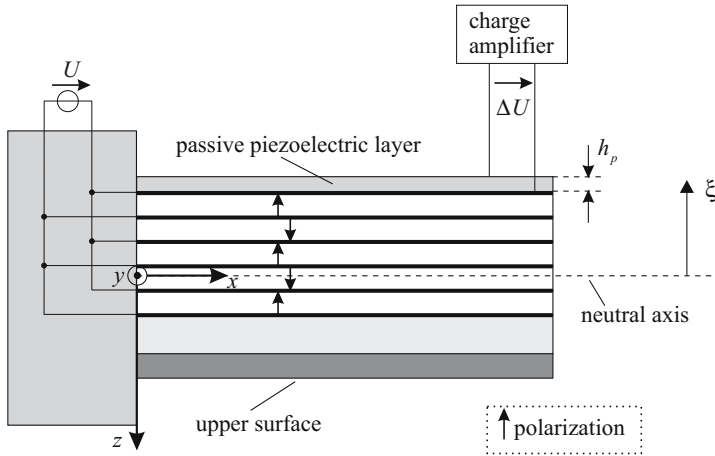
Fig. N.6. Passive piezoelectric layer as displacement sensor in combination with a piezoelectric bending actuator

$$T_1 = -\frac{\varepsilon_{33}^T}{d_{31}} E_3 \qquad (N.39)$$

Insertion of (N.39) into (N.37) and following rearranging with respect to the electric field E_3 yields

$$E_3 = S_1 \frac{d_{31}}{d_{31}^2 - \varepsilon_{33}^T s_{11}^E}. \qquad (N.40)$$

In combination with the correlation

$$E_3 = \frac{\Delta U}{h_p}, \qquad (N.41)$$

the potential difference ΔU in equation (N.40) results in

$$\Delta U = S_1 h_p \frac{d_{31}}{d_{31}^2 - \varepsilon_{33}^T s_{11}^E}. \qquad (N.42)$$

With the chosen quantities $S_1 = \overline{S} = 135 \cdot 10^{-6}$, $h_p = 20\,\mu\text{m}$ and the values of the piezoelectric constant d_{31}, the permittivity ε_{33}^T and the compliance s_{11}^E listed in Table 9.1, section 9.1, the potential difference can be estimated:

$$\Delta U = 2.14\,\text{V} \qquad (N.43)$$

The potential difference in (N.43) results from a charge displacement. However due to this fact, static displacement measurements are impossible. In order to ensure a signal processing for quasi-static and dynamic displacement measurements, expensive charge amplifiers are necessary.

N.4 Inductive Distance Sensor

Inductive sensor principles also allows for deflection measurements of piezo-electric bending actuators. In order to estimate the measurement signal, in the following, an inductive displacement sensor is considered, which consists of an iron core and a pair of planar coils applied to the bender's tip [198]. The iron core is assumed to be integrated into the housing of a pneumatic valve. The planar coils integrated on the bending actuator and the iron core form a magnetic circuit. The structure of the considered sensor-actuator-system is shown in figure N.7a (side view). Figure N.7b shows the the pair of planar coils applied to the thermal adjustment layer (NiCo 2918).
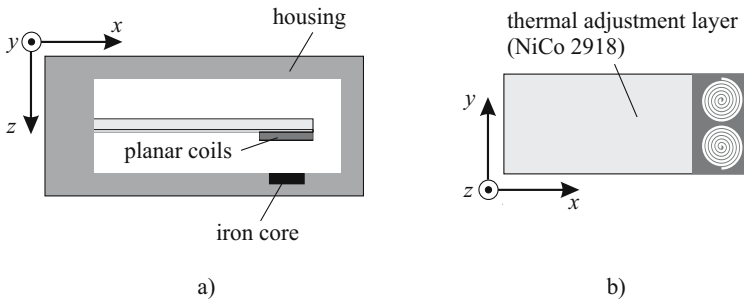
Fig. N.7. Inductive displacement sensor. - **(a)** Magnetic circuit consisting of a pair of planar coils and an iron core; **(b)** Arrangement of the planar coils on the thermal adjustment layer

By applying the planar coils to the thermal adjustment layer it is to be en-sured, that a large part of the magnetic induction B is carried within the magnetic circuit. The magnetic circuit with its necessary geometrical quan-tities (front view) and the corresponding circuit representation are shown in figure N.8.

In order to calculate a magnetic circuit, generally the magnetic flux Φ is considered. It allows for the determination of the magnetic induction B_ν in the individual sections ν of the magnetic circuit. The leakage flux is neglected [199]. If A_ν represents the cross section of the magnetic flux in the individual sections ν, then it can be written:

$$B_\nu = \frac{\Phi}{A_\nu} \tag{N.44}$$

By means of the magnetization curve of the respective material in section ν, the magnetic field strength H_ν results from the magnetic induction B_ν. The line integral of the magnetic field strength yields approximately
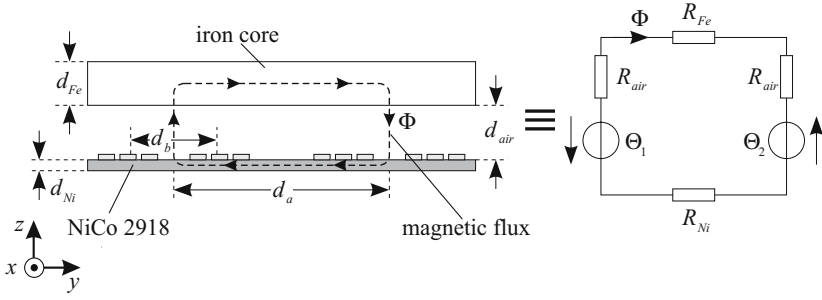
Fig. N.8. Magnetic circuit and corresponding circuit representation

$$\oint \mathbf{H} \cdot d\mathbf{s} \approx \sum_{\nu} H_\nu l_\nu. \tag{N.45}$$

The quantity l_v denotes the average length of the field lines in the individual sections ν. Thereby, it has to be summarized over the entire magnetic circuit. By means of *Ampère's law*, the constant Θ is defined by the total number of turns and the current i according to

$$\sum_{\nu} H_\nu l_\nu = \Theta = Ni. \tag{N.46}$$

In the following, the permeability μ_ν is assumed to be constant in the individual sections ν. Furthermore, the *magnetic resistance* (reluctance) is introduced. In combination with equation (N.44) and the material correlation

$$H_\nu = \frac{B_\nu}{\mu_\nu} \tag{N.47}$$

Ohm's law of the magnetic circuit will result from (N.46), if the magnetic flux Φ and the constant Θ correspond to the current and the source voltage, respectively:

$$\Phi \sum_{\nu} \frac{l_\nu}{\mu_\nu A_\nu} = \Theta \tag{N.48}$$

By analogy with the electric resistance, the magnetic resistance R_m results from (N.48) [200]:

$$R_m = \frac{\Theta}{\Phi} = \sum_{\nu} \frac{l_\nu}{\mu_\nu A_\nu} \tag{N.49}$$

At any time, the magnetic flux Φ is proportional to the instantaneous current i and the number of turns N. Thus, it can generally be written [201]:

$$L = \frac{N\Phi}{i} \tag{N.50}$$

Insertion of (N.46) into (N.50) yields with respect to (N.49) the inductance L of the magnetic circuit:

$$L = N^2 \frac{\Phi}{\Theta} = \frac{N^2}{R_m} \tag{N.51}$$

In accordance with the circuit representation shown in figure N.8, the magnetic resistance results in

$$R_m = 2R_{air} + R_{Ni} + R_{Fe}. \tag{N.52}$$

Thus, the inductance L of the magnetic circuit can be determined in accordance with (N.51):

$$L = \frac{N^2}{2R_{air} + R_{Ni} + R_{Fe}} = \frac{\mu_0 N^2}{\frac{l_{air}}{A_{air}} + \frac{l_{Ni}}{\mu_{r,Ni} A_{Ni}} + \frac{l_{Fe}}{\mu_{r,Fe} A_{Fe}}} \tag{N.53}$$

The geometrical quantities illustrated in figure N.8 allow for the formulation of the average field line length l_ν and the cross section A_ν in each individual section ν. It is assumed, that the effective flux-carrying surfaces over the individual planar coils are circular, having an effective diameter d_b. Thus, (N.53) can be reformulated:

$$L = \frac{\mu_0 N^2}{\frac{8 d_{air}}{\pi d_b^2} + \frac{d_a}{\mu_{r,Ni} d_{Ni} d_b} + \frac{d_a}{\mu_{r,Fe} d_{Fe} d_b}} \tag{N.54}$$

Now it is assumed, that the distance between the planar coils and the iron core amounts to $d_{air} = d_{air,0} = 300\,\mu\text{m}$ during the off-state of the bending actuator. This results in the nominal inductance L_0. Since the bending actuator is driven in such a manner, that the tip deflection in negative z-direction amounts to $\xi = 100\,\mu\text{m}$, the distance between the planar coils and the iron core increases to $d_{air,1} = 400\,\mu\text{m}$. In accordance with equation (N.54), the inductance decreases to L_1. Thus, the relative inductance change can be calculated according to

$$\frac{\Delta L}{L_0} = \frac{L_0 - L_1}{L_0}. \tag{N.55}$$

The geometrical quantities used for the calculations are listed in Table N.3. The relative permittivities of the iron core and the thermal adjustment layer NiCo 2918 are assumed to be equal $\left(\mu_{r,Ni} = \mu_{r,Fe} = 1000\right)$. The calculated inductances as well as the absolute and relative inductance change are listed in Table N.4.

Table N.3. Geometrical quantities used for the calculation of the magnetic circuit

N	$d_{air,0}$ [μm]	$d_{air,1}$ [μm]	d_a [mm]	d_b [mm]	d_{Ni} [μm]	d_{Fe} [mm]
10	300	400	4	2	100	1

Table N.4. Calculated inductances as well as the absolute and relative inductance change of the magnetic circuit

L_0 [μH]	L_1 [μH]	ΔL [μH]	$\Delta L/L_0$
0.590	0.454	0.135	0.23

Table N.4 shows, that the relative inductance change can be expected in the %-range. Compared to the resistive and capacitive sensor principles discussed before, this fact represents an enormous advantage. Due to the high sensor sensitivity of the inductive displacement sensor, a high interference immunity is expected. A high-accuracy tip deflection measurement of bending actuators is ensured.

O

Methods of Measuring Small Capacitances with High Resolution

The capacitance C_x of an capacitor is usually determined by means of the voltage, the current, the frequency and the time, respectively. The capacitance change of the foil capacitor during bending deformation of the actuator can be expected in the sub-pF-range up to the fF-range according to the capacitor's structure. Thus, special requirements to the sensor electronics are necessary. The measurement of small capacitances is problematic, since the parasitic capacitances and the capacitances of the shielded connections can be somewhere in the order of the capacitances to be measured (see Fig. O.1).
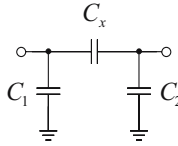
Fig. O.1. Parasitic capacitances of the capacitor to be measured and its shielded connections

Thus, it has to be an aim to suppress the parasitic capacitances efficiently by means of an appropriate sensor electronics. In the following, different circuit variants are discussed, that are suitable for suppressing parasitic capacitances.

O.1 Direct Method

Figure O.2 shows two possible circuit variants for the minimization of the influence of parasitic capacitances. In figure O.2a, the capacitor to be measured is applied by a voltage U_1 and the current I_1 is measured. In figure O.2b the capacitor is measured in reverse order. In both circuit variants, the parasitic capacitance C_1 and C_x are applied by the same voltage, however, the current

through C_2 is not measured. Thus, the influence of the parasitic capacitance C_1 is eliminated. In both circuit variants, an almost ideal current sensing is done in parallel connection to C_2. The voltage of the parasitic capacitance C_2, and thus the current is forced to zero ideally. This is achieved by an operation amplifier negatively fed back, that attempts to set the potential at its inverting input to zero [202, 203].
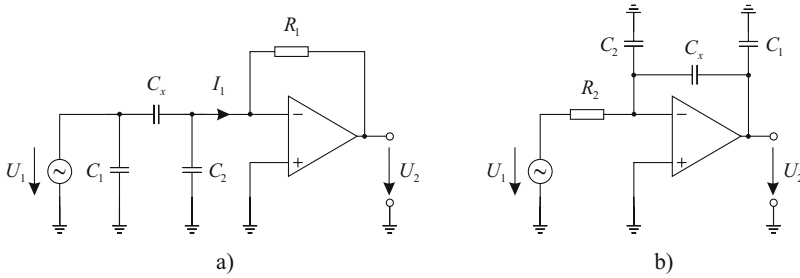
Fig. O.2. Circuit variants for the elimination of the influence of parasitic capacitances

However, the loop gain has to be chosen high enough. It determines the suppressing of the parasitic capacitance. The capacitance of the circuit variant a) is calculated according to

$$C_x = \frac{U_2}{\omega R_1 U_1}. \tag{O.1}$$

The capacitance of the circuit variant b) results in

$$C_x = \frac{U_1}{\omega R_2 U_2} = \frac{U_1}{2\pi R U_2} T. \tag{O.2}$$

Both circuit variants can be extended by a rectifier and a following A/D converter. However, the resolution is strongly limited by the linearity error of the individual electronic circuits. This is caused by the non-ideal behavior of the operational amplifier.

O.2 Self-balancing Capacitance Bridge

In figure O.3, a self-balancing capacitance bridge is illustrated. The current through the capacitance to be measured generated by the voltage $\underline{U}_1$ is compensated in the bridge diagonal S by the second bridge arm with the constant capacitance C_{ref} and the *variable* voltage $\underline{U}_{ref}$.
The bridge is operated in balanced condition. It can be written:
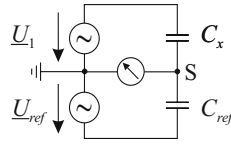
Fig. O.3. Structure of a self-balancing capacitance bridge

$$C_x = C_{ref} \frac{U_{ref}}{U_1} \qquad (O.3)$$

The sensor electronics shown in figure O.2a can be implemented into the bridge diagonal. Figure O.4 shows the block diagram of a self-balancing capacitance bridge with the senor electronics implemented into the bridge arm.

Fig. O.4. Block diagram of a self-balancing capacitance bridge with the sensor electronics implemented into the bridge arm

The problem of the presented circuit generally exists in the fact, that the voltages $\underline{U}_1$ and $\underline{U}_{ref}$ have to agree very exactly on amplitude and frequency. Therefore, the sine signal should be generated digitally.

A phase-selective rectifier working as demodulator generates in combination with the lowpass the rectified output voltage of the I/U converter. Compared to a peak value rectifier, the averaging rectifier eliminates the amplifier noise, that causes a noise-dependent offset error, if a peak value rectifier is used. The bridge is balanced in such a way, that the output signal of the A/D converter is zero. The measurement value corresponds to the input signal of the

multiplying D/A converter.

Furthermore, the complex circuit structure may not be neglected. Since sensitive analog and digital circuits affect mutually, the circuit structure is also problematic with respect to electromagnetic shielding.

O.3 Charge Measurement

A further possibility for the determination of the capacitance C_x represents a charge measurement. Figure O.5 illustrates the structure of a circuit working on the basis of charge measurement [204, 205]. If the switches S_{11} and S_{12} are closed, the capacitance C_x will be subjected to a DC voltage U_{ref}. Thus, C_x is charged with the charge $Q = C_x U_{ref}$, the switches S_{21} and S_{22} remain opened. In the next step, S_{11} and S_{12} are opened, S_{21} and S_{22} are closed. Thus, the capacitance C_x is connected with the inverting input of the operational amplifier, that forces the potential difference to zero. So C_x is short-circuited and therefore discharged by the parallel connection of C_f and R_f.
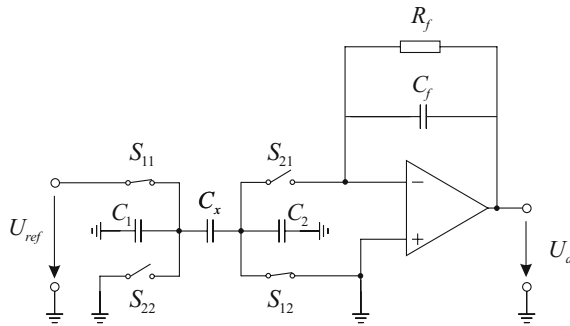
Fig. O.5. Determination of the capacitance by measurement of charging currents

In combination with the switching frequency f_s, the output voltage results in

$$U_a = f_s U_{ref} R_f C_x. \tag{O.4}$$

The time constant $\tau = C_f R_f$ must be long in relation to the period of the switching frequency f_s. The capacitance C_1 is also charged during the first phase, however, its discharge current is not measured. During the first phase the capacitance C_2 is short-circuited, during the second phase it is grounded ideally. Thus, the parasitic capacitances are also eliminated by means of this circuit variant.

O.4 Measurement of the Integration Time

The circuit variant O.2b is used as input of the circuit shown in figure O.6. The voltage U_2 is integrated as long as the non-inverting Schmitt trigger responds. Now, the voltage U_2 changes the polarity. Thus, a triangular wave voltage U_1 and a square wave voltage U_2 develop with the period

$$T = 4\frac{R_1 R_2}{R_3}C_x. \tag{O.5}$$

The period T is a measure for the unknown capacitance and can be determined with a frequency counter.
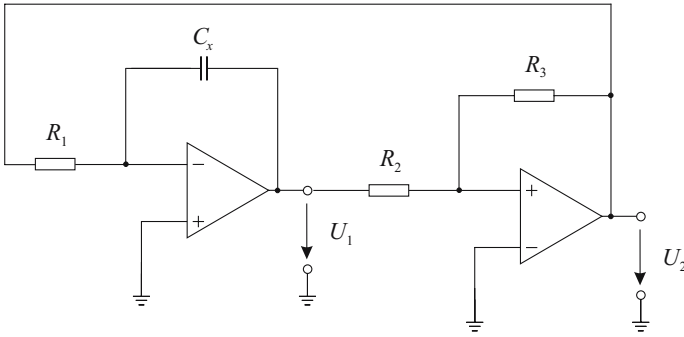
Fig. O.6. Circuit structure for capacitance measurement by means of the integration time

O.5 Oscillator Method

The following method uses the dependence of the resonant frequency of an LC- or RC-resonant circuit on the unknown capacitance C_x. The frequency is measured either by a digital counter or transformed into an analog voltage by a frequency-to-voltage converter. Thus, the unknown capacitance C_x can be determined [206].

RC-oscillator
Multivibrators, variation timers and phase locked loops belong to the class of RC-oscillators. Generally, following points turn out to be problematic:

- high susceptibility to parasitic capacitances
- the parallel conductance G_x of the capacitance C_x influences the resonant frequency

- small sensitivity with respect to small capacitance changes
- bad frequency stability

The method is not suitable for applications, that require a resolution of less than 10 fF.

LC-oscillator

LC-oscillators allow for capacitance measurements in a frequency range from some hundred kHz upto some hundred MHz. The resonant frequency change can be described by

$$\Delta f = -\frac{f_0}{2\left(C_x + C_s\right)}\Delta C_x. \tag{O.6}$$

C_s represents the parasitic capacitance. Equation (O.6) shows, that an LC-oscillator is sensitive to parasitic capacitances. Besides, the resolution decreases with increasing nominal capacitances C_x.

P

To the Output Signal of the Instrumentation Amplifier

In order to calculate the output signal $\underline{U}_{a1}$ of the the instrumentation amplifier, figure P.1 has to be considered.
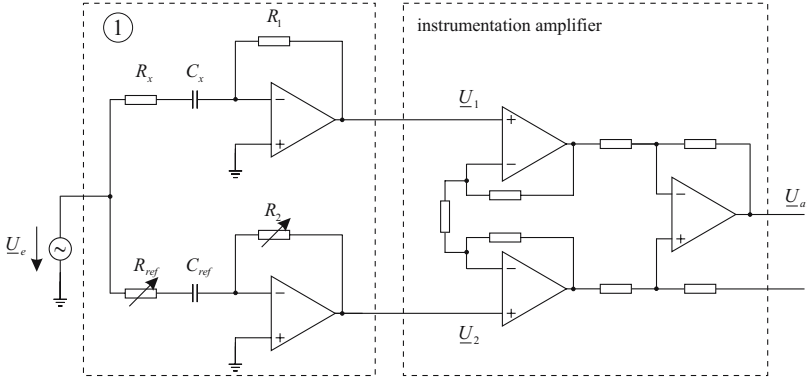
Fig. P.1. Differential amplifier for suppressing parasitic capacitances and following instrumentation amplifier

Taking the potentials $\underline{U}_1$ and $\underline{U}_2$ applied to the input of the instrumentation amplifier into account (see Fig. P.1), the output signal $\underline{U}_{a1}$ can be calculated according to following expression [207]:

$$\underline{U}_{a1} = A_1 \left[\underline{U}_2 - \underline{U}_1 \right] \tag{P.1}$$

The quantity A_1 corresponds to the total gain factor of the instrumentation amplifier. In combination with two *inverting* operational amplifier circuits added to the instrumentation amplifier, equation (P.1) yields

$$\underline{U}_{a1} = \underline{U}_e A_1 \left[\frac{R_1}{R_x + \frac{1}{j\omega C_{x0}}} - \frac{R_2}{R_{ref} + \frac{1}{j\omega C_{ref}}} \right]. \tag{P.2}$$

The quantity C_{x0} represents the capacitance of the unstressed foil capacitor. Reformulation of the expression (P.2) and following extraction of $j\omega$ results in

$$\underline{U}_{a1} = j\omega \underline{U}_e A_1 \left[\frac{R_1 C_{x0}}{1 + j\omega R_x C_{x0}} - \frac{R_2 C_{ref}}{1 + j\omega R_{ref} C_{ref}} \right]$$

$$\Leftrightarrow \underline{U}_{a1} = j\omega \underline{U}_e A_1 \left[\frac{R_1 C_{x0} \left(1 + j\omega R_{ref} C_{ref}\right) - R_2 C_{ref} \left(1 + j\omega R_x C_{x0}\right)}{\left(1 + j\omega R_x C_{x0}\right) \left(1 + j\omega R_{ref} C_{ref}\right)} \right].$$

$$\text{(P.3)}$$

Extension of (P.3) and following arranging of the terms finally yields:

$$\underline{U}_{a1} = j\omega \underline{U}_e A_1 \left[\frac{R_1 C_{x0} - R_2 C_{ref} + j\omega C_{x0} C_{ref} \left(R_{ref} R_1 - R_x R_2\right)}{1 - \omega^2 R_x R_{ref} C_{x0} C_{ref} + j\omega \left(R_x C_{x0} + R_{ref} C_{ref}\right)} \right] \quad \text{(P.4)}$$

Q

Alternating Magnetic Field Within a Conductive Layer

The time and position dependence of the z-component of the magnetic field H within a conductive layer is described by the differential equation

$$\frac{1}{r}\frac{\partial}{\partial r}\left(r\frac{\partial H_z}{\partial r}\right) + \frac{\partial^2 H_z}{\partial z^2} - \kappa\mu\frac{\partial H_z}{\partial t} = 0, \tag{Q.1}$$

which can be reformulated as follows:

$$\frac{\partial^2 H_z}{\partial r^2} + \frac{\partial^2 H_z}{\partial z^2} + \frac{1}{r}\frac{\partial H_z}{\partial r} - \kappa\mu\frac{\partial H_z}{\partial t} = 0 \tag{Q.2}$$

In order to find a solution of (Q.2), the *method of separation of variables* is considered:

$$H_z\left(r, z, t\right) = V\left(r, z\right)W\left(t\right) \tag{Q.3}$$

Since the circular loop is subjected to a sinusoidal alternating current, the real time function $H_z\left(r, z, t\right)$ is replaced by the complex time function $\underline{H}_z\left(r, z, t\right)$. Thus, (Q.3) can be reformulated as follows:

$$\underline{H}_z\left(r, z, t\right) = \underline{V}\left(r, z\right)e^{j\omega t} \tag{Q.4}$$

Insertion of (Q.4) into (Q.2) and following separation of the variables (r, z, t) yields

$$\frac{1}{\underline{V}}\left(\frac{\partial^2 \underline{V}}{\partial r^2} + \frac{\partial^2 \underline{V}}{\partial z^2} + \frac{1}{r}\frac{\partial \underline{V}}{\partial r}\right) = j\omega\kappa\mu =: -v^2. \tag{Q.5}$$

Here, ν is a constant, since the left side of equation (Q.5) is independent of t and the right side is independent of r and z. By applying the method of separation of variables again, it can be written

$$\underline{V}\left(r, z\right) = \underline{X}\left(r\right)\underline{Y}\left(z\right). \tag{Q.6}$$

Insertion of (Q.6) into (Q.5) yields after separation of the variables r and z

$$\frac{1}{\underline{X}(r)}\frac{d^2\underline{X}(r)}{dr^2} + \frac{1}{\underline{X}(r)}\frac{1}{r}\frac{d\underline{X}(r)}{dr} = -\frac{1}{\underline{Y}(z)}\frac{d^2\underline{Y}(z)}{dz^2} - v^2 =: -u_n^2, \qquad (Q.7)$$

where u_n denotes also a constant.

Two ordinary differential equations for $\underline{X}(r)$ and $\underline{Y}(z)$ result from (Q.7):

$$\frac{d^2\underline{Y}(z)}{dz^2} - \underline{Y}(z)\left(u_n^2 - v^2\right) = 0 \qquad (Q.8)$$

and

$$\frac{d^2\underline{X}(r)}{dr^2} + \frac{1}{r}\frac{d\underline{X}(r)}{dr} + \underline{X}(r)\,u_n^2 = 0 \qquad (Q.9)$$

The solution of the homogeneous linear differential equation (Q.8) results from the linear combination of two linear independent solutions (basis solutions) with the solution approach $\underline{Y}(z) = e^{\lambda z}$:

$$\underline{Y}(z) = \underline{A}_{1n}\,e^{-z\sqrt{u_n^2+j\omega\kappa\mu}} + \underline{A}_{2n}\,e^{z\sqrt{u_n^2+j\omega\kappa\mu}} \qquad (Q.10)$$

By transition to the variable $\rho := u_n r$, from (Q.9) with

$$\underline{Z}(\rho) := \underline{X}(\rho/u_n)\,, \qquad (Q.11)$$

Bessel's differential equation follows:

$$\frac{d^2\underline{Z}(\rho)}{d\rho^2} + \frac{1}{\rho}\frac{d\underline{Z}(\rho)}{d\rho} + \underline{Z}(\rho) = 0 \qquad (Q.12)$$

Its solution results in [208]

$$\underline{Z}(\rho) = \underline{C}_1 J_0(\rho)\,. \qquad (Q.13)$$

If $\underline{C}_1 = 1$ is chosen, which does not influence the total solution at all, then the general solution yields

$$\underline{X}(r) = J_0(u_n r)\,. \qquad (Q.14)$$

The function $J_0(u_n r)$ represents the Bessel function of first kind of order zero. Taking (Q.4) and (Q.6) into account, the formal solution is achieved by superposition [208]:

$$\underline{H}_z(r,z,t) = e^{j\omega t}\sum_{n=1}^{\infty} J_0(u_n r)\left[\underline{A}_{1n}\,e^{-z\sqrt{u_n^2+j\omega\kappa\mu}} + \underline{A}_{2n}\,e^{z\sqrt{u_n^2+j\omega\kappa\mu}}\right] \qquad (Q.15)$$

Due to continuous spectrum of the eigenvalues u, (Q.15) can be written in integral form [209]

$$\underline{H}_z(r,z,t) = e^{j\omega t}\int_0^{\infty} J_0(ur)\left[\underline{A}_1\,e^{-z\sqrt{u^2+j\omega\kappa\mu}} + \underline{A}_2\,e^{z\sqrt{u^2+j\omega\kappa\mu}}\right] du. \qquad (Q.16)$$

R

Magnetic Field Calculation of a Circular Loop

Figure R.1 illustrates the geometrical quantities being necessary for the calculation of the magnetic field of a circular loop with radius a along its axis in distance z from the center (point of origin) [210].
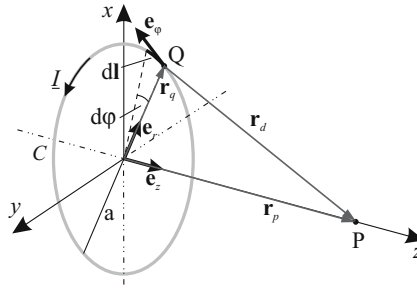
Fig. R.1. Geometry of a circular loop for the calculation of the magnetic field along the z-axis

$d\mathbf{l}$ shows in direction of the alternating current $\underline{I}(t) = \underline{I}\,e^{j\omega t}$ (see Fig. R.1). The current loop in space is characterized by the quantity C, the vector $\mathbf{r}_d$ points from the source point Q at the space point P. Due to the present symmetry, in further consideration cylindrical coordinates are used.

In order to calculate the magnetic field of a circular loop along its axis of symmetrie, the *Biot-Savart law* is considered [211]:

$$\underline{\mathbf{H}}(\mathbf{r}_p, t) = e^{j\omega t}\, \frac{\underline{I}}{4\pi} \int\limits_{C} \frac{d\mathbf{l} \times \mathbf{r}_d}{r_d^3} \qquad (\text{R.1})$$

The vector $d\mathbf{l}$ can be defined by means of the unit vector $\mathbf{e}_\varphi$:

$$dl = a\, d\varphi\, \mathbf{e}_\varphi \tag{R.2}$$

The vector $\mathbf{r}_d$ pointing from source point Q at space point P results from the difference of the position vectors $\mathbf{r}_p$ and $\mathbf{r}_q$ of points P and Q:

$$\mathbf{r}_d = \mathbf{r}_p - \mathbf{r}_q = z\mathbf{e}_z - a\mathbf{e}_r \tag{R.3}$$

The vector product $dl \times \mathbf{r}_d$ can be determined by means of (R.2) and (R.3).

$$dl \times \mathbf{r}_d = a\, d\varphi\, \mathbf{e}_\varphi \times (z\mathbf{e}_z - a\mathbf{e}_r) = za\, d\varphi\, \mathbf{e}_r + a^2\, d\varphi\, \mathbf{e}_z \tag{R.4}$$

Furthermore, (R.3) yields

$$|\mathbf{r}_d| = \sqrt{z^2 + a^2}. \tag{R.5}$$

Insertion of (R.4) and (R.5) into (R.1) yields the axial component of the magnetic field

$$\underline{H}_z\,(r = 0, z, t) = \frac{a^2 \underline{I}}{2\,(z^2 + a^2)^{3/2}}\, e^{j\omega t}. \tag{R.6}$$

In order to provide a general representation of the magnetic field of a circular loop in the following form (see eq. 12.46, section 12.4.1)

$$\underline{H}_z\,(r, z, t) = e^{j\omega t} \int_0^\infty J_0\,(ur) \left[\underline{B}_1\, e^{-zu} + \underline{B}_2\, e^{zu}\right] du, \tag{R.7}$$

the following integral has to be determined [186]

$$\int_0^\infty e^{-zu}\, J_0\,(au)\, du \tag{R.8}$$

The Bessel function of first kind and order zero can be represented by means of a complex exponential function (*generating function*) in integral form [107, 212]

$$J_0\,(au) = \frac{1}{2\pi} \int_0^{2\pi} e^{jau \cos\varphi}\, d\varphi. \tag{R.9}$$

Insertion of (R.9) into (R.8) results in

$$\frac{1}{2\pi} \int_0^{2\pi} \int_0^\infty e^{-(z - ja \cos\varphi)u}\, du = \frac{1}{2\pi} \int_0^{2\pi} \underbrace{\frac{1}{z - ja \cos\varphi}}_{(*)}\, d\varphi. \tag{R.10}$$

Rewriting $(*)$ in the following form

$$\frac{1}{z - ja\cos\varphi} = \frac{z}{z^2 + a^2\cos^2\varphi} + j\frac{a\cos\varphi}{z^2 + a^2\cos^2\varphi}, \tag{R.11}$$

insertion in (R.10) and following integration yields in combination with appropriate integral tables [213] following correlation

$$\int_0^\infty e^{-zu}\, J_0\left(au\right) du = \frac{1}{\sqrt{z^2 + a^2}}. \tag{R.12}$$

Derivation on both sides according to

$$\int_0^\infty e^{-zu}\, \frac{d}{da} J_0\left(au\right) du = \frac{d}{da}\frac{1}{\sqrt{z^2 + a^2}} \tag{R.13}$$

yields with the general derivation rule for the Bessel function [214, 215]

$$\frac{d}{dx} J_p\left(x\right) = \frac{p}{x} J_p\left(x\right) - J_{p+1}\left(x\right) \tag{R.14}$$

the expression

$$\int_0^\infty e^{-zu}\, J_1\left(au\right) u\, du = \frac{a}{\left(z^2 + a^2\right)^{3/2}}. \tag{R.15}$$

Multiplication with $\underline{I}\,e^{j\omega t}\, a/2$ on both sides of (R.15) finally results in

$$\frac{1}{2} e^{j\omega t} \int_0^\infty e^{-zu}\, J_1\left(au\right) au\underline{I}\,du = \frac{a^2\underline{I}}{2\left(z^2 + a^2\right)^{3/2}} e^{j\omega t}, \tag{R.16}$$

which exactly corresponds to the analytical description (R.6) of the magnetic field of a circular loop along the z-axis.

Since the origin of the coordinate system in figure 12.9, section 12.4, is not located in the center of the circular loop, but shifted in z-direction ($z = -d$), by means of coordinate transformation, (R.16) results in

$$H_z\left(r = 0, z, t\right) = \frac{1}{2} e^{j\omega t} \int_0^\infty e^{-(z+d)u}\, J_1\left(au\right) au\underline{I}\,du$$

$$= \frac{1}{2} e^{j\omega t} \int_0^\infty e^{-zu}\, e^{-du}\, J_1\left(au\right) au\underline{I}\,du. \tag{R.17}$$

For $r = 0$, equation (R.17) has to be equivalent to the general formulation of the magnetic field in (R.7), thus with $J_0\left(0\right) = 1$ following condition can be formulated [216]:

$$\int_0^\infty \left[\underline{B}_1\,\mathrm{e}^{-zu} + \underline{B}_2\,\mathrm{e}^{zu}\right] du \stackrel{!}{=} \frac{1}{2}\int_0^\infty \mathrm{e}^{-zu}\,\mathrm{e}^{-du}\,J_1\,(au)\,au\underline{I}\,du$$

$$(\text{R}.18)$$

A comparison of the left and right side of (R.18) immediately yields

$$\underline{B}_2 = 0, \qquad\qquad (\text{R}.19)$$

resulting in

$$\int_0^\infty \underline{B}_1\,\mathrm{e}^{-zu}\,du = \frac{1}{2}\int_0^\infty \mathrm{e}^{-zu}\,\mathrm{e}^{-du}\,J_1\,(au)\,au\underline{I}\,du. \qquad (\text{R}.20)$$

By comparison of the left and right side of (R.20), the constant $\underline{B}_1$ can be formulated according to

$$\underline{B}_1 = \frac{1}{2}au\underline{I}\,\mathrm{e}^{-du}\,J_1\,(au)\,. \qquad\qquad (\text{R}.21)$$

By insertion of (R.21) into (R.7) and taking (R.19) into consideration, the general description of the magnetic field of a circular loop dependent on the coordinates r, z, and t is achieved:

$$\underline{H}_z\,(r, z, t) = \mathrm{e}^{j\omega t}\int_0^\infty \underline{B}_1\,\mathrm{e}^{-zu}\,J_0\,(ur)\,du \qquad (z > -d) \qquad (\text{R}.22)$$

References

1. G. H. Heartling. *Ferroelectric Ceramics - History and Technology.* Journal of the American Ceramic Society, Vol. 82, No. 4, pp. 797-818, 1999.
2. K. Uchino. *Piezoelectric Actuators 2004-Materials, Design, Drive/Control, Modeling and Applications.* Actuator 2004, 9th International Conference on New Actuators, Bremen, pp. 38-47, June 2004.
3. A. J. Schmid. *Piezokeramische Systeme - Physikalische Eigenschaften und Anwendungen.* 1. Auflage. Technische Keramik in der Praxis, Seminarreihe 2002, Verband der Keramischen Industrie e.V., pp. 455-485, 2002.
4. S. Büttgenbach. *Mikromechanik.* Teubner Studienbücher, 2. Auflage. B. G. Teubner, pp. 100-120, Stuttgart, 1994.
5. A. Lenk. *Elektromechanische Systeme, Band 2.* 2. Auflage. VEB Verlag Technik, p. 249, Berlin, 1977.
6. Q. M. Wang; X. H. Du; B. Xu; L. E. Cross. *Electromechanical Coupling and Output Efficiency of Piezoelectric Bending Actuators.* IEEE Transactions on Ultrasonics, Ferroelectrics and Frequency Control, Vol. 46, No. 3, pp. 638-646, May 1999.
7. Q. M. Wang; Q. Zhang; B. Xu; R. Liu; L. E. Cross. *Nonlinear piezoelectric behavior of ceramic bending mode actuators under strong electric fields.* Journal of Applied Physics, Vol. 86, No. 6, pp. 3352-3360, September 1999.
8. M. J. Cunningham; D. F. L. Jenkins; M. M. Bakush. *Experimental investigation of optimum thickness of a piezoelectric element for cantilever actuation.* Proc. IEE, Science, Measurement and Technology, Vol. 144, No. 1, pp. 45-48, January 1997.
9. H. Kueppers; M. Hoffmann; T. Leuerer; T. Schneller; U. Boettger; R. Waser; W. Mokwa; U. Schnakenberg. *Basic Investigations on a Piezoelectric Bending Actuator for Micro-Electro-Mechanical Applications.* Integrated Ferroelectrics, Vol. 35, pp. 269-281, 2001.
10. M. Brissaud; S. Ledren; P. Gonnard. *Modelling of a cantilever non-symmetric piezoelectric bimorph.* Journal of Micromechanics and Microengineering, Vol. 13, pp. 832-844, July 2003.
11. C. Huang; Y. Y. Lin; T. A. Tang. *Study on the tip-deflection of a piezoelectric bimorph cantilever in the static state.* Journal of Micromechanics and Microengineering, Vol. 14, pp. 530-534, January 2004.

12. T. S. Low; W. Guo. *Modeling of a Three-Layer Piezoelectric Bimorph Beam with Hysteresis.* IEEE Journal of Microelectromechanical Systems, Vol. 4, No. 4, pp. 230-237, December 1995.

13. Q. M. Wang; L. E. Cross. *Constitutive Equations of Symmetrical Triple Layer Piezoelectric Benders.* IEEE Transactions on Ultrasonics, Ferroelectrics and Frequency Control, Vol. 46, No. 6, pp. 1343-1351, November 1999.

14. E. B. Tadmor; G. Ksa. *Electromechanical Coupling Correction for Piezoelectric Layered Beams.* IEEE Journal of Microelectromechanical Systems, Vol. 12, No. 6, pp. 899-906, December 2003.

15. J. G. Smits; Wai-shing Choi. *The Constituent Equations of Piezoelectric Heterogeneous Bimorphs.* IEEE Transactions on Ultrasonics, Ferroelectrics and Frequency Control, Vol. 38, No. 3, May 1991.

16. D. L. DeVoe; A. P. Pisano. *Modeling and Optimal Design of Piezoelectric Cantilever Microactuators.* IEEE Journal of Microelectromechanical Systems, Vol. 6, No. 3, pp. 266-270, September 1997.

17. Q. Meng; M. Mehregany; K. Deng. *Modeling of the electromechanical performance of piezoelectric laminated microactuators.* Journal of Micromechanics and Microengineering, Vol. 3, pp. 18-23, February 1993.

18. M. S. Weinberg. *Working Equations for Piezoelectric Actuators and Sensors.* IEEE Journal of Microelectromechanical Systems, Vol. 8, No. 4, December 1999.

19. J. G. Smits; A. Ballato. *Dynamic Admittance Matrix of Piezoelectric Cantilever Bimorphs.* Journal of Microelectromechanical Systems, Vol. 3, No. 3, September 1994.

20. M. F. Coughlin; D. Stamenovic; J. G. Smits. *Determining Material Stiffness Using Piezoelectric Bimorphs.* IEEE Ultrasonics Symposium, pp. 1607-1610, 1996.

21. J. G. Smits; W. Choi; A. Ballato. *Resonance and Antiresonance of Symmetric and Asymmetric Cantilevered Piezoelectric Flexors.* IEEE Transactions on Ultrasonics, Ferroelectrics and Frequency Control, Vol. 44, No. 2, pp. 250-258, March 1997.

22. K. Yao; K. Uchino. *Analysis on a composite cantilever beam coupling a piezoelectric bimorph to an elastic blade.* Sensors & Actuators A, Vol. 89, pp. 215-221, 2001.

23. M. Sitti; D. Campolo; J. Yan; R. S. Fearing. *Development of PZT and PZT-PT Based Unimorph Actuators for Micromechanical Flapping Mechanisms.* IEEE International Conference on Robotics and Automation, Vol. 4, pp. 3839-3846, 2001.

24. A. Fernandes; J. Pouget. *Analytical and numerical approaches to piezoelectric bimorph.* International Journal of Solids and Structures, Vol. 40, pp. 4331-4352, 2003.

25. H. Seitz; J. Heinzl. *Modelling of a microfluidic device with piezoelectric actuators.* Journal of Micromechanics and Microengineering, Vol. 14, pp. 1140-1147, 2004.

26. N. N. Rogacheva; C. C. Chou; S. H. Chang. *Electromechanical Analysis of a Symmetric Piezoelectric/Elastic Laminate Structure: Theory and Experiment.* IEEE Transactions on Ultrasonics, Ferroelectrics and Frequency Control, Vol. 45, No. 2, pp. 285-294, March 1998.

27. S. K. Ha. *Admittance Matrix of Asymmetric Piezoelectric Bimorph with Two Separate Electrical Ports Under General Distributed Loads.* IEEE Transactions

on Ultrasonics, Ferroelectrics and Frequency Control, Vol. 48, No. 4, pp. 976-984, July 2001.

28. S. K. Ha. *Analysis of the asymmetric triple-layered piezoelectric bimorph using equivalent circuit models.* Journal of the Acoustical Society of America, Vol. 110, No. 2, pp. 856-864, August 2001.

29. H. Tanaka. *Generalized basic equations for bending motions of piezoelectric bars formulated from Hamilton's principle.* Journal of the Acoustical Society of America, Vol. 95, No. 4, April 1994.

30. J. A. Mitchell; J. N. Reddy. *A Refined Hybrid Plate Theory for Composite Laminates with Piezoelectric Laminae.* International Journal of Solids and Structures, Vol. 32, pp. 2345-2367, 1995.

31. C. Y. K. Chee; L. Tong; G. P. Steven. *A mixed model for composite beams with piezoelectric actuators and sensors.* Smart Materials and Structures, Vol. 8, pp. 417-432, 1999.

32. Q. Wang; S. T. Quek. *Flexural vibration analysis of sandwich beam coupled with piezoelectric actuator.* Smart Materials and Structures, Vol. 9, pp. 103-109, 2000.

33. S. K. Ha; Y. H. Kim. *Analysis of a Piezoelectric Multimorph in Extensional and Flexural Motions.* Journal of Sound and Vibration, Vol. 253, No. 5, pp. 1001-1014, 2002.

34. A. Ballato. *Network Representation for Piezoelectric Bimorphs.* IEEE Transactions on Ultrasonics, Ferroelectrics and Frequency Control, Vol. 38, No. 6, pp. 595-602, 1991.

35. S. Sherrit; H. D. Wiederick; B. K. Mukherjee; M. Sayer. *An accurate equivalent circuit for the unloaded piezoelectric vibrator in the thickness mode.* Journal of Applied Physics, Vol. 30, pp. 2354-2363, 1997.

36. H. A. C. Tilmans. *Equivalent circuit representation of electromechanical transducers: II. Distributed-parameter systems.* Journal of Micromechanics and Microengineering, Vol. 7, pp. 285-309, 1997.

37. R. Aoyagi; H. Tanaka. *Equivalent Circuit Analysis of Piezoelectric Bending Vibrators.* Journal of Applied Physics, Vol. 33, pp. 3010-3014, 1994.

38. A. E. Holman; W. C. Heerens; F. Tuinstra. *Using capacitive sensors for in situ calibration of displacements in a piezo-driven translation stage of an STM.* Sensors & Actuators A, Vol. 36, No. 1, pp. 37-42, 1993.

39. R. A. Callafon; D. H. F. Harper; R. E. Skelton; F. E. Talke. *Experimental Modeling and Feedback Control of a Piezobased Milliactuator.* Journal of Information Storage & Processing Systems, Vol. 1, pp. 217-224, 1999.

40. K. Kuhnen; H. Janocha. *Nutzung der inhärenten sensorischen Eigenschaften von piezoelektrischen Aktoren.* tm - Technisches Messen, Oldenbourg Verlag, Vol. 66, Iss. 04, pp. 132-138, 1999.

41. S. Leleu; H. Abou-Kandil; Y. Bonnassieux. *Piezoelectric Actuators and Sensors Location for Active Control of Flexible Structures.* IEEE Transactions on Instrumentation and Measurement, Vol. 50, No. 6, pp. 1577-1582, December 2001.

42. J. Han; I. Lee. *Optimal placement of piezoelectric sensors and actuators for vibration control of a composite plate using genetic algorithms.* Smart Materials and Structures, Vol. 8, pp. 257-267, 1999.

43. W. J. Manning; A. R. Plummer; M. C. Levesley. *Vibration control of a flexible beam with integrated actuators and sensors.* Smart Materials and Structures, Vol. 9, pp. 932-939, 2000.

44. H. Shen. *Analysis of beams containing piezoelectric sensors and actuators.* Smart Materials and Structures, Vol. 3, pp. 439-447, 1994.

45. I. Bruant; G. Coffignal; F. Lene. *A Methodology for Determination of Piezoelectric Actuator and Sensor Location on Beam Structures.* Journal of Sound and Vibration, Vol. 243, pp. 861-882, 2001.

46. Young-Sik Kim; Hyo-Jin Nam; Seong-Moon Cho; Dong-Chun Kim; Jong-Uk Bu. *A self-actuating PZT cantilever integrated with piezoresistor sensor for AFM with high speed parallel operation.* The 15th IEEE International Conference on MEMS, pp. 689-692, January 2002.

47. T. Takigami; K. Oshima; Y. Hayakawa. *Application of self-sensing actuator to control of a cantilever beam.* ACC 1997, American Control Conference, Albuquerque, pp. 1867-1872, June 1997.

48. A. F. Vaz. *Composite Modeling of Flexible Structures with Bonded Piezoelectric Film Actuators and Sensors.* IEEE Transactions on Instrumentation and Measurement, Vol. 47, No. 2, April 1998.

49. H. Abramovich. *Deflection control of laminated composite beams with piezoceramic layers - closed form solutions.* Composite Structures, Vol. 43, pp. 217-231, 1998.

50. K. Furutani; M. Urushibata; N. Mohri. *Displacement control of piezoelectric element by feedback of induced charge.* Nanotechnology, Vol. 9, pp. 93-98, 1998.

51. Lien-Wen Chen; Chung-Yi Lin; Ching-Cheng Wang. *Dynamic stability analysis and control of a composite beam with piezoelectric layers.* Composite Structures, Vol. 56, pp. 97-109, 2002.

52. U. Gabbert; H. Köppe; T. N. Trajkov. *Entwurf intelligenter Strukturen unter Einbeziehung der Regelung.* Automatisierungstechnik, Vol. 50, pp. 432-438, 2002.

53. Bor-Tsuen Wang; Chung-Chei Wang. *Feasibility analysis of using piezoceramic transducers for cantilever beam modal testing.* Smart Materials and Structures, Vol. 6, pp. 106-116, 1997.

54. S. Fahlbusch; S. Fatikow. *Force sensing in microrobotic systems - an overview.* IEEE International Conference on Electronics, Circuits and Systems, Vol. 3, pp. 259-262, September 1998.

55. K. Furutani; M. Urushibata; N. Mohri. *Improvement of Control for Piezoelectric Actuator by Combining Induced Charge Feedback with Inverse Transfer Function Compensation.* IEEE International Conference on Robotics and Automation, Vol. 2, pp. 1504-1509, May 1998.

56. Y. K. Kang; H. C. Park; J. Kim; Seung-Bok Choi. *Interaction of active and passive vibration control of laminated composite beams with piezoceramic sensors/actuators.* Materials and Design, Vol. 23, pp. 277-286, 2002.

57. K. Kuhnen; H. Janocha. *Inverse Steuerung für den Großsignalbetrieb von Piezoaktoren.* Automatisierungstechnik, Vol. 50, pp. 439-450, 2002.

58. C. Lee; T. Itoh; T. Suga. *Micromachined Piezoelectric Force Sensors Based on PZT Thin Films.* IEEE Transactions on Ultrasonics, Ferroelectrics and Frequency Control, Vol. 43, pp. 553-559, July 1996.

59. M. Goldfarb; N. Celanovic. *Modeling Piezoelectric Stack Actuators for Control of Micromanipulation.* IEEE Control Systems Magazine, Vol. 17, Iss. 3, pp. 69-79, June 1997.

60. P. J. Costa Branco; J. A. Dente. *On the electromechanics of a piezoelectric transducer using a bimorph cantilever undergoing asymmetric sensing and actuation.* Smart Materials and Structures, Vol. 13, pp. 631-642, 2004.

61. A. Kugi; K. Schlacher. *Passivitätsbasierte Regelung piezoelektrischer Strukturen.* Automatisierungstechnik, Vol. 50, pp. 422-431, 2002.

62. S. V. Gosavi; A. G. Kelkar. *Passivity-based Robust Control of Piezo-actuated Flexible Beam.* ACC 2001, American Control Conference, Albuquerque, pp. 2492-2497, June 2001.

63. G. Schitter; R. W. Stark; A. Stemmer. *Sensors for closed-loop piezo control: strain gauges versus optical sensors.* Measurement Science and Technology, Vol. 13, pp. N47-N48, 2002.

64. G. S. Choi; Y. A. Lim; G. H. Choi. *Tracking position control of piezoelectric actuators for periodic reference inputs.* Mechatronics, Vol. 12, pp. 669-684, 2002.

65. Chien-Chang Lin; Huang-Nan Huang. *Vibration control of beam-plates with bonded piezoelectric sensors and actuators.* Computers and Structures, Vol. 73, pp. 239-248, 1999.

66. A. J. Schmid. *Aufbau und Charakterisierung von smarten piezokeramischen Multilayer-Biegewandlern mit integrierter Auslenkungs- und Kraftsensorik.* Technische Universität Darmstadt, FB 18, Elektrotechnik und Informationstechnik, Dissertation D 17, pp. 12-13, 2005.

67. A. J. Schmid. *Aufbau und Charakterisierung von smarten piezokeramischen Multilayer-Biegewandlern mit integrierter Auslenkungs- und Kraftsensorik.* Technische Universität Darmstadt, FB 18, Elektrotechnik und Informationstechnik, Dissertation D 17, 2005.

68. P. Curie; J. Curie. *Contractions et dilations produits par des tensions électriques dans les cristeaux hémieèdres à faces inclineés.* Comptes Rendus de l'Académie des Sciences, 93, pp. 1137-1140, 1881.

69. M. G. Lippmann. *Principe de la conservation de l'électricité.* Annales de Chimie et de Physique , 5, p. 159, 1881.

70. J. Wehr. *Temperaturabhängige Untersuchungen zum mikroskopischen und makroskopischen Dehnungsverhalten von akzeptor- und donatordotierten PZT-Keramiken.* Universität Karlsruhe (TH), Fakultät für Maschinenbau, Dissertation, pp. 13-14, 2003.

71. D. Zhou. *Experimental Investigation of Non-linear Constitutive Behaviour of PZT Piezoceramics.* Forschungszentrum Karlsruhe, Wissenschaftliche Berichte, FZKA 6869, Dissertation, pp. 6-12, 2003.

72. S. Hackemann. *Ortsaufgelöste röntgendiffraktometrische Charakterisierung von Domänenumklappvorgängen in ferroelektrischen Keramiken.* Universität Karlsruhe (TH), Fakultät für Maschinenbau, Dissertation, pp. 8-10, 2001.

73. G. Krüger. *Untersuchung der Domänenprozesse und der Koerzitivkraft ferroelektrischer PLZT 6/65/35-Keramik.* Universität Karlsruhe (TH), Fakultät für Elektrotechnik, Dissertation, 1975.

74. A. Schäufele. *Ferroelastische Eigenschaften von Blei-Zirkonat-Titanat-Keramiken.* Fortschritt-Berichte VDI Reihe 5, Nr. 445, VDI-Verlag, Düsseldorf, 1996.

75. K. Kuhnen. *Inverse Steuerung piezoelektrischer Aktoren mit Hysterese-, Kriech- und Superpositionsoperatoren.* Shaker Verlag, pp. 7-14, Aachen, 2001.

76. M. Fischer. *Mikromechanische piezoelektrische Hörer.* Shaker Verlag, pp. 12-13, Aachen, 2001.

77. A. J. Schmid. *Aufbau und Charakterisierung von smarten piezokeramischen Multilayer-Biegewandlern mit integrierter Auslenkungs- und Kraftsensorik.*

Technische Universität Darmstadt, FB 18, Elektrotechnik und Informations-technik, Dissertation D 17, pp. 41-43, 2005.

78. R. Werthschützky; G. Pfeifer; A. Lenk. *Elektromechanische Systeme*. Springer-Verlag, pp. 234-236, Heidelberg, 2001.

79. H. J. Schreiner; R. Binding; G. Helke. *Characterization of Piezoelectric Multi-layer Actuators: Low- and High Field Behaviour*. 7th International Conference on New Actuators, Actuator 2000, Bremen, June 2000.

80. R. Solecki; R. J. Conant. *Advanced Mechanics of Materials*. Oxford University Press, pp. 196-201, New York, 2003.

81. R. Solecki; R. J. Conant. *Advanced Mechanics of Materials*. Oxford University Press, p. 60, New York, 2003.

82. T. Weiland. *Technische Elektrodynamik I*. Vorlesungsskript, Institut Theorie Elektromagnetischer Felder, TU Darmstadt, p. 2.65, 2002.

83. H. Frohne. *Elektrische und magnetische Felder*. B. G. Teubner, pp. 148-151, Stuttgart, 1994.

84. G. Strassacker. *Rotation, Divergenz und das Drumherum*. 4. Auflage. B. G. Teubner, p. 258, Stuttgart Leipzig, 1999.

85. G. B. Arfken; H. J. Weber. *Mathematical method for physicists*. 4th ed. Academic Press, pp. 58-59, San Diego, 1995.

86. E. Hering; R. Martin; M. Stohrer. *Physik für Ingenieure*. 4. Auflage. VDI-Verlag, p. 160, 1992.

87. M. L. Boas. *Mathematical Methods in the Physical Sciences*. 2nd ed. John Wiley & Sons, pp. 189-190, New York, 1983.

88. H. Stoecker. *Taschenbuch der Physik*. 3. Auflage. Verlag Harri Deutsch, p. 81, Frankfurt am Main, 2001.

89. A. Lindner. *Grundkurs Theoretische Physik*. Teubner Studienbücher, 2. Auflage. B. G. Teubner, pp. 557-559, Stuttgart, 1996.

90. J. Tichy; G. H. Gautschi. *Piezoelektrische Messtechnik*. Springer-Verlag, Berlin, 1980.

91. H. F. Tiersten. *Linear Piezoelectric Plate Vibrations - Elements of the Linear Theory of Piezoelectricity and the Vibrations of Piezoelectric Plates*. Plenum Press New York, pp. 51-61, 1969.

92. R. Markert. *Einführung in die Technische Mechanik*. Vorlesungsskript, Fachbereich Mechanik, TU Darmstadt, pp. 62-63, 2002.

93. H. Dankert; J. Dankert. *Technische Mechanik*. 2. Auflage. B. G. Teubner, pp. 199-201, Stuttgart, 1995.

94. C. M. Wang; J. N. Reddy; K.H. Lee. *Shear Deformable Beams and Plates*. Elsevier Science Ltd., pp. 14-15, Oxford, 2000.

95. G. Pfeifer. *Piezoelektrische lineare Stellantriebe*. Wissenschaftliche Schriftenreihe der Technischen Hochschule Karl-Marx-Stadt, Bd. 6, pp. 17-19, 1982.

96. W. Nolting. *Grundkurs Theoretische Physik 2, Analytische Mechanik*. 5. Auflage. Springer-Verlag, p. 112, Heidelberg, 2002.

97. W. Greiner. *Theoretische Physik, Mechanik Teil 2*. 6. Auflage. Verlag Harri Deutsch, pp. 406-411, Frankfurt am Main, 1998.

98. H. Dankert; J. Dankert. *Technische Mechanik*. 2. Auflage. B. G. Teubner, pp. 404-414, Stuttgart, 1995.

99. H. Dankert; J. Dankert. *Technische Mechanik*. 2. Auflage. B. G. Teubner, pp. 618-620, Stuttgart, 1995.

100. R. Solecki; R. J. Conant. *Advanced Mechanics of Materials*. Oxford University Press, pp. 245-248, New York, 2003.

101. H. Dankert; J. Dankert. *Technische Mechanik*. 2. Auflage. B. G. Teubner, pp. 637-642, Stuttgart, 1995.

102. R. P. Feynman; R. B. Leighton; M. Sands. *The Feynman Lectures on Physics*. 6th ed. Addison-Wesley Publishing Company, pp. 38-9 - 38-11, Massachusetts, 1977.

103. H. Clausert; G. Wiesemann. *Grundgebiete der Elektrotechnik 1*. 5. Auflage. Oldenbourg Verlag, pp. 171-172, München, 1992.

104. R. Werthschützky; G. Pfeifer; A. Lenk. *Elektromechanische Systeme*. Springer-Verlag, pp. 229-231, Heidelberg, 2001.

105. W. Nolting. *Grundkurs Theoretische Physik 2, Analytische Mechanik*. 5. Auflage. Springer-Verlag, p. 2, Heidelberg, 2002.

106. R. Greve. *Theoretische Mechanik*. Vorlesungsskript, Fachbereich Mechanik, TU Darmstadt, pp. 126-128, 2001.

107. G. B. Arfken; H. J. Weber. *Mathematical method for physicists*. 4th ed. Academic Press, p. 633, San Diego, 1995.

108. C. B. Lang; N. Pucker. *Mathematische Methoden in der Physik*. Spektrum Akademischer Verlag, pp. 132-135, Heidelberg, 1998.

109. W. Greiner. *Theoretische Physik, Mechanik Teil 2*. 6. Auflage. Verlag Harri Deutsch, pp. 382-385, Frankfurt am Main, 1998.

110. R. Greve. *Theoretische Mechanik*. Vorlesungsskript, Fachbereich Mechanik, TU Darmstadt, pp. 131-133, 2001.

111. W. Nolting. *Grundkurs Theoretische Physik 2, Analytische Mechanik*. 5. Auflage. Springer-Verlag, p. 30, Heidelberg, 2002.

112. W. Greiner. *Theoretische Physik, Mechanik Teil 2*. 6. Auflage. Verlag Harri Deutsch, pp. 351-353, Frankfurt am Main, 1998.

113. H. F. Tiersten. *Linear Piezoelectric Plate Vibrations - Elements of the Linear Theory of Piezoelectricity and the Vibrations of Piezoelectric Plates*. Plenum Press New York, p. 44, 1969.

114. J. E. Sader. *Frequency response of cantilever beams immersed in viscous fluids with applications to the atomic force microscope*. Journal of Applied Physics, Vol. 84, No. 1, July 1998.

115. S. T. Smith. *Flexures - Elements of Elastic Mechanisms*. Taylor & Francis Group, pp. 124-129, Massachusetts, 2000.

116. N. N. Rogacheva. *The Theory of Piezoelectric Shells and Plates*. CRC Press, p. 140, Boca Raton, 1994.

117. K. Burg; H. Haf; F. Wille. *Höhere Mathematik für Ingenieure, Band 3*. 3. Auflage. B. G. Teubner, pp. 237-244, Stuttgart, 1993.

118. C. B. Lang; N. Pucker. *Mathematische Methoden in der Physik*. Spektrum Akademischer Verlag, pp. 469-481, Heidelberg, 1998.

119. M. Abu-Hilal. *Forced vibration of Euler-Bernoulli beams by means of dynamic Green functions*. Journal of Sound and Vibration, Vol. 267, pp. 191-207, 2003.

120. S. P. Timoshenko; W. Weaver; D. H. Young. *Vibration problems in engineering*. 5th ed. John Wiley & Sons , p. 418, New York, 1990.

121. W. Soedel. *Vibrations of shells and plates*. 2nd ed. Marcel Dekker, pp. 73-76, New York, 1993.

122. Y. Tang. *Numerical Evaluation of Uniform Beam Modes*. Journal of Engineering Mechanics, Vol. 129, No. 12, December 2003.

123. H. Lutz; W. Wendt. *Taschenbuch der Regelungstechnik*. Verlag Harri Deutsch, p. 76, Leipzig, 1995.

124. A. Lenk. *Elektromechanische Systeme, Band 2*. 2. Auflage. VEB Verlag Technik, p. 197, Berlin, 1977.

125. W. Soedel. *Vibrations of shells and plates*. 2nd ed. Marcel Dekker, p. 75, New York, 1993.

126. S. P. Timoshenko; W. Weaver; D. H. Young. *Vibration problems in engineering*. 5th ed. John Wiley & Sons , p. 421, New York, 1990.

127. M. Abu-Hilal. *Forced vibration of Euler-Bernoulli beams by means of dynamic Green functions*. Journal of Sound and Vibration, Vol. 267, pp. 191-207, 2003.

128. S. P. Timoshenko; W. Weaver; D. H. Young. *Vibration problems in engineering*. 5th ed. John Wiley & Sons , pp. 419-422, New York, 1990.

129. L. Papula. *Mathematik für Ingenieure und Naturwissenschaftler, Band 2*. 7. Auflage. Vieweg Verlag, p. 487, Wiesbaden, 1994.

130. K. F. Riley; M. P. Hobson; S. J. Bence. *Mathematical Methods for Physics and Engineering*. 2nd ed. Cambridge University Press, pp. 412-413, Cambridge, 1998.

131. R. Greve. *Theoretische Mechanik*. Vorlesungsskript, Fachbereich Mechanik, TU Darmstadt, pp. 49-53, 2001.

132. P. A. Tipler. *Physik*. Spektrum Akademischer Verlag, pp. 406-408, Heidelberg, 1995.

133. R. Werthschützky; G. Pfeifer; A. Lenk. *Elektromechanische Systeme*. Springer-Verlag, p. V, Heidelberg, 2001.

134. A. Lenk. *Elektromechanische Systeme, Band 1*. 2. Auflage. VEB Verlag Technik, pp. 156-157, Berlin, 1973.

135. G. Schroth. *Die näherungsweise Darstellung eines Biegestabes durch konzentrierte Schaltelemente*. Hochfrequenztechnik und Elektroakustik 77 H.3, p. 83, 1968.

136. A. Lenk. *Elektromechanische Systeme, Band 1*. 2. Auflage. VEB Verlag Technik, p. 157, Berlin, 1973.

137. R. Werthschützky; G. Pfeifer; A. Lenk. *Elektromechanische Systeme*. Springer-Verlag, p. 155, Heidelberg, 2001.

138. A. Lenk. *Elektromechanische Systeme, Band 2*. 2. Auflage. VEB Verlag Technik, pp. 52-53, Berlin, 1977.

139. S. P. Timoshenko; W. Weaver; D. H. Young. *Vibration problems in engineering*. 5th ed. John Wiley & Sons , pp. 416-432, New York, 1990.

140. S. M. Han; H. Benaroya; T. Wei. *Dynamics of Transversely Vibrating Beams Using Four Engineering Theories*. Journal of Sound and Vibration, Vol. 225, No. 5, pp. 935-988, March 1999.

141. R. Werthschützky; G. Pfeifer; A. Lenk. *Elektromechanische Systeme*. Springer-Verlag, p. 81, Heidelberg, 2001.

142. A. Lenk. *Elektromechanische Systeme, Band 2*. 2. Auflage. VEB Verlag Technik, p. 254, Berlin, 1977.

143. R. Werthschützky; G. Pfeifer; A. Lenk. *Elektromechanische Systeme*. Springer-Verlag, pp. 187-190, Heidelberg, 2001.

144. H. Lutz; W. Wendt. *Taschenbuch der Regelungstechnik*. Verlag Harri Deutsch, pp. 108-111, Leipzig, 1995.

145. S. Nolte. *Messplatz für Piezo-Biegeaktoren*. Technische Universität Darmstadt, FB 18, Elektrotechnik und Informationstechnik, Studienarbeit, 2002.

146. H. R. Tränkler; E. Obermeier. *Sensortechnik*. Springer-Verlag, pp. 571-572, Heidelberg, 1998.

147. A. Kolb. *Automatisierung eines Messplatzes für Miniatur-Piezo-Biegeaktoren mittels LabVIEW*. Technische Universität Darmstadt, FB 18, Elektrotechnik und Informationstechnik, Studienarbeit, 2004.

148. A. J. Schmid. *Aufbau und Charakterisierung von smarten piezokeramischen Multilayer-Biegewandlern mit integrierter Auslenkungs- und Kraftsensorik*. Technische Universität Darmstadt, FB 18, Elektrotechnik und Informationstechnik, Dissertation D 17, 2005.

149. W. Schatt. *Einführung in die Werkstoffwissenschaft*. 7. Auflage. Deutscher Verlag für Grundstoffindustrie, pp. 352-354, Leipzig, 1991.

150. K. Kuhnen. *Inverse Steuerung piezoelektrischer Aktoren mit Hysterese-, Kriech- und Superpositionsoperatoren*. Shaker Verlag, pp. 16-17, Aachen, 2001.

151. S. P. Timoshenko; W. Weaver; D. H. Young. *Vibration problems in engineering*. 5th ed. John Wiley & Sons , pp. 52-53, New York, 1990.

152. C. Gerthsen; H. O. Kneser; H. Vogel. *Physik*. 16. Auflage. Springer-Verlag, pp. 140-141, Heidelberg, 1989.

153. S. P. Timoshenko; W. Weaver; D. H. Young. *Vibration problems in engineering*. 5th ed. John Wiley & Sons , pp. 57-58, New York, 1990.

154. L. Merz; H. Jaschek. *Grundkurs der Regelungstechnik*. 13. Auflage. Oldenbourg Verlag, pp. 89-90, München, 1996.

155. R. Werthschützky; G. Pfeifer; A. Lenk. *Elektromechanische Systeme*. Springer-Verlag, pp. 30-31, Heidelberg, 2001.

156. A. Kolb. *Automatisierung eines Messplatzes für Miniatur-Piezo-Biegeaktoren mittels LabVIEW*. Technische Universität Darmstadt, FB 18, Elektrotechnik und Informationstechnik, Studienarbeit, 2004.

157. R. G. Ballas. *Linearittsfehler bei der Erfassung der Auslenkung piezoelektrischer Biegeaktoren mit integriertem kapazitiven Dehnungssensor*. Mechatronik 2005, Innovative Produktentwicklung, VDI-Berichte, Nr. 1892.2, VDI-Verlag, pp. 981-993, Düsseldorf, 2005.

158. Hoerbiger-Origa Systems GmbH. *Piezo-Technologie, Ex-Eigensichere 3/2-Wege-Sitzventile*. Katalog Piezo Ventile, Altenstadt.

159. T. Ikeda. *Fundamentals of Piezoelectricity*. Oxford University Press, pp. 1-30, New York, 1990.

160. W. G. Cady. *Piezoelectricity - An Introduction to the Theory and Applications of Electromechanical Phenomena in Crystals*. McGraw-Hill, pp. 282-283, London, 1946.

161. A. J. Schmid. *Aufbau und Charakterisierung von smarten piezokeramischen Multilayer-Biegewandlern mit integrierter Auslenkungs- und Kraftsensorik*. Technische Universität Darmstadt, FB 18, Elektrotechnik und Informationstechnik, Dissertation D 17, pp. 3-4, 2005.

162. R. G. Ballas. *Hocheffektive Miniatur-Piezo-Biegeaktorsysteme mit integrierter Sensorik, Ansteuer- und Auswerteelektronik*. 40 Jahre Institut für Elektromechanische Konstruktionen - Von der Elektromechanik zur Mechatronik und Mikrosystemtechnik, TUD-Schriftenreihe Wissenschaft und Technik, Band 85, pp. 146-152, Darmstadt, 2003.

163. R. G. Ballas; H. F. Schlaak; A. Kolb; A. Mössinger; P. Meissner; A. J. Schmid; U. Töpfer; H. Murmann-Biesenecker; G. Munz; M. Maichl. *High-Accuracy Sensor Electronics for Deflection Measurement of a Piezoelectric Bending Beam Multilayer Actuator*. Actuator 2004, 9th International Conference on New Actuators, Bremen, pp. 60-63, June 2004.

164. A. J. Schmid. *Aufbau und Charakterisierung von smarten piezokeramischen Multilayer-Biegewandlern mit integrierter Auslenkungs- und Kraftsensorik.* Technische Universität Darmstadt, FB 18, Elektrotechnik und Informationstechnik, Dissertation D 17, pp. 69-72, 2005.

165. A. J. Schmid. *Aufbau und Charakterisierung von smarten piezokeramischen Multilayer-Biegewandlern mit integrierter Auslenkungs- und Kraftsensorik.* Technische Universität Darmstadt, FB 18, Elektrotechnik und Informationstechnik, Dissertation D 17, pp. 85-92, 2005.

166. R. G. Ballas; H. F. Schlaak; A. J. Schmid. *Linearity Error of a High-Accuracy Electronic in Combination with an Integrated Capacitive Strain Sensor for Deflection Measurements of a Piezoelectric Beam Multilayer Actuator.* Sensor 2005, 12th International Conference, Nürnberg, pp. 67-72, May 2005.

167. U. Tietze; Ch. Schenk. *Halbleiterschaltungstechnik.* 11. Auflage. Springer-Verlag, pp. 1203-1205, Heidelberg, 1999.

168. L. Papula. *Mathematik für Ingenieure und Naturwissenschaftler, Band 2.* 7. Auflage. Vieweg Verlag, pp. 340-348, Wiesbaden, 1994.

169. R. Werthschützky. *Mess- und Sensortechnik, Elektrisches Messen mechanischer Größen, Band 1.* Vorlesungsskript, Institut für Elektromechanische Konstruktionen, TU Darmstadt, pp. 4/7-4/9, 2002.

170. R. Werthschützky. *Mess- und Sensortechnik, Elektrisches Messen mechanischer Größen, Band 1.* Vorlesungsskript, Institut für Elektromechanische Konstruktionen, TU Darmstadt, pp. 4/9-4/10, 2002.

171. P. Kejk; C. Kluser; R. Bischofberger; R. S. Popovic. *A Low-Cost Inductive Proximity Sensor for Industrial Applications.* Sensors & Actuators A, Vol. 110, pp. 93-97, 2004.

172. R. G. Ballas; P. F. Greiner; H. F. Schlaak; A. J. Schmid. *Piezoelectric Bending Actuators with Integrated Capacitive and Inductive Sensors for Deflection Measurement.* 7. GMA-Kongress - Automation als interdisziplinäre Herausforderung, VDI/VDE-Gesellschaft Mess- und Automatisierungstechnik, Baden-Baden, pp. 319-326, June 2005.

173. E. O. Doebelin. *Measurement Systems Application and Design.* 3rd ed. McGraw-Hill, New York, 1983.

174. H. Stoecker. *Taschenbuch der Physik.* 3. Auflage. Verlag Harri Deutsch, p. 560, Frankfurt am Main, 2001.

175. T. Weiland. *Technische Elektrodynamik I.* Vorlesungsskript, Institut Theorie Elektromagnetischer Felder, TU Darmstadt, p. 6.1, 2002.

176. P. F. Greiner. *Design and Calibration of a New Integrated Inductive Proximity Sensor.* Studienarbeit, École Polytechnique Fédérale de Lausanne, Institute of Microelectronics and Microsystems, Schweiz, pp. 4-6, 2004.

177. H. Clausert; G. Wiesemann. *Grundgebiete der Elektrotechnik 2.* 2. Auflage. Oldenbourg Verlag, pp. 146-148, München, 1992.

178. H. Clausert; G. Wiesemann. *Grundgebiete der Elektrotechnik 2.* 2. Auflage. Oldenbourg Verlag, pp. 154-155, München, 1992.

179. T. Weiland. *Technische Elektrodynamik I.* Vorlesungsskript, Institut Theorie Elektromagnetischer Felder, TU Darmstadt, pp. 5.5-5.6, 2002.

180. E. Zeidler. *Teubner-Taschenbuch der Mathematik.* B. G. Teubner, p. 376, Stuttgart, 1996.

181. I. N. Bronstein; K. A. Semendjajew. *Taschenbuch der Mathematik.* 25. Auflage. B. G. Teubner, p. 575, Stuttgart, 1991.

182. J. Vine. *Impedance of a Coil Placed Near to a Conducting Sheet.* Journal of Electronics and Control, Vol. 16, No. 1, pp. 569-577, 1964.

183. C. B. Lang; N. Pucker. *Mathematische Methoden in der Physik.* Spektrum Akademischer Verlag, pp. 451-453, Heidelberg, 1998.

184. H. Fischer; H. Kaul. *Mathematik für Physiker.* Teubner Studienbücher. B. G. Teubner, p. 94, Stuttgart, 1998.

185. H. Lindner; H. Brauer; C. Lehmann. *Taschenbuch der Elektrotechnik und Elektronik.* 6. Auflage. Fachbuchverlag Leipzig, p. 83, Leipzig, 1995.

186. E. W. Marchant; J. L. Miller. *The Loss of Energy in Metal Plates of Finite Thickness due to Eddy Currents Produced by Alternating Magnetic Fields.* Proceedings of the Royal Society of London, Series A, Vol. 111, pp. 604-614, 1926.

187. P. F. Greiner. *Design and Calibration of a New Integrated Inductive Proximity Sensor.* Studienarbeit, École Polytechnique Fédérale de Lausanne, Institute of Microelectronics and Microsystems, Schweiz, p. 60, 2004.

188. P. F. Greiner. *Design and Calibration of a New Integrated Inductive Proximity Sensor.* Studienarbeit, École Polytechnique Fédérale de Lausanne, Institute of Microelectronics and Microsystems, Schweiz, p. 55, 2004.

189. R. Werthschützky. *Mess- und Sensortechnik, Elektrisches Messen mechanischer Größen, Band 1.* Vorlesungsskript, Institut für Elektromechanische Konstruktionen, TU Darmstadt, pp. 4/19-4/31, 2002.

190. E. Zeidler. *Teubner-Taschenbuch der Mathematik.* B. G. Teubner, p. 66, Stuttgart, 1996.

191. H. Schaumburg. *Werkstoffe und Baulemente der Elektrotechnik, Band 3.* Sensoren. B. G. Teubner, pp. 139-141, Stuttgart, 1992.

192. P. A. Tipler. *Physik.* Spektrum Akademischer Verlag, pp. 765-768, Heidelberg, 1995.

193. K. Hoffmann. *Eine Einführung in die Technik des Messens mit Dehnungsmessstreifen.* Hottinger Baldwin Messtechnik GmbH, pp. 1-13, Darmstadt, 1987.

194. H. R. Tränkler; E. Obermeier. *Sensortechnik.* Springer-Verlag, pp. 332-334, Heidelberg, 1998.

195. H. Schaumburg. *Werkstoffe und Baulemente der Elektrotechnik, Band 3.* Sensoren. B. G. Teubner, pp. 150-165, Stuttgart, 1992.

196. K. Hoffmann. *Eine Einführung in die Technik des Messens mit Dehnungsmessstreifen.* Hottinger Baldwin Messtechnik GmbH, pp. 62-64, Darmstadt, 1987.

197. G. W. Farnell; I. A. Cermak; P. Silvester; S. K. Wong. *Capacitance and Field Distributions for Interdigital Surface-Wave Transducers.* IEEE Transactions on Sonics and Ultrasonics, Vol. SU-17, No. 3, July 1970.

198. R. Werner. *Entwicklung einer Auswerteelektronik für induktive Sensoren auf einem piezoelektrischen Biegewandler.* Technische Universität Darmstadt, FB 18, Elektrotechnik und Informationstechnik, Studienarbeit, 2004.

199. K. Küpfmüller; G. Kohn. *Theoretische Elektrotechnik und Elektronik.* 14. Auflage. Springer-Verlag, pp. 286-291, Heidelberg, 1993.

200. H. F. Schlaak. *Mikrotechnische Systeme.* Vorlesungsskript, Institut für Elektromechanische Konstruktionen, TU Darmstadt, pp. 145-147, 2003.

201. K. Simonyi. *Theoretische Elektrotechnik.* 7. Auflage. VEB Deutscher Verlag der Wissenschaften, p. 362, Berlin, 1979.

202. J. Franz. *Methods to Measure Small Capacitances with High Resolution.* tm - Technisches Messen, Oldenbourg Verlag, Vol. 67, Iss. 04, pp. 177-181, 2000.

203. D. Marioli; E. Sardini; A. Taroni. *Measurement of Small Capacitance Variations.* IEEE Conference on Precision Electromagnetic Measurements, pp. 22-23, June 1990.

204. S. M. Huang; C. G. Xie; R. Thorn; D. Snowden; M. S. Beck. *Design of Sensor Electronics for Electrical Capacitance Tomography.* Circuits, Devices and Systems, IEEE Proceedings G, pp. 83-88, February 1992.

205. S. M. Huang; R. G. Green; A. Plaskowski; M. S. Beck. *A High Frequency Stray-Immune Capacitance Transducer Based on the Charge Transfer Principle.* IEEE Transactions on Instrumentation and Measurement, Vol. 37, Iss. 3, pp. 368-373, September 1988.

206. S. M. Huang; A. L. Stott; R. G. Green; M. S. Beck. *Electronic Transducers for Industrial Measurement of Low Value Capacitances.* Journal of Physics E: Scientific Instruments, Vol. 21, pp. 242-250, 1988.

207. R. C. Jaeger. *Microelectronic Circuit Design.* International Edition. McGraw-Hill, pp. 498-500, New York, 1997.

208. K. Burg; H. Haf; F. Wille. *Höhere Mathematik für Ingenieure, Band 4.* 2. Auflage. B. G. Teubner, pp. 538-541, Stuttgart, 1994.

209. S. A. Nasar. *2000 Solved Problems in Electromagnetics.* Schaum's Outline Series. McGraw-Hill, pp. 86, New York, 1992.

210. P. A. Tipler. *Physik.* Spektrum Akademischer Verlag, pp. 848-850, Heidelberg, 1995.

211. T. Weiland. *Technische Elektrodynamik I.* Vorlesungsskript, Institut Theorie Elektromagnetischer Felder, TU Darmstadt, p. 3.5, 2002.

212. A. Gray; G. B. Mathews; T. M. MacRoberts. *A Treatise on Bessel Functions and their Applications to Physics.* 2nd ed. MacMillan and Co., p. 64, London, 1952.

213. E. Zeidler. *Teubner-Taschenbuch der Mathematik.* B. G. Teubner, p. 175, Stuttgart, 1996.

214. N. W. McLachlan. *Bessel Functions for Engineers.* 2nd ed. Oxford University Press, p. 33-34, London, 1955.

215. M. L. Boas. *Mathematical Methods in the Physical Sciences.* 2nd ed. John Wiley & Sons, p. 514, New York, 1983.

216. N. W. McLachlan. *Bessel Functions for Engineers.* 2nd ed. Oxford University Press, p. 11, London, 1955.

Index